

21

Mechanical Testing of Solid Materials at the Micro-Scale

by

Sauri Gudlavalleti

B. Tech, Mechanical Engineering (1999)
Indian Institute of Technology, Madras

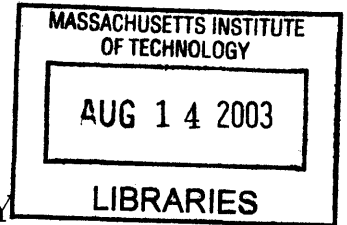
Submitted to the Department of Mechanical Engineering
in partial fulfillment of the requirements for the degree of

Master of Science in Mechanical Engineering

at the

MASSACHUSETTS INSTITUTE OF TECHNOLOGY

February 2002



© Massachusetts Institute of Technology 2002. All rights reserved.

Author

Department of Mechanical Engineering

January 18, 2002

Certified by..

.....
Lallit Anand

Professor of Mechanical Engineering

Thesis Supervisor

Accepted by

Ain A Sonin

Chairman, Department Committee on Graduate Students

ARCHIVES

Mechanical Testing of Solid Materials at the Micro-Scale

by

Sauri Gudlavalleti

Submitted to the Department of Mechanical Engineering
on January 18, 2002, in partial fulfillment of the
requirements for the degree of
Master of Science in Mechanical Engineering

Abstract

Successful design and fabrication of structures and systems at the micro-scale requires a sound theoretical understanding and reliable experimental data on the mechanical behavior of materials at that scale. Generation of experimental data requires accurate, robust, reliable, versatile and yet simple micro-scale mechanical testing devices.

This thesis describes the design, development and applications of materials testing technologies at the micro-scale. Using the rectilinear travel characteristics of compound flexures, two novel testing machines have been designed and built to conduct tension, bending and indentation tests in the force regime of $10 \mu\text{N}$ - 35 N and displacement regime of 20 nm - 6 mm . These machines have been used in measuring the mechanical properties of free-standing gold thin films, rolled metallic foils, elastomeric fibers and other materials. Numerical simulations of the mechanical behavior of gold thin films and rolled copper foils have been conducted and compared with experimental results. Microstructural investigations into deformation mechanisms of the free-standing gold thin films have also been conducted.

Thesis Supervisor: Lallit Anand

Title: Professor of Mechanical Engineering

Acknowledgments

The work presented herein would not have been possible without the support I gained from many quarters. It is my foremost duty to thank them all.

My deepest sense of gratitude is to my advisor Prof. Lallit Anand whose guidance, resourcefulness, encouragement and patience have enabled me make my years spent at MIT some of my most exciting. Working with him, I have grown - I look forward to a life-long association with him.

My special appreciation to Brian P Gearing, my constant companion in the journey through the world of micro-mechanical materials testing, for his terrific support.

Sincere thanks to Prof. Sharvan Kumar (Brown University) , Mr. Randy Jezowski (Ramco Machine LLC) and Jinh Yi (MIT Mechanics and Materials) for experimental support and many fruitful discussions during my projects.

I am deeply grateful to Ray Hardin and Leslie Regan, for doing everything possible to facilitate my work.

Instrumental in my work, were the excellent facilities provided by MIT's Microsystems Technologies Laboratories (ICL & TRL), Center for Materials Science & Engineering, Central Machine Shop, Pappalardo Laboratories and Laboratory for Manufacturing and Productivity.

I sincerely acknowledge the financial support provided by the MIT Rosenblith Fellowship, the Singapore-MIT Alliance, and ONR-DURINT.

My labmates, Nicoli Ames, Jeremy Levitan, Rajdeep Sharma, Cheng Su and Prakash Thamburaja were all involved, in ways more than one, in my research. It was a pleasure working in such a collaborative environment. Computer administration with Mats Danielsson was enjoyable as ever. These and the other students of Mechanics and Materials have provided me some of my most intellectually challenging and memorable years as a student. I wish them all success in their endeavors.

Finally, my greatest sense of appreciation is to my family across the globe for their selfless sacrifice, unerring love and support that helped me accomplish what I have achieved.

Contents

1	Introduction	21
2	Development of Micromechanical Testing Technologies	25
2.1	Introduction	25
2.2	Mechanical Testing at the Small Scale	26
2.3	A brief survey of some existing testing machines	30
2.4	Development of an improved testing machine	31
2.4.1	Leaf Spring Mechanisms	32
2.4.2	A Flexure-Based Testing Machine	34
2.4.3	Load and Displacement Control	35
3	Low Load Testing Machine	41
3.1	Design and construction of low load testing machine	41
3.1.1	Selection of Specifications and Components	41
3.1.2	Design and Fabrication of the Testing Frame	44
3.1.3	Grips and Fixtures	45
3.1.4	Data acquisition and control	47
3.2	Characterization of the Machine	47
3.2.1	Load Cell Calibration	47
3.2.2	Machine Compliance	48
3.3	Machine Validation	48
3.3.1	Tensile testing of aluminum foil	49
3.3.2	Bend Testing of Steel Strip	51

4	High Load Testing Machine	67
4.1	Design and Construction	67
4.1.1	Design Features, Specifications and Components	67
4.1.2	Grips and Fixtures	69
4.1.3	Data Acquisition and Control	70
4.1.4	Calibration	71
4.1.5	Machine Compliance	71
4.2	Verification Tests: Tensile Testing of Stainless Steel and Aluminum Foils	71
5	Mechanical Response of Free-Standing Gold Thin Films	85
5.1	Introduction	85
5.1.1	Literature Review	86
5.2	Specimen Preparation and Characterization	92
5.2.1	Specimen preparation	92
5.2.2	TEM investigations	92
5.2.3	Crystallographic texture	93
5.3	Microtensile testing	93
5.4	Results and Discussion	94
5.5	Simulations	95
5.6	TEM of deformed films	98
5.7	Membrane bend-stretching experiments and simulations	98
5.7.1	Experiments	99
5.7.2	Analysis and prediction	99
5.8	Conclusions	101
6	Anisotropy of Roller Copper Foil using Microtensile Testing	117
6.1	Introduction	117
6.2	Specimen Preparation	118
6.3	Measurement of Crystallographic Texture	119
6.4	Testing Procedure and Results	119
6.5	Simulations	120

6.6	Conclusions	122
7	Other Applications	129
7.1	Mechanical Behavior of Nanocrystalline Ni Alloys	129
7.2	Instrumented Indentation of Aluminum 6061	131
7.3	Tensile Testing of an Elastomeric Fibers	131
8	Closure	143
A	Equations for Flexure Mechanisms	151
B	Low Load Testing Machine: Operation Manual	157
B.1	General Operating Procedure	157
B.2	Special Instruction for Tensile Testing of Gold Thin Film Specimens .	162
B.3	Extended Displacement Range	166
B.4	Bill of Materials	167
B.5	Specifications	168
C	Low Load Testing Machine: Technical Drawings	171
D	High Load Testing Machine: Operation Manual	191
D.1	General Operating Procedure	191
D.2	Loading Rate Calculation	196
D.3	Bill of Materials	198
D.4	Specifications	199
E	High Load Testing Machine: Technical Drawings	201
E.1	Fabrication of Free Standing Gold Thin Films	218
F	MATLAB Script for Membrane Bend-Stretching Calculation	225

List of Figures

1-1	Force and displacement regimes in micro-scale mechanical testing . . .	22
2-1	JHU Microtensile Testing Machine	37
2-2	Harvard Microtensile Testing Machine	37
2-3	Schematic sketches of flexure mechanisms	38
2-4	Schematic of flexure based testing machine	39
2-5	Equivalent spring diagram of the flexure-based testing system	39
3-1	MIT Mechanics and Materials Low Load Testing Machine	52
3-2	Close-up of low load testing machine.	53
3-3	Flexures left attached to frame for subsequent machining.	53
3-4	Testing machine in various orientations with respect to gravity.	54
3-5	Foil tension grips	55
3-6	Three-point bend assembly	56
3-7	Indentation assembly	57
3-8	Calibration fixtures for low-load LCF	58
3-9	Load cell calibration graph low-load testing machine	59
3-10	Equivalent spring diagram of testing machine including machine compliance	60
3-11	Engineering drawing of foil tension specimen	61
3-12	Machine compliance test	62
3-13	Force-displacement graph obtained from tensile testing of 16.51 μm thick Aluminum foil	63

3-14 True Stress - true strain graph obtained from tensile testing of 16.51 μm thick Aluminum foil	64
3-15 Procedure for obtaining “effective” specimen gage length	65
3-16 Analytical estimation of over-all stiffness of an elastic dogbone shaped specimen from its geometry	65
3-17 Force-displacement graph from 3-point bend test of steel strip	66
4-1 High load testing machine.	73
4-2 Close-up of the specimen stage region in the high load testing machine.	74
4-3 A cut away view of the high load testing machine showing assembly of the foil tension grips.	75
4-4 Insulating tension grips on high load testing machine	76
4-5 Bow-tie shaped tensile specimen geometry	77
4-6 Multiple-span bend fixtures	78
4-7 LCF calibration graph for high load testing machine	79
4-8 ACF calibration graph for high load testing machine	80
4-9 Engineering drawing of modified foil tension specimen. All current grips and fixtures are made for this geometry.	81
4-10 Stress-strain graph from tensile test on 25.4 μm thick stainless steel sheet.	82
4-11 Stress-strain graph from tensile test on 25.4 μm thick Aluminum foil.	83
4-12 Foil tension specimen gripped in machine (Photograph by Cheng Su)	83
4-13 Stress-strain graph of aluminum foil measured by non-contact measurement	84
5-1 (a) Free-standing aluminum thin film tensile specimen; (b) Testing machine configuration. (From Read <i>et.al</i> [37])	103
5-2 Length scales affecting material strength: (a) Microstructural constraints; (b) Dimensional constraints. (From Arzt [2])	103
5-3 Figure showing a single threading dislocation on a slip plane in a constrained thin film	104

5-4	Free-standing gold thin film tensile specimen, Type A (long). Numbers in parentheses are corresponding dimensions for type B (short) specimens. All dimensions are in mm.	105
5-5	Photograph showing gold thin film specimen	105
5-6	TEM images of as-received gold thin film (TEM by Prof. K. Sharvan Kumar)	106
5-7	Crystallographic texture of gold thin films (popLA pole figure representation): (a) Measured, (b) Numerical fit (334 crystals), (c) Numerical fit (44 crystals) (Pole figure measurement and representations courtesy Prakash Thamburaja)	107
5-8	Micro-mechanical testing machine	108
5-9	Photograph showing gold thin film specimen mounted in testing machine (side arms unbroken).	108
5-10	Tensile test results: Force-displacement response of (a) 4 mm specimen; (b) 2.5 mm specimen.	109
5-11	Tensile tests with loading-unloading cycles: (a) on a 4 mm specimen; (b) on a 2.5 mm specimen.	109
5-12	Procedure for obtaining “effective” specimen gage length	110
5-13	Stress-strain graphs from tensile tests: (a) on a 4 mm specimen; (b) on a 2.5 mm specimen.	110
5-14	Stress-strain graphs from tensile tests with unload-reload cycles	111
5-15	ABAQUS finite element mesh used in simulating response of gold thin film specimen. Mesh consists of 1 layer of 76 elements.	111
5-16	Fit of simulation to experimental force-displacement data (short specimen).	112
5-17	Stress-strain response. Stress-strain calculated from an interior element in the simulations is compared with experimental results converted using the L_{eff} method	113

5-18	TEM images of deformed gold thin film: (a) & (b) Images showing dislocation activity, (c) Image showing pile-up at grain boundary, (d) Image showing no dislocation activity in a 100 nm grain (TEM by Prof. K. Sharvan Kumar)	114
5-19	Schematic of the set-up used for membrane bending experiments on the gold thin film specimens.	115
5-20	Schematic free-body diagram of the membrane bending experiments on the gold thin film specimens.	115
5-21	Experimental response and numerical prediction of roller force-displacement response during membrane bending experiments: (a) comparison of data on the long specimen; (b) comparison of data on short specimen.	116
6-1	Crystallographic texture of rolled copper foil	123
6-2	Photograph showing foil tensile specimen clamped in testing machine (Photograph by Cheng Su)	123
6-3	Force-displacement curves from several tensile tests on rolled copper foil in rolling and transverse directions	124
6-4	Stress-strain graphs from tensile tests on rolled copper foil in rolling and transverse directions	125
6-5	Finite element mesh used for simulate force-displacement response of copper foil specimens	125
6-6	Comparison between experimental and simulated force-displacement responses	126
6-7	Stress-strain response of one of the rolled foil as obtained from one of the interior elements in the finite element simulation.	127
7-1	Stress-strain graphs from tension test on 14 μm thick nanocrystalline Ni-20%Fe foil	133
7-2	Stress-strain graphs from tension test on 40 μm thick nanocrystalline Ni-20%Fe foil	134

7-3	Stress-strain graphs from tension test on 45 μm thick nanocrystalline Ni foil	135
7-4	P-h curves from indentation on polished nano-Ni foil glued to an aluminum substrate.	136
7-5	Images of micro-indent in nano-Ni foil	137
7-6	Force - depth of penetration response of Al 6061 indentation.	138
7-7	Force-displacement graph from tensile test on a group of 11 thermoset elastomer fibers	139
7-8	Nominal stress-stretch graph from tensile test on a group of 11 thermoset elastomer fibers	140
7-9	Force-displacement graph from tensile test on 100 μm diameter thermoset elastomer fibers	141
A-1	Free body diagram of simple flexure	152
B-1	Photograph showing inchworm installed in testing machine	157
B-2	Close-up photo of specimen stage area in low load testing machine showing displacement and force position sensors and foil tension grips during installation.	158
B-3	Screen-shot of LabVIEW virtual instrument for acquiring data from the low load testing machine.	160
B-4	Screen-shot of LabVIEW virtual instrument for controlling the Burleigh inchworm.	161
B-5	Thin film tensile specimen mounting procedure	164
C-1	Part GS 0200-01. Low load testing machine flexure frame (Sheet 1 of 3)	172
C-2	Part GS 0200-01. Low load testing machine flexure frame (Sheet 2 of 3).	173
C-3	Part GS 0200-01. Low load testing machine flexure frame: Close up of specimen stages (Sheet 3 of 3).	174
C-4	Part GS 0200-02. Calibration fixtures. Assembly shown in Fig. 3-8. .	175
C-5	Part GS 0200-03. L-Brackets for general mounting purposes.	176

C-6	Part GS 0200-04. Bend testing fixture (bottom).	177
C-7	Part GS 0200-05. 3-Point Bend testing fixture. Replaced by GS1201-01	178
C-8	Part GS 1201-01. Modified 3-Point Bend testing fixture.	179
C-9	Part GS 0200-06. 4-Point Bend testing fixture.	180
C-10	Part GS 0200-07. Nutplate for mounting inchworm.	181
C-11	Part GS 0200-08 and 09. Locks to prevent movement of flexures during set-up.	182
C-12	Part GS 0500-03. Flat faced clamps for foil specimens.	183
C-13	Part GS 0500-05. Mounting blocks for thin film specimens	184
C-14	Part GS 0500-07. Thin film mounting dock, provides an ex-situ speci- men mounting station.	185
C-15	Part GS 0601-08. Foil tension grip with slot for specimens with 3 mm wide grip section. Assembly shown in Fig. (3-5.)	186
C-16	Part GS 0601-08. Foil tension grip clamp. Assembly shown in Fig. (3-5.)	187
C-17	Part GS 0900-01. Adapter to fix indenter head onto low load testing machine. Assembly shown in Fig. (3-7.)	188
C-18	Part GS 0900-02. Indentation specimen stage. Assembly shown in Fig. (3-7.)	189
D-1	Close-up of specimen stage region in high load testing machine showing displacement sensors and foil tension grips.	192
D-2	Multi-span bend fixtures installed in high load testing machine. As- sembly is shown in Fig. 4-6	192
E-1	Part GS 1100-05. High load testing machine flexure frame (Sheet 1 of 2)	202
E-2	Part GS 1100-05. High load testing machine flexure frame (Sheet 2 of 2)	203
E-3	Part GS 0201-02. High load testing machine frame base plate	204
E-4	Part GS 0201-03. High load testing machine frame support stand-offs	205
E-5	Part GS 0201-04. High load testing machine bearing mount	206

E-6	Part GS 0301-04. High load testing machine voice coil mount	207
E-7	Part GS 0601-01. Foil tension grip (bottom grip). Ref. Fig. 4-3 for an assembly drawing	208
E-8	Part GS 0601-02. Clamp for foil tension grip. Ref. Fig. 4-3 for an assembly drawing	209
E-9	Part GS 0601-03. Nutplate for grips and fixtures	210
E-10	Part GS 1100-03. Grip for bowtie shaped tension specimen. These grips need to be used in association with Part. GS1100-01 or GS0601- 01. Ref. Fig. 4-4 for an assembly drawing.	211
E-11	Part GS 1100-04. Clamp for bowtie shaped tension specimen. These grips need to be used in association with Part. GS1100-01 or GS0601- 01. Ref. Fig. 4-4 for an assembly drawing.	212
E-12	Part GS 1100-01. Insulation plate for use with Part GS1100-03, 04 or other appropriately designed grips. Ref. Fig. 4-4 for an assembly drawing.	213
E-13	Part GS 1100-02. Insulating nut-plate for use with Part GS1100-03, 04 or other appropriately designed grips. Ref. Fig. 4-4 for an assembly drawing.	214
E-14	Part GS 0601-06. Multiple span bending fixtures. Ref. Fig. 4-6 for an assembly drawing.	215
E-15	Part GS 0601-05. 4 Point bend fixture with 8 mm span for use in the multiple span bending fixtures. Ref. Fig. 4-6 for an assembly drawing.	216
E-16	Part GS 0500-01 and 02. Fixtures to mount displacement sensors lo- cally on the specimen stages, for example, in the multispan bend fix- tures, when the fixture blocks the designated sensor mount. Ref. Fig. 4-6 for an assembly drawing.	217
E-17	Arrangement of tensile specimens on a 4" wafer	221
E-18	Unit cell for backside mask. Dimensions are in mm.	222
E-19	Unit cell for backside mask. Dimensions are in mm.	223
E-20	Expose under backside mask.	223

E-21	The wafer now has a hard mask of nitride on the backside, and the patterned gold film on the front side.	223
E-22	Anisotropic etch of wafer using KOH.	224
E-23	Final step: Removal of nitride film.	224

List of Tables

2.1	Small-scale actuators	28
2.2	Small-scale position sensors	29

Chapter 1

Introduction

Recent trends in materials research indicate rapid growth in production and implementation of small-scale systems (*e.g.*, MEMS, microfluidic devices, nanotechnology) with characteristic lengths ranging from several nm to several mm. It is well recognized that lack of standardized experimental methods for materials characterization at this scale is one of the key limitations in the robust design of micro and nano systems [43]. While commercially available testing equipment cater to the ultra-fine regime of total displacements and forces $O(10\ \mu\text{m}, 1\ \text{N})$ and below, and the coarse regime of $O(10^2\ \mu\text{m}, 10^2\ \text{N})$ and above, there is a distinct dearth of testing machines for the meso-scale of displacements and forces $O(10^{-1}\text{-}10^3\ \mu\text{m}, 10^{-3}\text{-}10\ \text{N})$ which are encountered in applications such as microtensile testing of micron-sized films, foils and wires, bending of mm sized beams and micro-indentation (Fig. 1-1). For example: (i) microtensile testing of a 1 mm wide, 1 μm thick metallic film upto stresses of 500 MPa requires 0.5 N; (ii) generation of a stress of 1 GPa in a 12 mm long, 6 mm wide strip of 500 μm thick silicon wafer by 4 point bending requires a force of 30 N; (iii) Berkovich micro-indentation of a sample of aluminum 6061 to a depth of 10 μm requires a force of the order of 1 N.

The previous experiments (See, *e.g.* Ruud *et al.* [39], Read *et al.* [38]; Sharpe *et al.* [40]) in this very important range for MEMS applications, have been conducted on testing machines which use complex assemblies of moving parts which limit the degree of precision which is attainable. Difficulties encountered in micro-scale me-

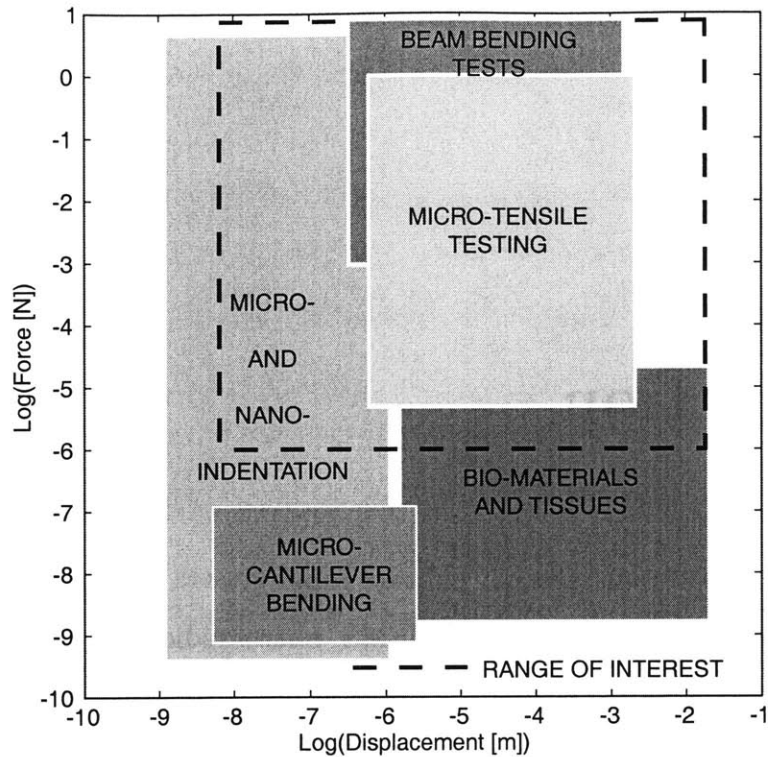


Figure 1-1: Force and displacement regimes in micro-scale mechanical testing of materials.

mechanical testing of materials include the application and measurement of small forces and displacements and the fabrication, handling, alignment and fixturing of small specimens.

In the present work, an elaborate attempt to address some of the issues arising in micro-mechanical materials testing is made. A novel, simple and high resolution micro-mechanical testing machine is developed in chapter 2. Two versions, operating in different load regimes, a low force regime of $10 \mu\text{N} - 1.5 \text{ N}$, and a high force regime of $0.5 \text{ mN} - 35 \text{ N}$, are designed and constructed. The details of these machines are provided in chapters 3 and 4.

The low-load testing machine is used in a study of the mechanical behavior of free-standing thin films of gold in the thickness range $500 - 700 \text{ nm}$. Chapter 5 describes the stress-strain response of these films obtained from microtensile and membrane bend-stretch tests.

Chapters 6 and 7 report studies conducted on several other materials using the low-

load and high load testing machines. Detailed drawings and operating instructions for the testing machines are provided in the appendices.

Chapter 2

Development of Micromechanical Testing Technologies

2.1 Introduction

The first step in the investigation of mechanical properties of materials is the development of suitable experimental techniques to characterize the material behavior. While mechanical testing at the bulk level is a well developed field, there is a distinct lack of robust methods of material evaluation at the small scale. Experimental methods are required to obtain the elastic, plastic, fracture, fatigue and interfacial properties of materials synthesized and used in dimensions $O(\text{nm} - \text{mm})$. Such properties are typically obtained from tension tests, torsion tests, 3 and 4 point bend tests, indentation tests and friction tests.

The primary focus of this research is to develop test methods for free standing thin films, foils and fibers at the meso-size scale where the specimen sizes are in the $\mu\text{m} - \text{mm}$ range. Examples of materials chosen for this study are free-standing e-beam deposited gold films ($0.5 \mu\text{m} - 1.5 \mu\text{m}$ thick), rolled copper and aluminum foils ($10 \mu\text{m} - 25 \mu\text{m}$ thick), electro-deposited nanocrystalline foils ($5 \mu\text{m} - 40 \mu\text{m}$ thick), and metallic fibers ($50 \mu\text{m}$ to $250 \mu\text{m}$ in diameter). The geometry of the specimen is chosen based on several factors such as desired deformation/stress state, availability of material, ease of handling, method of gripping, feasibility and tolerance

of fabrication techniques. In general, in-plane dimensions of specimens are expected to be $O(\text{mm})$. Anticipated stress-strain levels in these materials indicate that one might encounter forces ranging from several tens of micronewtons to several tens of Newtons. Maximum specimen elongations could be between 0.01 mm and 1 mm. Very few testing machines are currently available to test at this meso-scale of μN - N and μm - mm. The purpose of this report is to present our new testing machine and representative results that may be obtained by their use.

2.2 Mechanical Testing at the Small Scale

Mechanical testing of materials involves five subsystems:(a) the specimen; (b) a fixturing system to hold the specimen; (c) an actuation system to apply a prescribed load or displacement history; (d) a load cell to measure the force being carried by the specimen; and (e) a system to measure the specimen deformation. Mechanical testing of materials at the small scale places some very special demands on each of these systems. The material to be tested is often available only in limited quantities, and in predetermined forms, such as wire, foil or film. This places stringent requirements on the specimen design and fabrication process, as well as fixturing. The forces and displacements encountered are likely to be small, and often test the resolution limits of the actuation and measurement systems. What follows is a brief discussion of each these subsystems and the special requirements placed on these subsystems by small scale testing.

Specimen

Design and fabrication of the test specimen is the most critical part of experimental investigation of a material's mechanical behavior. The specimen shape and dimensions must be chosen such that the desired stress/strain state is induced from the applied boundary conditions. It must conform to the fixturing system and be convenient to handle. The fabrication process must be chosen so as to minimize damage to the specimen while maintaining dimensional tolerances. Wire electro discharge machining (EDM), die-punching, shearing and grinding are some of the techniques

in fabricating micro-specimens from foil stock. When material quantity is limited, specimens and fabrication processes must be designed to minimize wastage. However, dimensions must be large enough to minimize the boundary effects due to fabrication and fixturing.

Specimen Fixturing

The specimen fixturing system has two parts (called cross heads), one to interface with the actuation system and the other with the load measurement system. The specimen spans the cross heads. This system must ensure coaxiality of the specimen with the other components of the testing machine. Mechanical, hydraulic or pneumatic clamping are commonly used methods to fixture, or grip, a specimen for a uniaxial tension test. Bend specimens are supported and loaded by suitably arranged arrays of cylindrical rollers or mandrels. Specimen fixturing is relatively simple for indentation tests, and involves gluing or supporting the specimen on a flat surface precisely normal to the loading axis. The deformation of the fixturing system itself under the applied load is the major component of machine compliance, and must be minimized. For small-scale testing, assembly tolerances are high, and the simplest fixturing mechanisms are preferred. Damage to specimen and boundary effects of fixturing must be minimized. This is particularly important in tensile testing where positive gripping to avoid slipping is required. Very fragile specimens may be held by gluing. Mechanical clamping using conforming grips provides positive gripping for less fragile specimens.

Actuation System

The actuation system consists of a controlled actuator and a suitable bearing to transmit the forces and displacements generated by it to the specimen fixturing system. An actuation system is selected based on the required static and dynamic resolution and range of force and displacement. Small scale testing requires actuators that are compact and have fine resolutions, large dynamic range, minimal play, backlash, friction and other assembly-related errors. Typically used actuators include electromagnetic force coils, motor driven screws and various piezoelectric crystal based ac-

tuators ranging from simple stacks to inchworms and screw drives. Motor drives have a long displacement range but limited resolution and force capacity. They also often have play and backlash problems. Electromagnetic actuators are force controlled and are available for a wide range of forces and reasonable range of displacements. Simple piezoelectric stacks have a very high force capacity and displacement resolution over a very short displacement range. Other piezo-driven actuators, such as inchworms and picomotors have excellent displacement resolution and range and limited force capacity. Table 2.1 is a comparison of several common small-scale actuators.

Table 2.1: Small-scale actuators

Actuator type	Min. Incr. Disp. (μm)	Typical Range (mm)	Comments
Piezo-stack	0.001	0.05	Very low range
Inchworm (piezoelectric)	0.005	6	Compact, low speed
Picomotor TM (Piezo driven micrometer)	0.03	25	Low speeds
DC/Stepper motors	0.1	10	Backlash
Voice coils	-	10	Force controlled

The bearing system between the actuator and specimen fixturing system guides the actuation along the testing axis. Sliding stages, screw based systems, guide rails, guide posts, air bearings and flexures are commonly used bearing systems. Flexures are often used in precision actuators for their high repeatability.

Load Cell

The load cell is used to measure the force being carried by the specimen along the testing axis at any point of time. A load cell is typically an elastic element in series with the specimen. The Deflection or strain of this element is proportional to the applied force by a stiffness calibration factor. Most commercial load cells use strain gaged flexure elements. It is desirable that the load cell be substantially stiffer than the specimen itself, so that its own deflection under the applied load is not excessive, which might cause measurement and control difficulties. However low-force load cells

need to be significantly compliant compared to conventional load cells so that their deflection under very small forces is still measurable.

Deformation Measurement

The deformation measurement system measures the response of the specimen to the applied load in terms of dimensional changes. The most basic deformation measurement systems measure the relative displacements of the two crossheads. One of several small-scale position sensors surveyed in Table 2.2 may be used for this purpose.

Table 2.2: Small-scale position sensors

Sensor type	Typical Resolution (μm)	Typical Range (μm)	Comments
Capacitive	0.001	50	Very low range, high resolution
Inductive	0.02	1500	Compact, needs metallic target
Optical fiber	0.02	1500	Needs reflective surface
LVDT	1	5000	Large range, not compact

Crosshead displacement measurement is afflicted by machine compliance due to deformation of parts of the machine outside the specimen itself. The ideal deformation measurement system provides complete information about the deformation of every portion of the specimen in all directions. Some CCD camera based systems combined with image analysis algorithms come close to achieving this goal of full-field strain measurement. Other systems track the relative displacement of two suitably spaced points on the specimen. Such local strain measurement techniques are significantly more complex to implement on small specimens undergoing small changes in dimensions.

2.3 A brief survey of some existing testing machines

A survey of micro-tensile testers built and being used by other researchers provides useful information and guidance in the design and construction of our own system. Three representative systems are discussed: the microsample tensile tester at Johns Hopkins University developed by Sharpe *et.al*[40], the NIST microtensile testing machine developed by Read *et.al*[36] and the microtensile testing machine at Harvard University developed by Ruud *et. al.* [39].

A schematic of the JHU microtensile testing machine is shown in Fig. 2-1. The machine consists of a motorized dovetail slide for the actuation system, a commercial 90 N load cell and facility for different types of tensile grips. The actuation system is gear reduced to rotate a lead screw that provides translation rates from 2 $\mu\text{m/s}$ to 20 $\mu\text{m/s}$. The end of the tensile grip mounted on this stage is supported by a linear air bearing to overcome friction. The other tensile grip is attached to the load cell. The inherent problem with such a system is its complexity. Insurance of high dimensional component and assembly tolerances, accuracy of travel and alignment is time consuming and expensive. Gears, lead screws and slides bring in play and backlash into the system. Depending on the nature of the specimen, it is held either by gluing or inserting into cutouts in the tensile grips and locking using a setscrew. The most innovative component of this testing system is the strain measurement, which is conducted by tracking interference fringes arising from two markings on the specimen defining a gage length. This Interferometric Strain/Displacement Gaging (ISDG) technique provides accurate information about strain unaffected by machine compliance.

The NIST microtensile tester is driven by two 60 mm long piezoelectric stacks acting as actuators. The specimen is fixtured between a fixed grip and a moving grip. The moving grip is carried on a load sensing cantilever beam with a load range of 1 N. The displacement of this cantilever beam, measured using non-contacting eddy current displacement sensor, is proportional to the load being carried by the

specimen. Specimen extension is measured by similar sensors that in terms of the displacement of the moving grip with respect to the fixed grip. In some experiments, a video recording system and optical microscopy are also used to observe specimen deformation. The limitation of such a system is the small displacement range of the piezoelectric actuator. The cantilever load sensing beam will be useful only for small deflections beyond which curvilinear travel of a cantilever beam affects the coaxiality of the testing axis and specimen extension.

The mechanical construction of the Harvard microtensile tester developed by Ruud *et. al.* and most other microtensile testers (*e.g.* [9] and [27]) is essentially similar to the JHU apparatus, with motor or piezo driven actuation and a commercial low force range load cell. The special feature of the Harvard microtensile tester is the strain measurement system. This is pictured in the schematic in Fig. 2-2. A regular square grid of dots previously patterned on the specimen is projected onto a screen using a laser system. The grid of dots is magnified during the projection. The movement of these projected dots is tracked to obtain information about both longitudinal and transverse strain over the entire specimen. While this is one of the closest implementations to full-field strain measurement, creating a regular pattern on the specimen adds extra steps to the fabrication process that might not always be convenient or desirable.

2.4 Development of an improved testing machine

The main problem in most of the above-described testing systems is seen to be the complexity of the assembly of the different subsystems. The current research aims to develop relatively simple testing systems without compromising performance. Inspired by their frequent use in precision positioning mechanisms, flexure elements were investigated as a candidate for the moving parts of the system. Flexures in moving systems are wear free and eliminate play and backlash and ensure high repeatability. The linear force-displacement characteristics of flexures also make them ideal candidates for force measurement, as used by Read [36] and in stylus profilom-

etry [42]. While there exist many kinds of flexures [42], this work focusses mainly on leaf-spring systems.

2.4.1 Leaf Spring Mechanisms

The simplest kind of leaf spring is a cantilever beam, shown in Fig. 2-3(a). Its stiffness k in terms of load P and deflection δ at the free end is given by:

$$k = \frac{P}{\delta} = \frac{3EI}{L^3} \quad (2.1)$$

where E is the Young's Modulus of the beam material, L is the length of the beam, and I is the area moment of inertia of the cross-section. The maximum stress σ in the beam due to the deflection is proportional to the deflection δ of the free end, and is given by:

$$\sigma_{max} = \frac{3Eh}{2L^2}\delta \quad (2.2)$$

The maximum allowable deflection δ of the flexure is hence determined by the yield strength σ_y (or fatigue strength σ_f) of the beam material, reduced by a suitable factor of safety S . However, the travel of the free end of a cantilever beam is curvilinear, with both a parasitic deflection (q) and a rotation (θ), also indicated in the figure. The rotation of the free end is given in terms of its deflection is given by Eq. 2.3:

$$\theta = \frac{PL^3}{2EI} \quad (2.3)$$

The simple leaf spring mechanism, shown in Fig. 2-3(b), on the other hand, is a linear system, where displacements are achieved with little (ideally, zero) rotations. The stiffness for this system is given by Eq. 2.4:

$$k = \frac{P}{\delta} = \frac{2AEI}{L^3} \quad (2.4)$$

Such a flexure mechanism is still not rectilinear, and exhibits some parasitic deflection. It is seen that the system, when loaded along the line through the ends of the parallel

leaf spring elements (P in Fig. 2-3) still behaves like a cantilever and has a small, but finite rotation. Experimental investigation of the curvilinear travel and rotations is detailed in Jones [17, 18]. It was found that a simple spring mechanism of length $L = 45$ mm and flexure separation $d = 24$ mm, when driven by $\delta = 1$ mm along P , gave a parasitic height variation q of $28.5 \mu\text{m}$ and a pitch of 30 seconds of arc. The parasitic deflection of 3% of travel could be significant for the application at hand. Nevertheless, it is possible to achieve very accurate translations over small displacements. Owing to his extensive work on these springs, they are often called Jones springs.

The curvilinear motion of the simple spring mechanism can be compensated by combining two simple springs in a more symmetrical design to produce the compound spring mechanism illustrated by Fig. 2-3(c). One simple spring mechanism is attached to the underside of the other. If all four leaf spring elements are identical in dimensions and material, application of the force P at the indicated location causes identical deflection of all four flexures. Consequently, any parasitic motion of platform A with respect to the fixed frame C will be equally compensated by an equal and opposite change in height of platform B with respect to A. The net effect is “perfectly” rectilinear travel of platform B with respect to the base C. The stiffness of such a mechanism will be half of that of a simple leaf spring mechanism since it is composed of two leaf springs in series (Eq. 2.5). Similarly, the maximum allowable travel will be double that of a simple leaf spring mechanism:

$$k = \frac{P}{\delta} = \frac{12EI}{L^3}, \quad (2.5)$$

$$\delta = \frac{2L^2\sigma_f}{3SEh}. \quad (2.6)$$

While flexures have the above-mentioned and other advantages, they also have some disadvantages. Flexures are susceptible to Euler (columnar) buckling due to forces along the length of the leaf springs. Out-of-plane stiffness of a leaf spring mechanism tends to be rather low. However, these are issues that could be circum-

vented by taking suitable precautions. The major difficulty with leaf spring mechanisms is the fabrication of such mechanisms. Assembly of components and errors could lead to significant deviations from desired behavior (Smith, 1990). One way to overcome these problems is the use of a monolithic structure. This requires close control during fabrication and so it is expensive to machine high quality monolithic leaf springs from plates. However, recent advancements in manufacturing technologies such as Wire Electro Discharge Machining and Abrasive Water Jet Machining have significantly improved tolerances and reduced fabrication times and costs for such monolithic mechanisms. This work takes extensive advantage of these machining techniques to develop the core components of the testing machines.

2.4.2 A Flexure-Based Testing Machine

Based on the concepts described in 2.2 and 2.4.1, a novel flexure-based testing machine has been conceived. Fig. 2-4 is a schematic of such a testing machine. The load cell is made of a relatively compliant, rectilinear compound flexure. One part of the specimen fixturing system is attached to this flexure. The specimen (SP) is hence loaded in series with this load cell flexure (LCF). The other end of the specimen is attached to another compliant rectilinear flexure, the actuation flexure (ACF). An appropriate actuator displaces the other end of the specimen through this ACF. The stiffness of the LCF is calibrated using dead-weights. The load carried by the specimen may be then obtained by measuring the displacement of the LCF using a high-resolution non-contact displacement sensor. Specimen extension can be measured in terms of cross-head displacement by placing non-contact displacement sensors on the ACF reading off of a target on the LCF. This arrangement also lends itself to the other forms of local strain measurement described previously.

For the range of flexure dimensions required in this research, it is convenient and advantageous to arrange all these components in a monolithic frame, as shown in the figure.

The advantages of a common testing frame consisting of a load cell and an actuator guide are many. First and foremost, the number of assembled components is

minimal. Integrated fabrication of the load cell and actuation guide ensures the best possible alignment of the travel axes of both components achievable by the best machining techniques. Conventional load cells are predominantly strain-gage based and have a limited range/resolution ratio. Several non-contact displacement measurement techniques allow much larger range/resolution ratio for this load cell.

This frame may be fabricated by machining all in-plane features by feeding a computer-generated outline into a computer-controlled abrasive water jet or wire electro discharge machine followed by other machining operations for out-of-plane features and finishing features. This constitutes a rapid and highly accurate method for fabricating the frame. Owing to this, it is easy to construct different machines for different load and displacement ranges by merely changing the design dimensions of the leaf springs. Due to the compactness of the monolithic frame, it is easy to orient the testing axis along or perpendicular to the ground, by tilting and rotating the entire frame. This makes it possible to make optimal use of gravity during the test, such as during specimen handling. The use of appropriate modular testing fixtures permits several tests, such as tension, 3 and 4 point bending, and indentation etc. All these are described in the following sections, where the design, development and applications of two implementations of this concept are detailed: A low load testing machine (25 μ N - 1.5 N range), and a mid-load testing machine (1 mN - 30 N range).

2.4.3 Load and Displacement Control

Fig. 2-5 is the equivalent spring diagram of this system. K_L and K_A are the stiffnesses of the LCF and ACF and specimen respectively, while δ_L and δ_A are the deflections of the LCF and ACF. K_S is the instantaneous tangent stiffness of the specimen when it has extended by δ_S . As can be seen from the figure, the force endured by the specimen is the same as the force deflecting the LCF, $K_L\delta_L$. The actuator driving the system applies a total force F_T given by

$$F_T = K_A\delta_A + K_L\delta_L \quad (2.7)$$

As the specimen behavior deviates from one of linear elasticity, its stiffness K_S changes depending on the tangent modulus of the specimen at each strain state. In other words K_S is a function of δ_S . However, for a given value of K_S , it is possible to relate *incremental* changes in the controllable stimulus F_T (or δ_T) to the desired response F_S and δ_S in order to be able to impose a prescribed load or displacement pattern on the specimen. The following expressions are derived by applying force balance to the various components in Fig. 2-5.

$$\frac{\Delta\delta_S}{\Delta F_T} = \frac{K_L}{K_L K_A + K_L K_S + K_A K_S} \quad (2.8)$$

$$\frac{\Delta\delta_S}{\Delta\delta_T} = \frac{K_L}{K_L + K_S} \quad (2.9)$$

In most conventional testing machines, $K_A \approx 0$, because the actuator is guided by low friction guides (air bearings, rollers etc), as opposed to resistive flexures, and $K_L \gg K_S$, *i.e.* the load cell is very stiff relative to the specimen. Under these conditions, $\Delta F_A \approx \Delta F_S$ and $\Delta\delta_A \approx \Delta\delta_S$. As a result, a desired force or displacement profile can be imposed on the specimen simply by prescribing the same to the actuator.

In the case of small-scale testing, the absolute displacement resolutions available influence the choice of K_L . Often, the resolution with which specimen extension δ_S is measured is usually close to the best achievable displacement resolution. Under such conditions, the resolution with which load cell deflection can be measured can not be much finer than this. Hence, $K_L (=F_S/\delta_L)$ can not be much higher than $K_S (=F_S/\delta_S)$. It is hence not always possible to ensure that $K_L \gg K_S$ in low-load testing. As a result, how an incremental force or displacement change in the actuator translates into a change in force or displacement for the specimen depends on the current stiffness of the specimen also. This may be continuously calculated during the progress of a test using the data gathered and used to determine force/displacement increments required from the actuator. However, for best results, force or position feedback control of the actuator is necessary in order to obtain the desired force or displacement profile in the specimen.

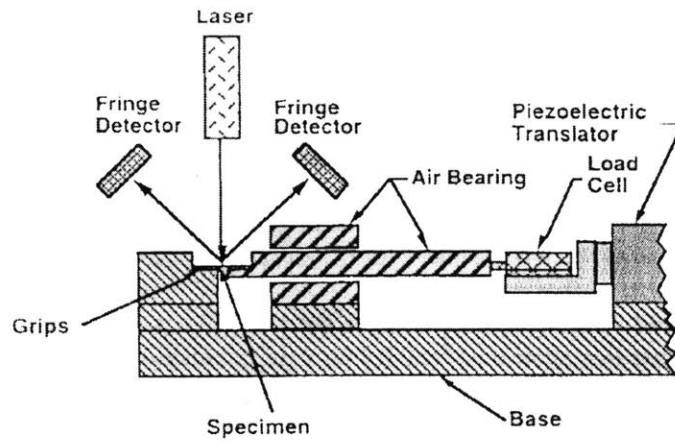


Figure 2-1: JHU Microtensile Testing Machine (Reproduced from [40]).

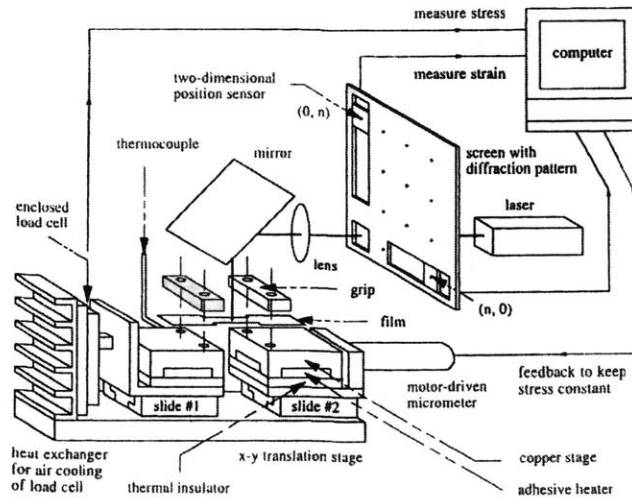


Figure 2-2: Harvard Microtensile Testing Machine (Reproduced from [16]).

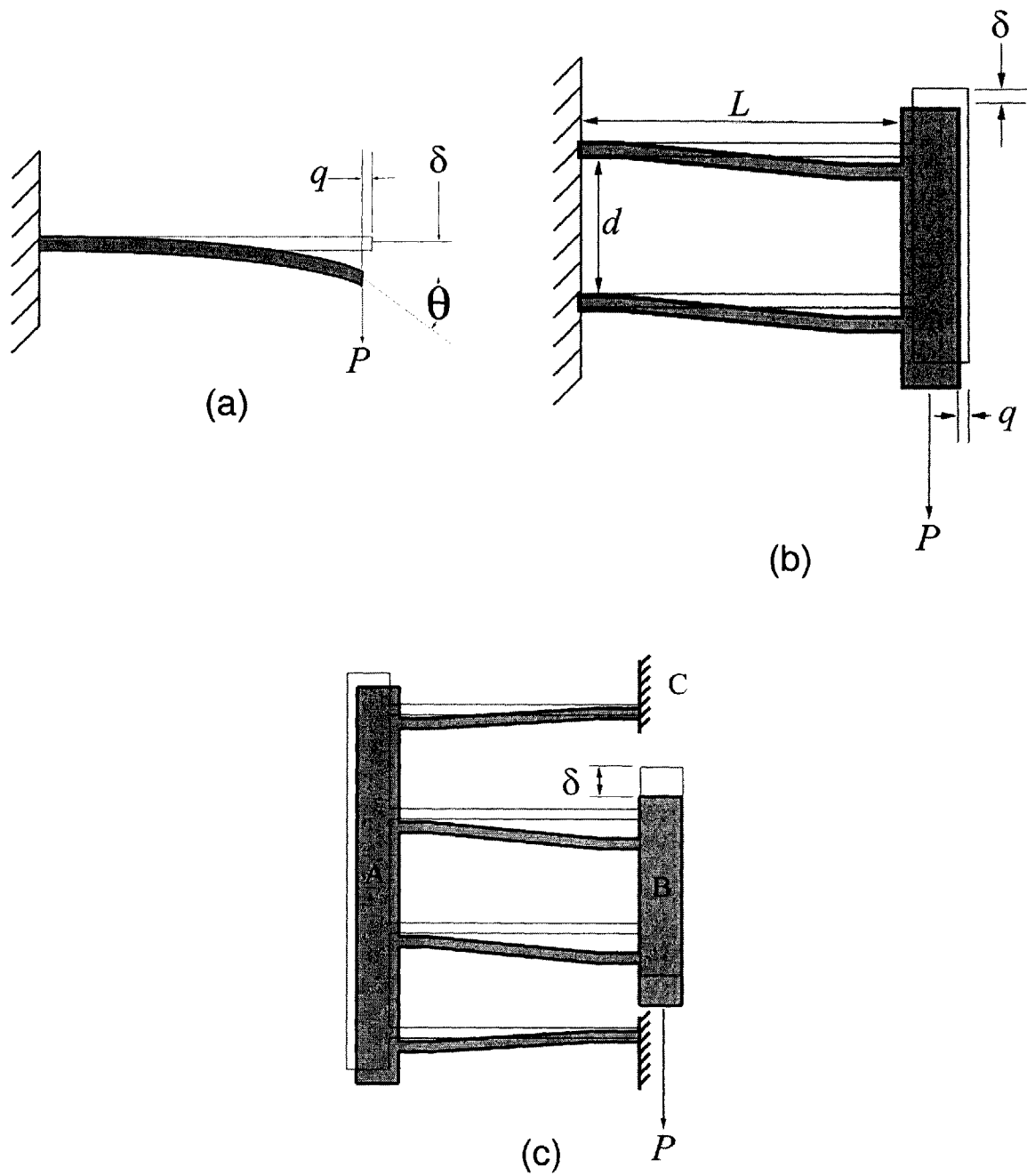


Figure 2-3: Flexure mechanisms: (a) Cantilever beam (b) Simple flexure (Jones spring) (c) Compound flexure.

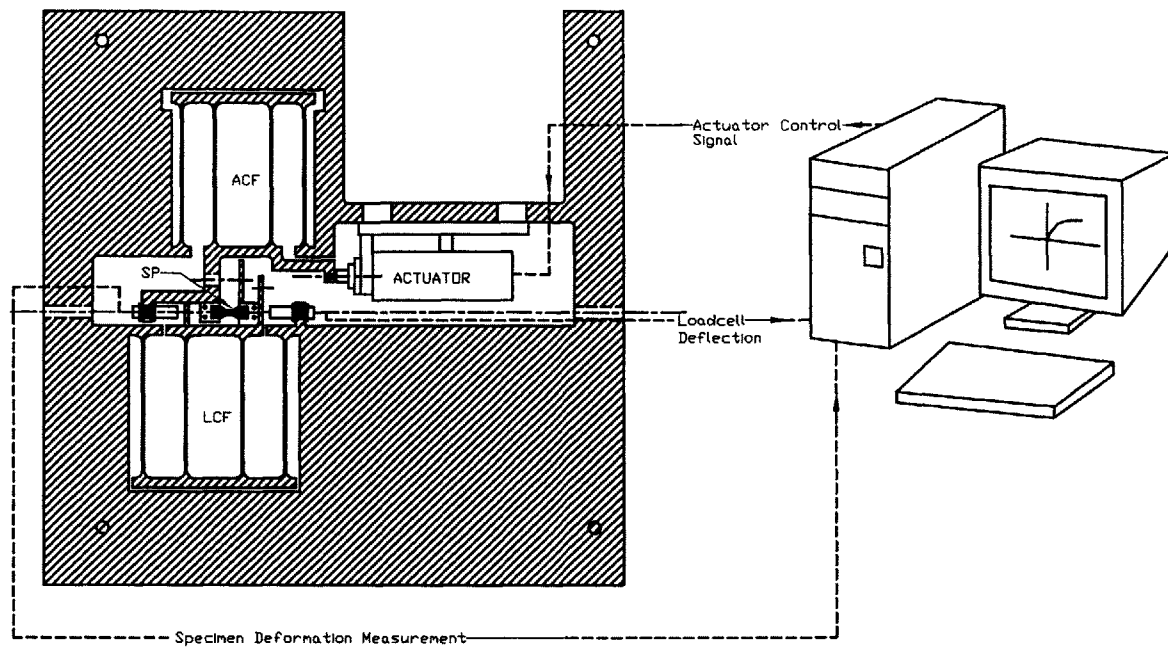


Figure 2-4: Schematic of flexure based testing machine

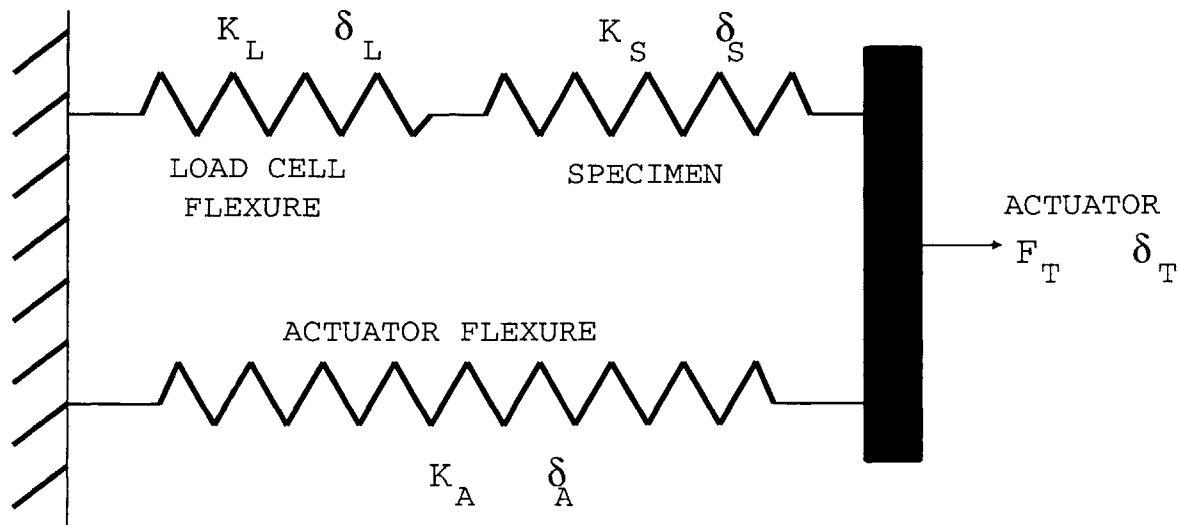


Figure 2-5: Equivalent spring diagram of the flexure-based testing system

Chapter 3

Low Load Testing Machine

The first implementation of the generic flexure-based testing machine concept discussed in chapter 2 is the low-load testing machine shown in Fig. 3-1. This machine is capable of applying and measuring forces up to 1.5 N with a resolution as fine as 25 μN and displacements up to 6.35 mm with resolutions up to 20 nm. The primary motivation behind a machine in this range comes from the need to test free-standing thin metallic films. This chapter discusses the design, construction and several applications of this machine.

3.1 Design and construction of low load testing machine

3.1.1 Selection of Specifications and Components

Specimen

In choosing a specimen to allow for, previous microtensile experiments [5, 16, 38] were studied. The largest specimens used were typically 1 mm wide and several millimeters in gage length. The testing machine is hence designed to provide a space of 30 mm x 10 mm x 10 mm for specimens and fixtures.

Displacement Sensors

One of the objectives in the design of this machine has been established as maximization of the range/resolution ratio. This is governed by the displacement sensors used in the load cell and for deformation measurement. For the specimens at hand, displacement ranges of the order of millimeters may be encountered. A non-contact sensor is required to measure LCF deflection. Any contact with the LCF could apply extraneous loads on it, which could be significant in the case of ultra-low load measurement. Referring to Table 2.2, inductive sensors present themselves as the ideal candidates for the present application, owing to their compactness, large range, high resolution and ease of use. After a survey, the 2-channel SMU9000 system with 5U sensors from Kaman Instrumentation is chosen. The SMU9000 unit is a transducer which is calibrated to output an analog signal increasing from -5 V and +5 V as the distance of the sensor from its target changes from 0.1 mm to 1.35 mm. The calibration curve relating output voltage to target distance is approximated to an accuracy of better than 0.1 % by a 5th order polynomial function. The distance and voltage range are calibrated by the manufacturer as per the user's specifications. Displacement resolution is limited by the signal/noise ratio. Signals measured using a personal computer have noise levels as high as 5 mV, which for these sensors translates to 0.6 μm of displacement. However, with the use of suitable software filters available in LabVIEW, low frequency signals can be measured with noise levels suppressed to about 20 nm. Further details on the use of these sensors are provided in the sensors' instruction manual [22].

Flexures

The next step is the selection appropriate flexure specifications. LCF stiffness is chosen based on required force resolution. A 0.2 MPa change in stress in a film 0.1 μm thick and 1 mm wide can be measured with a 0.1 mN force resolution. Given sensors with a 20 nm resolution, an LCF stiffness of about 1 N/mm would suffice. The ACF is designed to maximize travel. Aluminum 7075 is chosen to be the material of the flexures owing to its high yield strength, long fatigue life, low stiffness, low density, and high thermal conductivity. A low stiffness metal helps achieve the chosen low

spring stiffness with more manageable dimensions. Weight of the material is a concern in out-of-plane deflections due to gravity. A 0.5" thick plate is chosen to accommodate the $\phi 0.25$ " O.D. displacement sensors. Al 7075 has a Young's modulus of 70 GPa and an endurance limit (to 10^8 cycles) of 145 MPa [1]. Using these property values, it can be seen that a compound flexure 75 mm long and 0.8 mm thick has a calculated stiffness (Eq. 2.5) of 1.07 N/mm and a maximum travel of about 6.7 mm (Eq. 2.6). The maximum required actuation distances being of this same order, identical flexures are chosen for the ACF the LCF.

Actuator

The actuator for this machine is chosen based on the required displacement resolution and range. Assuming that the specimen gage length is $O(1 \text{ mm})$, and that the minimum acceptable strain resolution is 10^{-5} , it is seen that displacement increments of the order of tens of nanometers are required. A range of several millimeters is required. Another important consideration for the actuator is its maximum force capacity, which must exceed the total of the forces required to deflect the LCF and ACF through their maximum ranges. In our cases, both have stiffness of about 1 N/mm. The LCF can travel at most by 1.5 mm (the maximum range of the sensor), and the ACF by 6 mm. The total force required is about 10 N. After considering the various actuators compared in Table 2.1, the inchworm is seen to be the best choice for actuation in the current system. The Burleigh¹ Instruments IW700 is one of the most commonly used models. It is capable of 4 nm steps over 6.35 mm of travel when controlled by the Model 6000 ULN controller also from Burleigh. It has a maximum force capacity of 10 N. The actuator, along with the IW450 mounting bracket, is convenient to interface with the machine. Details on the use and operation of this actuator are provided in appendix B.

¹<http://www.burleigh.com>

3.1.2 Design and Fabrication of the Testing Frame

The testing frame is designed to incorporate the flexures, displacement sensors, actuator and specimen fixturing system (specimen stages) in a compact monolithic arrangement. The two flexures (ACF and LCF) are placed in an opposing configuration as shown in Fig. 3-1 so that the specimen stages can be closest to the midlines of the compound flexures. Having such a compact design helps reduce effects of thermal expansion, machining tolerances and machine compliance. Fig. 3-2 is a close-up view of the region around the specimen stages.

The specimen stages are regions on the travelling ends of the flexures specially machined to accept different grips and fixtures for various tests. These are marked on the load cell and actuator flexures in Fig. 3-2. Each stage provides an area of 10 mm x 10 mm with three tapped mounting holes (#0-80 UNC Tapped) for test fixtures. The stages are milled down to a thickness of 1/8" so that the specimen can be along the mid-plane of the plate when mounted using a fixture. This is important in order to minimize torsional loading on the flexures. The space between the stages when the flexures are relaxed is 10 mm, but can be changed by ± 6 mm, by suitably displacing the ACF.

The load cell sensor and displacement sensor are mounted in the indicated $\phi 1/4$ " holes on the frame, and use the indicated target surfaces for measurement. Both these sensors are placed in-line with the testing axis in order to reduce Abbé errors of measurement. Also, neither of the sensors is placed on the LCF to avoid forces on it other than those from the specimen. One other notable feature of the arrangement chosen for this machine is that the sensors are always moving away from the target during a tension test, which facilitates utilization of their full range.

Calibration holes are provided on the LCF for mounting calibration fixtures (Fig. 3-8). The load cell is calibrated by placing precision weights on these mounts and measuring the resulting deflection. Actuator interface hole is a #6 (O.D. 0.136") hole on the ACF through which a #6-32 screw threads into a mating hole in the actuator (Fig. B-1).

The integrated testing frame is 300 mm x 300 mm in size. The frame is fabricated by a combination of wire EDM and conventional machining, in three stages. In the first stage, the flexures and other major in-plane features are machined by wire EDM. At this stage, the compound flexure is left attached to the rest of the frame. Fig. 3-3 schematically shows a flexure which is still attached to the frame at the shaded regions. This way, the flexures don't deflect during the second stage, where out of plane features such as sensor holes, specimen stages etc. are machined. Once all the features have been machined, the flexures are released to move freely by a final series of wire EDM cuts to remove the material in the shaded regions in Fig. 3-3.

The flexure frame is mounted on an overall machine frame that provides mounting holes on an inch grid. The frame also provides convenient access to the flexures from all sides in the various orientations. The machine with its frame can be oriented with the testing axis lateral, horizontal, or vertical, as shown in Fig. 3-4. These three orientations, MOL, MOH and MOV respectively, facilitate use of gravity in different ways for different tests. For example, MOH is convenient for placing tensile specimens onto the stages. MOV is convenient for load cell calibration, bend and indentation tests. MOL completely eliminates the effect of the weight of the grips and specimen stages and fixture. Detailed drawings of the machine frame and specimen stages are provided in appendix C.

3.1.3 Grips and Fixtures

A variety of grips and fixtures are made to enable testing of various kinds of specimens in different modes on this testing machine. Detailed engineering drawings of all these fixtures are provided in appendix C. Other grips may be designed based on the engineering drawings of the specimen stages in appendix C. All grips are attached to the specimen stages using #0-80 screws through Interface Holes (IH) in the grips that screw into the mounting holes on the specimen stages.

Thin film tension

Thin film tensile specimens tested in this program are available in the form of dogbone shaped strips surrounded by silicon frames. Each specimen is glued to mounting blocks on either end using cyanoacrylate glue. The blocks, 1/8" thick, are then fixed onto the specimen stages using machine screws, thereby bringing the specimen to the mid-plane of the machine. The blocks are made from Al 7075 for its high strength/weight ratio. The detailed procedure for aligning and mounting a thin film specimen mounting is given in section B.2.

Foil tension

Foil tensile specimens are best gripped by clamping. Fig. 3-5 is a solid model of the clamps designed for this testing machine. These clamps are made to accept specimens with a grip section width of 3 mm. The key features of these clamps are: (1) confirming slots for aligning specimens; (2) aligning faces to mate and align the grips with the machine; (3) resting keys to ensure positive clamping of specimens of various thicknesses; (4) rough surfaces on the faces that clamp the foil specimen, made by milling with a fast pass. The clamps are made of Aluminum 7075.

3 and 4 Point bend testing

Fig. 3-6 is a solid model of the fixtures used for 3 point bend testing. The key features of this set-up are: (1) integrated mandrels (MD) (R0.5 mm) on both the bottom and the top fixtures for supporting and loading the specimen; (2) aligning faces to mate and align the grips with the machine; (3) accommodating trough to accommodate the bent specimen while still maintaining rigid support for the mandrels. The span between the mandrels is 9 mm. These fixtures are made from hardened tool steel (HRC 60) to minimize deflections due to the small contact areas. The 4 point bend testing fixtures are essentially similar to the 3 point fixtures except that the top fixture has two mandrels. The specimen span is 9 mm and the distance between the inner rollers is 6 mm.

Indentation

The fine force and displacement resolutions of the machine make it possible to conduct ultra-micro indentation experiments. Fig. 3-7 shows the fixtures used for

indentation. The key features of these fixtures are: (1) #6-32 threaded hole in the top fixture to mount our custom-designed indenter head; (2) specimen stage, a platform to place the specimen to be indented; (3) clamping holes, #6-32 tapped, to accept additional fixtures necessary to glue or clamp the specimen in place. These fixtures are also made from hardened tool steel (HRC 60).

3.1.4 Data acquisition and control

Tests are monitored and controlled using a personal computer. Voltage signals from the sensors are acquired through a National Instruments PCI 6035E board through a BNC 2090 terminal interface block. The inchworm is controlled through the 6000 ULN controller interfacing with the computer through a CIO-DIO24 interface board manufactured by Computer Boards Inc., and supplied by Burleigh Instruments. LabVIEW virtual instruments (vi) provide the user interface for the tests. The inchworm is controlled through a Burleigh supplied vi (671_3ollv.vi), wherein the user simply inputs the speed of travel in $\mu\text{m/s}$. A custom developed vi (microtensile.vi) continuously reads in voltage signals from the transducer, converts them to displacement signals using the corresponding polynomial functions, plots force versus displacement on the screen and writes the data to disk. Detailed operating procedures are presented in appendix B.

3.2 Characterization of the Machine

3.2.1 Load Cell Calibration

While Eq. 2.5 gives an estimate of the stiffness of the LCF, its actual stiffness needs to be measured. It is important to calibrate the force-displacement characteristics of the LCF before and periodically during its use as a load cell. This is done by orienting the machine with the testing axis vertical (MOV) and loading the LCF with precision weights, noting the deflection at each weight. Calibration fixtures may be mounted on the LCF as shown in Fig. 3-8 in order to provide space to place calibration weights.

The calibration chart for the current load cell is shown in Fig. 3-9. The linear-fit stiffness is 1.21738 N/mm.

3.2.2 Machine Compliance

The specimen extension during a test is measured by measuring the crosshead displacement. The load carried by the specimen is transmitted to the cross heads through the grips and fixtures being used. Ideally, all components in this load train other than the specimen must be completely rigid, *i.e.* undergo no deformation under the load carried. However, in a real case, the parts around the specimen also have a finite compliance, and undergo some elastic deformation under the transmitted load. This compliance, called machine compliance, may be represented by an additional spring of stiffness K_M in series with the specimen. Fig. 3-10 is a modified version of Fig. 2-5 with this additional component. In this figure, δ_M is the measured specimen extension. By inspection, one may obtain the actual specimen extension δ_S by subtracting the deformation of the load train from δ_M in the following manner:

$$\delta_S = \delta_M - \frac{K_L \delta_L}{K_M} \quad (3.1)$$

K_M is measured by testing an ideally rigid specimen. Since such a specimen is not supposed to undergo any deformation during the test, any measured deformation is due to machine compliance. For our low load testing machine, a dogbone shaped tension specimen (Fig. 3-11) of 127 μm thick spring steel was tested in tension. Fig. 3-12 is the load-displacement graph obtained from the test. K_M is the slope of the graph, and is measured to be around 700 N/mm. In other words, at a load of 1.5 N, the δ_M exceeds δ_S by about 1 μm .

3.3 Machine Validation

The testing machine was verified for accuracy and repeatability by testing several samples of materials with known properties. These are briefly listed below.

3.3.1 Tensile testing of aluminum foil

16.51 μm thick aluminum foil was obtained from Reynolds Inc. and tested in tension. The geometry used for the test specimen is based on the classical dogbone shaped sheet tension specimen, recommended by ASTM as per standard E345 [3]. The actual specimen geometry is shown in Fig. 3-11. The specimen was clamped between grips 12 mm apart. Several tests were conducted and the results were seen to be repeatable. Fig. 3-13 is a typical load-displacement graph. The data plotted is adjusted for machine compliance as discussed in section 3.2.2. Comparison between the Young's modulus of aluminum measured during such tests with the bulk polycrystalline elastic modulus of aluminum is taken to be a measure of the machine's accuracy.

Conversion to stress-strain

Calculation of Young's modulus requires conversion of load-displacement data into stress and strain. The only extension being measured in the current setup is the cross-head displacement, which is a combination of the extension of the gage section and that of the regions outside of it. This makes it difficult to isolate the extensions in the gage section alone and calculate the strain. However, if the material is homogeneous and undergoing elastic deformation, the entire specimen between the two grips behaves like a linear spring of stiffness k_{eff} dependent only on the Young's modulus and geometry of the specimen. The Young's modulus may hence be determined from the known specimen geometry and an experimentally measured k_{eff} , as follows.

The elastically-extending specimen can be represented using an equivalent constant cross-section strip with a cross-sectional area the same as that of the gage section of the actual specimen and a length L_{eff} such that

$$L_{eff} = \frac{AE}{k_{eff}} \quad (3.2)$$

Where A is the cross sectional area of the gage section and E is the Young's modulus of the material. L_{eff} is determined almost entirely by the geometry of the

specimen, and can be determined by either analytical or numerical calculations. This procedure is shown schematically in Fig. 3-15.

The analytical approach starts with dividing the specimen into several segments each of length dx along the length, as shown in Fig. 3-16. Each of these segments has a width $b(x)$, where x is the distance of the segment from midpoint of the specimen. If the specimen has a uniform thickness t , the extension of this segment $d\lambda$ under an applied load F will be

$$d\lambda = \frac{F dx}{Eb(x)t} \quad (3.3)$$

The extension of the entire specimen λ is the integral of this over the length.

$$\lambda = \int_{-\frac{L}{2}}^{+\frac{L}{2}} \frac{F dx}{b(x)t} \quad (3.4)$$

k_{eff} is nothing but F/λ . The integral may be performed over 3 regions, the gage section, the shoulder region and the grip section. With reference to the dimensions indicated in Fig. 3-16, the integral turns out to be:

$$\lambda = \frac{F}{Et} \left[\frac{L_1}{w_1} + \frac{A}{\sqrt{(A+1)(A-1)}} \tan^{-1} \left(\frac{(A+1) \tan(\alpha/2)}{\sqrt{(A+1)(A-1)}} \right) - \frac{\alpha}{2} + \frac{L_3}{w_2} \right] \quad (3.5)$$

where

$$A = \frac{w_1}{2R} + 1 \quad (3.6)$$

$$\tan(\alpha) = \frac{2L_2}{w_2 - w_1} \quad (3.7)$$

L_{eff} may then be calculated from Eq. 3.2. For the current specimen geometry, L_{eff} calculated by this approach is 10.16 mm. However, the actual specimen has clamped boundary conditions, which constrain lateral contraction close to the ends. This makes the actual specimen stiffer than the idealized version in Fig. 3-16. A

better way to find the k_{eff} (and hence L_{eff}) is by numerical analysis. A finite element representation of the specimen geometry with known A and E may be subjected to elastic uniaxial tension. The elastic stiffness of the specimen, k_{eff} may be calculated from the results of the analysis. L_{eff} can then be calculated from Eq. 3.2. The specimen shown in Fig. 3-11 is modelled using 457 cuboidal elements in plane and one element layer through the thickness. In order to simulate clamping, both ends are completely constrained from displacements other than along the length of the specimen. A uniaxial tension test is then simulated by preventing one side from moving and applying a displacement profile to the other end. A specimen with a thickness of $16.51 \mu\text{m}$, Young's modulus of 70 GPa and Poisson's ratio of 0.3 was simulated and resulted in a k_{eff} of 113.75 N/mm. From Eq. 3.2, L_{eff} is calculated to be 10.36 mm.

Results

Fig. 3-14 shows the stress-strain graph obtained from the load-displacement data shown in Fig. 3-13. The Young's modulus calculated from several tests averages 65 GPa.

3.3.2 Bend Testing of Steel Strip

$127 \mu\text{m}$ thick spring steel was tested in 3 point bend configuration. The specimen was 4.9 mm wide and 9 mm long. The stiffness k of a specimen with area moment of inertia I , length L and Young's Modulus E under 3 point bending is given by

$$k = \frac{48EI}{L^3} \quad (3.8)$$

k may be measured experimentally, and the above equation may be used to calculate E of the specimen material. The load displacement graph from such a test is shown in Fig. 3-17. E calculated from this test is 210 GPa, which is very close to the bulk Young's modulus of steel.

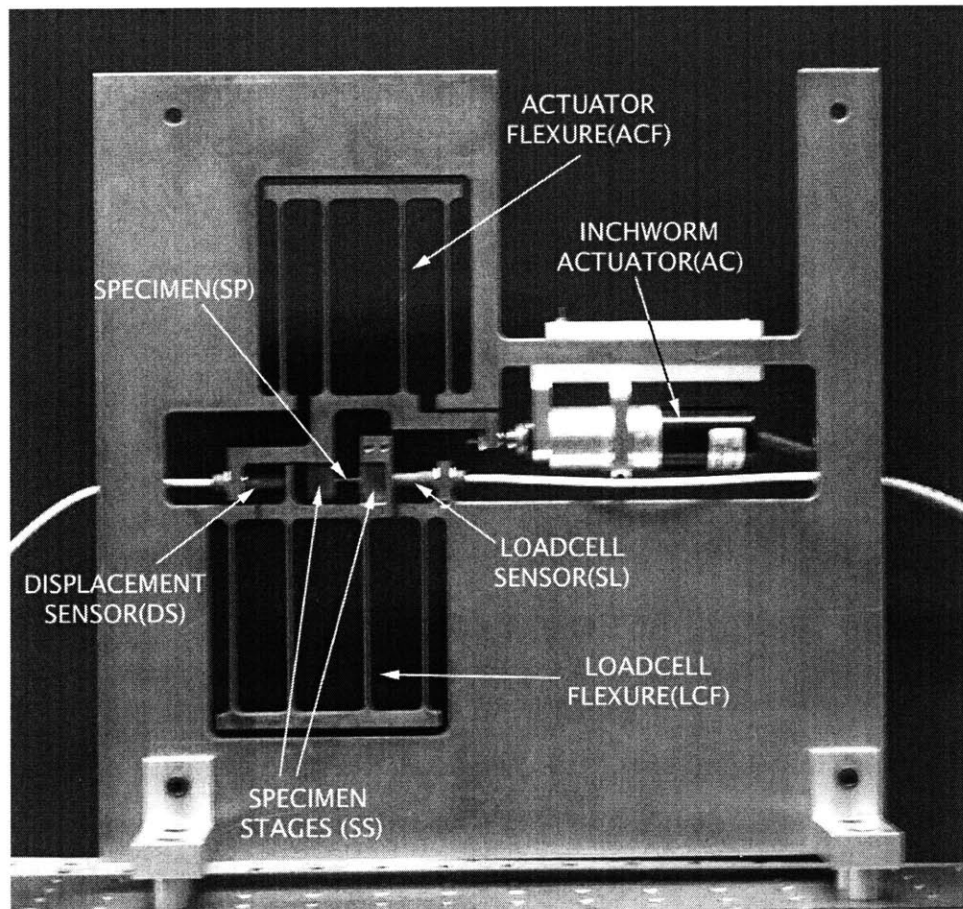


Figure 3-1: MIT Mechanics and Materials Low Load Testing Machine

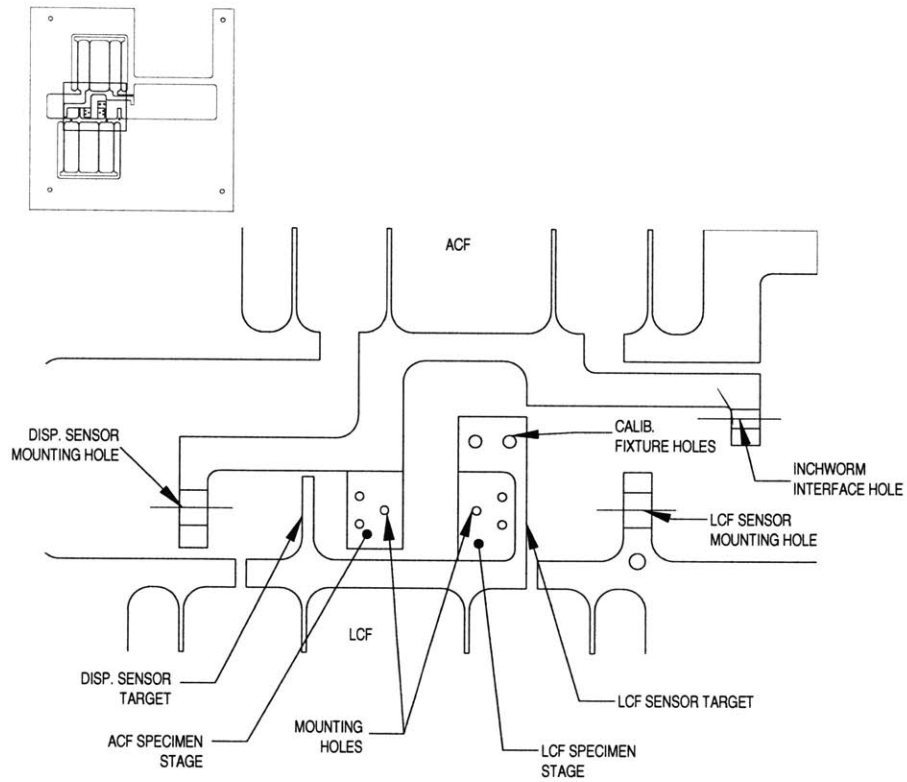


Figure 3-2: Close-up of low load testing machine.

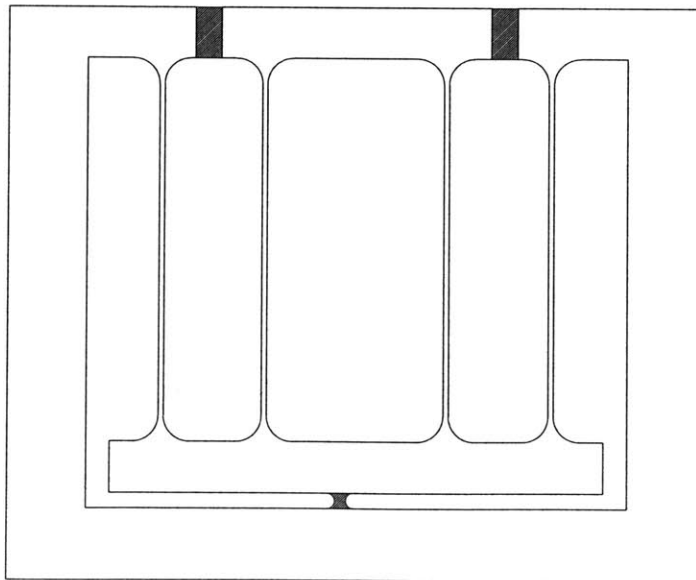
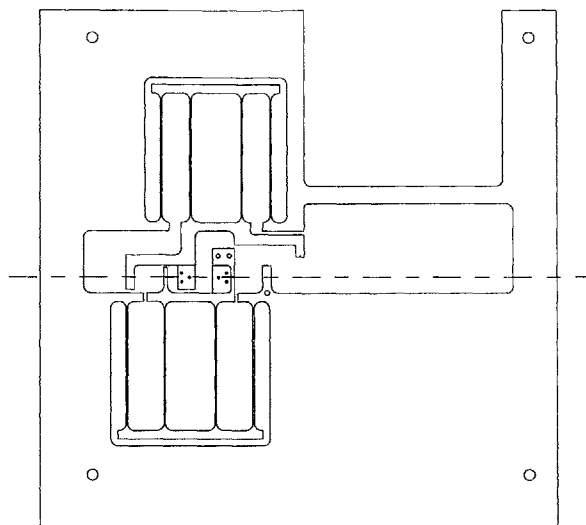
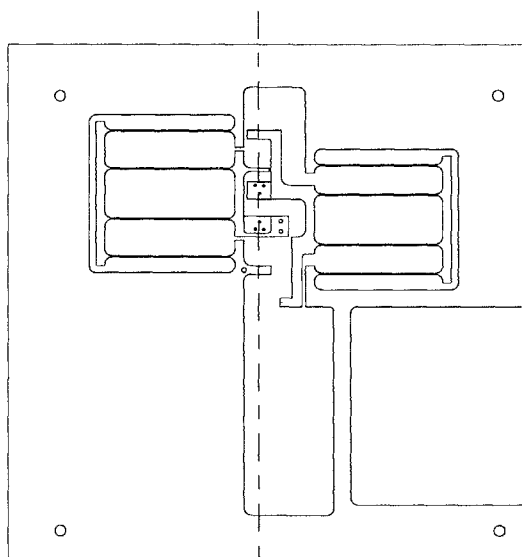


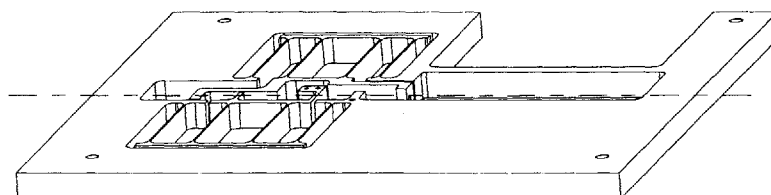
Figure 3-3: Flexures left attached to frame for subsequent machining.



(a) MACHINE ORIENTED LATERAL



(b) MACHINE ORIENTED VERTICAL



(c) MACHINE ORIENTED HORIZONTAL

Figure 3-4: Testing machine in various orientations with respect to gravity.

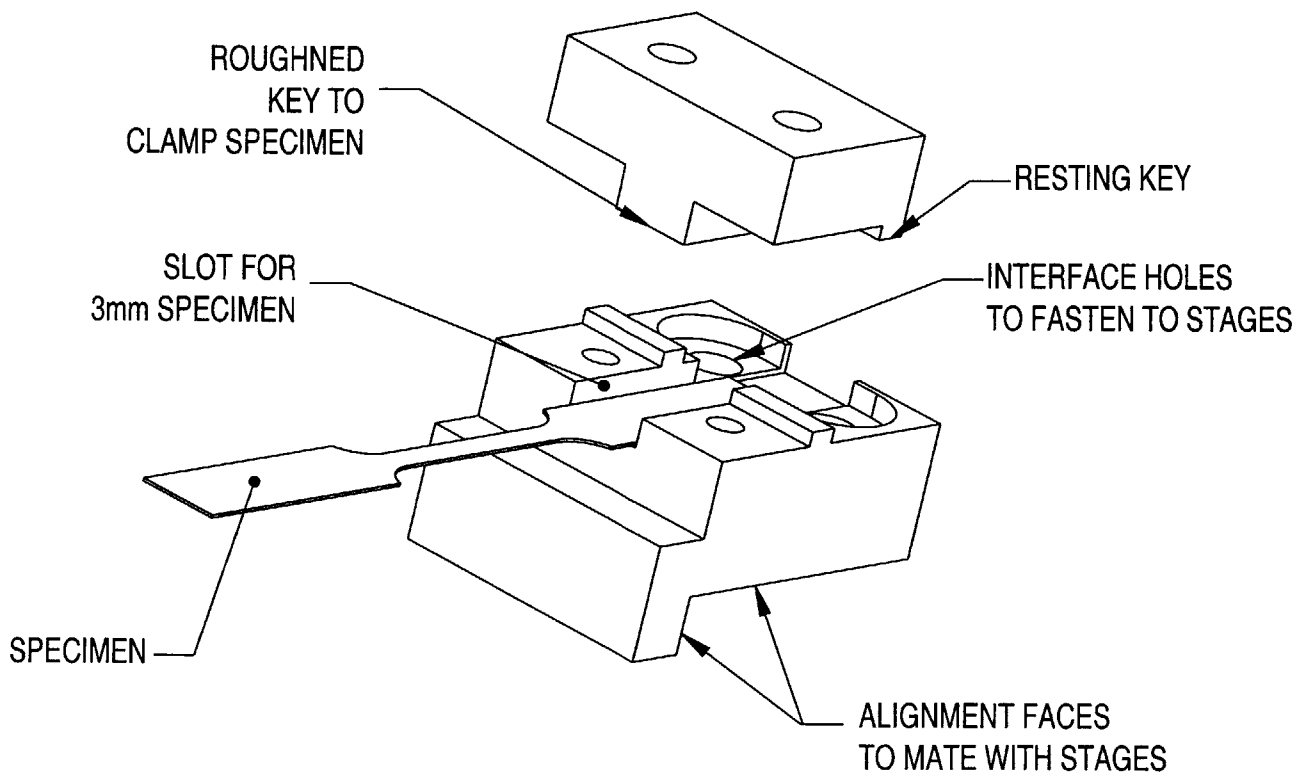


Figure 3-5: Foil tension grips. Bottom grip is Part GS0601-09, top clamp is Part GS0601-08.

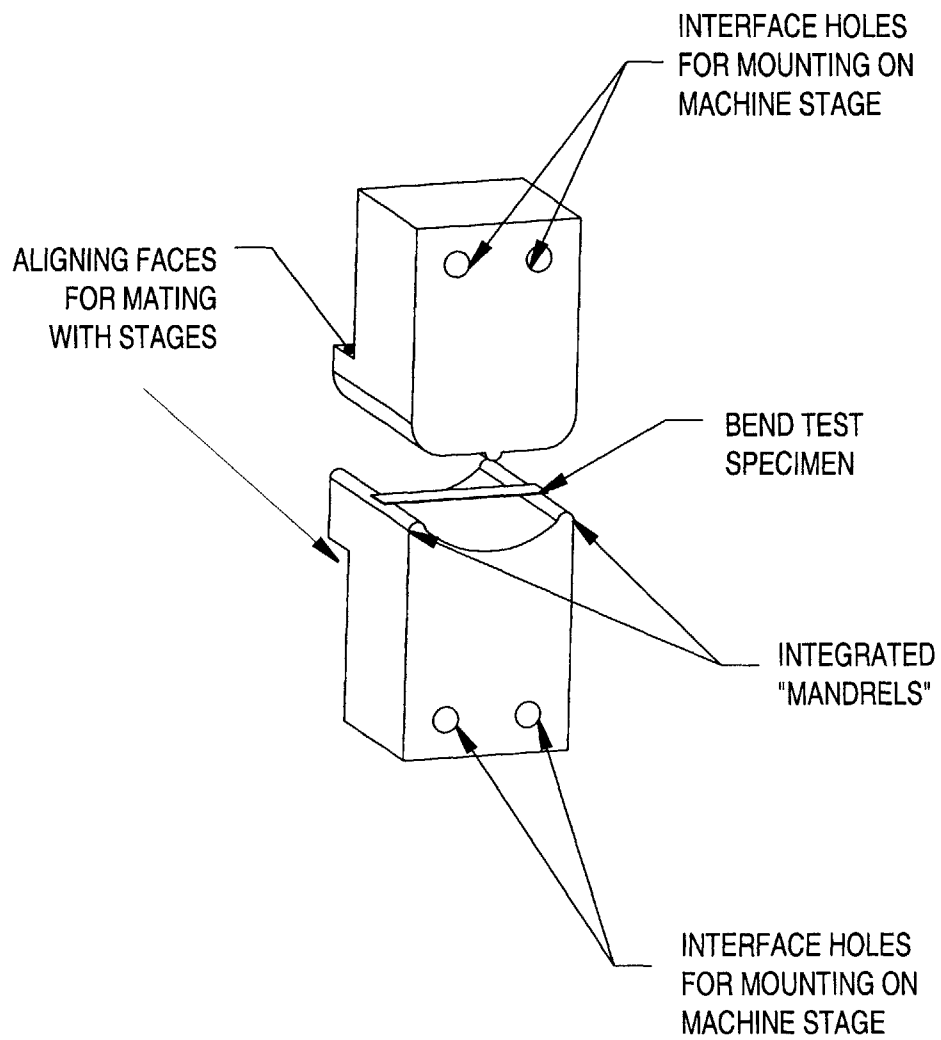


Figure 3-6: Three-point bend configuration. Bottom fixture is Part. GS0200-04. Top fixture is GS0200-05 for 3 point bend and GS0200-06 for 4 point bend testing.

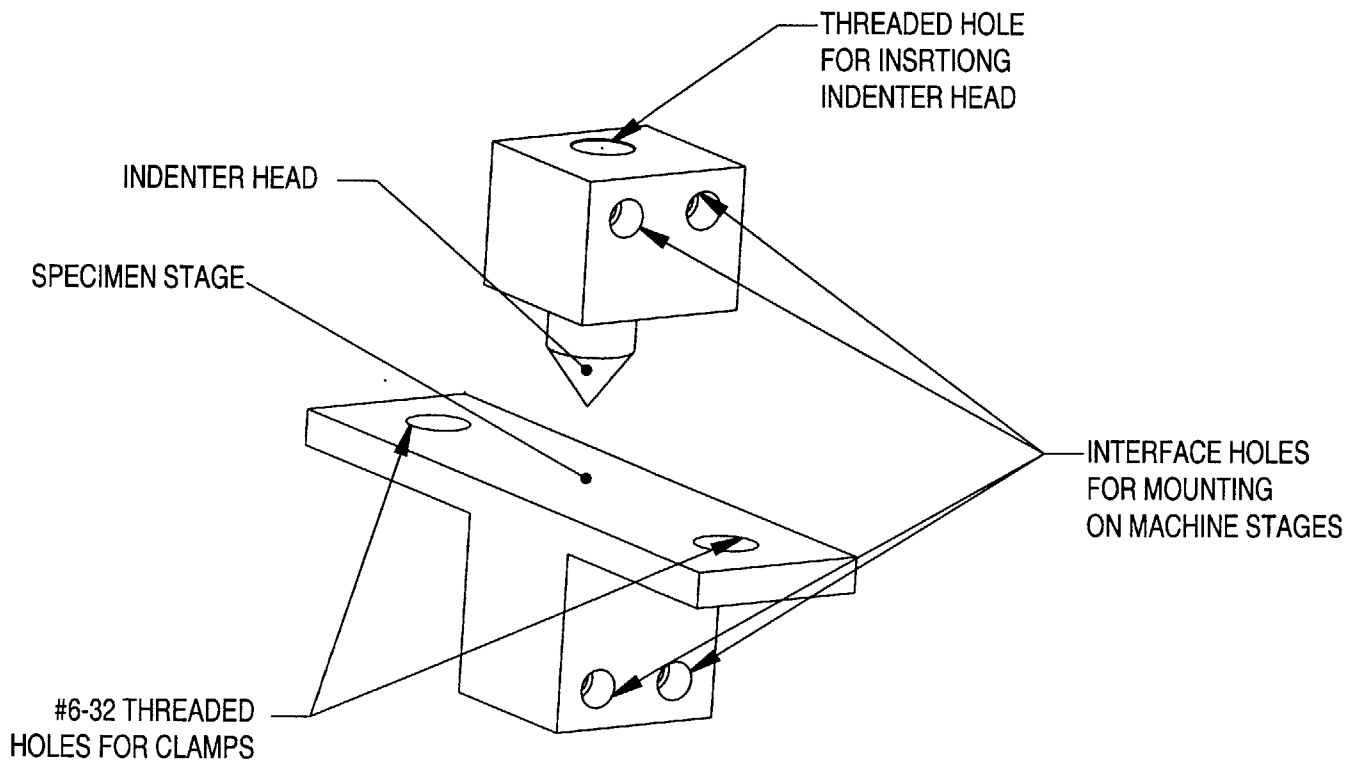


Figure 3-7: Indentation test configuration. Indentation stage is Part GS0900-02 and indenter holder is GS0900-01.

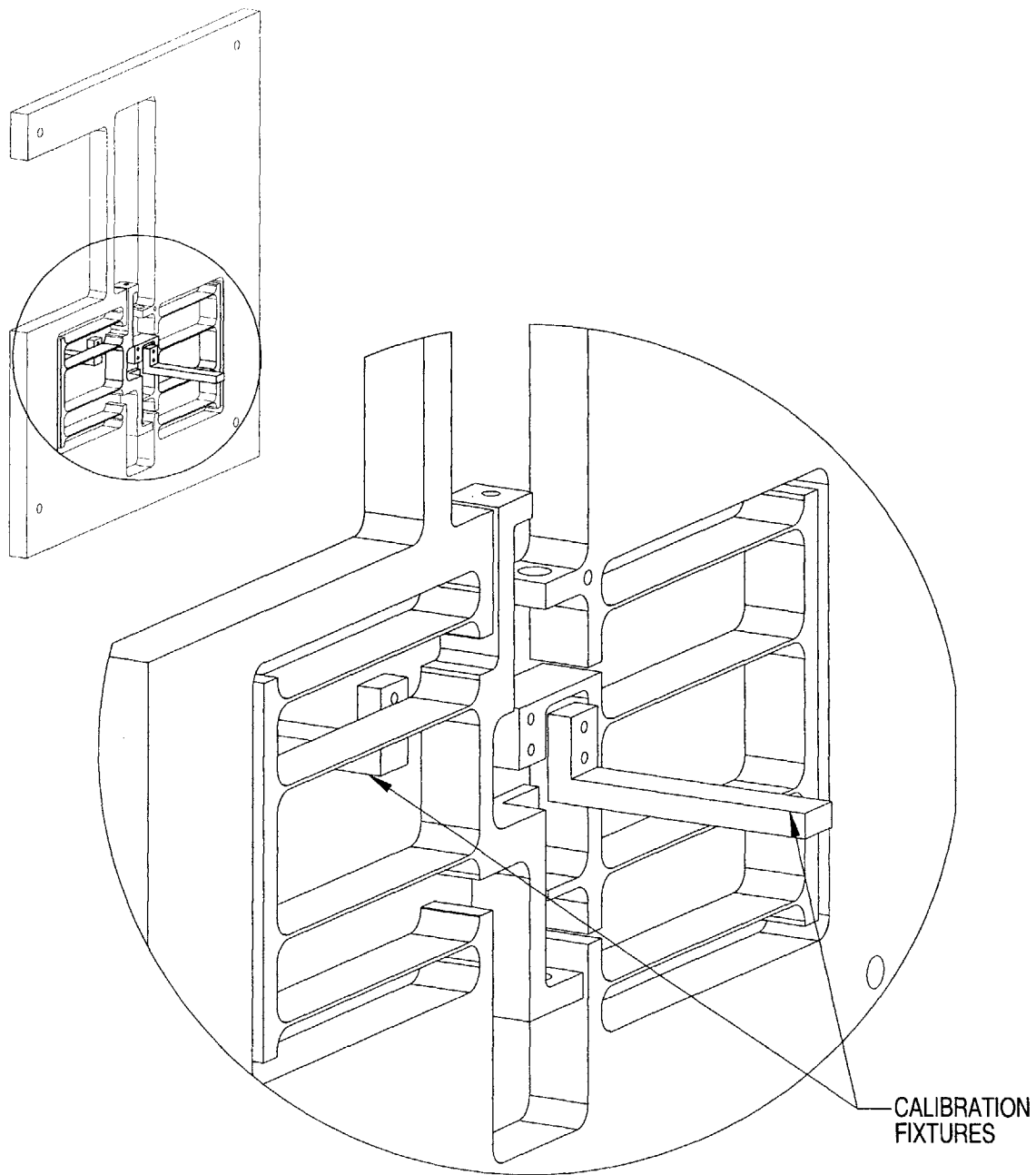


Figure 3-8: Calibration fixtures (Part GS0200-02) for low-load loadcell calibration.

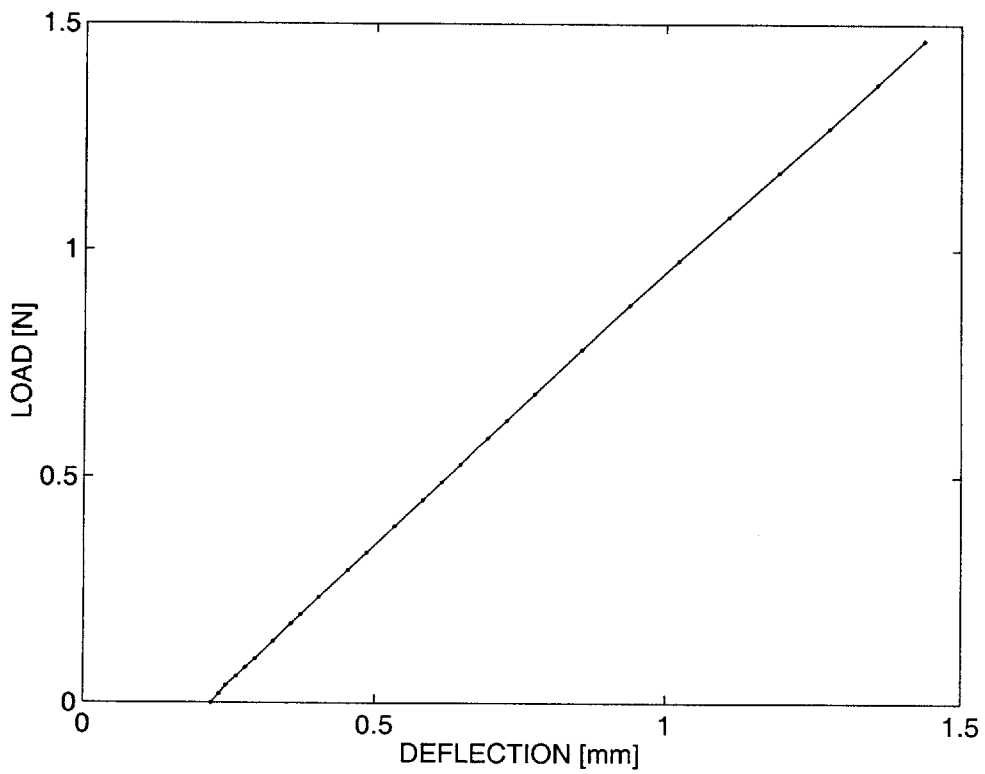


Figure 3-9: Load cell calibration graph low-load testing machine. Initial offset in deflection is a combination of the non-zero offset of the sensor from the target and deflection under self weight of the flexure.

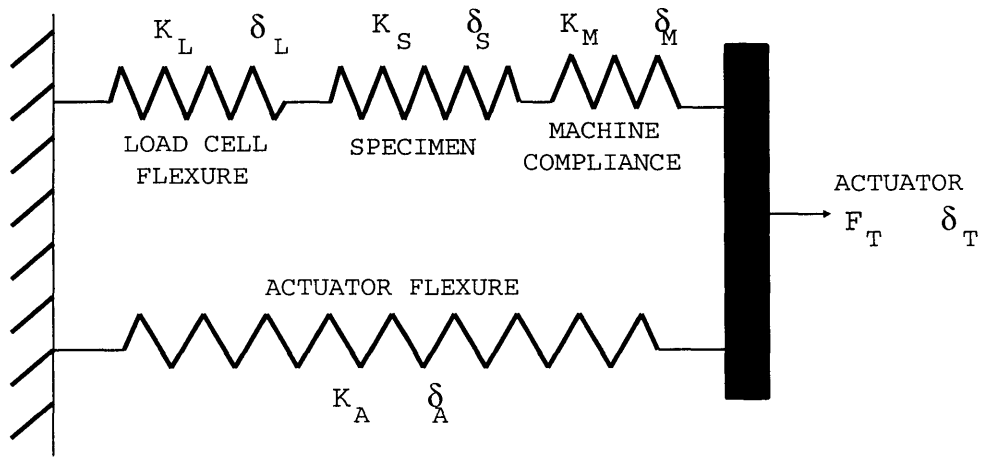


Figure 3-10: Equivalent spring diagram of testing machine including machine compliance

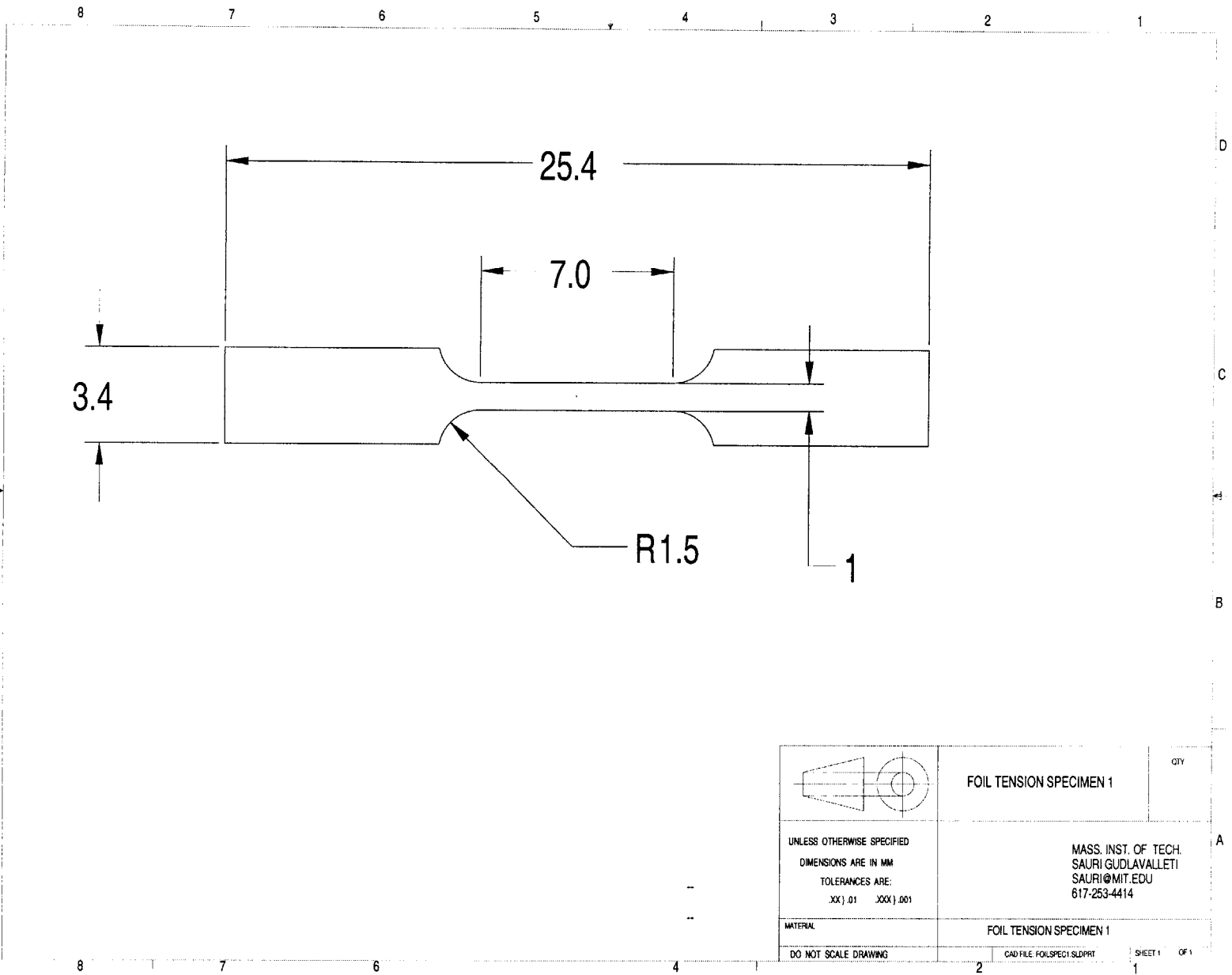


Figure 3-11: Engineering drawing of foil tension specimen

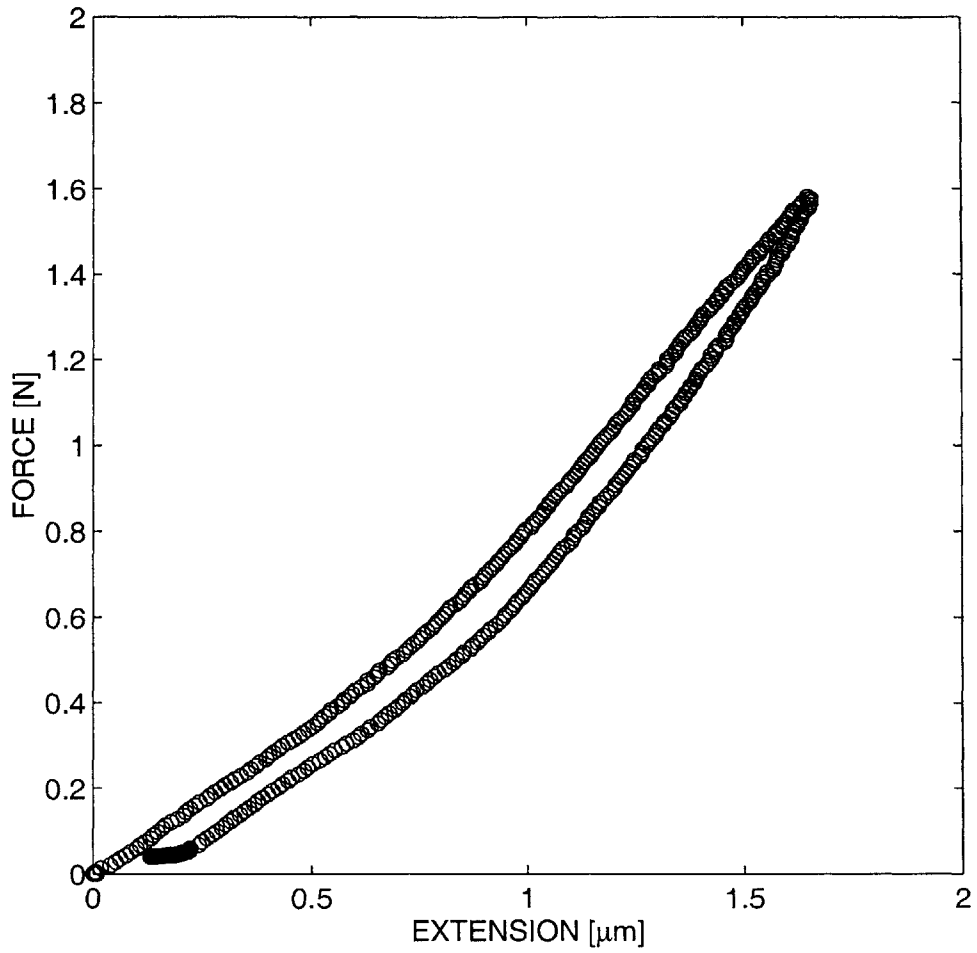


Figure 3-12: Force-displacement graph obtained during tensile testing of a very stiff specimen. The measured displacement is due to machine compliance.

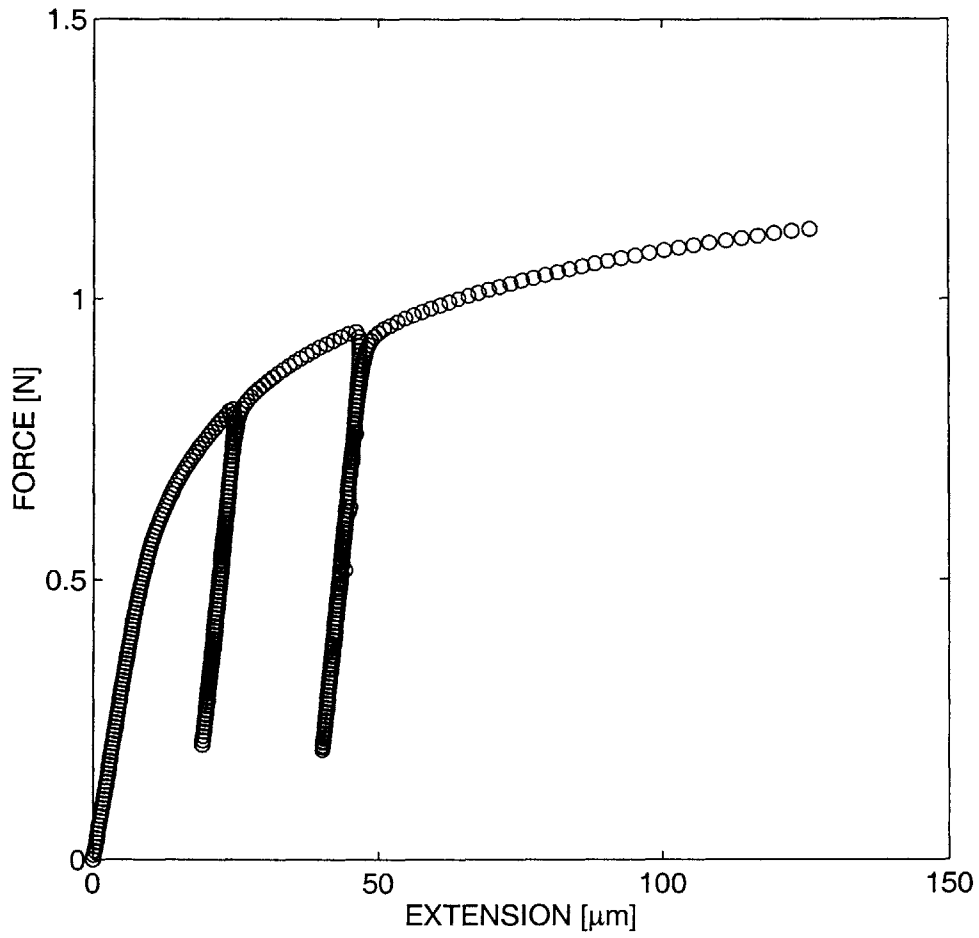


Figure 3-13: Force-displacement graph obtained from tensile testing of 16.51 μm thick Aluminum foil

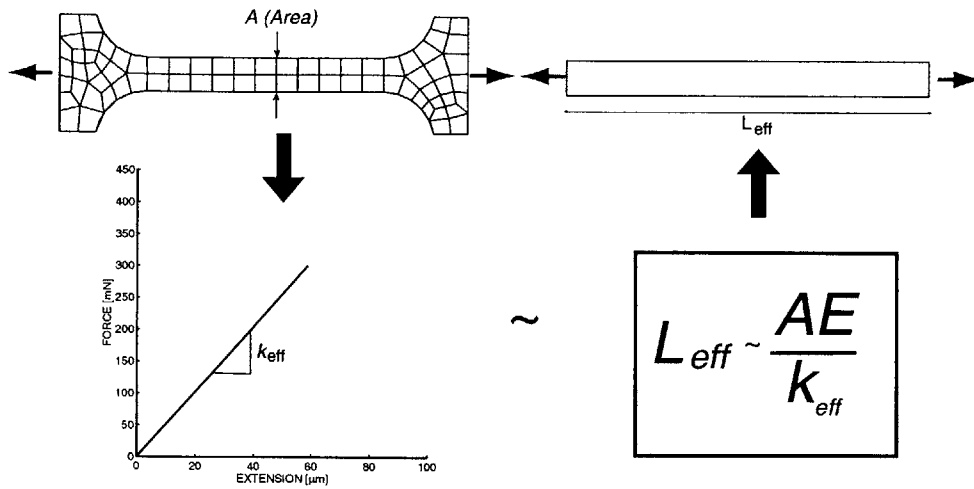


Figure 3-15: Procedure for obtaining “effective” specimen gage length from numerical simulations. The specimen geometry is subjected to tensile loading in a finite element simulation. The stiffness it exhibits is taken to be the stiffness of an equivalent specimen, with a constant cross-section, and length L_{eff} .

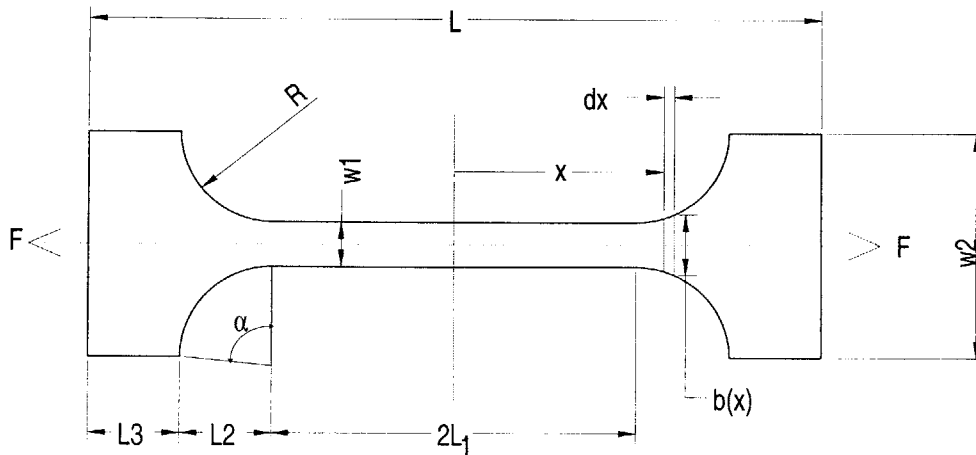


Figure 3-16: Analytical estimation of over-all stiffness of an elastic dogbone shaped specimen from its geometry

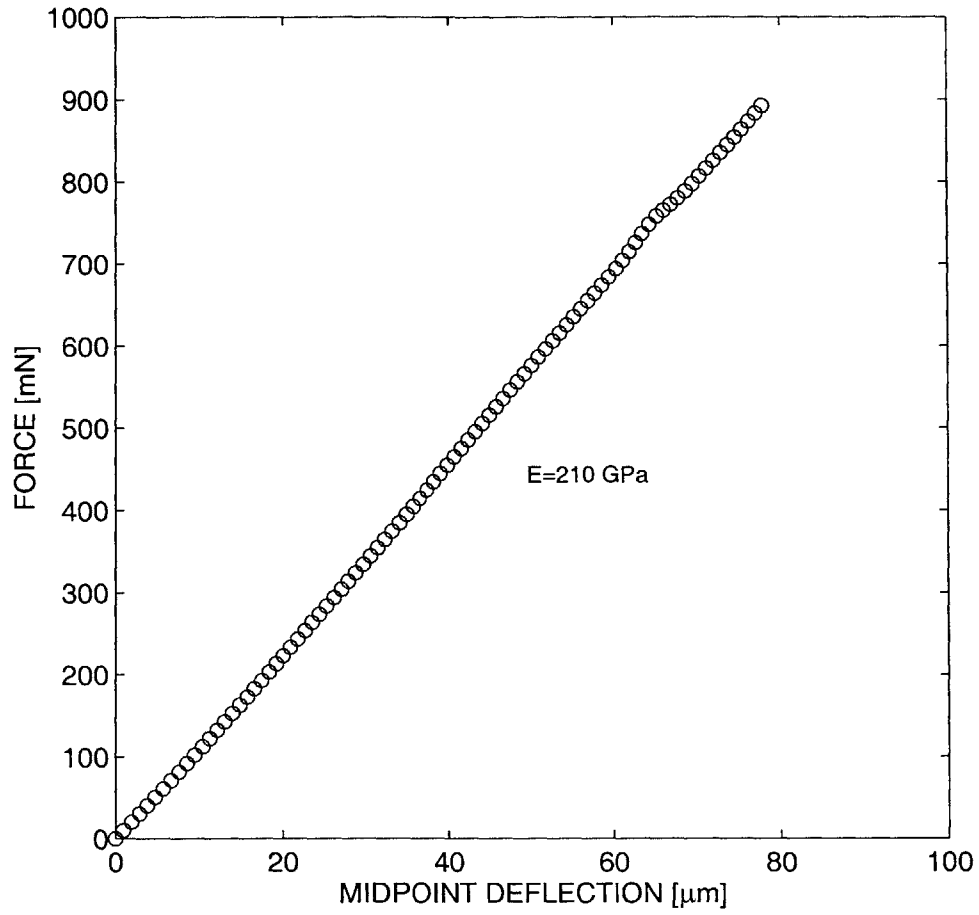


Figure 3-17: Force-displacement graph from 3-point bend test of steel strip. Specimen was 4.9 mm wide, 0.127 mm thick and 9 mm long. Young's modulus calculated from the slope is 210 GPa.

Chapter 4

High Load Testing Machine

The meso-scale of materials testing spans a wide range of loads, from several micronewtons to tens of newtons. The low load testing machine described in the previous chapter effectively addresses testing at the lower end of this spectrum. Described in this chapter is a second implementation of the generic flexure-based testing machine concept in the form of a “high load” version capable of applying and measuring loads up to 35 N. Loads in this range are found in tensile testing of foils and films several tens of microns in thickness and bend testing of specimens several hundreds of microns thick.

4.1 Design and Construction

4.1.1 Design Features, Specifications and Components

The high load testing machine is shown in Fig. 4-1. The conceptual design procedure for the high load testing machine is very similar to that for the low load testing machine described previously. Described here are the similarities and salient differences in the two machines.

The specimen sizes and dimensions, being regulated by the same constraints as before, are taken to be the same, $O(\text{mm})$. The thicknesses however, are likely to be much higher. A 1 mm wide metallic strip 30 μm thick can sustain load levels of 30 N

under stresses of 1 GPa. Similarly, a 3 point bend specimen 1 mm wide, 10 mm long and, 1 mm thick requires loads of 33 N to induce stresses of 1 GPa.

Due to the higher loads anticipated on the flexures, double compound springs are chosen for both the ACF and LCF in this implementation. These have higher rectilinearity, and better resistance to off-axis loads. For a given set of flexure dimensions, the stiffness of the compound flexure spring is double that of a single compound flexure, shown in Fig. 2-3(c). The maximum allowable deflection however, remains unchanged.

The same displacement sensors as in the previous machine are used, which means that the stiffness of the LCF, regulated by the maximum expected loads ≈ 35 N and the maximum measurable displacement ≈ 1.5 mm, is required to be around 23 N/mm. Leaf springs 1 mm thick and 50 mm long, with a root fillet radius of 4 mm are chosen for the LCF. The ACF is made of flexures 1 mm thick and 85 mm long. The LCF and ACF have maximum allowable deflections of about 1.6 mm and 6 mm respectively.

An electromagnetic voice coil actuator, BEI Kimco¹ model LA25-42-000A, with a maximum continuous stall force of 86.2 N, and a stroke of ± 12.7 mm is chosen for actuation. The actuator consists of a solenoid coil freely floating coaxially with a magnetic stator. It generates a force proportional to an input current, with a force constant of 21.33 N/Amp. The input current is generated by a linear amplifier, which is controlled by a voltage signal input.

The specimen stages (Fig. 4-2) in this machine are larger, and provide an array of 6 holes of $\phi 4.25$ mm in a space of 15 mm x 30 mm on each flexure for mounting various grips and testing fixtures. The ACF specimen stage provides two symmetrically placed slots for crosshead displacement sensors. This arrangement helps minimize the Abbé errors of measurement, given that the crosshead displacement is not being measured in-line with the specimen. Also, the sensors are placed very close to the specimen, in order to reduce the contribution of machine compliance in the measurement.

¹<http://www.beikimco.com>

The integral flexure frame is machined by abrasive waterjet machining. As in the case of the low load machine, the machine is designed to be used in vertical, horizontal and lateral orientations. The flexure frame is mounted on a separate machine frame to facilitate this. However, in the horizontal configuration, the weight of the freely floating coil results in a moment on the ACF. A linear roller bearing placed under the specimen stage is hence used to support the weight of the voice coil and align its travel with the stationary magnet.

4.1.2 Grips and Fixtures

The specimen stages in this machine provide mounting holes to accept the same fixtures used in the low load machine. Additional grips and fixtures are designed for tests at higher loads. These include foil tension grips, thermal/electrical insulation foil tension grips and multi-span 4 point bend fixtures. All fixtures mate with the specimen stages using 4 of the 6 mounting holes shown in Fig. 4-2, fastened using #2-56 machine screws and nuts. The foil tension grips (Fig. 4-3) are similar to their low-load machine counterparts. Described below are the other two fixtures, the insulation grips and multi-span bend grips.

Thermal/Electrical Insulation foil tension grips

Shown in Fig. 4-4 is the assembly diagram of the insulating foil tension grips. The actual grips, made of titanium are insulated from the flexure stages by using thermally/electrically insulating plates made from Garolite G-7, an electrical grade woven glass fabric laminate cured using silicone resin. G-7 has good tensile and impact strength and is useable in a temperature range of 0°C to 220°C. These grips are designed to enable resistive heating of the tensile specimen, which is necessary, for example in testing shape-memory alloys. The other key feature of these grips is the triangular slot for better clamping and alignment of a suitably shaped tensile

specimen, also shown in the assembly figure².

Multi-span bend grips

Depending on the thickness of the specimen being tested in bending, it might be desirable to vary the span of the bend specimen. Shown in Fig. 4-6 is a specially designed fixture on which can be placed bend specimens of various spans, 18 mm, 26 mm and 34 mm. The top fixture may contain 2 mandrels (shown) with a span of x mm for a 4 point bend test, or only 1 mandrel, for a 3 point bend test. The top fixture from the low-load machine fixture for 3 point bend testing (section 3.1.3) may be used for this purpose. These fixtures are made of hardened tool steel.

4.1.3 Data Acquisition and Control

The data acquisition hardware used for this machine is the same as that for the low load machine. Only the actuation system is different. The voice coil actuator is excited by a current generated by a linear amplifier (Aerotech 4020L Series). The amplifier generates a current proportional to a signal voltage with a transfer function of 2 Amp/V. Unlike in the case of the low load machine, where there were two simultaneously running virtual instruments (vi's): one for load-displacement monitoring and one for actuator control, the high load machine is monitored and controlled by a single vi. For tests involving quasistatic loading, hlmonotonic.vi outputs a voltage signal via the DAQ board to the amplifier to generate the desired force in the voice coil. For cyclic loading, a cyclic input voltage signal is required by the amplifier. This is generated using an Agilent 33120a function generator. The function generator may be operated by sending SCPI³ commands from a VI⁴ through the RS232 interface between the PC and the function generator.

²The original specimen geometry designed for use with these triangular slots is shown in Fig. 4-5. Specimens of this geometry were fabricated from 19.4 μ m thick Nitinol sheets by wire EDM. However, during testing, these specimens were seen to fail consistently at the fillets at the end of the gage section. This is thought to be due to a combination of the poor edge finish from the machining and the small fillet radius. It is recommended that better machining parameters be determined and specimens with more generous fillet radii be designed for use with these grips.

³SCPI: Standard Commands for Programmable Interfaces, <http://www.scipconsortium.org>

⁴An attempt at this approach may be found in masterdriver.vi stored within hiload.llb

The transfer function between the signal voltage (v_s) and force generated by the voice coil (F_{VC}) is given by the product of those of the amplifier (current/voltage) and the voice coil (force/current). Recalling figures quoted previously, we obtain a transfer function of 42.66 N/V. Since that the maximum continuous stall force of the voice coil is 86 N, a signal of only 2 V will use its full range. The DAQ board and function generator have a maximum output of 10 V, and it is desirable to use the maximum range in order to maximize signal to noise ratio. A voltage divider is used to scale down the 10 V range signal to a 2 V range signal.

4.1.4 Calibration

Both the ACF and LCF were calibrated by hanging weights. The flexures were found to be highly linear. Fig. 4-7 shows the force-displacement calibration graph of the LCF. The stiffness was found to be 21.85 N/mm. Fig. 4-8 shows the force-displacement calibration of the ACF. The stiffness was found to be 4.58 N/mm.

4.1.5 Machine Compliance

Machine compliance was estimated by testing a very stiff specimen in tension, as in Chapter 3. The present machine is estimated to have a compliance of 3000 N/mm using the foil tension grips.

4.2 Verification Tests: Tensile Testing of Stainless Steel and Aluminum Foils

Tensile properties of known materials were tested on the machine to verify its accuracy. Dogbone shaped tensile test specimens were punched out from stainless steel shim stock of two thicknesses, 0.001" (25.4 μm) and 0.002" (50.8 μm) and Aluminum foil of thickness 0.001" (25.4 μm). The geometry of the specimen used was slightly different from the one used in chapter 3, and is shown in Fig. 4-9⁵. A new punch was

⁵The L_{eff} for this geometry is 9.36 mm

made for specimens with these dimensions. Several samples of each type were tested to ensure repeatability. The results were seen to be consistent.

Fig. 4-10 is the stress-strain curve obtained from testing the 25.4 μm thick steel specimen. The Young's modulus measured from the test is 210 GPa, which is very close to the bulk Young's modulus of steel. Fig. 4-11 is the stress-strain graph of a test on the aluminum foil. The Young's modulus measured from the test is 66 GPa. Strain is calculated from cross-head displacement data by first compensating for machine compliance followed by dividing by the L_{eff} for this geometry, 9.35 mm.

Verification using a new non-contacting strain measurement technique

The performance of the machine has been further verified using a newly developed non-contact strain measurement⁶. This technique uses a CCD camera to periodically grab images of the specimen during a test. These images are then postprocessed using a digital image correlation algorithm to compute strains. The algorithm may be used to compute either the full strain field on the specimen, or the average strain between two points. For full-field strain computation, the algorithm uses the information contained in the surface pattern on the specimen. The surface pattern may be either inherent on the sample (*e.g.* rolling marks, electro-deposition hillocks), or artificially generated (by, say, paint spray). Average strain is best calculated by imaging two contrasting dots painted on the surface of the specimen. The resolution of this technique is currently 0.01% strain.

Shown in Fig. 4-12 is a photograph of an aluminum specimen prior to testing. Fig. 4-13 shows a tensile stress-strain graph from this specimen, calculated both using cross-head displacement as described above, and using the non-contact strain measurement technique described here. The Young's Modulus calculated from both techniques is about 66 GPa, which is close to the polycrystalline elastic modulus of aluminum. This non-contact strain measurement technique has been successfully applied in several other tests on this machine.

⁶System developed by Cheng Su. Details to be published

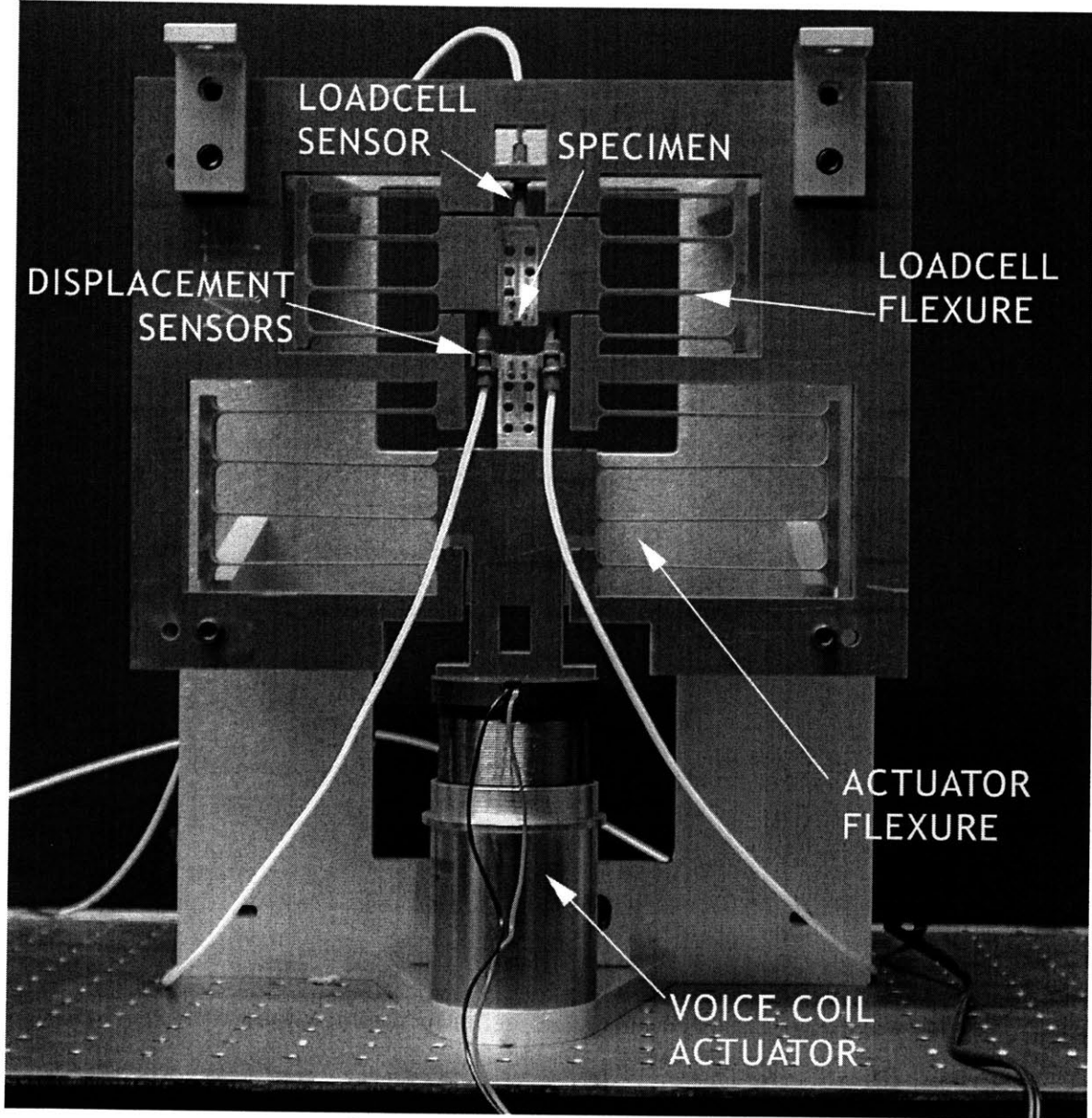


Figure 4-1: High load testing machine.

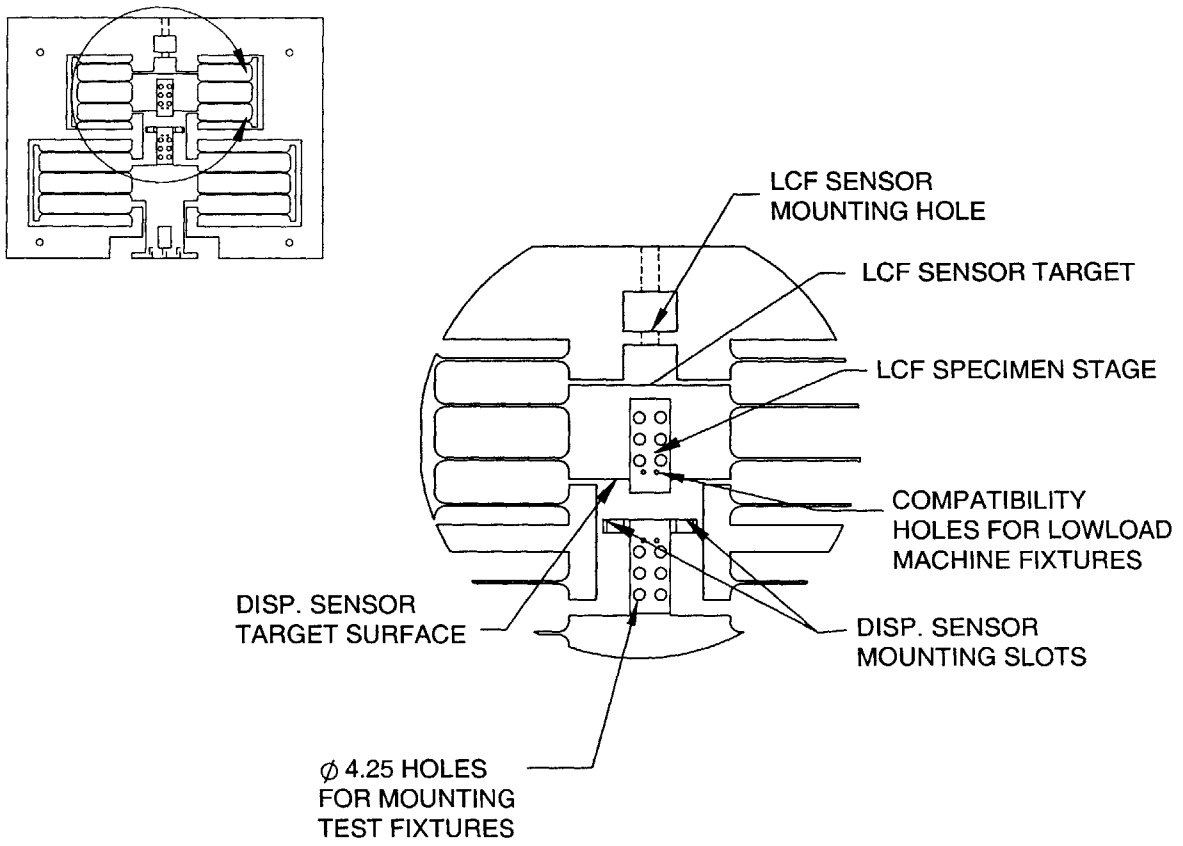


Figure 4-2: Close-up of the specimen stage region in the high load testing machine.

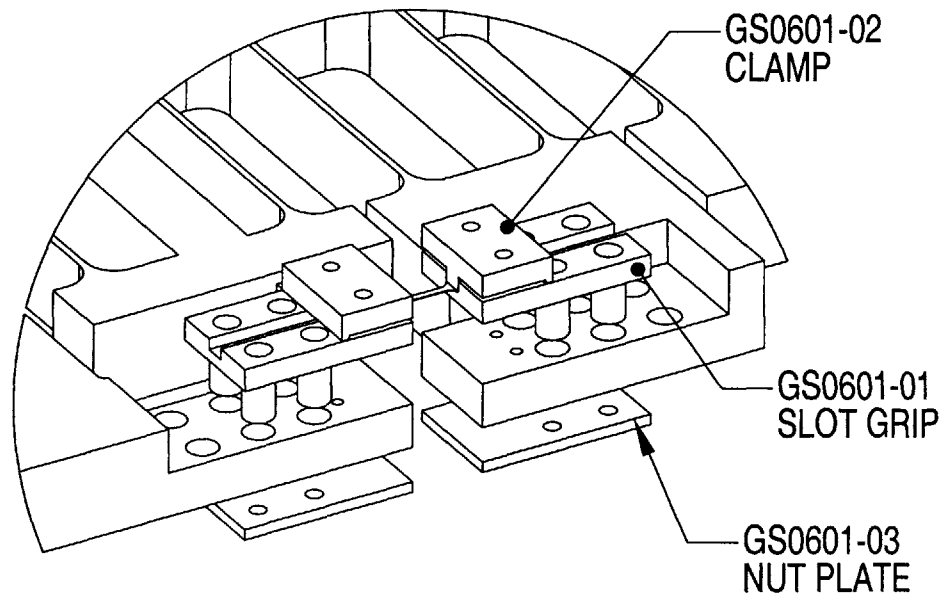
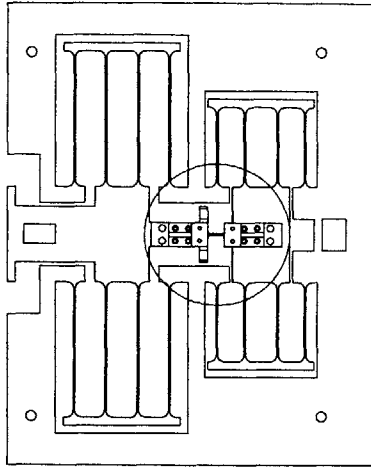


Figure 4-3: A cut away view of the high load testing machine showing assembly of the foil tension grips.

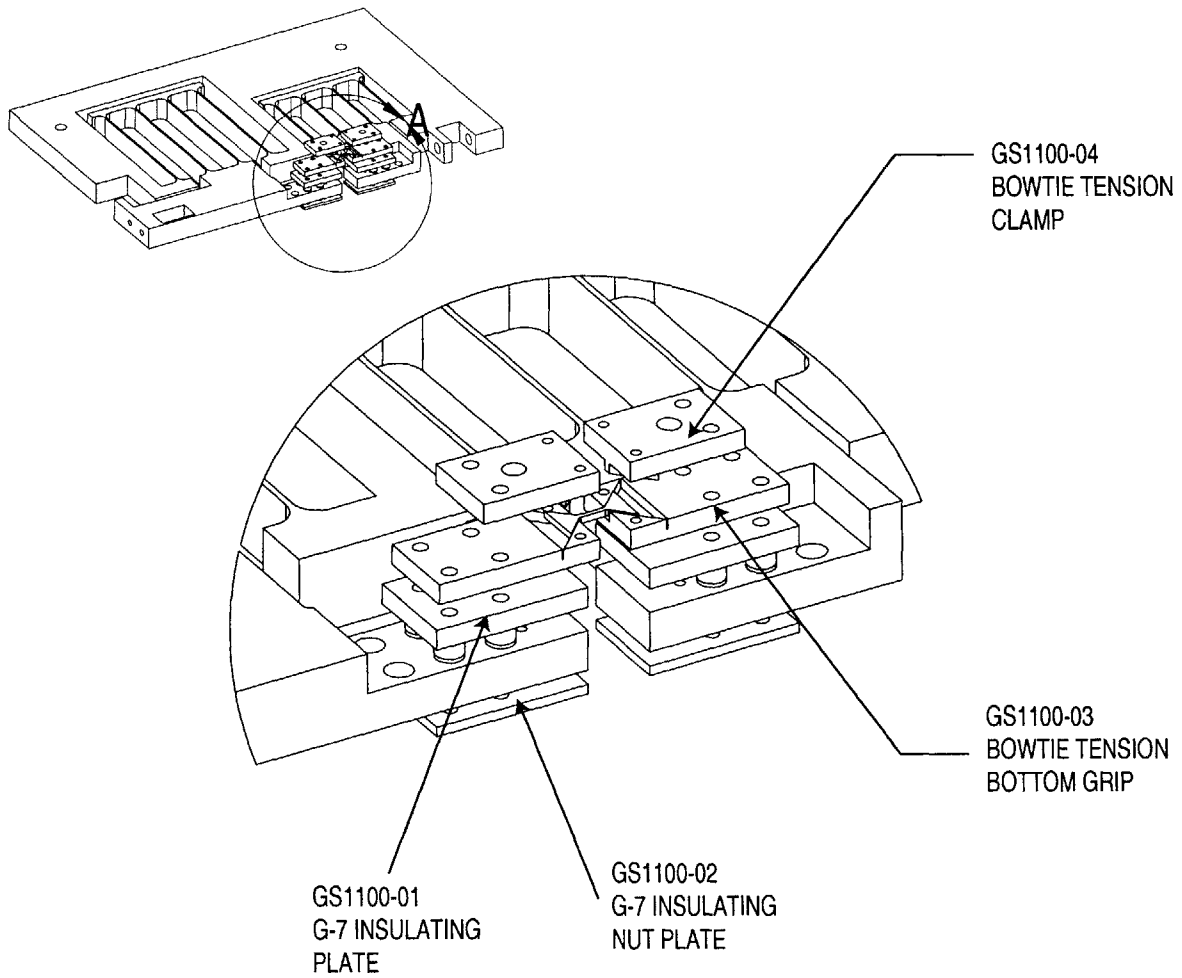


Figure 4-4: Insulating tension grips on high load testing machine (cut away view). The insulating parts may be replaced by Part GS0601-02 and GS0601-03 when insulation is not required.

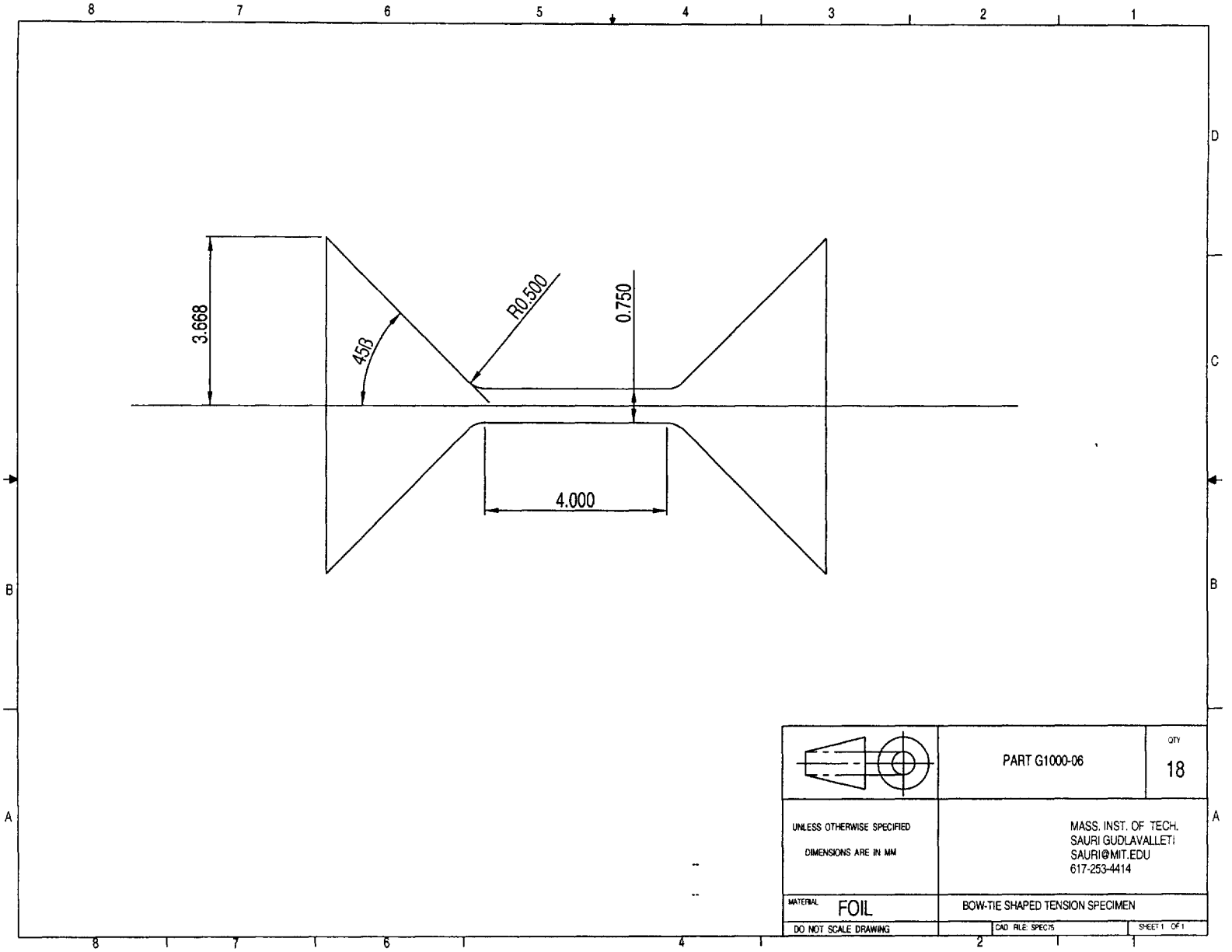


Figure 4-5: Bow-tie shaped tensile specimen geometry for use with grips shown in Fig. 4-4. This specimen geometry was found to be unsuccessful because it promoted failure at the ends of the gage section which have a small fillet radius.

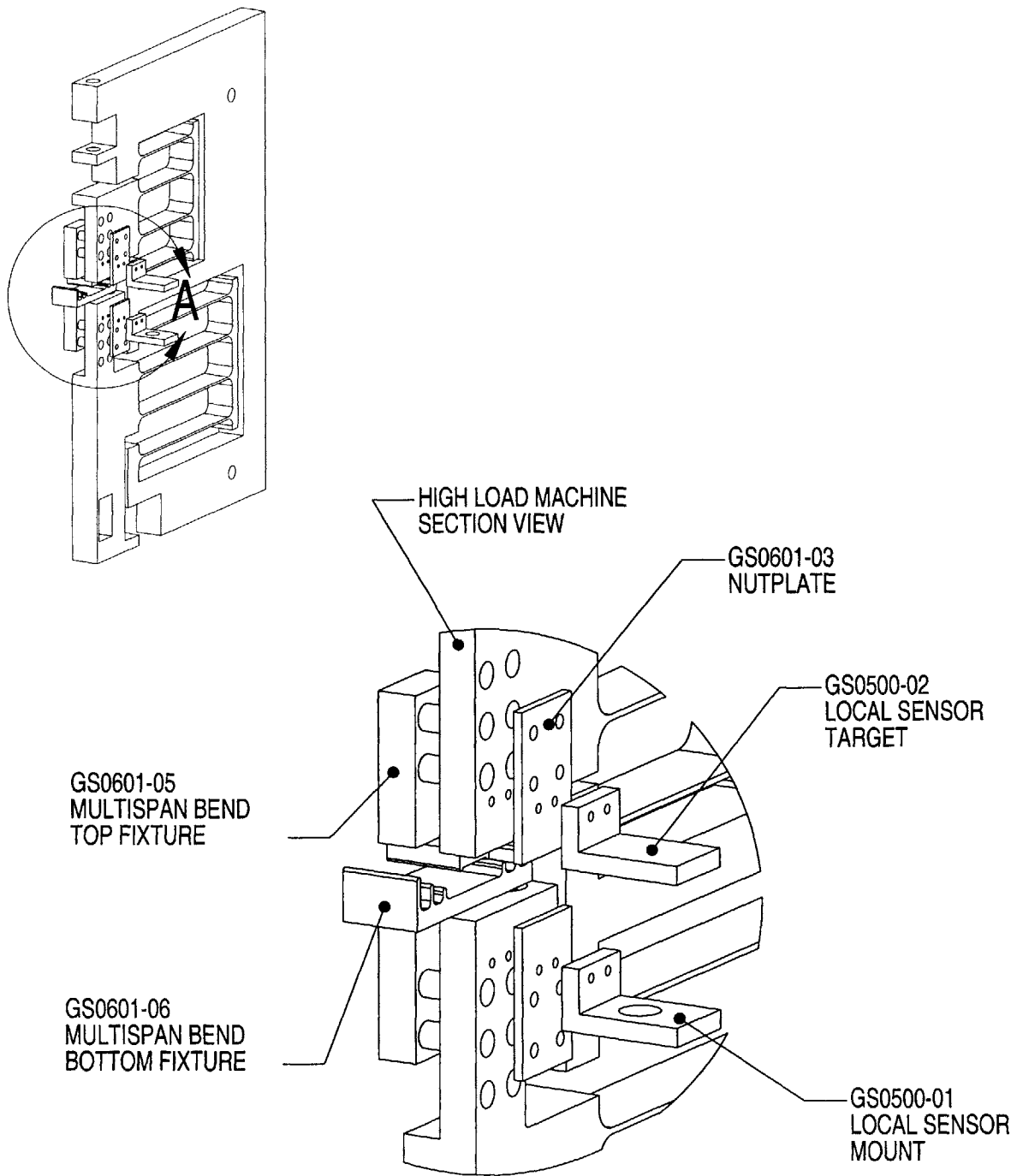


Figure 4-6: 3 and 4 point bend fixtures which enable bending of different specimen span lengths: 18, 26 and 34 mm. These fixtures require use of special mounts for the displacement sensor.

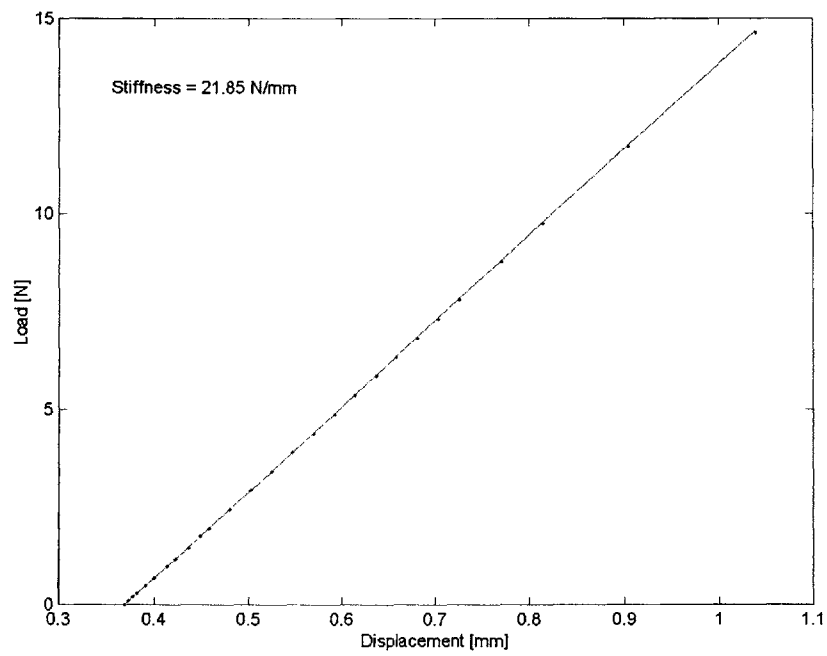


Figure 4-7: Load-displacement graph obtained during calibration of LCF of high load testing machine. The stiffness was obtained to be 21.85 N/mm

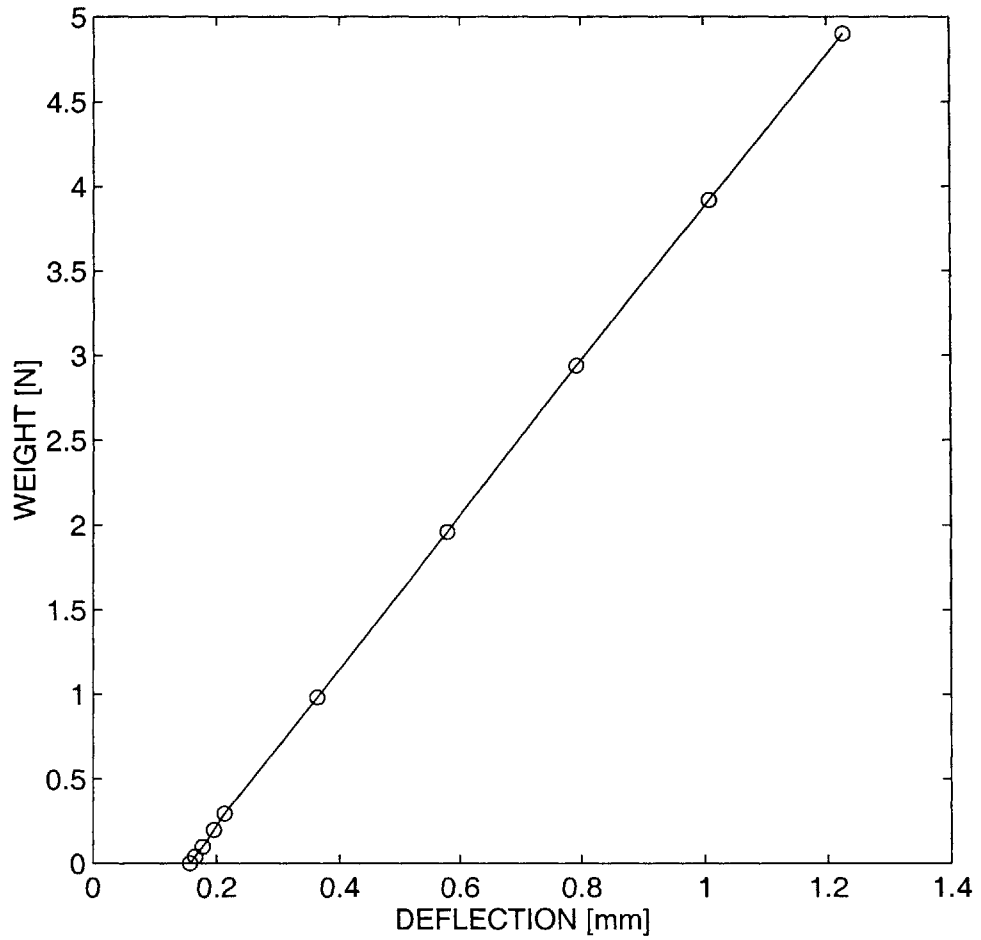


Figure 4-8: Load-displacement graph obtained during calibration of ACF of high load testing machine. The stiffness was obtained to be 4.58 N/mm

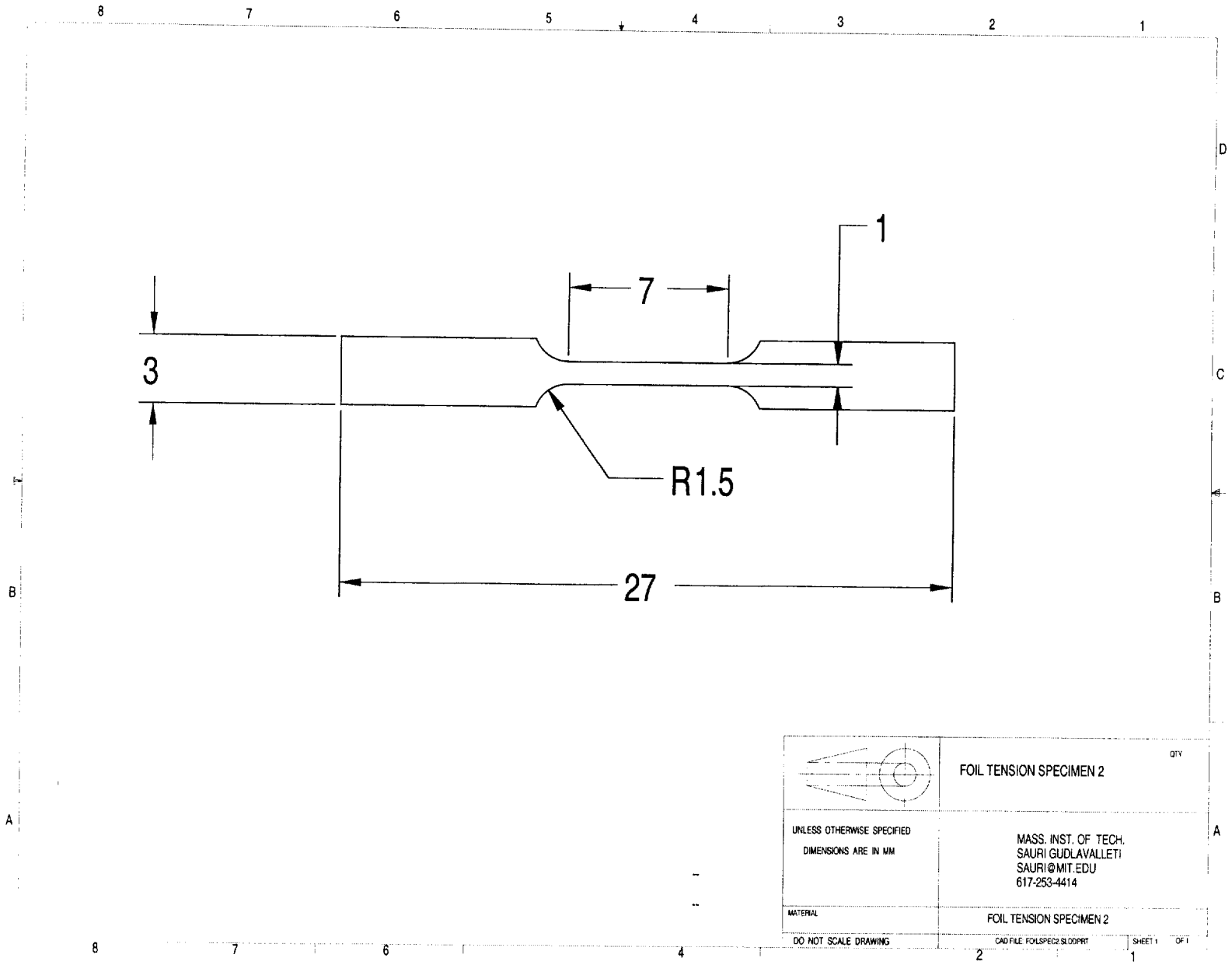


Figure 4-9: Engineering drawing of modified foil tension specimen. All current grips and fixtures are made for this geometry.

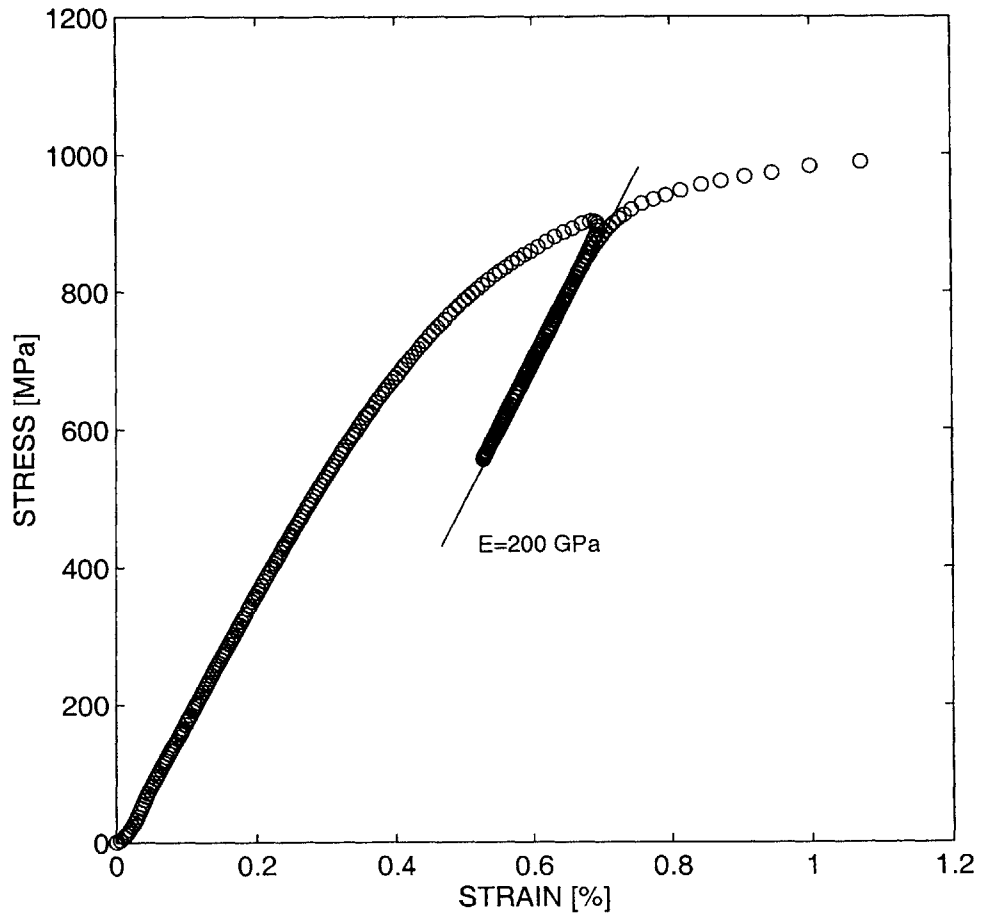


Figure 4-10: Stress-strain graph from tensile test on 25.4 μm thick stainless steel sheet.

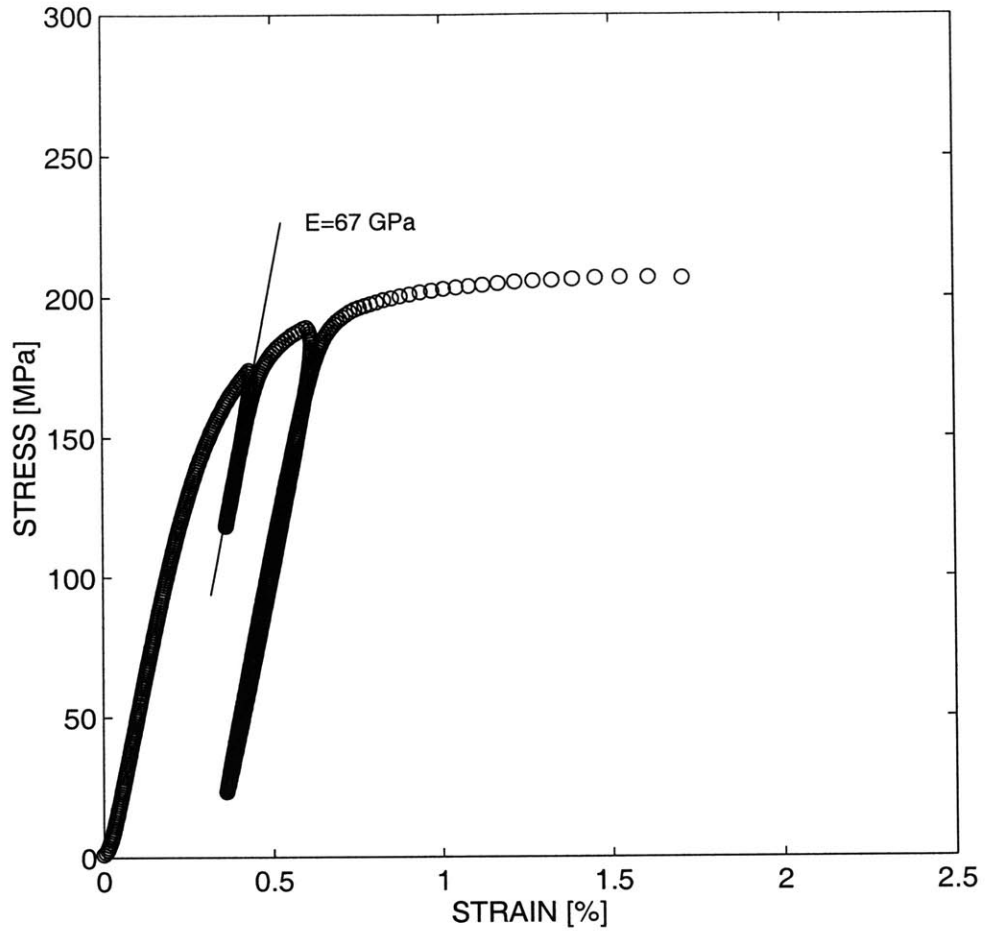


Figure 4-11: Stress-strain graph from tensile test on 25.4 μm thick Aluminum foil.

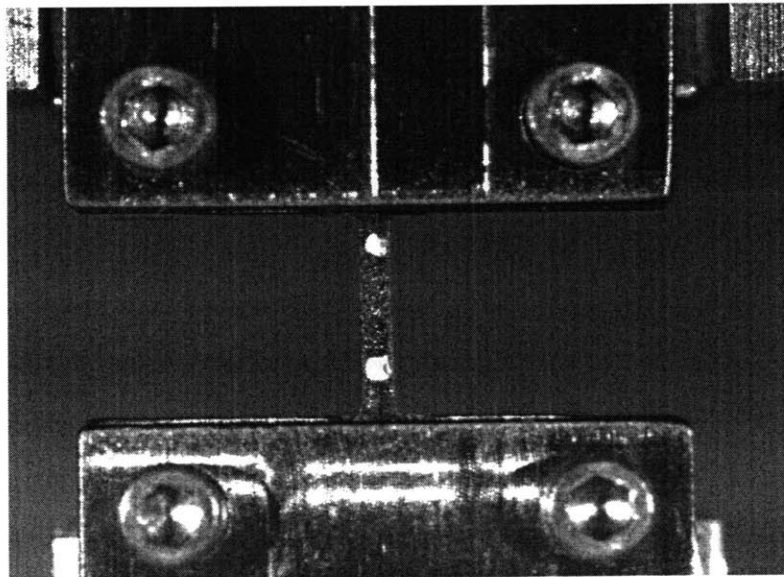


Figure 4-12: Foil tension specimen gripped in machine (Photograph by Cheng Su)

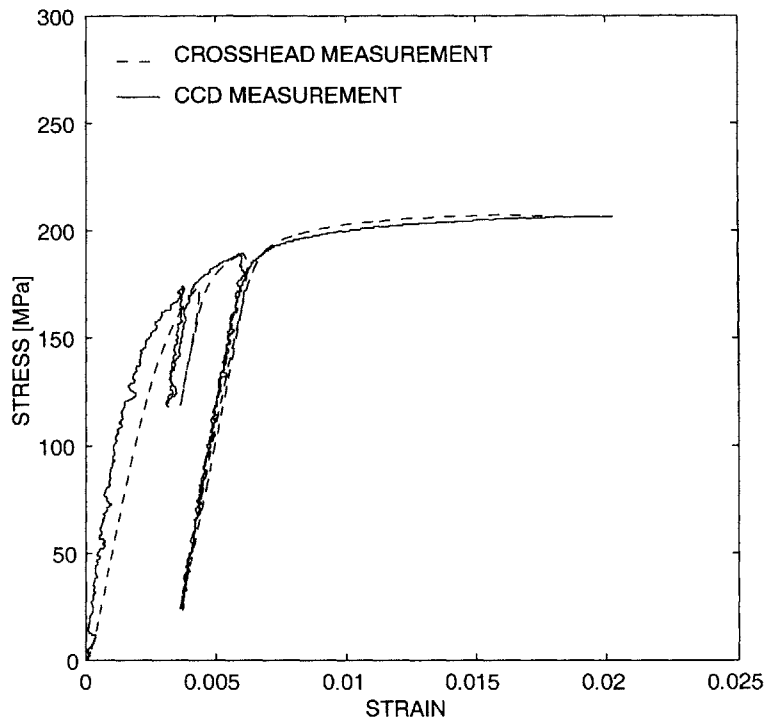


Figure 4-13: Stress-strain graphs from tension test on 25.4 μm thick aluminum foil. Comparison between non-contact measurement and cross-head measurement gives a machine compliance of 3000 N/mm. (Non contact measurement by Cheng Su)

Chapter 5

Mechanical Response of Free-Standing Gold Thin Films

5.1 Introduction

Thin film materials are being increasingly used in various applications due to their specialized electronic, magnetic, optical, thermal and mechanical behavior. One important class of materials widely used in thin film form are FCC metals such as Al, Cu, Au, Ag etc., used mainly as conducting elements in microelectronic devices. It is well known that metals in thin film form exhibit mechanical properties markedly different from those measured in bulk form. Several experimental techniques, such as micro-tensile testing (*e.g.* [38, 28]), nanoindentation (*e.g.* [33, 8]), wafer-curvature measurements (*e.g.* [32]), micro-cantilever beam bending (*e.g.* [48]) and bulge testing (*e.g.* [45]) have been employed to study both the elastic and plastic properties of metallic thin films both in free-standing forms and as bonded to substrates. The yield and ultimate strengths of metallic materials have been observed to be strongly dependent on grain size and film thickness. As the grain size is decreased, yield and ultimate strengths are seen to increase. Strengths have been seen to increase also with decreasing film thickness. Although they are stronger, thin films have been found to have very low ductilities when compared to their bulk counterparts. Free-standing specimens are seen to fail at total strains of only 1 - 2 % under tensile loading

(e.g. [25, 15]).

The purpose of this paper is to provide details of our own experiments on mechanical testing of free-standing gold thin films in the thickness range 450 - 700 nm. Gold is chosen as a model FCC metal for this program for its chemical inertness and ease of fabrication. Since gold does not oxidize easily, the free-standing films are uncapped by surface layers.

5.1.1 Literature Review

Experiments on thin film plasticity

Weihs *et.al* [48] performed bending experiments on gold microcantilever beams using a nanoindenter. The specimens, prepared by silicon micromachining techniques, were $0.87\ \mu\text{m}$ thick, $21\ \mu\text{m}$ long and $20\ \mu\text{m}$ wide. They found a Young's modulus of $57\ \text{GPa} \pm 11\%$ for the films. The yield strength was found to be 260 MPa and independent measurement of hardness gave a hardness of 1.2 GPa. The results from such experiments were found to be affected by the local effects of the sharp indenter tip used to apply the force, such as local indentation.

Microtensile tests on free-standing polycrystalline metallic specimens have been conducted by several groups. In most cases, the specimens consisted of dogbone shaped specimens supported by silicon frames. In Read *et.al* [38], results from microtensile testing of Ti-Al-Ti (0.1-2.0-0.1 μm) multilayers are presented. Arrays of 4 specimens, each 0.25 mm wide and 1 mm long were tested at a time. Ultimate strengths between 150 and 200 MPa and ductilities of 1-2 % are reported. Failure was thought to be due to strain localization as a result of the dimensional constraint that inhibits spreading of plasticity along the gage length of the specimens.

In Keller *et.al* [25] tensile and fracture behavior of free-standing copper thin films is described. Ultimate strength was seen to be inversely proportional to film thickness, decreasing from 380 MPa to 310 MPa as the film thickness was increased from 0.2 to 1.7 μm . However, ductilities measured for the 0.2 μm films were approximately half that of the 1.7 μm films.

In more recent work by Read *et.al* [37], results from microtensile testing of free-standing aluminum thin films are presented. 1 μm thick aluminum film specimens with a gage length of 180 μm and width of 10 μm (Fig. 5-1(a)) were tested in a testing machine shown schematically in Fig. 5-1(b). The load cell had a maximum range of 20 mN; digital image correlation was used to estimate strains with resolutions of upto 56 μstrain . The films had a mean grain size of about 0.3 μm . The Young's modulus calculated from the tests was in the range of 24 - 30 MPa. Average 0.2 % yield strength of 94 MPa and ultimate strength of 151 MPa were measured. While these findings are in agreement with other measurements of high strengths of aluminum films, the average ductility of 22% measured in this work is notable. This is explained as being due to the high measured rate sensitivity exponent of 0.2, which could have been leading to prolonged hardening and extension of the necked region in the plastically deforming specimen.

Huang *et.al* [15, 16] conducted microtensile tests on free-standing polycrystalline Cu, Ag and Al thin films and Ag/Cu multilayers. Young's modulus measurements were consistently 20 % less than values expected based on crystallographic texture. Yield strengths between 350 and 400 MPa were measured for Ag and Cu. Variation of yield strength with grain size was studied by varying the repeat length individual layers in the Ag/Cu bilayers. Yield strengths were seen to vary with film thickness in an inverse square root manner, indicating a Hall-Petch type variation. Strains to failure were typically found to be less than 1.5 %.

Several other reports are available on high yield and ultimate strengths of thin films in tension (*e.g.*[5, 23, 13]), indentation (*e.g.*[33]) and bulge testing (*e.g.*[46]).

Size effects on material behavior: Theoretical background

There are several theories on the effects of grain size and film thickness on the inelastic behavior of materials. A detailed review the effects of both microstructural and dimensional constraints can be found in Arzt [2]. The various length scales involved in thin film deformation are shown in Figs. 5-2(a) and (b). Microstructural length scales of importance are grain size (D), Burger's vector (b), obstacle spacing

(L), obstacle size (R), dislocation loop size (d), and grain boundary thickness (δ_b). Dimensional length scales are particle spacing (L), and for thin films, the thickness (H).

The dependence of film strength on microstructural dimensions arises from the relation between the equilibrium dislocation loop size (d) to the applied shear stress (τ) and dislocation line tension (T_d).

$$\tau = \frac{2T_d}{bd} \approx \frac{Gb}{d} \quad (5.1)$$

The Orowan stress (τ_{Or}) is related to the bowing of dislocations at obstacles. The critical dislocation loop diameter for plastic flow is of the order of the obstacle spacing. For dislocation bowing due to obstacles, this spacing is of the order of the obstacle spacing (L); these dislocations size require a shear stress τ_{Or} , to move them, given by:

$$\tau_{Or} \propto \frac{Gb}{L}, \quad (5.2)$$

where G is the shear modulus of the material.

Once the dislocation density increases to a point where hardening is achieved due to dislocation interaction, the obstacle spacing changes from obstacle size R to the average dislocation spacing, which is proportional to the inverse square root of the dislocation density ρ . The Taylor relation for work hardening is given by

$$\tau = \alpha Gb\sqrt{\rho} \quad (5.3)$$

In many cases, obstacles to dislocation motion are not impenetrable, but rather allow themselves to be cut by the moving dislocation at a stress lower than the Orowan stress. Such shearable particles impart strengthening of the following form:

$$\tau \propto \sqrt{R} \quad (5.4)$$

One of the most popular theories describing the dependence of material strength on grain size is the Hall-Petch (HP) effect, which is explained in terms of pile-ups of

dislocations at grain boundaries. The HP effect predicts a hardening proportional to the inverse square root of grain size:

$$\tau = \tau_0 + \frac{k_{HP}}{\sqrt{D}} \quad (5.5)$$

The HP effect has been seen to operate over a wide range of grain sizes in several metallic materials (*e.g.*[30], p.494). However, since the reasoning for this effect is based on the presence of several dislocations in a single grain, it is expected to break down at grain sizes which are of the order of the dislocation loop diameter or source size. The exact dimension at which this breakdown occurs is not clear. For Cu, the critical grain size has been estimated to be 50 nm [2], while for gold, it has been estimated to be around 100 nm [12]. At this limiting grain size, the microstructural dimension of importance is D itself, and the equilibrium shear stress to maintain a dislocation loop of diameter D becomes:

$$\tau = \frac{Gb}{D} \quad (5.6)$$

The plastic behavior of materials with grain sizes below this critical limit is not clearly understood. While there is evidence of limited dislocation activity in nanocrystalline materials, several other inelastic deformation mechanisms are expected to dominate. These include enhanced diffusional creep because of the small distances involved, grain boundary migration and sliding, grain rotation, and microcracking [25] at grain boundaries and triple junctions. There are several reports on an inverse HP effect, one of softening with decrease in grain size.

Variations in film thickness have seen to affect thin film strengths in much the same way as variation in grain size does. One reason for this is that grain size typically scales with film thickness, resulting in similar effects of either parameter on film strength. Another reason is that many of the constraints placed by grain boundaries on plasticity mechanisms are also placed by the film surfaces, especially in the case of constrained films, *i.e.*, those on substrates, and/or with overlayers. One of the features of dislocation motion in constrained films is the resulting misfit

dislocation generated at the interfaces of the film with the substrate (and/or the overlayer). Fig. 5-3 shows a threading dislocation with burgers vector b in a film of thickness h , gliding on a slip plane oriented at ϕ with respect to the film plane. The burgers vectors may have an angle λ with respect to the slip plane normal. In such a threading dislocation motion, the energy required to expand the dislocation loop and deposit the misfit dislocation(s) is provided by the work done applied shear stress in bringing about plastic flow. This energy balance is the basis of the model proposed by Freund [6] and Nix [32]. Assuming the shear moduli of the film, substrate and overlayer to be μ_f , μ_s and μ_o respectively, this energy balance gives a flow strength for the film as:

$$\sigma = \frac{\sin(\phi)}{\cos(\phi)\cos(\lambda)} \frac{b}{2\pi(1-\nu)} \frac{1}{h} \left[\left(\frac{\mu_f\mu_s}{\mu_f + \mu_s} \right) \ln \left(\frac{\beta_1 h}{b} \right) + \left(\frac{\mu_f\mu_o}{\mu_f + \mu_o} \right) \ln \left(\frac{\beta_2 h}{b} \right) \right] \quad (5.7)$$

Here, β_1 and β_2 are factors defining cut-off radii of the stress field of the dislocation. For $h \gg b$, this model predicts a $1/h$ variation of film strength. However, this model ignores effects of Peierls stress, grain boundaries, interactions with other dislocations, and has been seen to significantly under-predict film strengths [24]. This model was later modified by Thompson [44] to include constraints imposed by grain boundaries and by Nix [34] to include dislocation interaction effects. However, such models are still seen to underpredict film strengths [26].

Microstructural investigations

Kang *et.al* [23] performed TEM investigations on 120 nm thick aluminum thin films strained to 2% on a polyimide substrate. They found dislocation networks formed along some low-angle grain boundaries. Such dislocation networks nucleating from low-angle grain boundaries and triple junctions were also observed by Owusu-Boahen [35] in polycrystalline gold (grain size 390 nm) films on NaCl substrates. *In-situ* TEM imaging during substrate curvature experiments were carried out on Ag films by Kobrinsky *et.al* [26] and on Cu films by Weihnacht *et.al* [47]. Strain hardening due to dislocation tangles and pinning was found to be wide-spread. It

was also found that misfit dislocations were deposited at the film-substrate interface for only certain combinations of film and substrate materials. Microtensile tests were also carried out on Cu films with either no substrate [25] or a compliant substrate [14]. In both these cases, the threading dislocation phenomenon may be thought to have negligible effect on film strength. Substantial evidence for hardening by formation of dislocation tangles was found. In the experiments on Cu films by Keller *et.al* [25], hardening did not develop beyond stage I in most of the smaller grains, indicated by primarily single slip deformation. Dislocation tangles and pinning of dislocation at the tangles were found in some of the larger grains. Also reported in this paper are investigations on fracture behavior of the thin films. Stable crack growth accompanied by significant localized plasticity in the failed region was observed. However, much of the propagation of the crack observed involved the formation of microcracks in grain boundaries within a micrometer or so ahead of the crack tip. Final failure was seen to be by intergranular crack linkage in some cases, and transgranular crack propagation in some others, with no evident preference to either mechanism. Failure by grain boundary cracking was also measured in thin film gold of grain sizes 5 nm - 25 nm by Milligan *et.al* [31].

Summary

Currently available experimental evidence indicates that intense work hardening due to dislocations nucleated at grain boundaries and triple junctions contributes significantly to the high strengths of thin films. As the grains are made smaller, inelastic deformation mechanisms not based on dislocation motion begin to dominate. At room temperatures, when diffusional creep mechanisms are not dominant, grain boundary failures may lead to inelastic deformation. This is evidenced by microscopic observations of cracking at grain boundaries and triple junctions. These observations also explain the low ductilities observed in thin films and other fine grained materials.

5.2 Specimen Preparation and Characterization

5.2.1 Specimen preparation

The geometry of the micro-tensile test specimens is shown in Fig. 5-4, and Fig. 5-5 shows an actual specimen. The 500-700 nm thick specimens of a gage width of 1 mm were made with two different gage lengths, 4 mm and 2.5 mm. Each test specimen, surrounded by a silicon frame, constitutes a unit cell 8 mm wide and 16 mm long. Several such cells were arranged in an array and fabricated on 4" silicon wafers. The unit cells were separated by 250 μm deep etched grooves that facilitated their separation into individual cells. Details of the fabrication of the gold thin film specimens are given in appendix E.1. The silicon frame in each cell consists of two wide regions, GA1 and GA2, to glue the specimen to suitable stages on the testing apparatus. The side arms on the frame, SA1 and SA2, support the dog-bone shaped free-standing thin-film specimens during handling, and are broken-off just before the tension test¹.

5.2.2 TEM investigations

TEM samples of the thin-films were prepared by mounting the films on to copper grids followed by ion-beam milling on a liquid nitrogen cooled stage, to prevent any heating of the specimens. Fig. 5-6(a) shows a low magnification image of the grain structure. The grains were found to be columnar, each grain extending through the thickness of the film. It can be seen that there is substantial variation in the size of the grains. In this preliminary study we have not made any attempt at controlling the grain size and distribution of the thin-films. The in-plane grain-size distribution is bi-modal, with a collection of small grains with an average size of 130 nm, and another collection of larger grains with an average size of 380 nm; the largest grains were about 650 nm in diameter. Figs. 5-6(b), (c) and (d) are images of the undeformed film at higher magnifications. Most of the small grains were observed to be featureless in the

¹After the side arms are broken, any residual stresses in the film are relieved.

interior; however, some sub-grains were occasionally observed; Fig. 5-6(c). Many of the larger grains, Fig. 5-6(d), show several structures $\approx 10\text{-}20$ nm in size, which we suspect are dislocation loops.

5.2.3 Crystallographic texture

The crystallographic texture of as-received gold thin film was measured using a Rigaku RU200 x-ray diffractometer. Fig. 5-7(a) shows the measured pole figures (equal area projections). The films show a very strong texture with the $\{111\}$ crystallographic planes aligned with the plane of the film. The film is seen to exhibit isotropy in the plane. For our crystal-mechanics based calculations to be discussed shortly, we need a numerical representation of the film texture. Such a numerical representation of the measured pole figures using a finite number of crystal orientations was obtained using popLA, a texture analysis computer software package developed at the Los Alamos National Laboratories. Fig. 5-7(b) and (c) show numerical representations of the texture using 334 and 44 crystal orientations respectively.

5.3 Microtensile testing

Mechanical testing of the films was conducted on a newly developed micro-mechanical testing machine [10, 11]. The novel testing machine, shown in Fig. 5-8, consists of a frame containing two aligned compound flexures. The load cell flexure (LCF) acts as a linear spring in series with the specimen, and a measurement of the deflection of this spring with a high resolution displacement sensor provides an accurate measurement of the load on the specimen. The actuator flexure (ACF) acts as an integrated actuation guide for extension of the specimen. The elongation of the specimen is measured² in terms of relative cross-head displacements of the LCF and ACF. The flexures, which are integrally machined into the load frame, eliminate assembly errors and backlash, and ensure accuracy and co-linearity of the axes of travel. The testing

²A non-contacting strain measurement system using digital image correlation of frames captured using a CCD camera is currently under development.

machine has a force resolution of $10\ \mu\text{N}$ over a range of 1.5 N, and a displacement resolution of 20 nm over a range of 6.35 mm.

The gold thin film specimens were mounted on the testing machine by gluing the marked regions GA1 and GA2 marked in Fig. 5-4 to suitable platens mounted on the testing machine (Fig. 5-9). The specimens were first glued to the platens *ex-situ* for ease of positioning and alignment. The specimen assembly with the platens was then mounted on to the machine. At this stage, the flexures were prevented from moving using appropriate stop plugs. Once glued, the side arms SA1 and SA2 were broken by careful scratching using a diamond-tipped scribe. This is the most critical and delicate step, and in close to half the attempts, the gold thin film itself was damaged during the process. Once the side arms were broken, the stop plugs were removed, and actuation started, thus pulling the specimen in tension. The tests were conducted at a nominal strain rate of $10^{-4}/\text{s}$, at room temperature.

5.4 Results and Discussion

Several microtensile experiments were conducted on both the long (type A) and short (type B) specimens. The results were found to be consistent. Fig. 5-10(a) is a typical force-displacement curve from a 4 mm specimen (thickness 650 nm). Fig. 5-10(b) is a force displacement graph obtained from a 2.5 mm specimen (thickness 570 nm).

Several unloading-reloading cycles were conducted during similar tests on additional specimens. The purpose of the unload - reload cycles was (1) to estimate the elastic modulus and (2) to estimate the yield strength in terms of onset of permanent deformation. Figs. 5-11(a) and (b) are force-displacement plots of such tests on the long and short specimens respectively.

The deformation of the films in the experiments is measured in terms of cross-head displacement. This is a combination of the extension of the gage section as well as the regions outside the gage section. As a result, conversion of this displacement to strain using the gage length alone will not be accurate. In this work, an effective length measure L_{eff} , has been used for this conversion. If A is the cross-sectional

area of the gage section, E the elastic modulus of the material, and k_{eff} the stiffness of the dogbone-shaped specimen in tension, L_{eff} is defined as

$$L_{eff} = \frac{AE}{k_{eff}} \quad (5.8)$$

i.e. L_{eff} is the length of a rectangular strip of the same material with a cross-sectional area A and an elastic stiffness k_{eff} . Calculation of L_{eff} from Eq. 5.8 requires k_{eff} , which may be calculated by performing a finite element simulation of the specimen geometry. The schematic procedure for estimating L_{eff} is shown in Fig. 5-12. Using such calculations, L_{eff} was found to be 4.94 mm for the short specimen and 6.33 mm for the long specimen. It must be noted that the L_{eff} method of calculating strain provides accurate estimates of elastic strains, and only estimates during plastic behavior when not all parts of the specimen are deforming in the same manner.

Using these measures of L_{eff} , the force-displacement data of Fig. 5-10(a) and (b) were converted to stress-strain. Fig. 5-13(a) and (b) show the stress-strain plots. The specimens show high yield strengths (≈ 100 MPa) and ultimate strengths (300 - 350 MPa). The total ductilities are only between 1% and 1.5%. Results from tests with unload-reload steps were also converted to stress-strain. These are plotted in Fig. 5-14. These results indicate initial onset of permanent deformation at stress levels of around 100 MPa.

5.5 Simulations

The elastic-plastic properties of the films depend on its crystallographic texture. In order to account for this, finite element simulations of the complete specimen geometry, including the initial crystallographic texture were performed using a crystal plasticity model [20].

The behavior of the short specimen was simulated using the finite element program ABAQUS/Standard. Due to symmetry, only one quarter of the specimen was simulated, using appropriate symmetry boundary conditions. The finite element mesh

is shown in Fig. 5-15. The mesh consists of 1 layer of 76 elements, with a nominal specimen thickness of 1 μm . The elements used were continuum brick elements with 8 nodes (C3D8). Mesh convergence was verified by simulating a denser mesh with 3 elements through the thickness. The current mesh was chosen to minimize computational costs during the crystallographic texture-based simulations.

Symmetry boundary conditions were applied on node sets on the planes of symmetry. Gripping conditions were simulated by preventing all nodes on the right side face from moving in the thickness and width directions of the specimen. Tensile loading was simulated by applying displacement control, moving all the nodes on the right hand face towards the right. The net reaction force resulting from the tensile loading was calculated, and was used to estimate the force-displacement response of the specimen(s). The force-displacement response of the full specimen is the same as that of the quarter specimen; this is a direct consequence of the assumed symmetry.

A rate-dependent polycrystal plasticity model [20] was used for the simulations. The inputs required for this model are the elastic constants, initial crystallographic texture, and hardening parameters for the single crystal constitutive model. Standard values of elastic constants for gold, $\{C_{11} = 186 \text{ GPa}, C_{12} = 157 \text{ GPa}$ and $C_{44} = 42 \text{ GPa}\}$ [41] were used. A numerical representation of the measured crystallographic texture using 44 crystal orientations, shown in Fig. 5-7(c) was used for the calculations³. Based on this assumption, each integration point was taken to consist of grains in all 44 orientations. The Taylor assumption, imposing the same uniform macroscopic deformation gradient on all the texture components at an integration point was invoked.

The hardening parameters required by the model[20] are (i) s_0 , the initial slip-system yield strength; (ii) h_0 , the initial hardening rate coefficient; (iii) s_s , the saturation deformation resistance of the slip system; (iv) a , the hardening exponent. These parameters were adjusted in order to fit the simulated force-displacement response of the short specimen to the experimental data. Fig. 5-16 shows the fit obtained using

³The adequacy of using only 44 crystal orientations was ascertained by comparing results with simulations conducted with more a accurate numerical texture representation, consisting of 334 orientations (Fig. 5-7(b)). The results were found to be very close.

$s_0 = 35$ MPa, $h_0 = 80$ GPa, $s_s = 140$ MPa and $a = 2.2$. An unload-reload cycle was also included in the simulation. The elastic unloading slope obtained from the simulation is 9.94 N/mm. The average elastic unloading slope from several tests is 9.89 N/mm. There is good agreement between the experimentally measured elastic modulus and expected modulus calculated using the measured texture and *known elastic constants of gold*.

The stress-strain response of the film was deduced from the calculations by extracting the stress-strain response of one of the elements in the interior of the gage section, marked in Fig. 5-15. The stress-strain response calculated here is compared with the stress-strain converted from experimental force-displacement data using the L_{eff} method described before in Fig. 5-17. The simulations indicate higher strain levels in the gage section than that calculated by the schematic L_{eff} procedure. This is because, the L_{eff} method underestimates the plastic strains in the gage section; it assumes the same strain levels in all parts of the specimen, while in reality, strains are higher in the narrow gage section and lower in the wider grip sections. This is reflected in Fig. 5-17, where the actual strains in the gage section calculated by finite element simulations are higher than the strains calculated using the L_{eff} procedure, although the force-displacement data have been made to match (Fig. 5-16).

The elastic modulus calculated from the unloading slope in the simulation is 84.3 GPa. This may be considered the expected “Young’s Modulus” for a sample of gold with the texture measured from the film.

The stress-strain graphs indicate an initial yield stress of around 100 MPa. This is also reflected in the slip system yield strength of 35 MPa, which when multiplied by the Schmidt factor of 3, is 105 MPa. The specimen is seen to harden rapidly from this initial yield strength to an ultimate strength of about 350 MPa. The ductility of the films is very low, as indicated by the strains to failure of less than 1.5%.

5.6 TEM of deformed films

The microstructural basis for the high yield and rapid hardening behavior of the films was investigated by post-deformation transmission electron microscopy. TEM samples were prepared from regions in the gage section of the film away from the failed region in the same manner as described before. Fig. 5-18 shows several images of regions of the deformed film. There is clear evidence of dislocation activity in the large grains as indicated in Fig. 5-18(a), (b) and (c). Figs. 5-18(a) and (b) show forest dislocations which serve as pinning obstacles for dislocation movement.

Fig.5-18(c) is an image of a grain tilted to show both the top and bottom surfaces of the grain. Indicated in the figure are several dislocations through the film thickness piled up against the grain boundary. Fig. 5-18(d) is an image of one of the smaller grains. Absence of dislocation structures in grains smaller than 100 nm was found to be common through out the sample.

Yielding and plastic deformation by wide-spread dislocation activity in thin film copper has been recently observed elsewhere (see, *e.g.* Weihnacht *et.al* [47] and Hommel *et.al* [14]). Read *et.al* [36] report difference in dislocation activity levels with grain size during in-situ TEM of tensile experiments on free-standing copper thin films. Further, they report failure initiation by grain boundary cracking. We believe that the reason for the low ductility in our gold films is such grain boundary failure.

5.7 Membrane bend-stretching experiments and simulations

Membrane bending experiments were carried out on the same free-standing gold thin film specimens in an attempt to (i) develop an easier experimental technique for obtaining mechanical properties of the films and (ii) compare experimental results obtained in tension and bending modes by predicting the response in bending using the stress-strain characteristics obtained from the tensile experiments.

5.7.1 Experiments

Fig. 5-19 shows a schematic of the experimental set up used in the experiments. To conduct these experiments the testing machine was re-oriented so that the testing axis was vertical. The specimens were placed perpendicular to the testing axis on a fixture that supports the GA1 and GA2 regions of the silicon frame (indicated in Fig. 5-4). A suitable fixture with a 0.5 mm radius roller fixed to the other stage was moved towards the specimen to bend it at its mid-point. In the bend tests the side-arms SA1 and SA2 of the silicon frame were not broken prior to testing. Tests were conducted on both the long and short specimens. The force-displacement ($P - \delta$) response at the roller was measured in the experiment.

5.7.2 Analysis and prediction

In this section, we present a simplified analysis of the membrane bending experiment in order to predict the force-displacement response of the roller using the stress-strain response obtained from the tensile simulations. The following assumptions are made: (i) the film is taken to have negligible bending stiffness; (ii) the loading is taken as a point load at the mid-point of the specimen; (iii) friction at the roller-film contact is neglected; (iv) the film is taken to be homogeneous.

Fig. 5-20 is a diagram of one half of the bending set-up. The specimen has a total length $2L$, thickness h , and width (perpendicular to the plane of the drawing) $w(x)$. At the point shown in the drawing, a total force of $2P$ causes the midpoint to deflect by δ , and the film to stretch by $2\delta L$. In the following analysis, we will solve for the $P - \delta$ response by comparing the change in specimen length calculated from geometry, and from the strain due to the tension T developed due to the load P .

From force balance, the tension T in the film is related to the applied load P as:

$$T = \frac{P}{\sin(\theta)} \quad (5.9)$$

The extension δL of the half-specimen may be calculated geometrically as:

$$\delta L = \sqrt{L^2 + \delta^2} - L \quad (5.10)$$

The extension of the specimen may also be calculated from the strain (ϵ) it undergoes, which depends on the tensile stress (σ) in the film.

$$\delta L = \int_0^L \epsilon(x) dx = \int_0^L \hat{\epsilon}(\sigma(x)) dx \quad (5.11)$$

$\hat{\epsilon}(\sigma(x))$ is the constitutive response of the material, and is obtained from the finite element simulation of the tensile response, shown in Fig. 5-17.

The tensile stress developed in the film due to the tension T varies with position along its length due to the dog-bone shape of the specimen. At a position x , the tensile stress $\sigma(x)$ is

$$\sigma(x) = \frac{T}{hw(x)} = \frac{P}{hw(x)\sin(\theta)} \quad (5.12)$$

θ itself may be calculated from geometry ($\tan(\theta) = \delta/L$). Using Eq. 5.12 in Eq. 5.11, and equating the δL thus obtained to that obtained from geometry (Eq. 5.10), we obtain

$$\sqrt{L^2 + \delta^2} - L = \int_0^L \hat{\epsilon}\left(\frac{P}{hw(x)\sin(\theta(\delta))}\right) dx \quad (5.13)$$

This equation is implicit in δ and P and was solved numerically using a MATLAB script. For each value of δ , P was solved for by iteration using a bisection scheme. $\hat{\epsilon}(\sigma(x))$ was calculated by interpolating the stress-strain data of Fig. 5-17. Using this script, the complete $P - \delta$ response of both the long and short specimens was calculated.

Figs. 5-21(a) and (b) show the comparison between experimental results and numerical calculations for the long and short specimens respectively. The agreement between experimental data and the calculations is excellent. The experiments show a slightly stiffer response at highest loads, which could be a result of the friction between the roller and the films.

5.8 Conclusions

- Free-standing gold thin-film specimens of thicknesses in the range 500-700 nm were fabricated by e-beam deposition methods. The films have grains which have thicknesses essentially equal to the film thickness, and an in-plane grain-size distribution which is bi-modal, with a collection of small grains with an average size of 130 nm, and another collection of larger grains with an average size of 380 nm. The films also show a strong texture with the $\{111\}$ crystallographic planes aligned with the plane of the film.
- The thin-film specimens were tested in simple tension. The experiments show that the gold thin-films have a Young's modulus of ≈ 83 GPa, an initial yield strength of ≈ 100 MPa, which is followed by rapid strain hardening to a stress level of ≈ 360 MPa at a strain of only $\approx 1.4\%$.
- TEM investigations of the deformed films show that the rapid strain hardening is attributable to extensive dislocation activity in the larger grains. However, there is a distinct lack of dislocation activity in grains smaller than ≈ 100 nm. The reason behind the low ductility in our gold specimens is still unclear. However, we speculate that since the smaller grains do not easily deform plastically, it may be easier to activate grain boundary sliding and decohesion processes to generate micro-cracks at their triple-point junctions, which is what leads to premature failure and low ductility. Low ductilities of the same order of magnitude are also observed in other nano-crystalline materials with grains of more uniform size in the sub 100 nm range.
- The apparent plastic deformation inhomogeneity at the microscopic level indicate that the Taylor-model based crystal plasticity simulations must be viewed with caution. Better, more physically based models are needed to describe the high strength of the thin films.
- Membrane bending experiments were conducted on the films. The response from these experiments were predicted using the stress-strain curve fit to the tension

tests in a simple analysis of the experiment. The good agreement obtained indicates that the bending experiments, that are easier to conduct, may be used to obtain the stress-strain response of the films using an inverse approach. In this case, it would be advantageous to make specimens with a constant width.

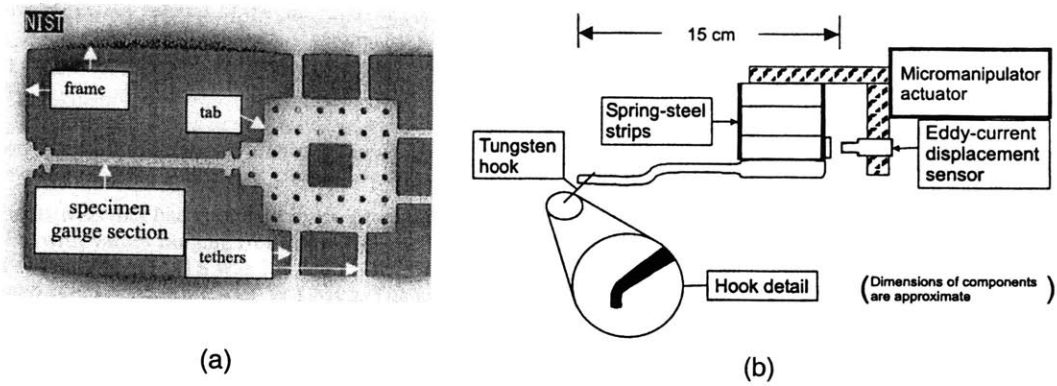


Figure 5-1: (a) Free-standing aluminum thin film tensile specimen; (b) Testing machine configuration. (From Read *et.al* [37])

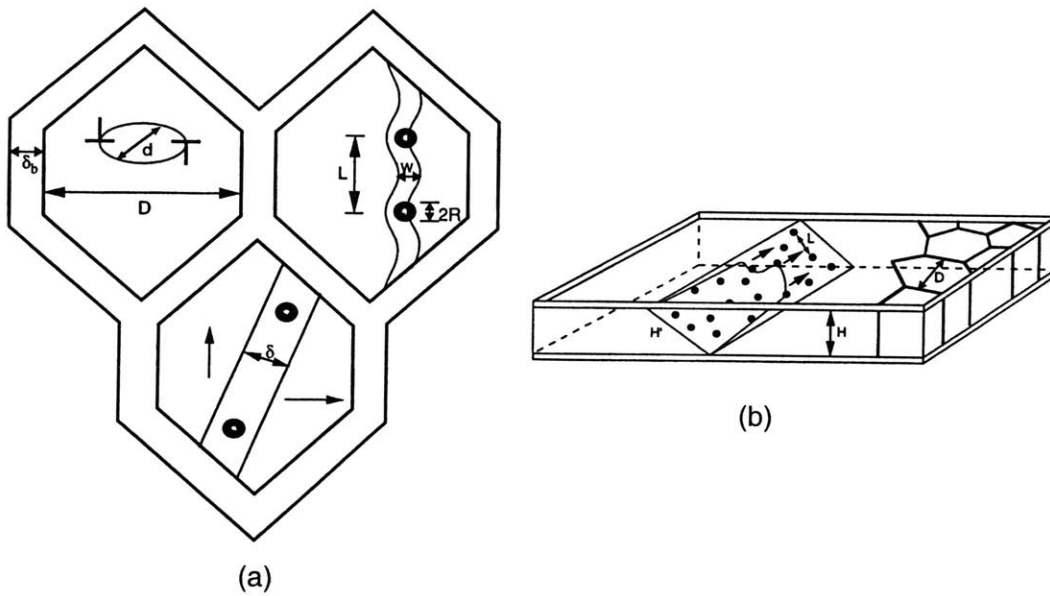


Figure 5-2: Length scales affecting material strength: (a) Microstructural constraints; (b) Dimensional constraints. (From Arzt [2])

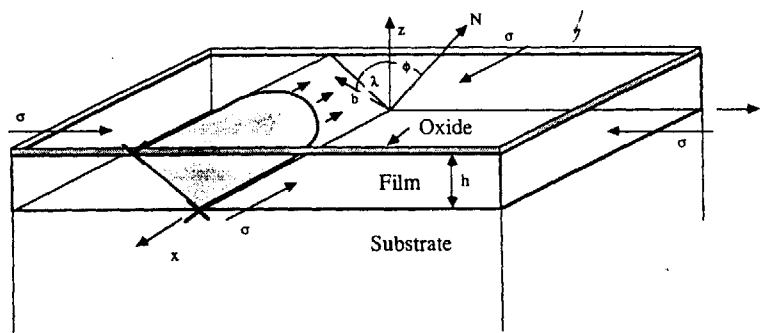


Figure 5-3: Figure showing a single threading dislocation on a slip plane in a constrained thin film

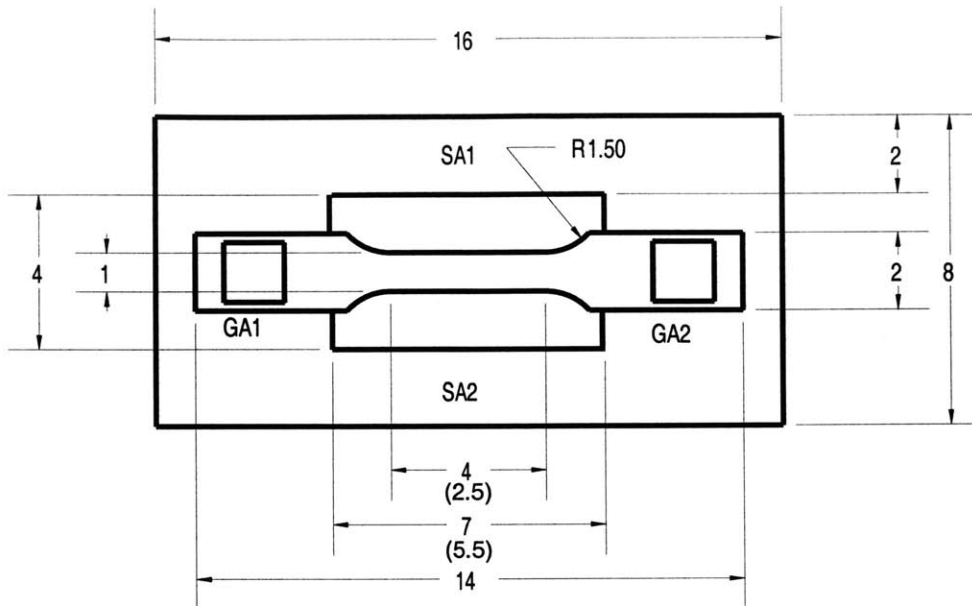


Figure 5-4: Free-standing gold thin film tensile specimen, Type A (long). Numbers in parentheses are corresponding dimensions for type B (short) specimens. All dimensions are in mm.

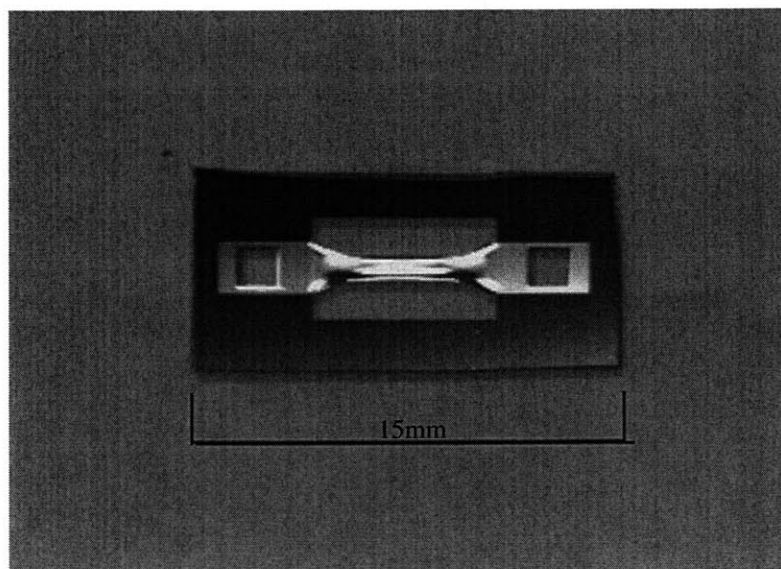


Figure 5-5: Photograph showing gold thin film specimen

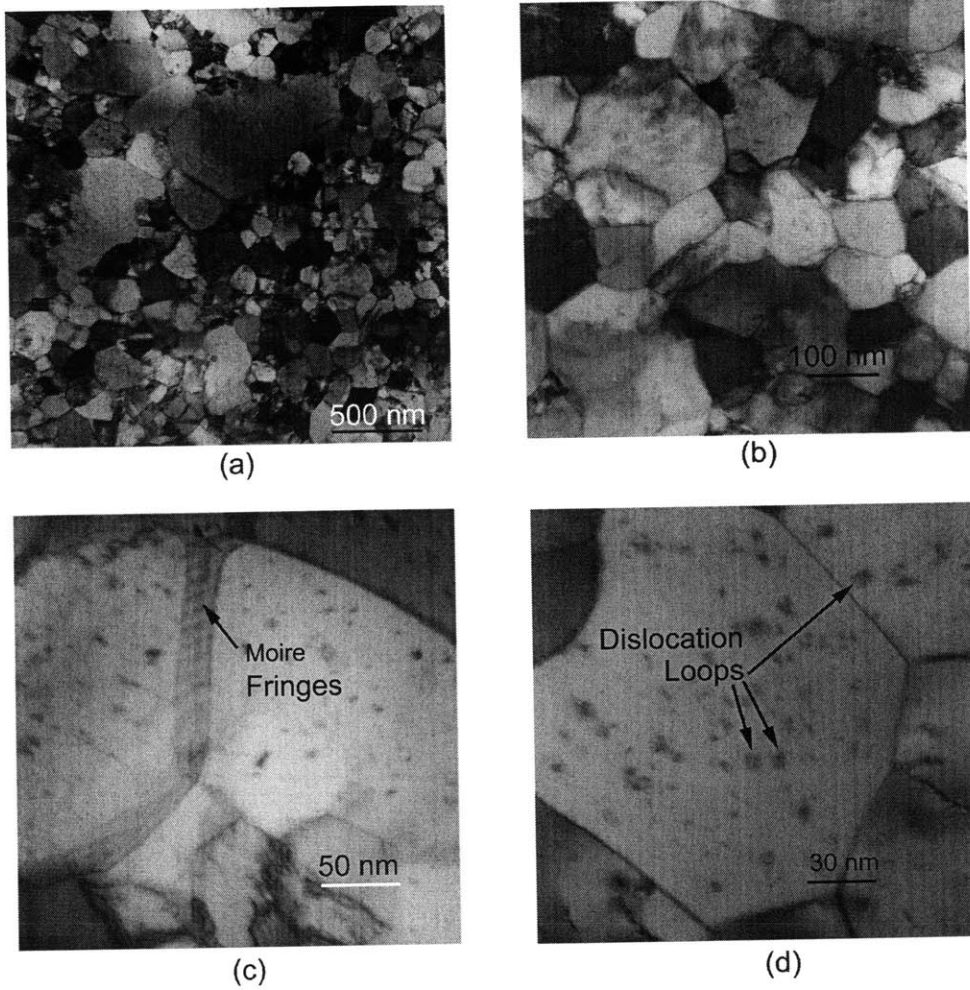


Figure 5-6: TEM images of as-received gold thin film (TEM by Prof. K. Sharvan Kumar)

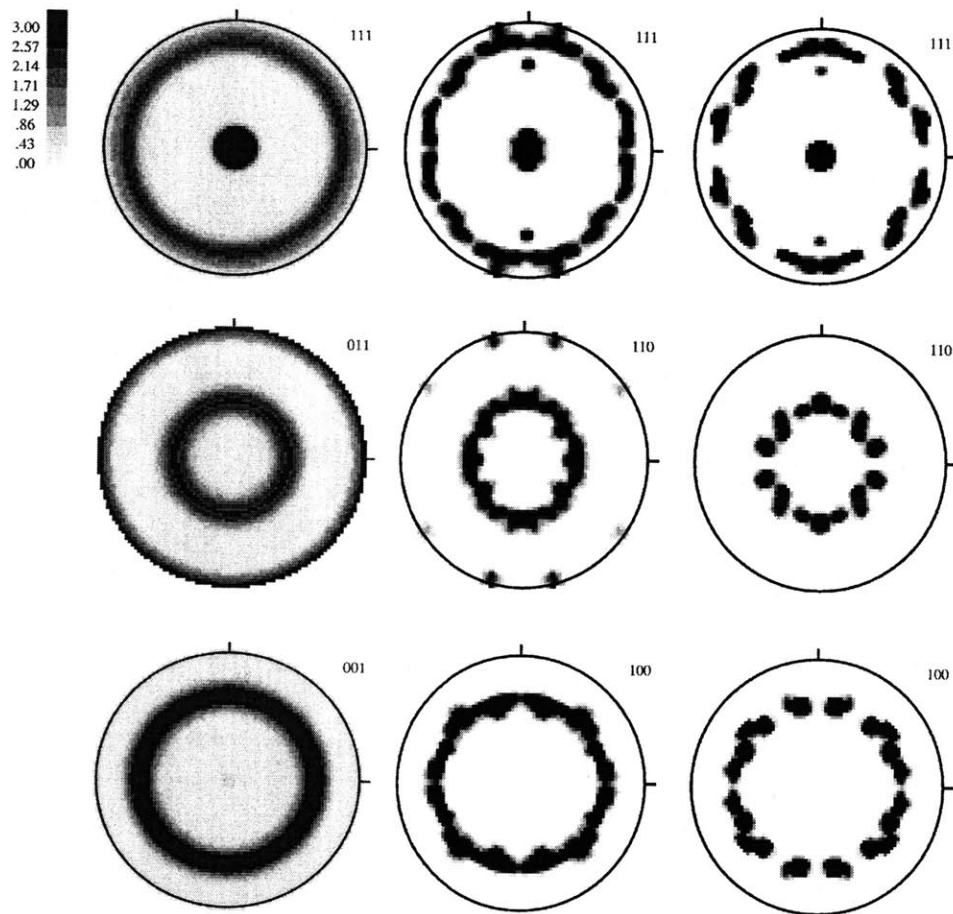


Figure 5-7: Crystallographic texture of gold thin films (popLA pole figure representation): (a) Measured, (b) Numerical fit (334 crystals), (c) Numerical fit (44 crystals) (Pole figure measurement and representations courtesy Prakash Thamburaja)

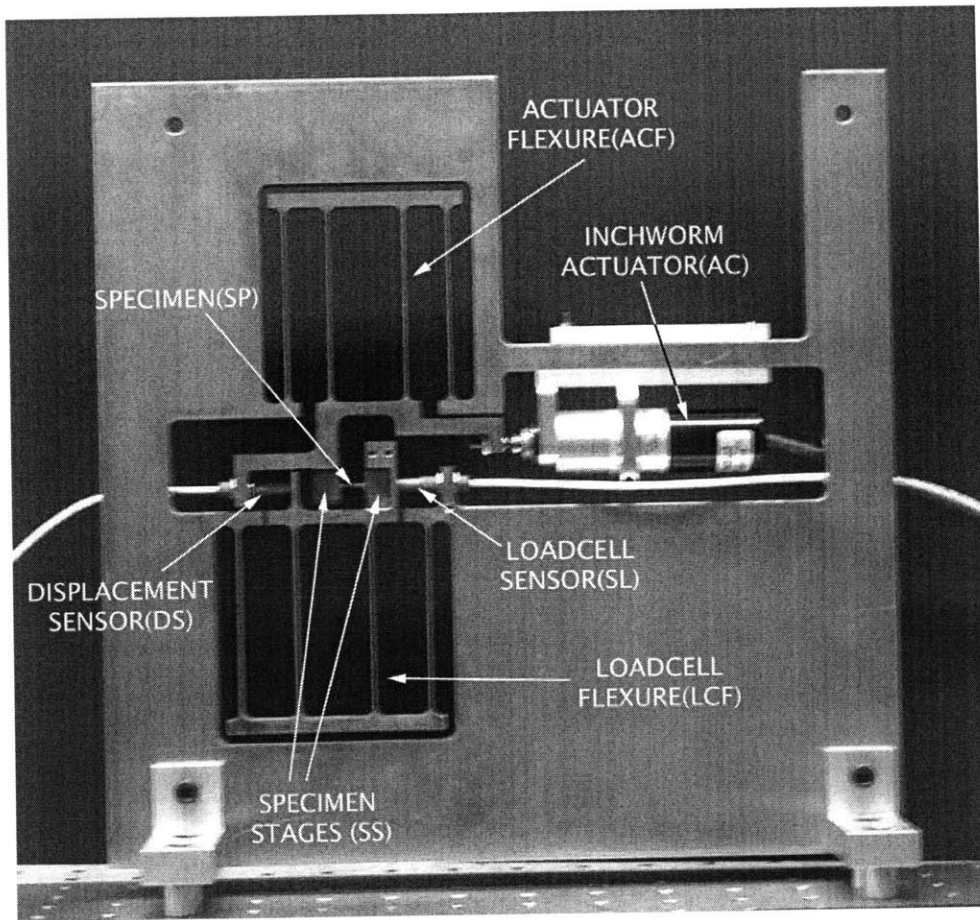


Figure 5-8: Micro-mechanical testing machine

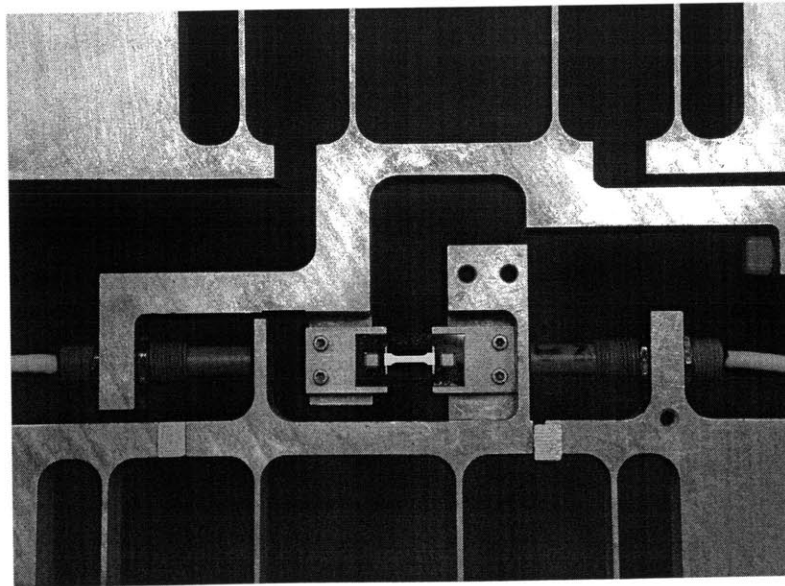


Figure 5-9: Photograph showing gold thin film specimen mounted in testing machine (side arms unbroken).

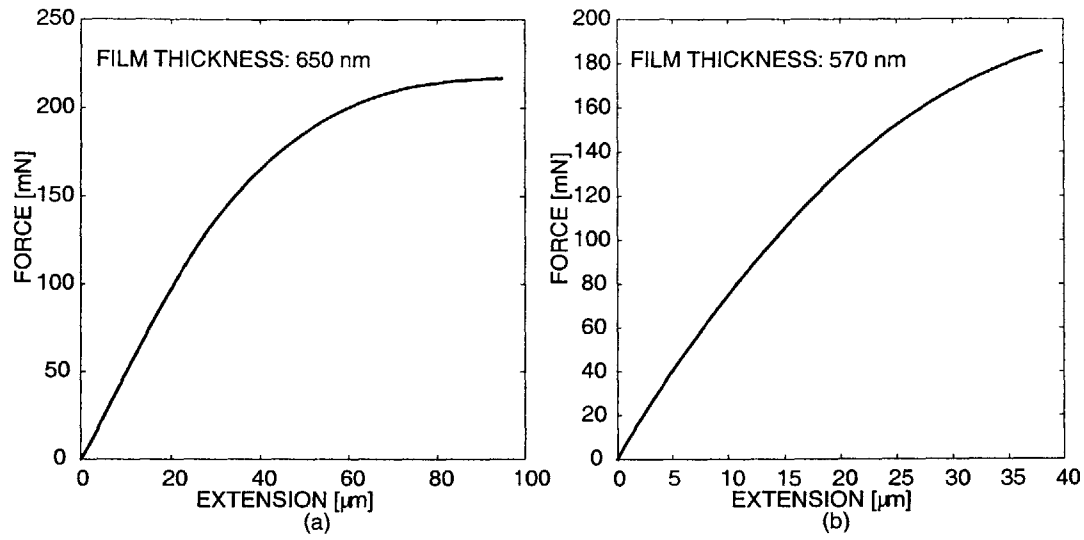


Figure 5-10: Tensile test results: Force-displacement response of (a) 4 mm specimen; (b) 2.5 mm specimen.

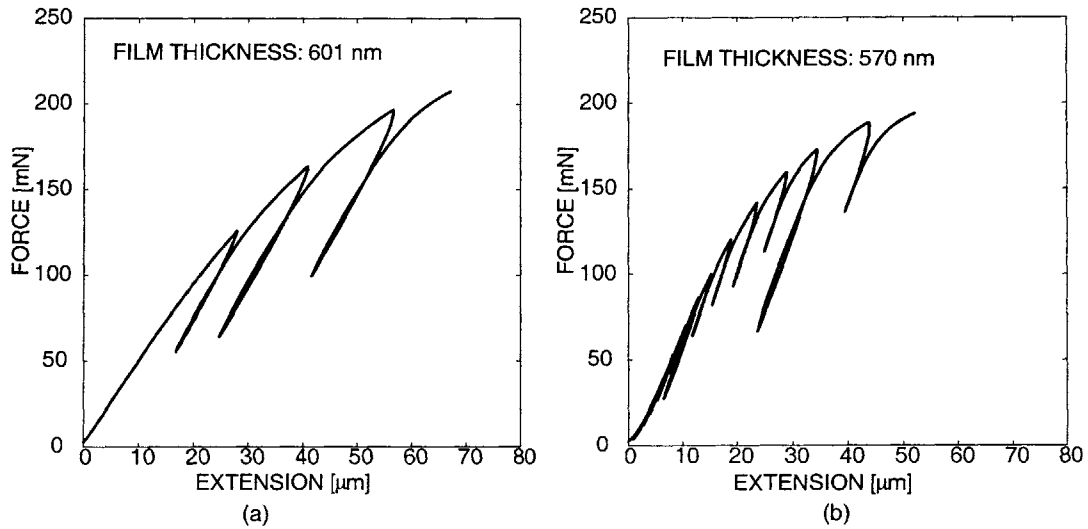


Figure 5-11: Tensile tests with loading-unloading cycles: (a) on a 4 mm specimen; (b) on a 2.5 mm specimen.

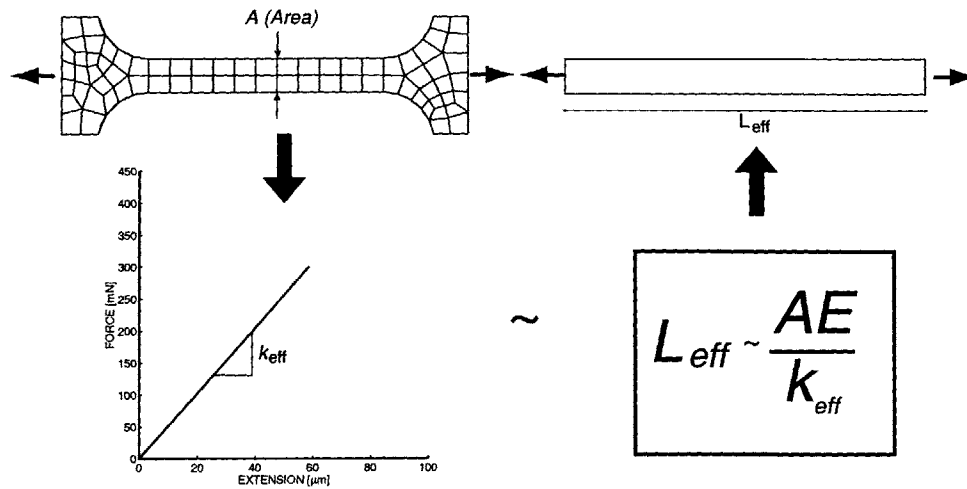


Figure 5-12: Procedure for obtaining “effective” specimen gage length from numerical simulations. The specimen geometry is subjected to tensile loading in a finite element simulation. The stiffness it exhibits is taken to be the stiffness of an equivalent specimen, with a constant cross-section, and length L_{eff} .

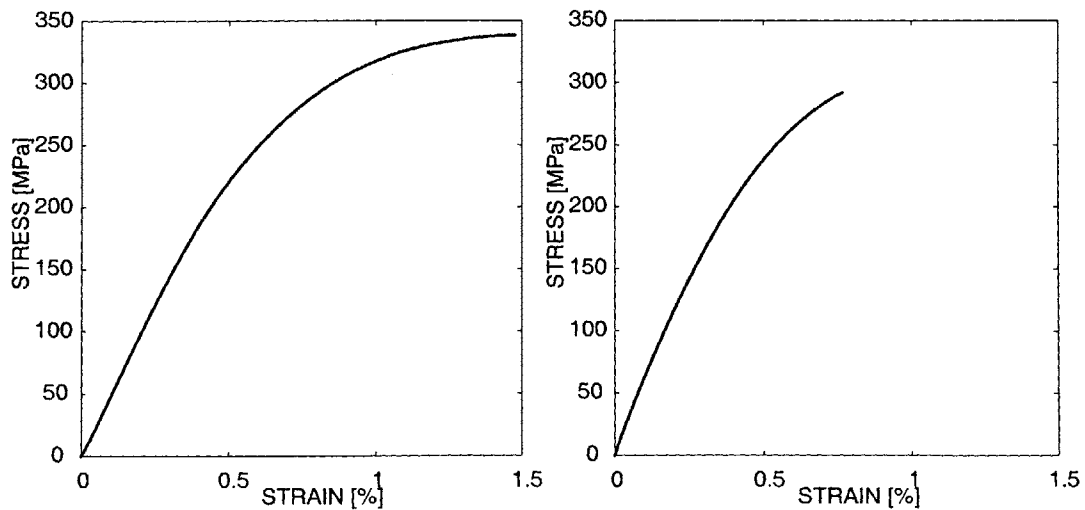


Figure 5-13: Stress-strain graphs from tensile tests: (a) on a 4 mm specimen; (b) on a 2.5 mm specimen.

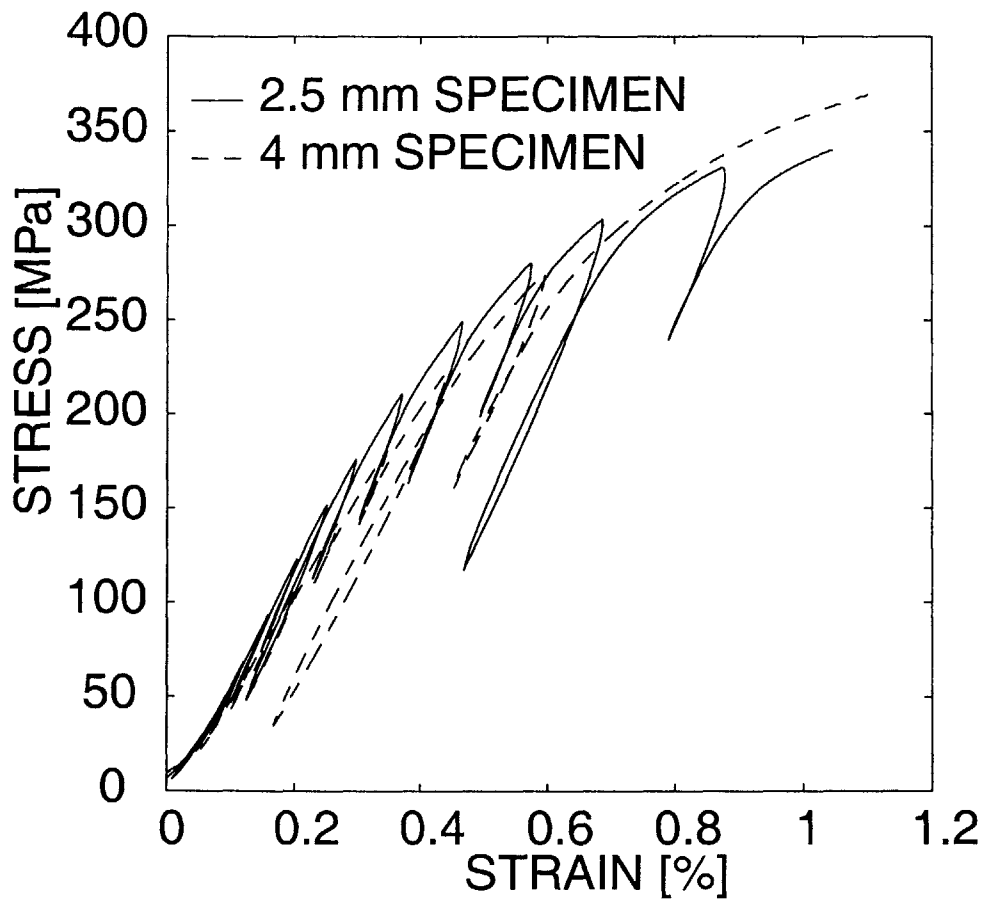


Figure 5-14: Stress-strain graphs from tensile tests with unload-reload cycles

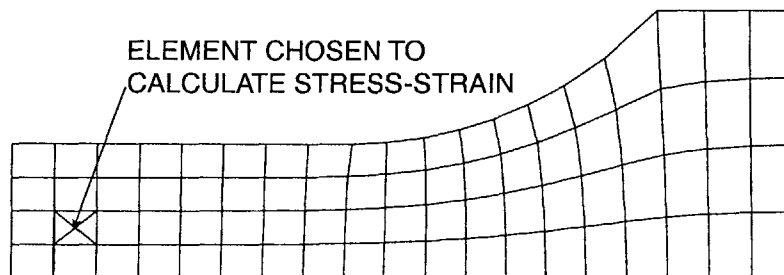


Figure 5-15: ABAQUS finite element mesh used in simulating response of gold thin film specimen. Mesh consists of 1 layer of 76 elements.

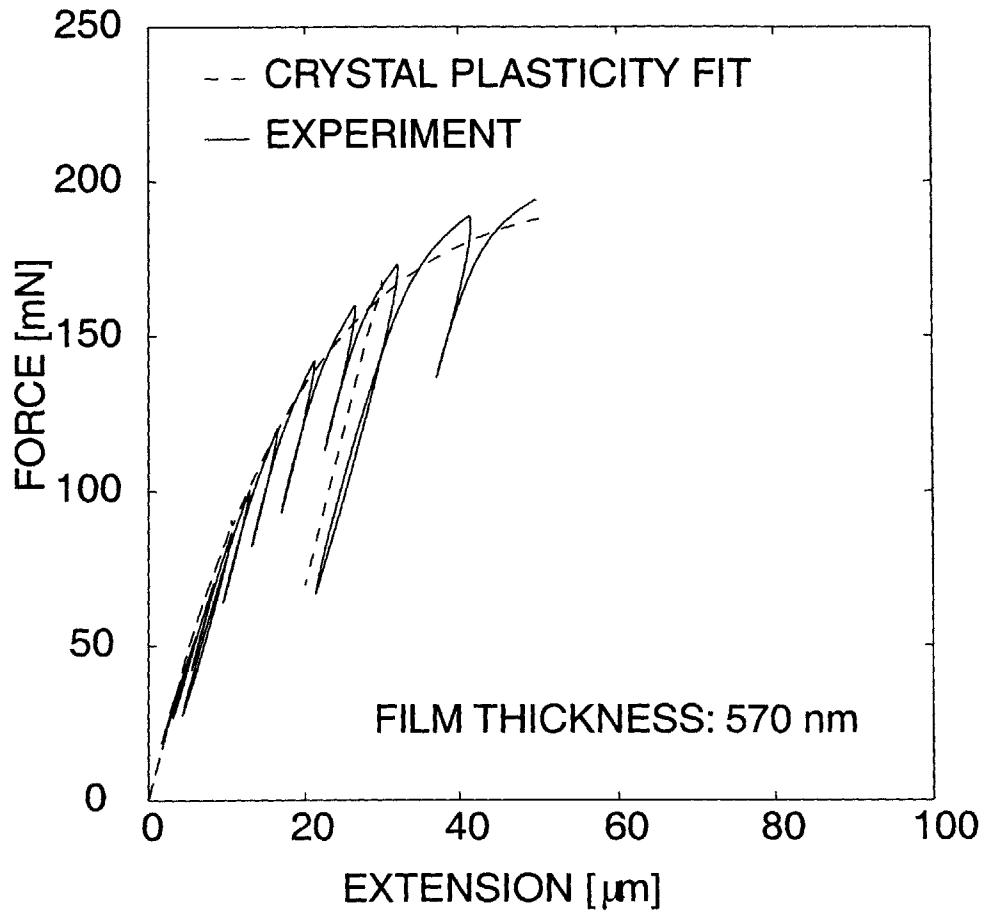


Figure 5-16: Fit of simulation to experimental force-displacement data (short specimen)

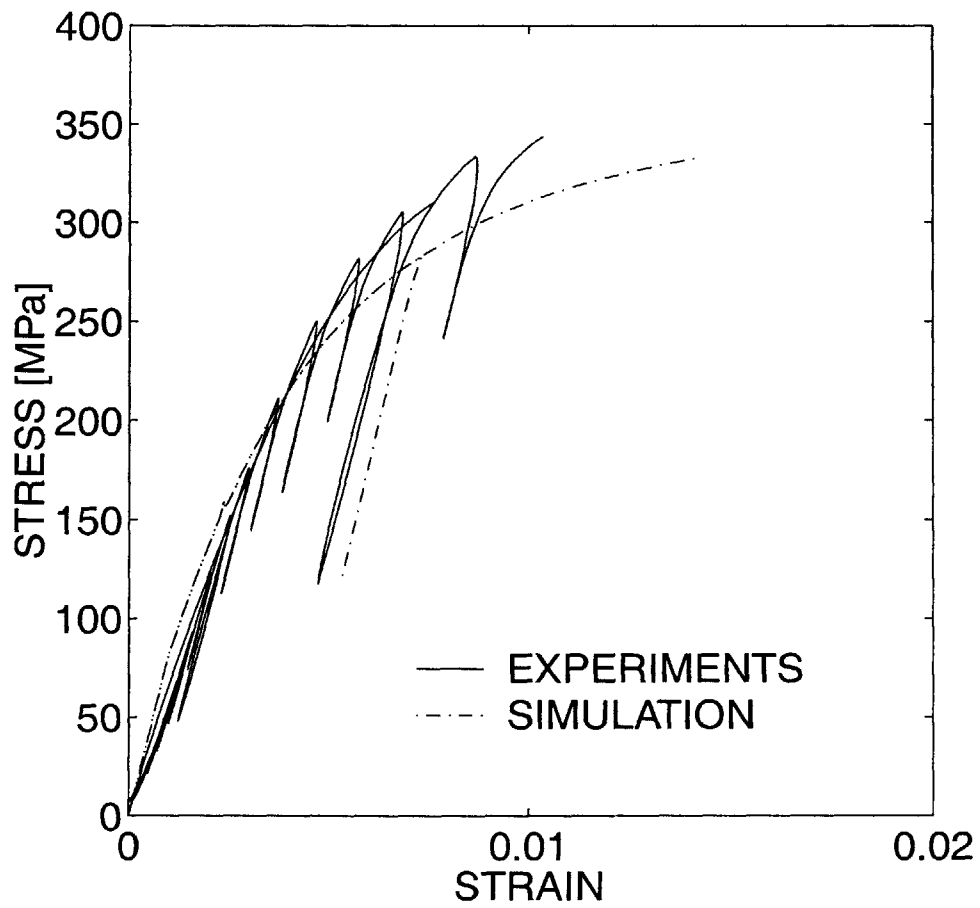


Figure 5-17: Stress-strain response. Stress-strain calculated from an interior element in the simulations is compared with experimental results converted using the L_{eff} method

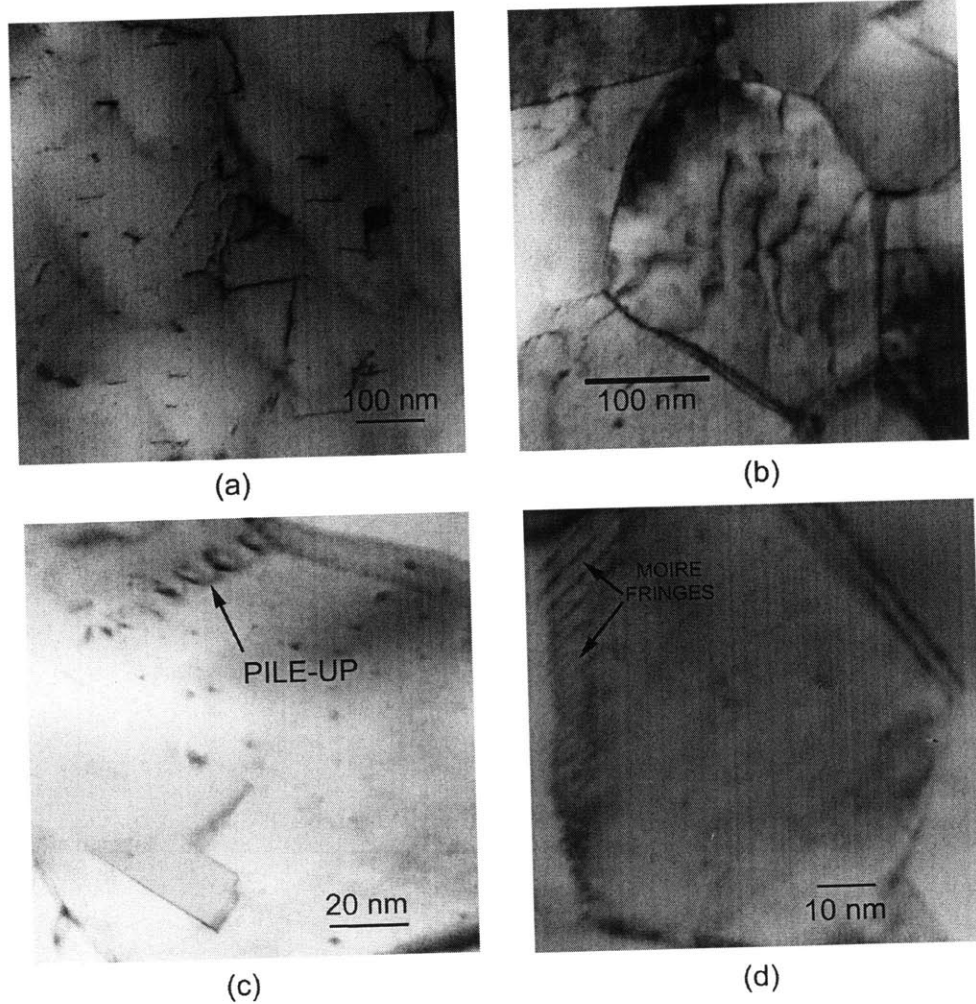


Figure 5-18: TEM images of deformed gold thin film: (a) & (b) Images showing dislocation activity, (c) Image showing pile-up at grain boundary, (d) Image showing no dislocation activity in a 100 nm grain (TEM by Prof. K. Sharvan Kumar)

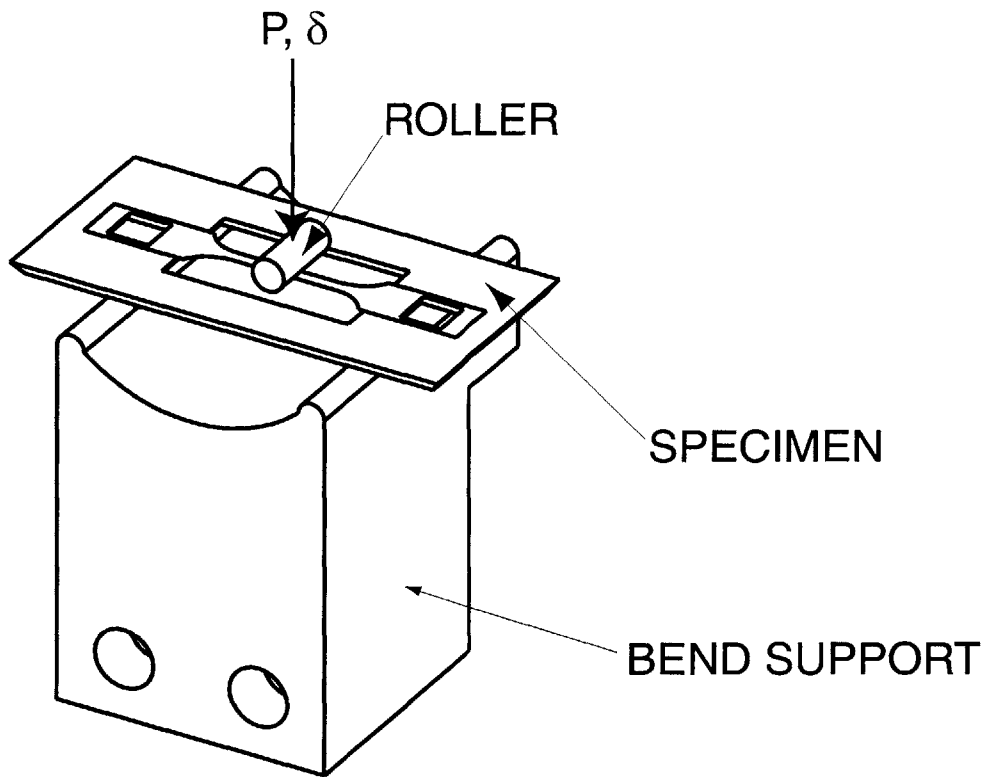


Figure 5-19: Schematic of the set-up used for membrane bending experiments on the gold thin film specimens.

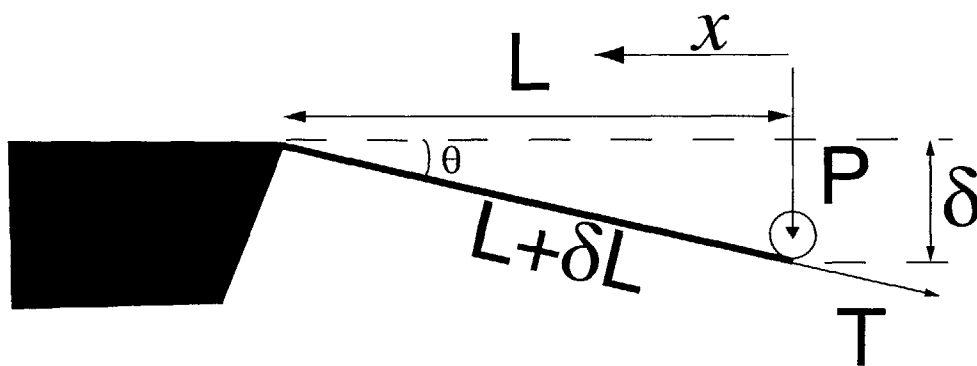


Figure 5-20: Schematic free-body diagram of the membrane bending experiments on the gold thin film specimens.

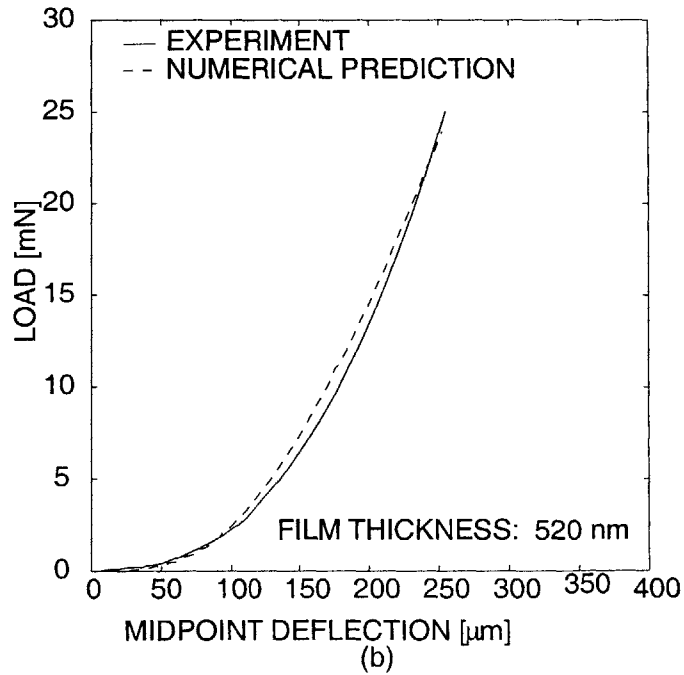
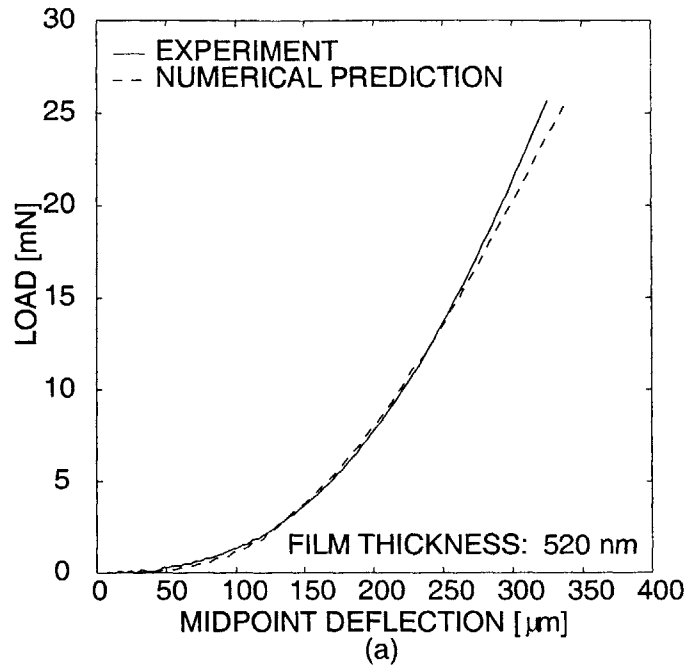


Figure 5-21: Experimental response and numerical prediction of roller force-displacement response during membrane bending experiments: (a) comparison of data on the long specimen; (b) comparison of data on short specimen.

Chapter 6

Anisotropy of Rolled Copper Foil using Microtensile Testing¹

6.1 Introduction

The effects of crystallographic texture on the elastic-plastic response of FCC metals has been extensively documented. Bronkhorst *et.al* [4] present a Taylor-type model for large deformation polycrystal plasticity, and verify it using experiments and simulations on large deformations of initially (nominally) isotropic polycrystalline OFHC copper. The utility of the Taylor-type approach is further demonstrated by Kalidindi *et.al* [19]. In Kalidindi *et.al* [21], the evolution of crystallographic texture and its effects on the deformation of *pre-textured* OFHC copper is reported.

In the present work, the low-load testing machine was used to conduct microtensile tests on thin (10 μm) rolled polycrystalline copper foil to investigate the anisotropy in mechanical behavior arising from the strong initial rolling texture. The foil may be thought to be in a length scale regime where macroscopic continuum crystal plasticity theory still holds, so that the anisotropy in plastic behavior may be predicted based on its crystallographic texture using such a theory. The aim of this study was multifold: (i) Demonstration of microtensile testing as a method to obtain useful mechanical

¹Part of this study was conducted in association with Nicoli Ames and Mats Danielsson as a term project for course 2.073

behavior information from small quantities of materials; (ii) Demonstration of the utility of our small-scale testing machines in small-volume materials testing; (iii) Investigation of the applicability of Taylor-type polycrystalline plasticity formulation in [4] to thin rolled copper foil.

Dogbone shaped tensile specimens were punched from free-standing rolled copper foils in the rolling and transverse directions. These were subsequently annealed to relieve the effects of work hardening. The crystallographic texture of a coupon of the annealed foil was measured by X-ray diffraction. Microtensile tests were conducted on several specimens in both the rolling and transverse directions. A polycrystal plasticity model was then used to simulate the behavior of the foil. A finite element mesh representation of the complete foil geometry was simulated in uniaxial tension. The strain hardening parameters in the single crystal constitutive model were adjusted to fit the force-displacement response from the simulation to that from the experiment in the rolling direction. These parameters were then used to predict the response of a specimen with crystal orientations rotated by 90^0 . These predictions are compared to the results of experiments in the transverse direction.

6.2 Specimen Preparation

Free-standing rolled copper foil was obtained from Goodfellow Inc.², PA. These were available in the form of coupons 50mm x 50mm x 10 μ m. The coupons were cut into pieces slightly larger than the specimen size. The geometry of the specimen used for the microtensile test was adapted from ASTM foil testing standards [3]. Specimens were dogbone shaped with a 1 mm gage width, 7 mm gage length and shoulders with a 1.5mm fillet radius leading into a 3.5mm grip section as shown in Fig. 3-11. Specimens were prepared by punching the pieces cut from the coupons through an appropriately shaped die. Specimens were made both along and transverse to the rolling direction of the foil.

The foils had a history of severe work hardening due to the extreme rolling in-

²<http://www.goodfellow.com>

volved. The specimens were hence annealed for 2 hours at 550⁰C followed by in-furnace cooling, to minimize the effects of this work hardening. The suggested annealing temperatures for copper are 425 - 650⁰C [1]. The annealing was performed in a tube furnace in an inert environment of nitrogen to prevent oxidation. The annealing was performed after punching the specimens in order to avoid renewed strain hardening effects due to punching.

6.3 Measurement of Crystallographic Texture

The crystallographic texture of annealed copper foil was measured using a Rigaku RU200 x-ray diffractometer. Fig. 6-1(a) shows the measured pole figures (equal area projections). The texture indicates anisotropy between the rolling and transverse directions. Numerical representation of the measured pole figures using a finite number of crystal orientations was obtained using popLA, a texture analysis computer software package developed at the Los Alamos National Laboratories. Fig. 6-1(b) and (c) show numerical representations of the texture using 344 and 96 crystal orientations respectively.

6.4 Testing Procedure and Results

The punched and annealed specimens were tested in uniaxial tension in the low load testing machine. Specimens were gripped on the loading stages of the testing machine using flat clamps screwed together just beyond the free standing region of the specimens. Engineering drawings of the grips used are provided in Fig. C-12³. Fig. 6-2 is a photograph of a gripped specimen.

Three tests were conducted in each of rolling and transverse directions. The load-displacement graphs obtained from these tests are plotted in Fig. 6-3. The results are repeatable within experimental error. The experiments show a significant amount of

³With the design of new foil tension grips, it is not recommended to use these fixtures for such tests anymore.

plastic anisotropy. The ductility is also seen to be different; the transverse direction is less ductile than the rolling direction.

The load-displacement data was converted to stress-strain using the dimensions of the gage section. Fig. 6-4 shows the true stress-true strain graph obtained from one test each in the rolling and transverse directions. While this graph gives a good idea of the stress levels, the strain values need to be viewed with caution. This is because the specimen extensions measured in the experiments correspond to the cross-head displacement, which includes the extensions of both the gage section and the wider shoulders. The accuracy of strains obtained by converting cross-head displacement using the gage length depends on material behavior and specimen geometry. Rapidly widening shoulders, and non-hardening material behavior confine plasticity to the gage section, making such a conversion more accurate.

The elastic modulus obtained from the initial loading slope is close to half the modulus expected for polycrystalline copper. The tests were repeated with elastic unloading after being loaded into the regime in order to verify the elastic modulus; the slope measured was the same as that during the initial loading phase. The reason for the low measured elastic modulus is unknown.

Specimens in the rolling direction show an initial yield strength of about 35 MPa, and a failure strength of close to 190 MPa, with a ductility of around 20%. Specimens in the transverse direction demonstrate initial yield at a lower stress of 20 MPa, and failure after about 11% strain at a stress of around 80 MPa.

6.5 Simulations

The anisotropy in the stress-strain response of the pre-textured sample may be predicted through numerical simulations that take the measured initial texture into account. However, as described in the previous section, accurate estimation of stress-strain properties from the available experimental data of force-displacement is not possible. This problem may be circumvented by conducting numerical analysis of the complete specimen geometry, and comparing the theoretical (numerical) and experi-

mental *force-displacement* data rather than the stress-strain behavior.

The ABAQUS finite element mesh used to simulate the tensile behavior of the specimen is shown in Fig. 6-5. Due to symmetry, only one quarter of each specimen was simulated, using appropriate symmetry boundary conditions. The mesh consists of 55 elements in the plane and 1 element through the thickness. The elements used were 8 noded continuum brick elements (ABAQUS C3D8). Mesh convergence was verified by simulating denser meshes with upto 3 elements through the thickness. The current mesh was chosen to minimize computational costs while still yielding accurate results.

Symmetry boundary conditions were applied on nodes on the planes of symmetry. Gripping conditions were simulated by preventing all nodes on the right side face from moving in the thickness and width directions of the specimen. Tensile loading was simulated by applying displacement control, moving all the nodes on the right hand face towards the right. The net reaction force resulting from the tensile loading was calculated, and was used to estimate the force-displacement response of the specimen. The response of the full specimen is the same as that of the quarter specimen; this is a direct consequence of the assumed symmetry.

A rate-dependent polycrystal plasticity model [20] was used for the simulations. The inputs required for this model are the elastic constants, crystallographic texture and hardening parameters for the single crystal constitutive model. Standard values of elastic constants for copper, $\{C_{11} = 168 \text{ GPa}, C_{12} = 121 \text{ GPa}$ and $C_{44} = 75.4 \text{ GPa}\}$ [41] were used. A numerical representation of the measured crystallographic texture using 96 crystal orientations, shown in Fig. 6-1(c) was used for the calculations. The adequacy of 96 orientations was ascertained by comparing results with simulations conducted with more a accurate numerical texture representation, consisting of 347 orientations (Fig. 6-1(b)). The results were found to be very close. The measured texture was assumed to be representative of the entire film. Based on this assumption, each integration point was taken to consist of grains in all 96 orientations. The Taylor assumption, imposing the same uniform macroscopic deformation gradient on all the texture components at an integration point was invoked.

The hardening parameters required by the model are (i) s_0 , the initial slip-system yield strength; (ii) h_0 , the initial hardening rate coefficient; (iii) s_s , the saturation deformation resistance of the slip system; (iv) a , the hardening exponent. These parameters were tailored in order to fit the simulated force-displacement response to the experimental response in the rolling direction. Fig. 6-6 shows the fit obtained using $s_0 = 11$ MPa, $h_0 = 110$ MPa, $s_s = 120$ MPa and $a = 1.0$. Using the same parameters, the tensile force-displacement response of a specimen oriented at 90° with respect to the rolling texture representation was simulated. The results of this simulation are also shown in Fig. 6-6. The prediction is in good agreement with the experimental results.

The stress-strain behavior of the foil is best examined by extracting the stress-strain behavior of one of the elements in the gage section of the specimen. The stress-strain response from the element marked in Fig. 6-5 is shown in Fig. 6-7.

6.6 Conclusions

- $10\ \mu\text{m}$ thick rolled copper foils were annealed and tested in the low load testing machine. Consistent results were obtained, showing that samples taken along the rolling direction to have higher yield strength (35 MPa versus 20 MPa), ultimate strength (190 MPa versus 80 MPa) and ductility (20% versus 11%) as compared to those taken transverse to the rolling direction.
- Crystallographic texture of the foils was measured and found to be strongly directional. Numerical representations of the texture were generated for numerical calculations.
- Force-displacement response of the foils was simulated using a rate dependent Taylor-type polycrystal plasticity model. Hardening parameters were tailored to fit experimental data in the rolling direction. These parameters were then used to predict a specimen textured at 90° to the rolling direction. The prediction matches well with experimental results.

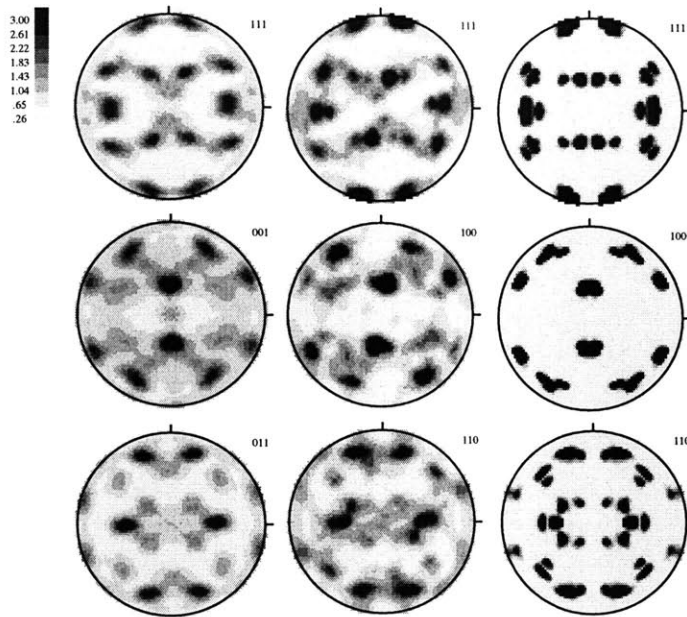


Figure 6-1: Crystallographic texture of rolled copper foil (popLA representation): (a) Measured; (b) Numerical representation with 347 weighted orientations; (c) Numerical representation with 96 weighted orientations (Pole figure measurement and representations courtesy Prakash Thamburaja)

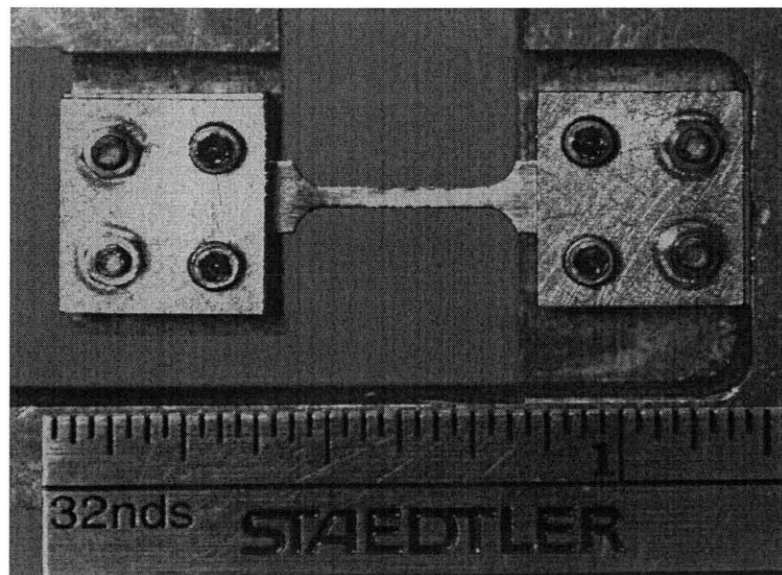


Figure 6-2: Photograph showing foil tensile specimen clamped in testing machine (Photograph by Cheng Su)

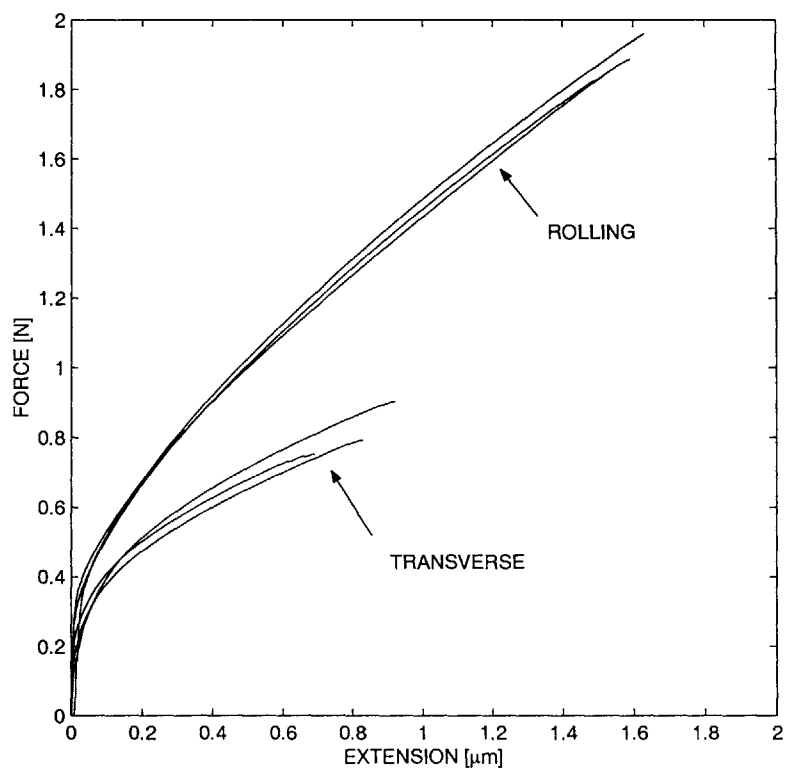


Figure 6-3: Force-displacement curves from several tensile tests on rolled copper foil in rolling and transverse directions

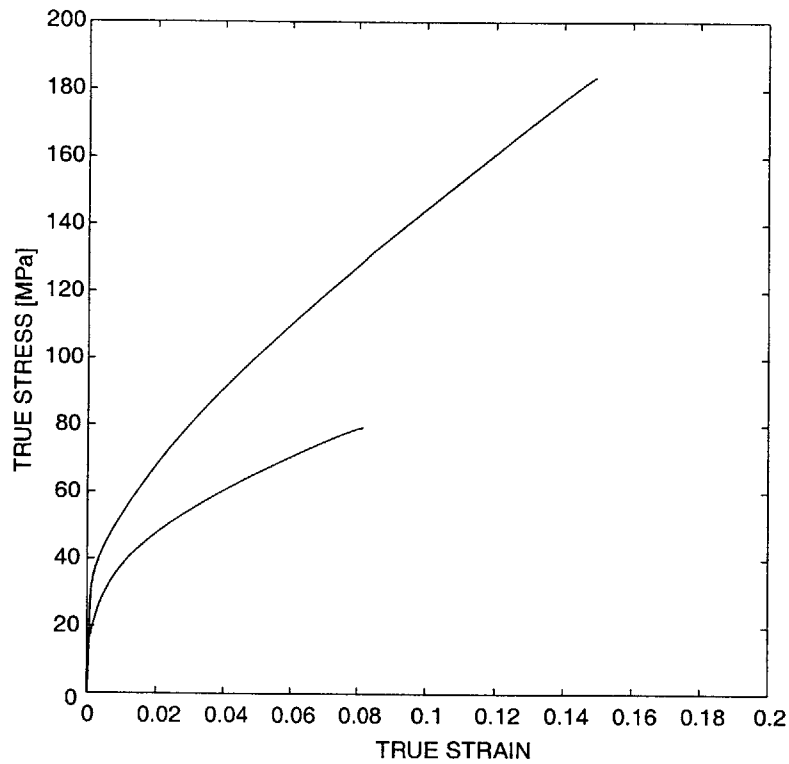


Figure 6-4: Stress-strain graphs from tensile tests on rolled copper foil in rolling and transverse directions

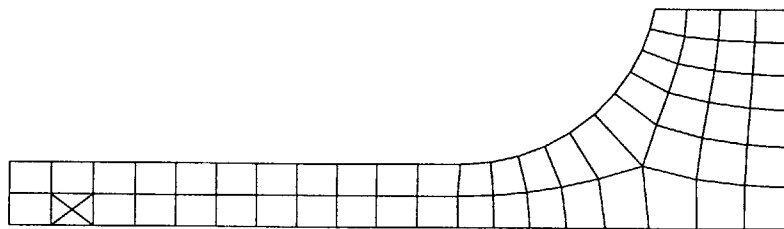


Figure 6-5: Finite element mesh used for simulate force-displacement response of copper foil specimens. Cross indicates element selected for extracting stress-strain response.

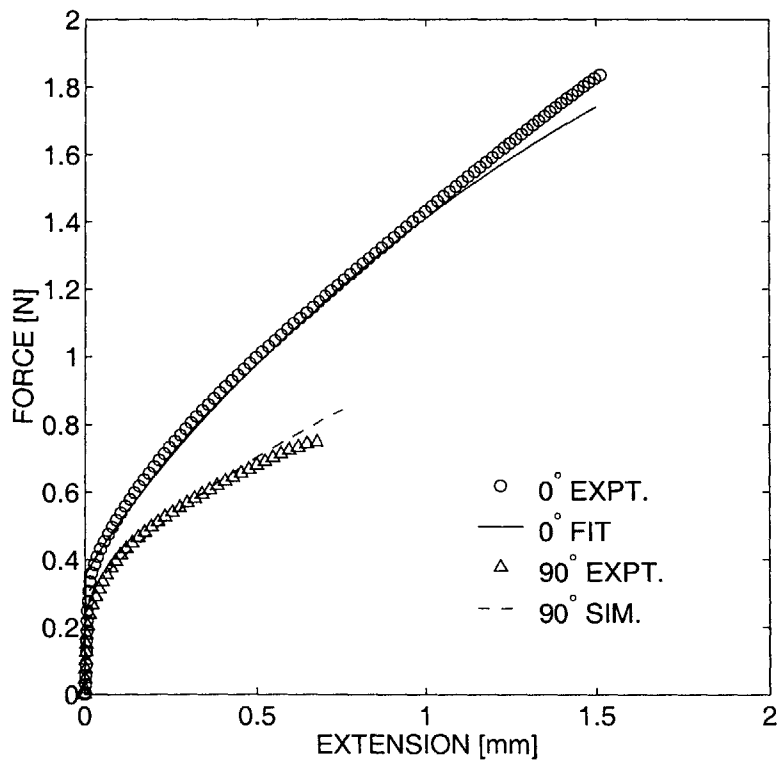


Figure 6-6: Comparison between experimental and simulated force-displacement responses. Graph shows numerical fit to experiment in rolling direction and prediction of experiment in transverse direction.

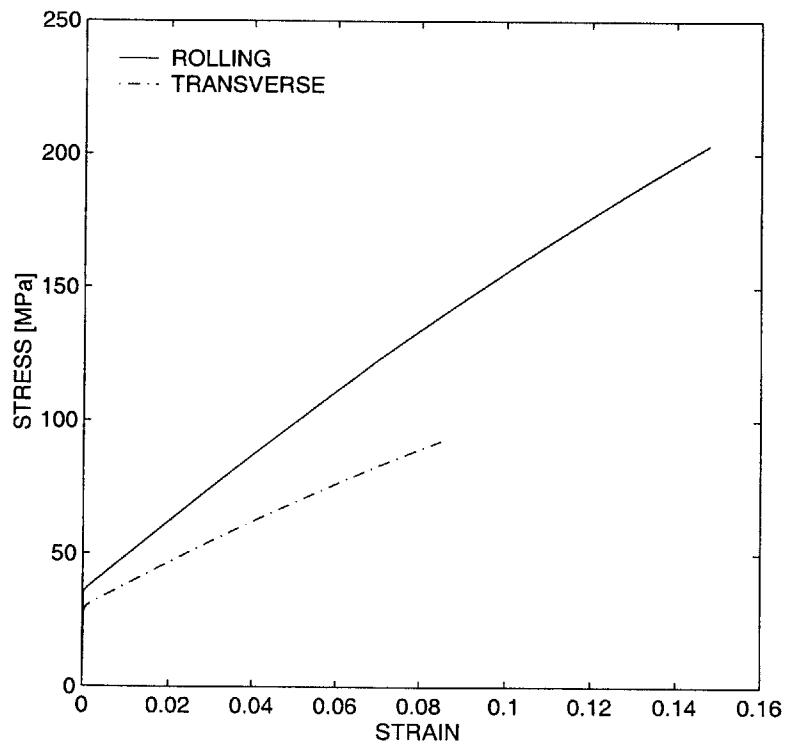


Figure 6-7: Stress-strain response of one of the rolled foil as obtained from one of the interior elements in the finite element simulation.

Chapter 7

Other Applications

7.1 Mechanical Behavior of Nanocrystalline Ni Alloys

One of the latest classes of materials being investigated for its extremely strength is nanocrystalline metals. These are specially fabricated polycrystalline forms of metals with grain sizes under 30 - 40 nm. Nanocrystalline samples of pure copper and nickel exhibit tensile strengths well over 1 GPa, an order of magnitude higher than bulk pure copper or nickel [29]. The most common methods for fabrication of nanocrystalline metals have been consolidation by high-pressure powder compaction and electrodeposition. The high pressures required in powder compaction restrict the total volume of consolidated metal to about 10 x 10 x 1 mm only. Electrodeposition, on the other hand, until recently, has been able to produce uniformly nanometer sized grains only in coatings several microns thick. However, recent advances in electrodeposition technologies have made it possible to fabricate free-standing nanocrystalline sheets of metals such as nickel, with thicknesses between 30 μm and 350 μm , several square inches in plane area. These advancements have sparked off investigations into mechanical properties of these materials for high-strength applications.

The small quantities of these materials available accentuate the utility of our micro-mechanical testing machines in obtaining their mechanical properties. The high

load machine has been used as part of these investigations to conduct micro-tensile and bend tests on nanocrystalline Ni and Ni-20%Fe. Samples tested in tension were Ni-20%Fe (14 μm and 40 μm thick) and pure Ni (30 μm and 45 μm thick). Dogbone shaped specimens were prepared by punching through an appropriately shaped die. The geometry of the specimens is shown in Fig. 4-9.

Fig. 7-1 is a stress-strain graph obtained from a tensile test on 14 μm thick nanocrystalline Ni-20%Fe foil. The foil exhibits very little plasticity and ductility; it fractured after a strain of 2%. Fig. 7-2 is a stress-strain graph obtained from a 40 μm thick sample of the same material, tested at the same strain rate. The maximum load capacity of the machine was insufficient to yield the sample. The elastic modulus was estimated to be 131.5 GPa using the L_{eff} measure for this geometry. Strains were also measured using the non-contact strain measurement technique described previously, and yielded the value for the Young's modulus. Also tested in tension was a sample of 45 μm thick pure nanocrystalline Ni. The stress-strain graph of this specimen is shown in Fig. 7-3. The elastic modulus is measured to be 200 GPa, which is closer to the bulk elastic modulus of Ni.

Indentation tests were also carried out on the nanocrystalline nickel foil. A coupon of the foil was glued onto a flat aluminum substrate, and polished with 3 μm diamond paste. The surface finish was measured using an optical profilometer and was estimated to have an R_a of less than 0.05 μm . Indentation experiments were carried out on a new micro-indenter, also developed as part of the micro-mechanical testing program [7, 11]. Fig. 7-4 shows three P-h curves. The hardness, defined as the ratio of the maximum force to the maximum contact area, is measured to have an average value of 2.7 GPa. Fig. 7-5 (a) shows an image of one of the indents using an interferometric profilometer. Fig. 7-5(b) shows an optical micrograph of one of the indents. These images confirm the alignment of the indenter and the symmetry of the indents. Little can be said about cracks, sink-in or pile up around the indent from these images.

7.2 Instrumented Indentation of Aluminum 6061

The fine force and displacement resolutions of the low-load apparatus allow for its use as an instrumented indenter. A Berkovich diamond tipped indenter was fixtured to the ACF specimen stage. A block of polished aluminum was fixtured to the LCF specimen stage. This set-up is shown in Fig. 3-7. The aluminum block was indented by the Berkovich indenter to a depth of about $7\ \mu\text{m}$. Fig. 7-6 shows the load, (P), versus the depth of penetration (h) graph. This data is in excellent agreement with that we have previously obtained from several commercially available nano-indenters.

7.3 Tensile Testing of an Elastomeric Fibers

The low force, high extension capabilities of the machine were exercised in tensile testing of fibers of a new elastomer being developed in the Fluid Mechanics Laboratory, MIT. These fibers, are produced by extruding a mixture consisting of KratonTM, a commercial block co-polymer, and a resin plasticizer through a syringe, onto a rotating drum. Handling, positioning and testing of these fibers is extremely challenging. The fibers were spun onto a rotating card-paper frame, just as in the case of the silicon-framed free-standing thin films also tested in this program. The supports enabled handling and fixturing. Once the frame was fixtured onto the machine stages, the side arms were cut off. Tensile testing then proceeded.

Diameters of fibers tested in this program varied from $5\ \mu\text{m}$ to $100\ \mu\text{m}$. The forces generated while pulling $5 - 10\ \mu\text{m}$ diameter fibers were too small to be measured. Groups of around 10 fibers were tested simultaneously. Fig. 7-7 shows the force-displacement graph obtained from one such tensile test¹. In this test, a group of 11 fibers (7 of dia. $5\ \mu\text{m}$ and 4 of dia. $7.5\ \mu\text{m}$), with an initial length of 3 mm was pulled in tension at $6.9\ \mu\text{m/s}$. The nominal stress-stretch plot is shown in Fig. 7-8.

Similar tests were conducted on thicker fibers. A 2.67 mm gage length of a similar fiber of diameter $100\ \mu\text{m}^2$ was tested at a crosshead velocity of $6\ \mu\text{m/s}$ to a total

¹fibers provided by Nikola Kojic

²Sample provided by Octavia Brauner

stretch of about 3.2. Fig. 7-9 shows the load-displacement response of this fiber. Note the very low forces (< 70 mN) but large extensions (≈ 6 mm).

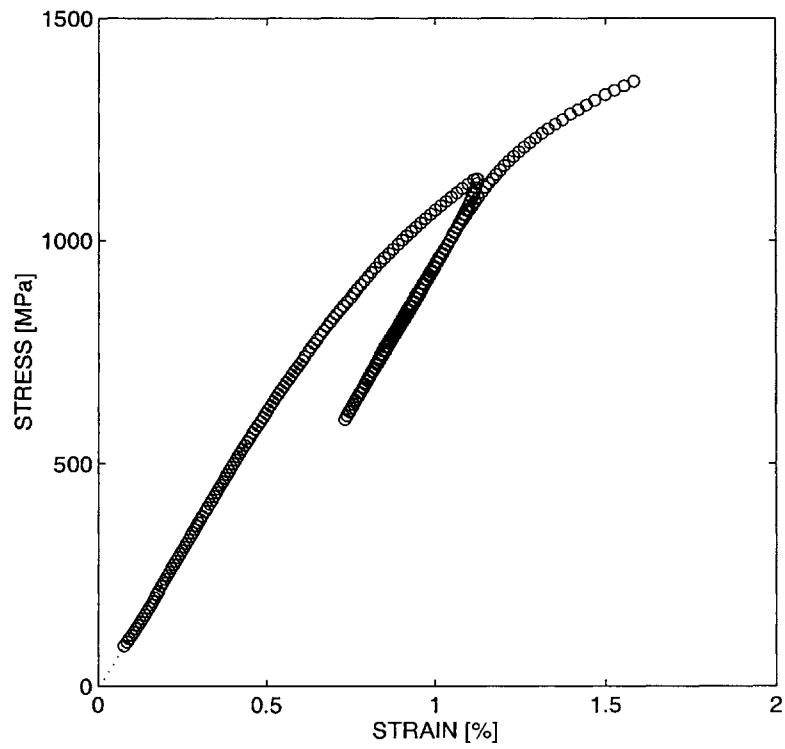


Figure 7-1: Stress-strain graphs from tension test on 14 μm thick nanocrystalline Ni-20%Fe foil. Initial regions are shown in graph correspond to the specimen not being fully taut before testing.

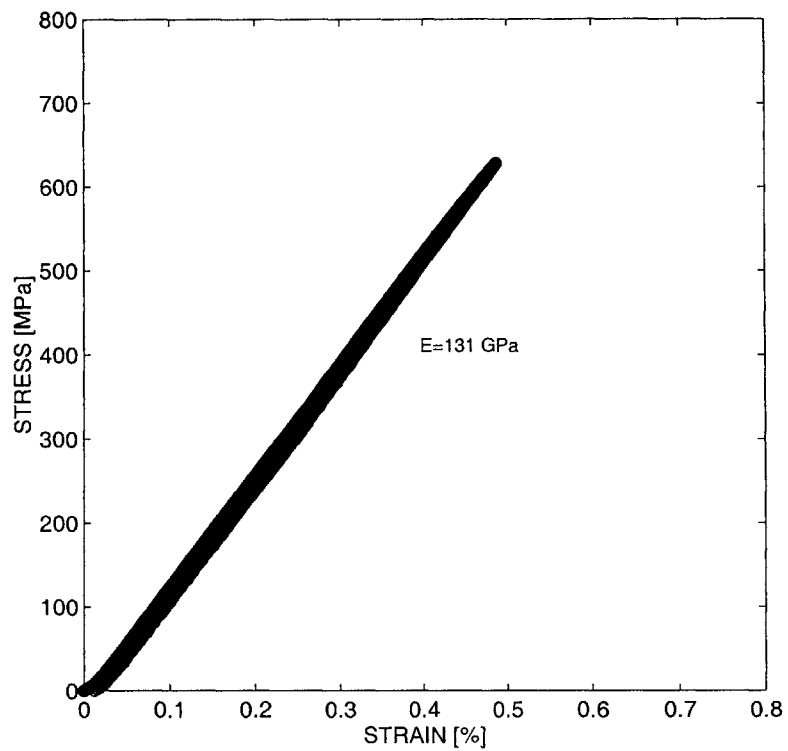


Figure 7-2: Stress-strain graphs from tension test on 40 μm thick nanocrystalline Ni-20%Fe foil. The capacity of the machine was insufficient to yield the foil.

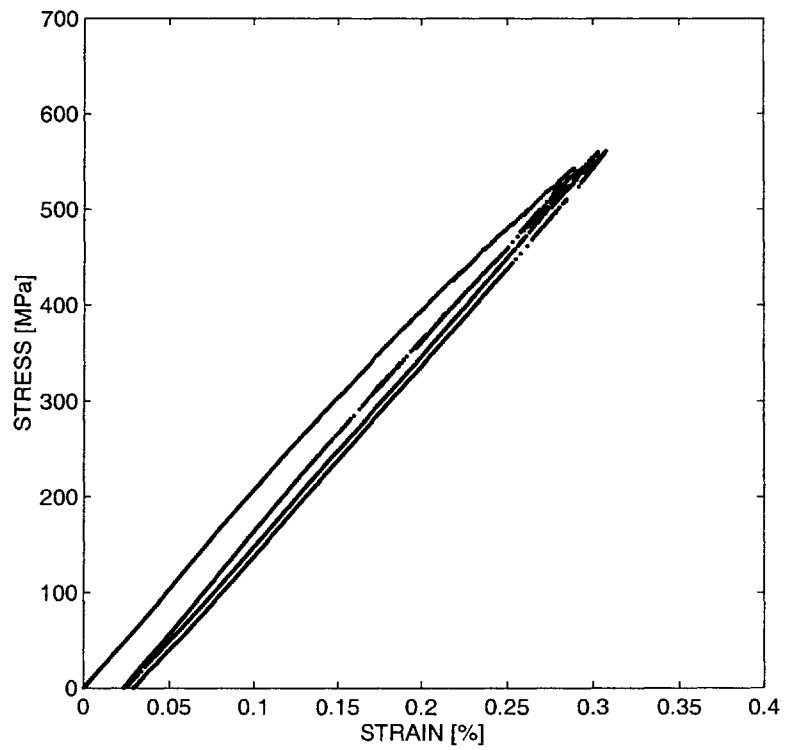


Figure 7-3: Stress-strain graphs from tension test on 45 μm thick nanocrystalline Ni foil. The capacity of the machine was insufficient to yield the foil. The small residual strain after the first unloading is more likely to be due to settling in the grips rather than “plastic” yielding.

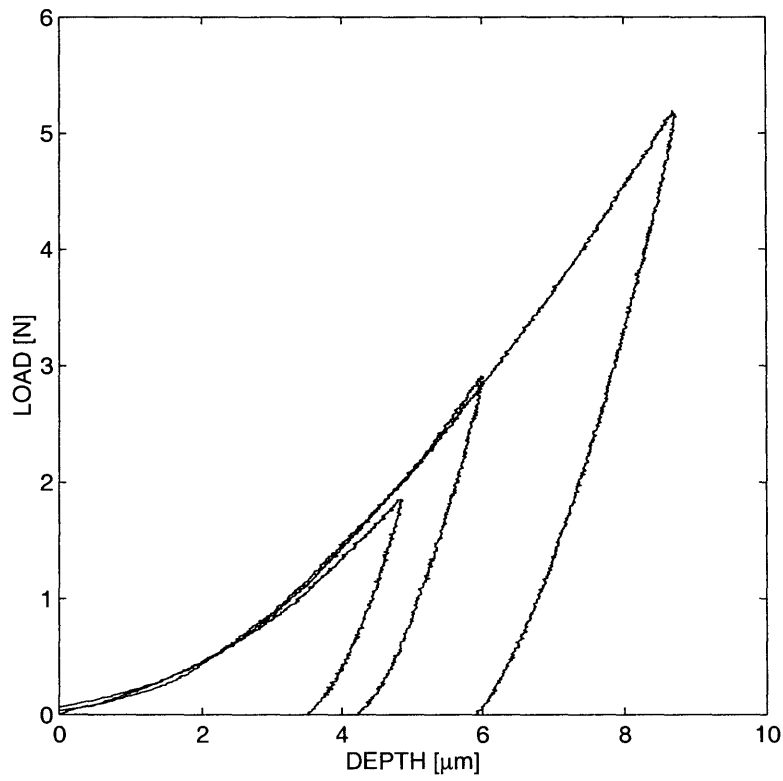
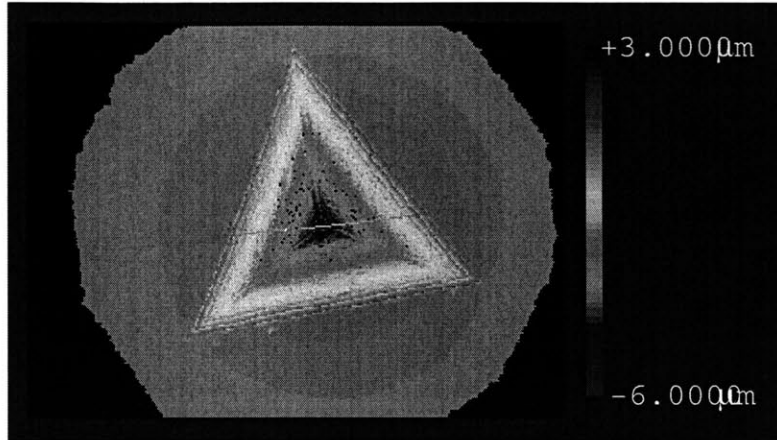
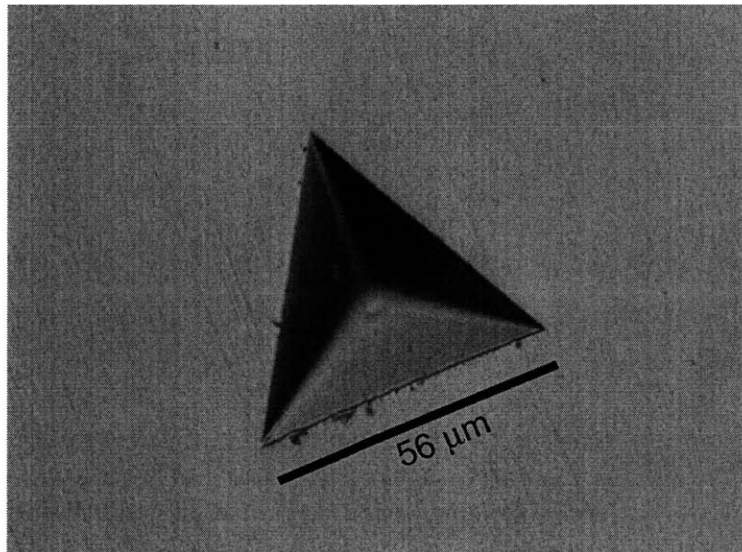


Figure 7-4: P-h curves from indentation on polished nano-Ni foil glued to an aluminum substrate.



(a)



(b)

Figure 7-5: Images of micro-indent in nano-Ni foil: (a) Height contours from interferometric profilometry; (b) Optical micrograph of indent.

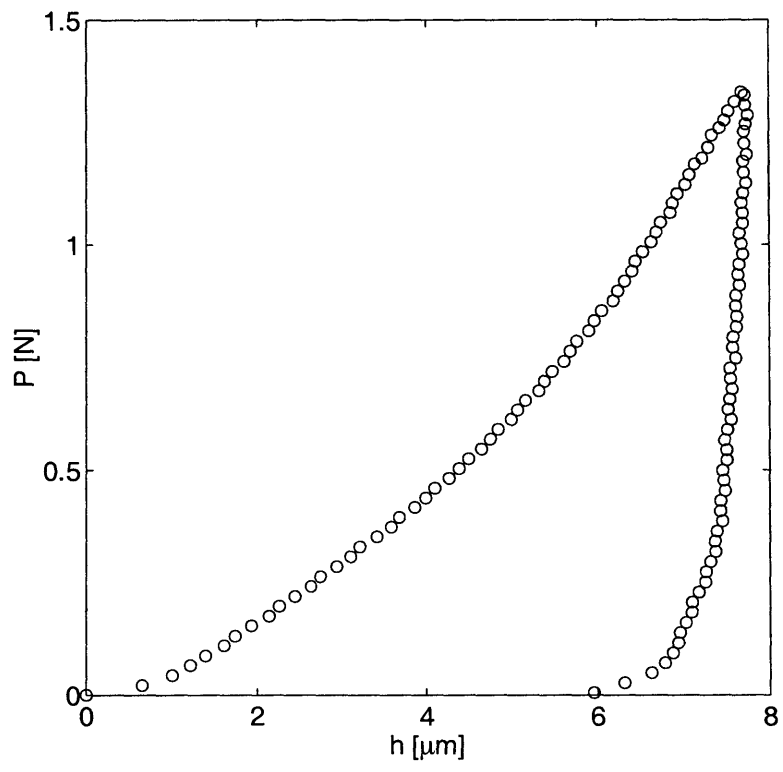


Figure 7-6: Force - depth of penetration response of Al 6061 indentation.

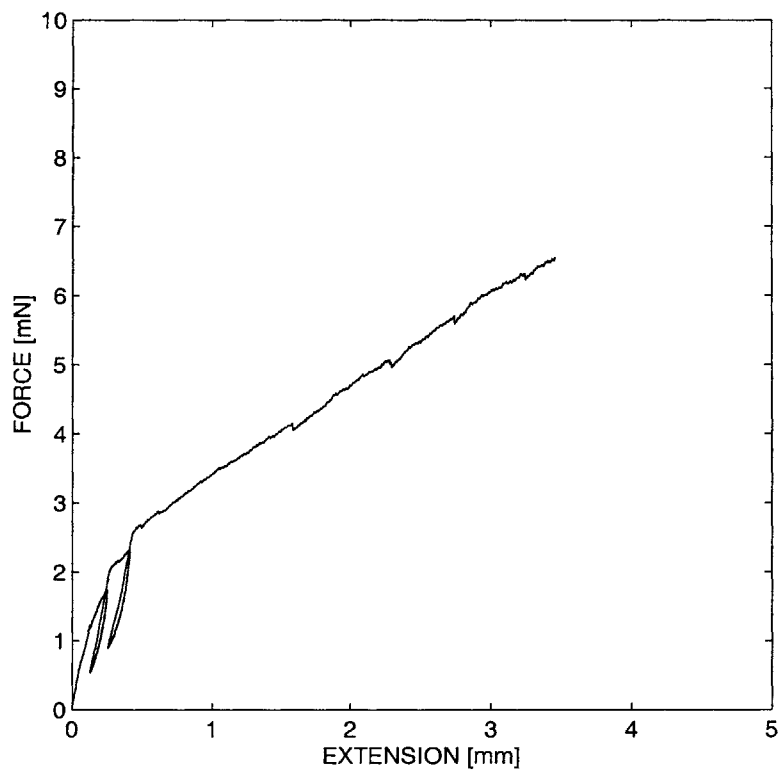


Figure 7-7: Force-displacement graph from tensile test on a group of 11 thermoset elastomer fibers. (Fibers provided by Nikola Kojic.) (7 of dia. $5 \mu\text{m}$ and 4 of dia. $7.5 \mu\text{m}$). Initial fiber length: 3 mm; Extension rate: $6.9 \mu\text{m/s}$.

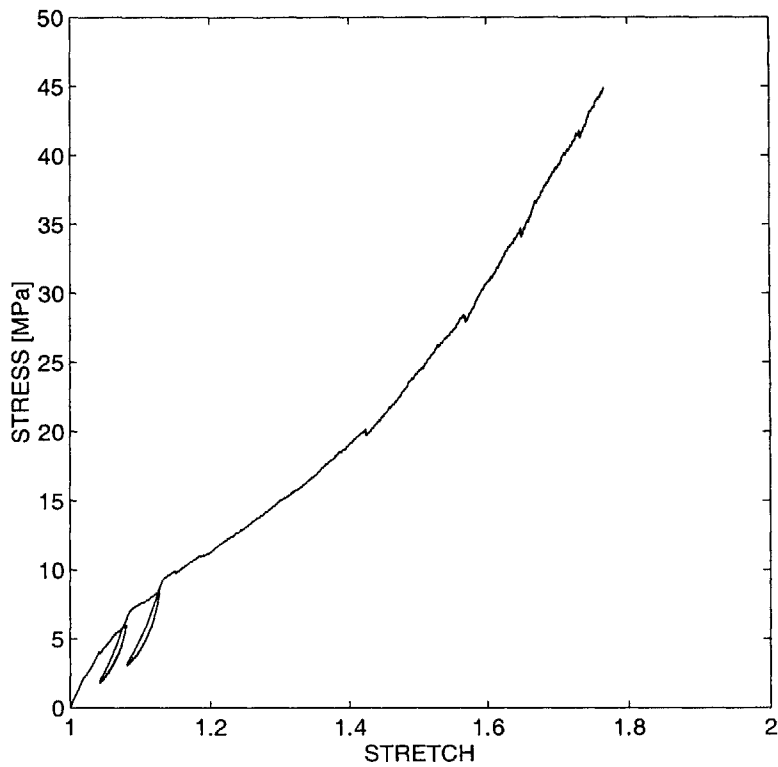


Figure 7-8: Nominal stress-stretch graph from tensile test on a group of 11 thermoset elastomer fibers (Fibers provided by Nikola Kojic.) (7 of dia. $5 \mu\text{m}$ and 4 of dia. $7.5 \mu\text{m}$).

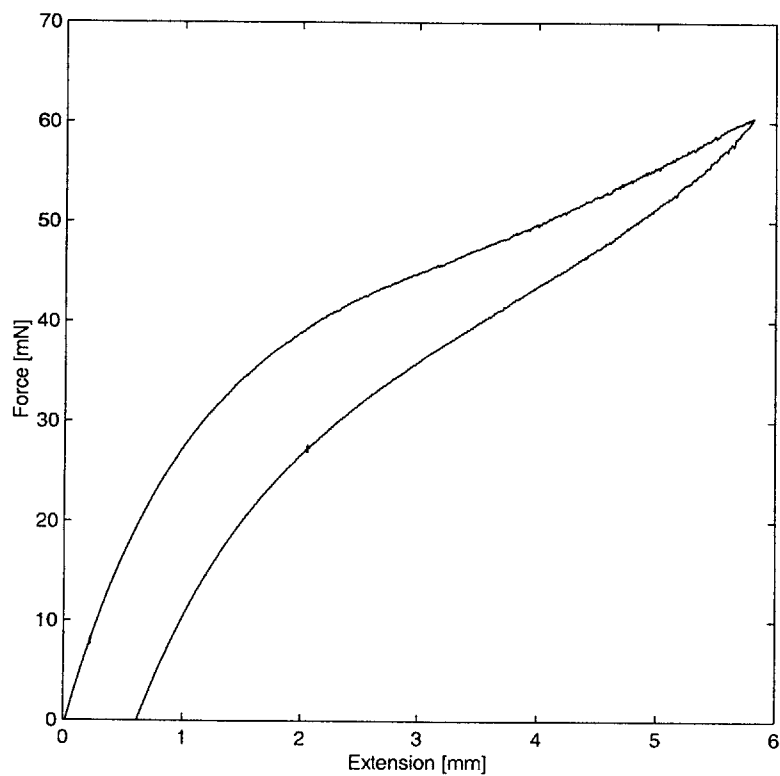


Figure 7-9: Force-displacement graph from tensile test on 100 μ m diameter thermoset elastomer fibers. (Sample provided by Octavia Brauner.)

Chapter 8

Closure

- A simple, scaleable, high resolution micro-mechanical testing machine has been invented. The machine is based on the use of compound flexures (in an integrated frame) as precision guides for actuation and as linear springs for force measurement.
- Detailed methodologies for design, fabrication, calibration and verification for two prototypes are developed. The procedures developed herein serve as a template for the development of other variants.
- A wide variety of fixtures and techniques to adapt these machines for various testing purposes are developed.
- Free-standing thin films of gold (thickness 450 - 700 nm) are fabricated and tested in tension and membrane bending modes. The experiments show that the gold thin-films have a Young's modulus of ≈ 83 GPa, an initial yield strength of ≈ 100 MPa, which is followed by rapid strain hardening to a stress level of ≈ 360 MPa at a strain of only $\approx 1.2\%$.
- A crystal plasticity model is successfully fit to the tensile behavior of the films. The stress-strain response thus fit is used to predict the response of the films during bending experiments. Experimental data is found to be in excellent agreement with the predictions

- Microstructural investigations are conducted on the free-standing gold thin films. Initial microstructure indicates a bimodal grain size distribution (130 nm and 380 nm). TEM investigations of the deformed films show that the rapid strain hardening is attributable to extensive dislocation activity in the larger grains. However, there is a distinct lack of of dislocation activity in grains smaller than ≈ 100 nm. The reason behind the low ductility in our gold specimens is still unclear. However, we speculate that since the smaller grains do not easily deform plastically, it may be easier to activate grain boundary sliding and decohesion processes to generate micro-cracks at their triple-point junctions, which is what leads to premature failure and low ductility.
- Dogbone shaped tensile specimens of $10\ \mu\text{m}$ thick rolled copper foil are annealed and tested along and transverse to the direction of rolling. The crystallographic texture of the foil is measured. A crystal plasticity model is fit to match the response of the specimens in the rolling direction and used to predict the response in the transverse direction. The agreement between experiment and prediction is excellent.
- Several other materials are tested in novel ways using these testing machines. These include $5 - 50\ \mu\text{m}$ diameter elastomer fibers, silicon wafers and nanocrystalline metals and alloys.
- **Future directions:** The following aspects of the testing machines require further development:
 1. Non-contact strain measurement.
 2. Feedback control for force and/or displacement.
 3. Enclosure(s) for physical protection and environmental control.
 4. Elevated temperature testing.
 5. Cyclic actuation.

Bibliography

- [1] American Society of Metals International. *Metals Handbook*, 1998.
- [2] E. Arzt. Size effects in materials due to microstructural and dimensional constraints: A comparative review. *Acta Mater.*, 46:5611–5626, 1998.
- [3] ASTM. *Standard Test Methods of Tension Testing of Metallic Foil : E 345 - 93 (Reapproved 1998)*, 1998.
- [4] C. A. Bronkhorst, S. R. Kalidindi, , and Anand L. Polycrystalline plasticity and the evolution of crystallographic texture in face-centered cubic metals. *Philosophical Transactions of the Royal Society of London, A* 341:443–477, 1992.
- [5] R. Emery, C. Simmons, B. Mazin, and G. L. Povirk. High temperature tensile behavior of free-standing gold films. *MRS Symposium Proceedings*, 505, 1998.
- [6] L. B. Freund. The stability of a dislocation threading a strained layer on a substrate. *Journal of Applied Mechanics*, 54:553, 1987.
- [7] B. P. Gearing and L. Anand. A novel testing machine for tribological properties at the mems scale. *Proc. ASME IMECE*, 2001.
- [8] A. E. Giannakopoulos and S. Suresh. Determination of elastoplastic properties by instrumented sharp indentation. *Scripta Materialia*, 40:1191–1198, 1999.
- [9] Staffan Greek and Stefan Johansson. Tensile testing of thin film microstructures. *SPIE*, 3224:344–351, 1997.

- [10] S. Gudlavalleti and L. Anand. A novel testing machine for characterization of materials for mems applications. *Proc. ASME IMECE*, 2001.
- [11] S. Gudlavalleti, B. P. Gearing, and L. Anand. Design and construction of micromechanical testing machines for measuring the bulk and surface properties of materials at the meso-scale. *To be submitted*, 2001.
- [12] S. A. Hackney, M. Ke, W. W. Milligan, and E. C. Aifantis. Grain size and strain rate effects on the mechanisms of deformation and fracture in nanostructured metals. *Processing and Properties of Nanocrystalline Materials; Published by Minerals, Metals & Materials Soc (TMS)*, 1998.
- [13] R. W. Hoffman. Nanomechanics of thin films: Emphasis: Tensile properties. *MRS Symposium Proceedings*, 130:295–306, 1989.
- [14] M. Hommel and O. Kraft. Deformation behavior of thin copper films on deformable substrates. *Acta Mater.*, 49:3935–3947, 2001.
- [15] H. Huang and F. Spaepen. Tensile testing of free-standing cu, ag and al thin films and ag/cu multilayers. *Acta Mater.*, 48:3261–3269, 2000.
- [16] Haibo Huang. *Mechanical properties of free-standing polycrystalline metallic thin films and multilayers*. PhD thesis, Harvard University, 1998.
- [17] R. V. Jones. Parallel and rectilinear spring movements. *Journal of Scientific Instrumentation*, 28:38–41, 1951.
- [18] R. V. Jones. Some parasitic deflections in parallel spring movements. *Journal of Scientific Instrumentation*, 33:11–15, 1956.
- [19] S. R. Kalidindi and L. Anand. An approximate procedure for predicting the evolution of crystallographic texture in bulk deformation processing of fcc metals. *International Journal of Mechanical Sciences*, 34:309–329, 1992.

- [20] S. R. Kalidindi, C. A. Bronkhorst, , and Anand L. Crystallographic texture evolution in bulk deformation processing of fcc metals. *Journal of the Mechanics and Physics of Solids*, 40:537–569, 1992.
- [21] S. R. Kalidindi and Anand L. Macroscopic shape change and evolution of crystallographic texture in pre-textured fcc metals. *Journal of the Mechanics and Physics of Solids*, 42:459–490, 1994.
- [22] Kaman Instrumentation Corporation, 1500 Garden of the Gods Road, Colorado Springs, CO 80907. *SMU 9000 User Manual*.
- [23] Young-Seok Kang and P. S. Ho. Thickness dependent mechanical behavior of submicron aluminum thin films. *Journal of Electronic Materials*, 26:805–813, 1997.
- [24] R-M. Keller, S. P. Baker, and E. Arzt. Quantitative analysis of strengthening mechanisms in thin cu films: Effects of film thickness, grain size and passivation. *Journal of Materials Research*, 13:1307–1317, 1998.
- [25] R. R. Keller, J. M. Phelps, and D. T. Read. Tensile and fracture behavior of free-standing copper films. *Materials Science and Engineering*, A214:42–52, 1996.
- [26] M. Kobrinsky and C. V. Thompson. Activation volume for inelastic deformation in polycrystalline ag thin films. *Acta Mater.*, 48:625–633, 2000.
- [27] J. Koskinen, J. E. Steinwall, R. Soave, and H. H. Johnson. Microtensile testing of free-standing polysilicon fibers of various grain sizes. *Journal of Micromechanical Microengineering*, 3:13–17, 1993.
- [28] D. A. LaVan and W. N. Sharpe. Tensile testing of microsamples. *Experimental Mechanics*, 39:210–216, 1999.
- [29] M. Legros, B. R. Elliott, M. N. Rittner, and J. R. and Hemker K. J. Weertman. Microsample tensile testing of nanocrystalline metals. *Philosophical Magazine A*, 80:1017–1026, 2000.

- [30] M. A. Meyers and K. K. Chawla. *Mechanical Metallurgy*. Prentice-Hall, 1984.
- [31] W. W. Milligan, S. A. Hackney, M. Ke, and E. C. Aifantis. In situ studies of deformation and fracture in nanophase materials. *Nanostructured materials*, 2:267–276, 1993.
- [32] W. D. Nix. Mechanical properties of thin films. *Metallurgical Transactions A*, 20A:2217–2245, 1989.
- [33] W. D. Nix. Elastic and plastic properties of thin films on substrates: nanoindentation techniques. *Materials Science and Engineering*, A234-236:37–44, 1997.
- [34] W. D. Nix. Yielding and strain hardening of thin metal films on substrates. *Scripta Materialia*, 39:545–554, 1998.
- [35] K. Owusu-Boahen and A. H. King. The early stages of plastic yielding in polycrystalline gold films. *Acta Mater*, 49:237–247, 2001.
- [36] D. T. Read. Tension-tension fatigue of copper thin films. *International Journal of Fatigue*, 3:203–209, 1998.
- [37] D. T. Read, YiWen Cheng, RM. Keller, and J. D. McColskey. Tensile properties of freestanding aluminum thin films. *Scripta Materialia*, 45:583–589, 2001.
- [38] D. T. Read and J. W. Dally. Strength, ductility and fatigue life of aluminum thin films. *The International Journal of Microcircuits and Electronic Packaging*, 16:313–318, 1993.
- [39] J. Ruud, D. Josell, A. L. Greer, and F. Spaepen. The elastic moduli of silver thin films measured with a new microtensile tester. *MRS Symposium Proceedings*, 239:239–243, 1992.
- [40] W. N. Sharpe, Bin Yuan, and R. L. Edwards. A new technique for measuring the mechanical properties of thin films. *Journal of Microelectromechanical Systems*, 6:193–198, 1997.

- [41] G. Simmons and H. Wang. *Single Crystal Elastic Constants and Calculated Aggregate Properties*. MIT Press, 1971.
- [42] S.T. Smith and D.G. Chetwynd. *Foundations of Ultraprecision Mechanism Design*. Gordon and Breach Science, 1992.
- [43] S. M. Spearing. Materials issues in microelectromechanical systems (mems). *Acta Mater.*, 48:179–196, 2000.
- [44] C. V. Thompson. The yield stress of polycrystalline thin films. *Journal of Materials Research*, 8:237, 1993.
- [45] J. J. Vlassak and W. D. Nix. A new bulge test technique for the determination of young's modulus and poisson's ratio of thin films. *Journal of Materials Research*, 7:3242–3249, 1992.
- [46] Y. Wang, R. L. Edwards, and K. J. Hemker. Mechanical properties of al thin films as measured by bulge testing. *MRS Symposium Proceedings*, 135:135–140, 1998.
- [47] V. Weihnacht and W. Bruckner. Dislocation accumulation and strengthening in cu thin films. *Acta Mater.*, 49:2365–2372, 2001.
- [48] T. P. Weihs, S. Hong, J. C. Bravman, and W. D. Nix. Mechanical deflection of cantilever microbeams: A new technique for testing the mechanical properties of thin films. *Journal of Materials Research*, 3:931–942, 1988.

Appendix A

Equations for Flexure Mechanisms

The compound flexure system shown in Fig. 2-3(c) is a series arrangement of two simple flexures (Fig. 2-3(b)). The following is a derivation of the stiffness of a simple flexure mechanism based on beam theory.

Fig. A-1 is a free body diagram of a section of a simple flexure. The distance d between the two leaf springs is assumed to be large enough so that the moments (M) and shear forces in both leaf springs are identical. From force balance in the y direction, it is clear that the shear force in each leaf spring is $P/2$, as shown. Summing the moments about point A :

$$Td + 2M = Px \tag{A.1}$$

$$\Rightarrow M - \frac{Px - Td}{2} = 0 \tag{A.2}$$

To calculate the deflections, we use the standard equation of beam theory

$$\frac{d^2v}{dx^2} = \frac{M(x)}{EI} \tag{A.3}$$

where $v(x)$ is the deflection of the natural axis of the beam in the y direction at a distance x from the free end. The area moment of inertia I is given by

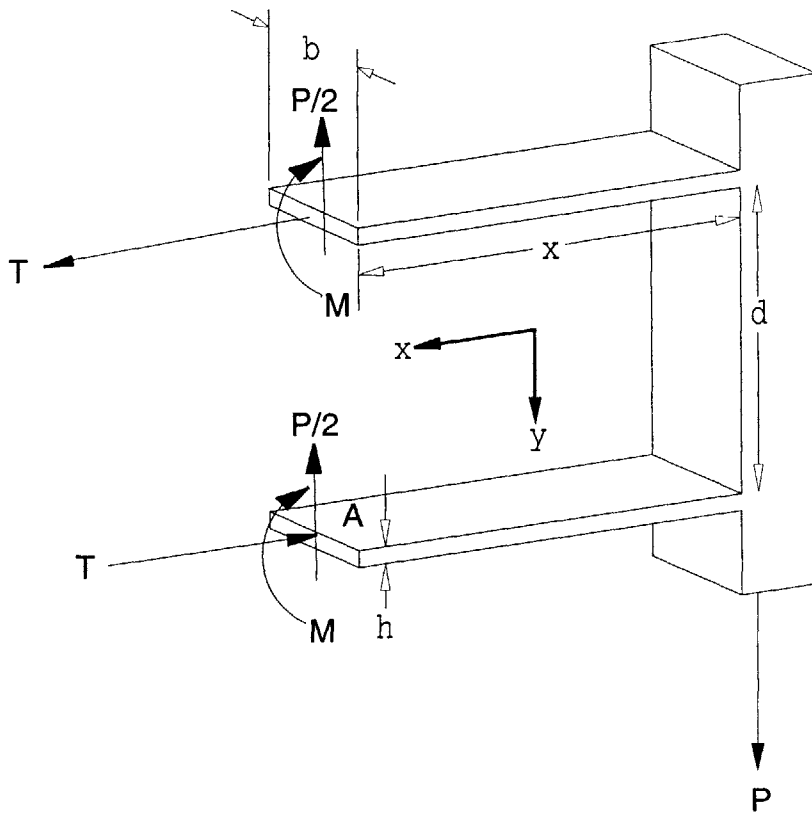


Figure A-1: Free body diagram of simple flexure

$$I = \frac{1}{12}bh^3 \quad (\text{A.4})$$

The boundary conditions on v are that there are no rotations at $x = 0$ and $x = L$ and that there is no deflection at $x = L$:

$$\begin{aligned} v'(0) &= v'(L) = 0 \\ v(L) &= 0 \end{aligned} \quad (\text{A.5})$$

Integrating Eq. A.3 over the length of the beams and applying these boundary conditions gives

$$\left[\frac{dv}{dx} \right]_0^x = \frac{1}{EI} \int_0^x \frac{Px - Td}{2} dx$$

$$v(L) - v(0) = \frac{1}{2EI} \left(\frac{PL^2}{2} - \frac{Td}{2} \right) = 0$$

$$\Rightarrow T = \frac{PL}{2d} \quad (\text{A.6})$$

Using this expression obtained for T and integrating once more gives

$$v(x) - v(0) = \frac{1}{EI} \left(\frac{Px^3}{12} - \frac{PLx^2}{8} \right) \quad (\text{A.7})$$

We may evaluate Eq. A.7 for the maximum deflection, δ ($=|v(0)|$) using second boundary condition from Eq. A.5:

$$0 - v(0) = \frac{1}{EI} \left(\frac{PL^3}{12} - \frac{PL^3}{8} \right)$$

$$\Rightarrow v(0) = \frac{PL^3}{24EI} \quad (\text{A.8})$$

The stiffness k of the simple flexure mechanism is hence obtained to be

$$k = \frac{P}{v(0)} = \frac{24EI}{L^3} \quad (\text{A.9})$$

The stress in the leaf spring is a combination of contributions from the bending moment and the tensile force. Hence

$$\sigma(x) = \frac{M(x)y}{I} + \frac{T}{bh} \quad (\text{A.10})$$

where y is the distance from the neutral axis in the y direction. At a given x , the stress is maximum at $y = h/2$. From Eq. A.2, it can be seen that M is maximum at $x = L$. Rewriting Eq. A.10 at $x = L$ in terms of P and the dimensions alone, we obtain the maximum stress σ_{max} at any point in the flexure system to be

$$\sigma_{max} = \frac{3 PL}{2 bh^2} \left(1 - \frac{h}{6d}\right) \quad (\text{A.11})$$

For leaf springs, it is very often the case that $h \ll d$. Neglecting the $h/6d$ term, the maximum stress in the flexure system can be approximated to

$$\sigma_{max} \approx \frac{3 PL}{2 bh^2} \quad (\text{A.12})$$

It is desirable to keep this stress level well below the fatigue strength σ_f of the material. It is useful to rewrite this maximum stress in terms of the deflection of the spring at the point of interest, $x = 0$ in this case, so that the maximum deflection permissible by material strength may be determined. For this, we may rewrite P in terms of δ by inverting Eq. A.8. Expanding,

$$\sigma_{max} = \frac{3Eh}{L^2} \delta \quad (\text{A.13})$$

However, Eq. A.12 does not take into account the effects of stress concentrations at the roots of the flexure. Hence, while calculating the maximum permissible deflection δ_{max} of the flexure, we include a factor of safety S .

$$\delta_{max} = \frac{\sigma_f L^2}{3SEh^2} \quad (\text{A.14})$$

The stiffness of a compound flexure is half that of the simple flexure, and is given by

$$k = \frac{P}{v(0)} = \frac{12EI}{L^3} \quad (\text{A.15})$$

Also, the maximum allowable travel of a compound flexure is twice that of a simple flexure because each simple flexure involved is permitted to deflect according to Eq. A.14

$$\delta_{max} = \frac{2\sigma_f L^2}{3SEh^2} \quad (\text{A.16})$$

A note on parasitic deflections

An ideal simple flexure mechanism, as shown in Fig. A-1 is expected to have a parasitic motion, but no parasitic twisting, *i.e.*, $\theta = (v'(0)) = 0$. However, manufacturing tolerances always degrade performance from the geometric ideal. There are two sources of potentially significant errors: (i) a twist due to the difference ϵ_b , in the separation between the flexures at $x = 0$ and $x = L$, and (ii) a twist due to the difference ϵ_l in the lengths of the two flexures. For a platform displacement δ , the total contribution of these twists is expected to be

$$\theta \approx \frac{\delta^2 \epsilon_b}{2dL^2} + \frac{\delta \epsilon_l}{dL} \quad (\text{A.17})$$

Appendix B

Low Load Testing Machine: Operation Manual

B.1 General Operating Procedure

1. Orient the machine with testing axis vertical or horizontal according to the test to be performed (Fig. 3-4).
2. Install the inchworm (if not already installed). Clamp it to the machine using #2-56 screws and the nutplate (Part GS0200-07). See Fig. B-1.

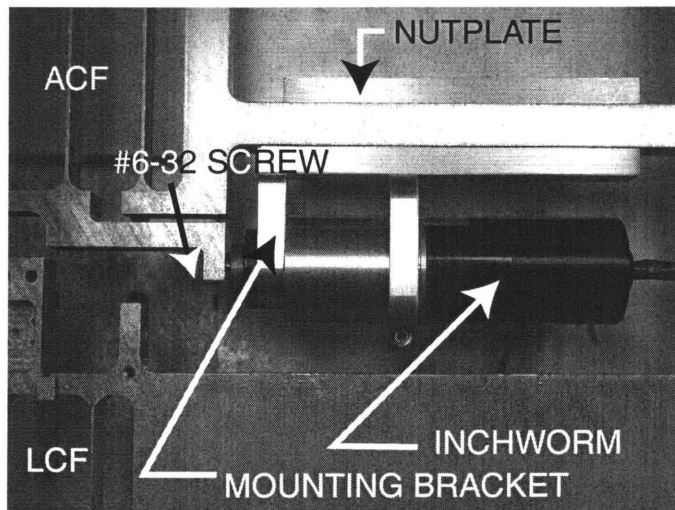


Figure B-1: Photograph showing inchworm installed in testing machine

3. Install load cell and displacement sensors, as shown in Fig. B-2. Use a 5/16" wrench to tighten the nuts.
4. Install grips/fixtures. Fig. B-2 shows the foil tension grips installed in the machine. Other grips and fixtures may be installed as seen in Figs. 3-6 and 3-7.

Caution: Avoid applying out-of-plane loads on the flexures while tightening.

Caution: Don't tighten screws too much.

Useful tip: Wherever possible, use mating faces between fixture and stage to align fixtures to machine. Do not tighten fixtures completely; Move flexures together to mate the two fixtures with respect to each other, and then tighten.

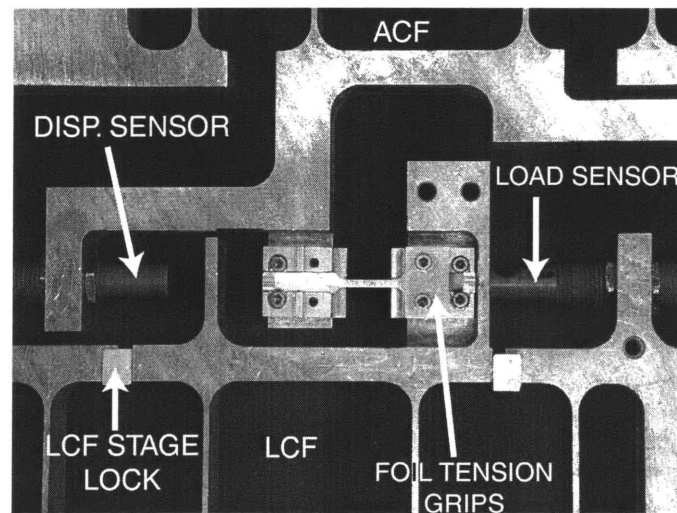


Figure B-2: Close-up photo of specimen stage area in low load testing machine showing displacement and force position sensors and foil tension grips during installation.

5. Position the inchworm for the test. This involves two parts: extending or retracting the actuator shaft according to if the test involves retracting (bending, indentation testing) or extending the actuator shaft (tension testing) respectively, and positioning the inchworm with respect to the testing frame to set the initial relative position of the specimen stages. The first part is done using the inchworm control virtual instrument (steps 13 - 16), whereas the second part is done by loosening the inchworm mounting screws and moving the inchworm, followed by re-tightening the screws.

Caution: Ensure that the inchworm travel axis is aligned with flexure travel axis.

6. Position the sensors such that the displacement range anticipated during the test is centered around the mid-range of the sensors (output voltage of 0 V), where sensor linearity is maximum. The direction of displacement also determines if the sensors are initially closer to or further from their targets.

Useful tip: Use “lookatonesensor.vi” to monitor the output of the sensors during adjustment.

Useful tip: “kamansensor.vi” is a simple vi to convert a voltage signal into a displacement reading in μm , using the 5th order polynomial function for any of the existing sensors of choice. Please keep this vi updated by adding/modifying the polynomial functions for new/existing sensors. This vi may be linked into any other vi that uses the sensors.

Caution: Anchor the sensor cables to a stable support, or using a weight. The sensors are very sensitive, any external disturbances to the cables could affect measurements. This is especially critical for the displacement sensor, which moves with the displacement stage and might drag against surrounding objects.

7. Install the specimen. This step and step 4 are interdependent. If necessary, lock stages using stage-lock plugs.

Useful tip: The two locks are different, one is smoothly machined and the other is hand-finished, and is rough. First insert the smooth lock on the left side, and then the rough lock on the right side. Don't force the right side lock to go in completely.

8. Open microtensile.vi¹. Fig.B-3 is a screenshot of the LabVIEW virtual instrument.

¹d:\ User Files\ Project\

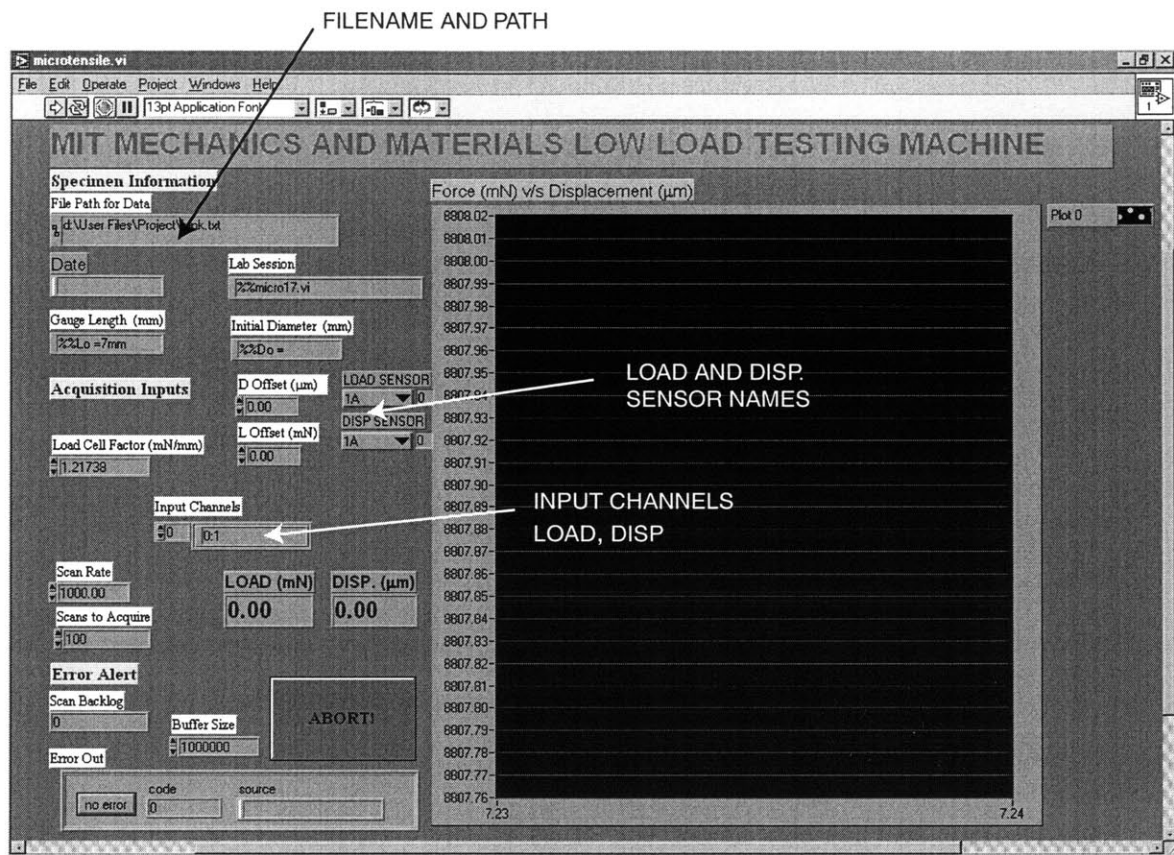


Figure B-3: Screen-shot of LabVIEW virtual instrument for acquiring data from the low load testing machine.

9. Enter the full path of the filename to store data in. Data will be stored in 3 columns, (displacement in μm , force in mN, time in s).
10. Enter other test information in the dialog boxes provided. Date will be automatically filled in.
11. Enter data acquisition information. Under input channels, there are 2 dialogue boxes. The left box reads '0', which should be left as is. In the right box, enter the channels into which the load cell and displacement sensor outputs are plugged in, in that order, separated by a comma (',').
12. Select the names of the load and displacement sensors (1A, 1B *etc.*)
13. Open the inchworm virtual instrument, 671_3ollv.vi². As can be seen, the vi is

²d:\Program Files\Burleigh\

set up to control 3 axes. Axis one controls the inchworm on the low load testing machine. Axis 2 controls the inchworm on the biaxial testing machine. Fig. B-4 is a screenshot of the LabVIEW virtual instrument.

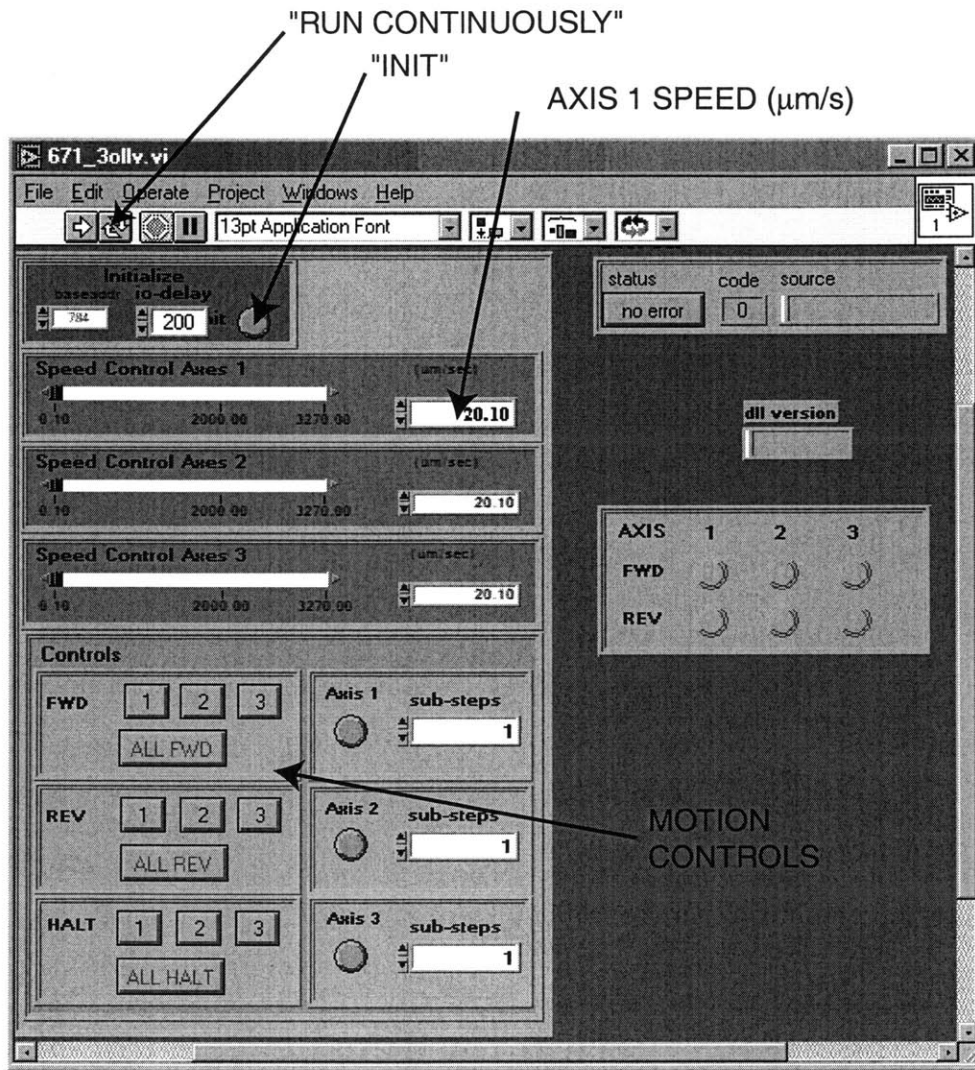


Figure B-4: Screen-shot of LabVIEW virtual instrument for controlling the Burleigh inchworm.

14. Press the "init" button on the vi and start the vi in "Run Continuous" mode.
15. Press the "halt 1" button to ensure that the inchworm is halted and turn on the power switch to the inchworm controller.
16. The inchworm may be moved by setting the speed for axis 1 in $\mu\text{m/s}$ and

pressing the "forward" or "reverse" button for axis 1 for extension or retraction of the shaft respectively.

17. Unlock specimen stages by removing stage-lock plugs
18. Start running microtensile.vi
19. Set the inchworm speed and set it in motion in the desired direction. Reverse direction when unloading is desired. The inchworm is running under open loop control. For a given input speed, it has been observed that while it maintains precisely constant speed over time, this speed is closer to 0.6 times the input speed. For axis 2, the actual inchworm speed obtained is closer to 0.85 times the input speed.
20. To stop the test, first press "halt" to stop the inchworm. Then stop microtensile.vi. As a precaution, change the data storage filename in microtensile.vi to a dummy filename, so that accidental restarting of the vi does not erase the recorded data.
21. Move the crossheads using the actuators as desired and unmount the specimen.
22. Power-off the inchworm controller.

B.2 Special Instruction for Tensile Testing of Gold Thin Film Specimens

1. Separate a specimen from the wafer: Place the wafer front side up on a compliant surface, such as a stack of paper. Using a diamond tipped scribe, scratch a short line (say 5 mm long) on the upper surface along the groove etched on the underside, towards the edge of the wafer. Using the scribe, press down gently on the line at the edge of the wafer. At sufficient force, the wafer will gently crack along the groove on the underside. Repeat this procedure on the groove across to separate each specimen.

2. Assemble mounting blocks (Part GS0500-05) on to the specimen mounting dock (Part GS0601-07) using #0-80 machine screws. The channels machined in the mounting dock are used to align the mounting blocks. The mounting holes are positioned closer in one channel than in the other; the mounting blocks are placed in this channel for mounting the short specimens, and in the other channel for mounting the longer specimens. (Fig. B-5).

Useful tip: Make sure the mounting block slides smoothly in the channel. If it doesn't, sand the sides down. It is undesirable to have the mounting blocks not come out smoothly once the specimen is glued. The silicon side arms could easily break.

3. Apply a thin layer of commercial cyanoacrylate glue (*e.g.* Krazy Glue, Loctite) on the mounting blocks and lay down the specimen with GA1 and GA2 on them with the gold side of the specimen on the face of the blocks. Align the inner edges of the GA's with the edges of the mounting blocks under a magnifying lens. This has to be done before the glue sets, which can be as soon as within 30 seconds. Once aligned, gently press down both sides of the specimen. Wait 10 minutes for complete setting of glue.

Caution: The specimen is likely to have a wafer curvature due to residual stresses from processing. Hence it may not lie flat. Avoid excessive pressure to flatten, the silicon side arms may break before testing.

4. Break one side arm: Breaking the side arms to free the thin film for the test is perhaps the most difficult step in the entire process. While this cannot be done until the specimen is mounted in the machine, it is easier to break the side arms when the specimen is outside the machine rather than mounted on the machine, due to space constraints. Hence it is suggested that one side arm be scratched and broken when the specimen is fixed onto the mounting dock.

Caution: Be very careful removing the specimen assembly (mounting blocks and specimen) from the channels in the mounting dock. The mounting blocks

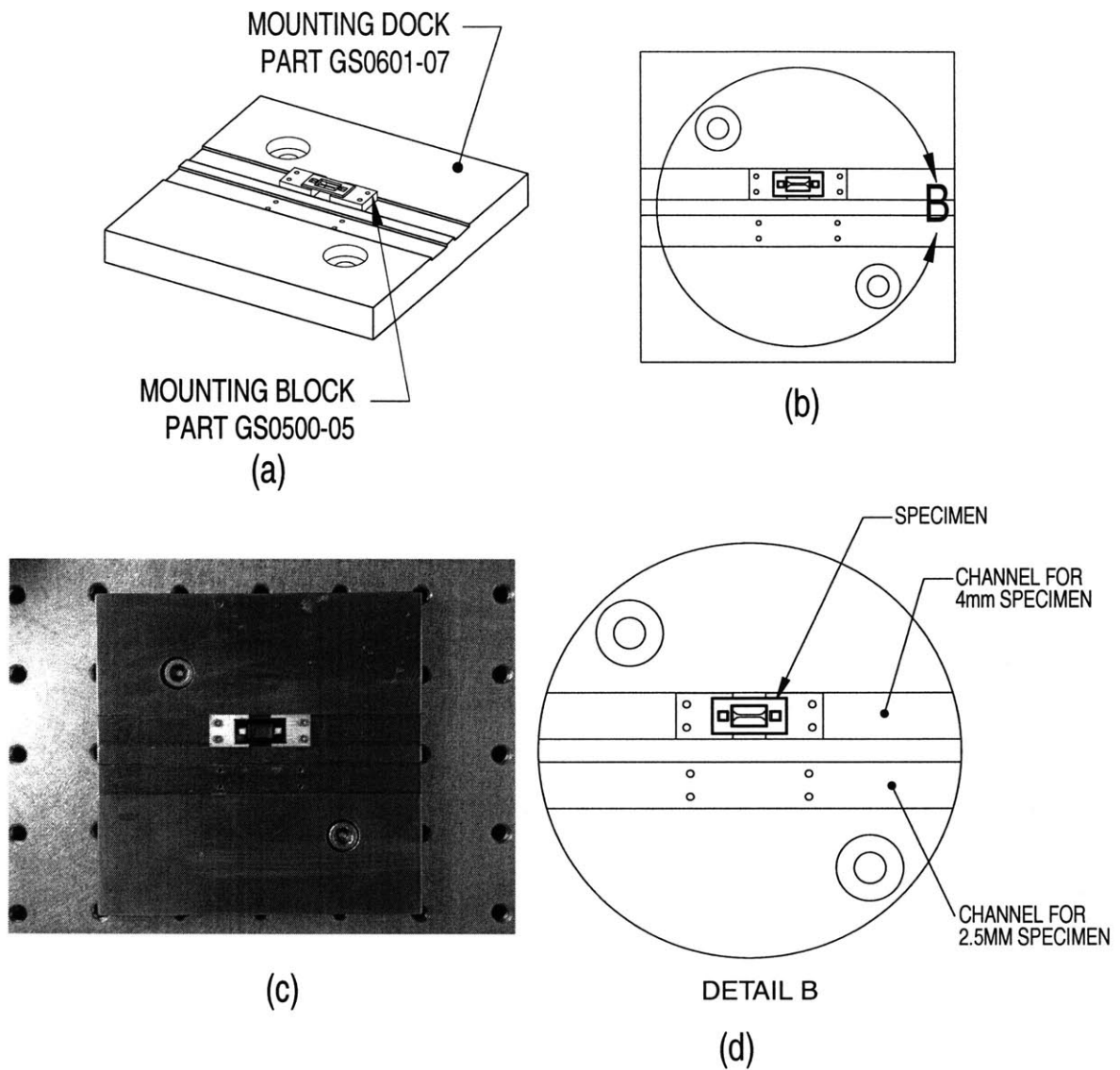


Figure B-5: Thin film tensile specimen mounting procedure

fit snugly in the channels; friction while removing the assembly could cause the specimen to break.

Set up machine for specimen

The initial distance between the specimen stages must be adjusted for each type of specimen. This also involves adjusting the initial position of the displacement sensor.

5. Lock the (LCF) using the stage locks.

6. Position load cell sensor such that load range anticipated from the test is centered around the mid-range of the sensors (output voltage of 0 V), where sensor linearity is maximum.
7. Place (but not fix) the test specimen assembly on the specimen stages with the thin film on top. It is preferable to have the unbroken side arm on the ACF side because of better access to breaking the remaining side arm from the ACF side. Using the inchworm, move the ACF into position to approximately align the mounting holes (MH) on the specimen stages with the holes on the mounting blocks.
8. Position the displacement sensor (SD) on the ACF such that the total specimen extension anticipated from the test is centered around the mid-range of the sensor (output voltage of 0 V).
9. Fix the mounting block on the LCF specimen stage using two #0-80 machine screws.
10. Drop #0-80 machine screws through the mounting holes on the ACF side mounting block on the ACF side and move the ACF using the inchworm until the screws align with the mounting holes on the specimen stages. Tighten screws.

Prepare specimen for test

11. Break remaining side arm: Carefully scratch the side arm with a diamond scribe. Care must be taken not to press the flexures too hard out of plane. The arm may be weakened and broken by flexing using bent-nose tweezers.
12. Carefully remove the LCF stage locks. Apply slight inward pressure on the flexures so that releasing the LCF does not cause it to suddenly spring back and apply a tension on the specimen. The specimen is now ready for testing.
13. Start and run the test starting from step 18 in the previous section.

14. Unmounting the specimen: The glued silicon may be separated from the mounting blocks by ultrasonical cleaning using acetone, leaving the mounting blocks reusable. The broken fragments of the film may be cut off using an exacto-knife and preserved for post-test investigations.

B.3 Extended Displacement Range

The range of the displacement sensor used in cross-head displacement measurement is 1.25 mm³. However, some specimens may undergo extensions larger than that. In such cases, the known constant speed of the actuator may be used to estimate the specimen extension beyond the sensor's range. Referring to Fig. 2-5,

$$\delta_A(t) = \delta_L(t) + \delta_S(t) \quad (\text{B.1})$$

During the test, $F_L (=K_L\delta_L)$, δ_S and t are recorded. Hence δ_A may be calculated accurately for the time when δ_S was still within sensor range. From this, $\dot{\delta}_A$ may be calculated using the recorded time data. The inchworm speed prescribed in its control vi is only nominal; the actual speed is found to be highly constant, but lesser by about 40% from this input value. It must hence be calculated exactly from the sensor outputs as described above. If the inchworm speed is not changed during a test, $\dot{\delta}_A$ is known even after the displacement sensor goes out of range. Now, if the load cell sensor is still within range, its recorded displacement, combined with t and $\dot{\delta}_A$ may be used to estimate δ_S for the rest of the test:

$$\delta_S(t) = \dot{\delta}_A t - \delta_L(t) \quad (\text{B.2})$$

Of course, care has to be taken in calculating the extended displacement $\delta_S(t)$ when the direction and speed of the inchworm are changed during the test. Using this calculation, tests involving extensions up to 6.35 mm may be performed with reasonable accuracy.

³With the purchase of the Keyence non-contact extensometers, this calculation may not be necessary.

B.4 Bill of Materials

Part #	Name	Material	Manufacturer	Cost(ea.)
GS0200-01	Flexure Frame	Al 7075-T6	Ramco	\$550
GS0200-02	Calibration Fixtures	Al 7075-T6	Ramco	\$45
GS0200-03	L Bracket	Al 6061	Ramco	\$55
GS0200-04	Bottom Bend Fixture	Tool Steel	Ramco	\$75
GS0200-05	3-Point Bend Fixture	Tool Steel	Ramco	\$75
GS1201-01	New 3-Point Bend Fixture ⁴	Tool Steel	CMS	-
GS0200-06	4-Point Bend Fixture	Tool Steel	Ramco	\$75
GS0200-07	Nut Plate	Al 6061	Ramco	\$40
GS0200-08	ACF Locks	Al 7075	Ramco	\$30
GS0200-09	LCF Locks	Al 7075	Ramco	\$35
GS0500-03	Flat Face Grips	Al 7075	CMS	-
GS0500-05	Thin Film Mounting Block	Al 7075	CMS	-
GS0500-07	Thin Film Mounting Dock	Stainless Steel	Ramco	\$240
GS0601-08	Tension Grip (Top)	Al 7075	Ramco	\$75
GS0601-09	Tension Grip (Bottom)	Al 7075	Ramco	\$75
GS0900-01	Indenter Holder	Tool Steel	Ramco	\$75
GS0900-02	Indentation Stage	Tool Steel	Ramco	\$75
SMU9000	Inductive Transducer		Kaman	\$2240
5U Sensor	Inductive Sensor		Kaman	\$350
PS150	Power Supply		Kaman	\$175
IW700	Inchworm Actuator		Burleigh	\$1595
IW450	Inchworm Mount	Al 6061	Burleigh	\$200
6000ULN	Inchworm Controller		Burleigh	\$2885
PCI6700	Motion Card		Burleigh	\$1600

Notes:

Ramco: Ramco Machine LLC, MA. <http://www.ramcomachine.com/>

CMS: MIT Central Machine Shop

Kaman: Kaman Instrumentation Inc., CO. <http://www.kamaninstrumentation.com/>
Burleigh: Burleigh Instruments Inc., NY. <http://www.burleigh.com/>

B.5 Specifications

- Flexure length: 75 mm
- Flexure fillet radius: 4 mm
- Flexure web thickness: 0.8 mm
- Out of plane system thickness: 12.7 mm (0.5 in)
- LCF stiffness (Calibrated): 1.217 N/mm
- ACF stiffness (Assumed equal to LCF): 1.217 N/mm
- Material of flexures: Aluminum Alloy 7075-T6
- Flexure travel range: 0-6mm (Identical LCF and ACF)
- Displacement sensors: Kaman Instrumentation Inc. Model SMU9000-5U 2 Channels

Range: 0-1.25 mm

Offset: 0.1 mm

Output signal: ± 5 V

Resolution with DAQ system: 20nm

- Data acquisition: National Instruments PCI 6035E 16bit 16Channel System
- Actuation: Burleigh Instruments Inchworm model IW700

Range: 0-6.35 mm

Nominal step size: 4 nm

Max velocity: 1.5 mm/s

Controller: Burleigh ULN6000 Ultra Low Noise Controller

Mounting: Burleigh IW450 mounting bracket

System specifications:

Load Range/Resolution: 0-1.5 N / 25 μ N

Displacement Range/Resolution: 0-1.25 mm / 20 nm

Extended Displacement Range : 6.35 mm

Space for specimen and grips (Nominal): 30 x 10 x 10 mm³

Space for specimen: 10 x 10 x 10 mm³

Appendix C

Low Load Testing Machine: Technical Drawings

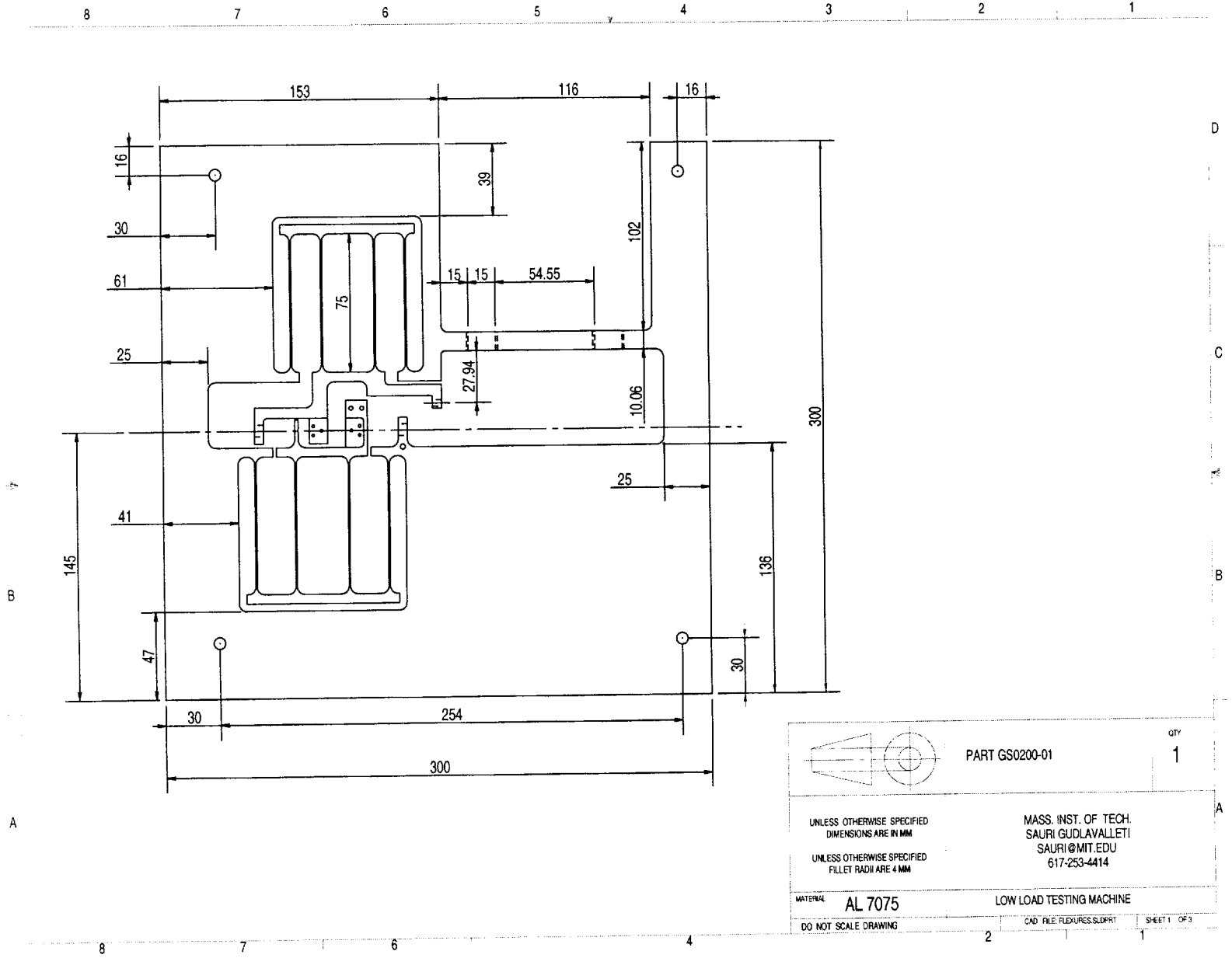


Figure C-1: Part GS 0200-01. Low load testing machine flexure frame (Sheet 1 of 3)

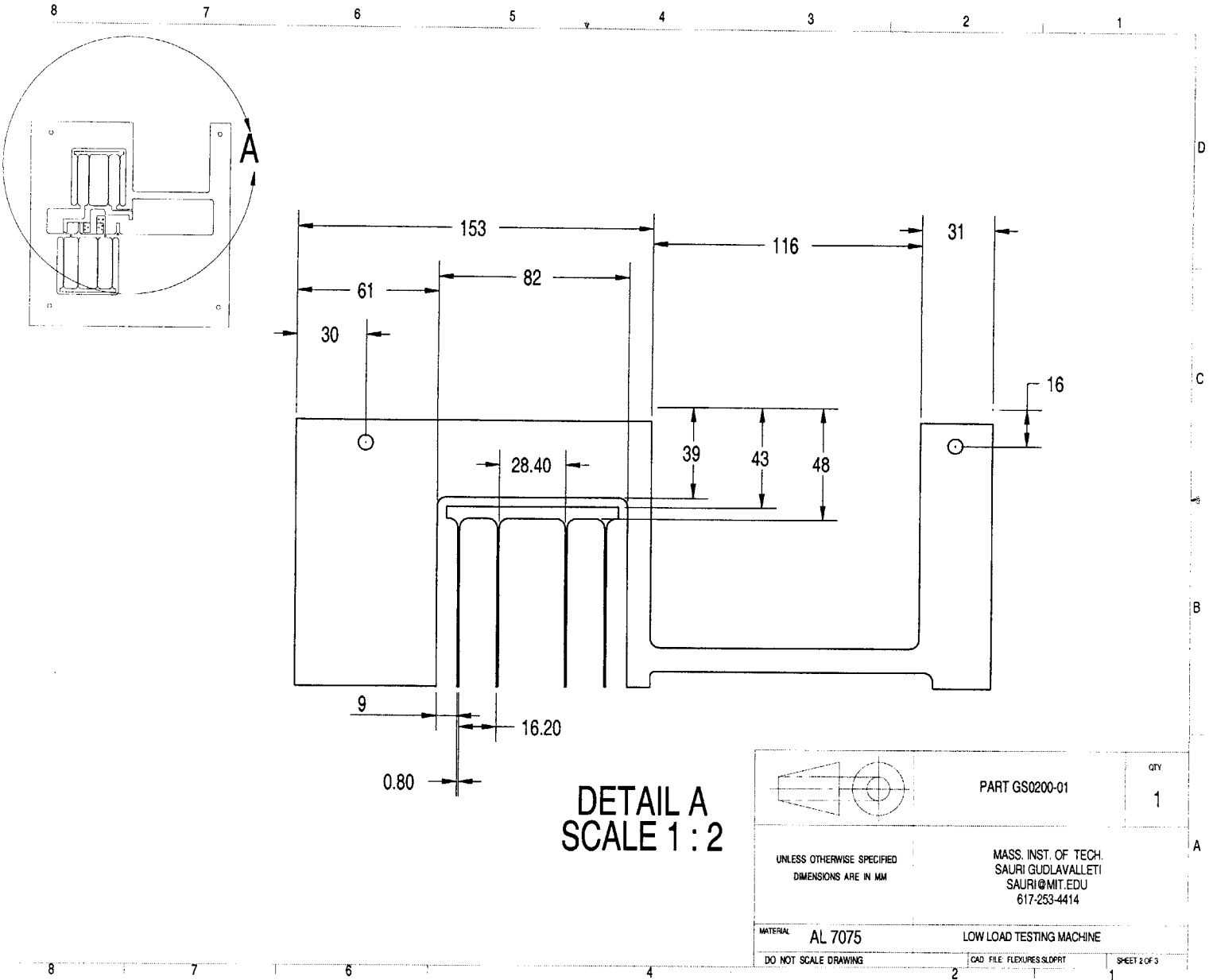


Figure C-2: Part GS 0200-01. Low load testing machine flexure frame (Sheet 2 of 3).

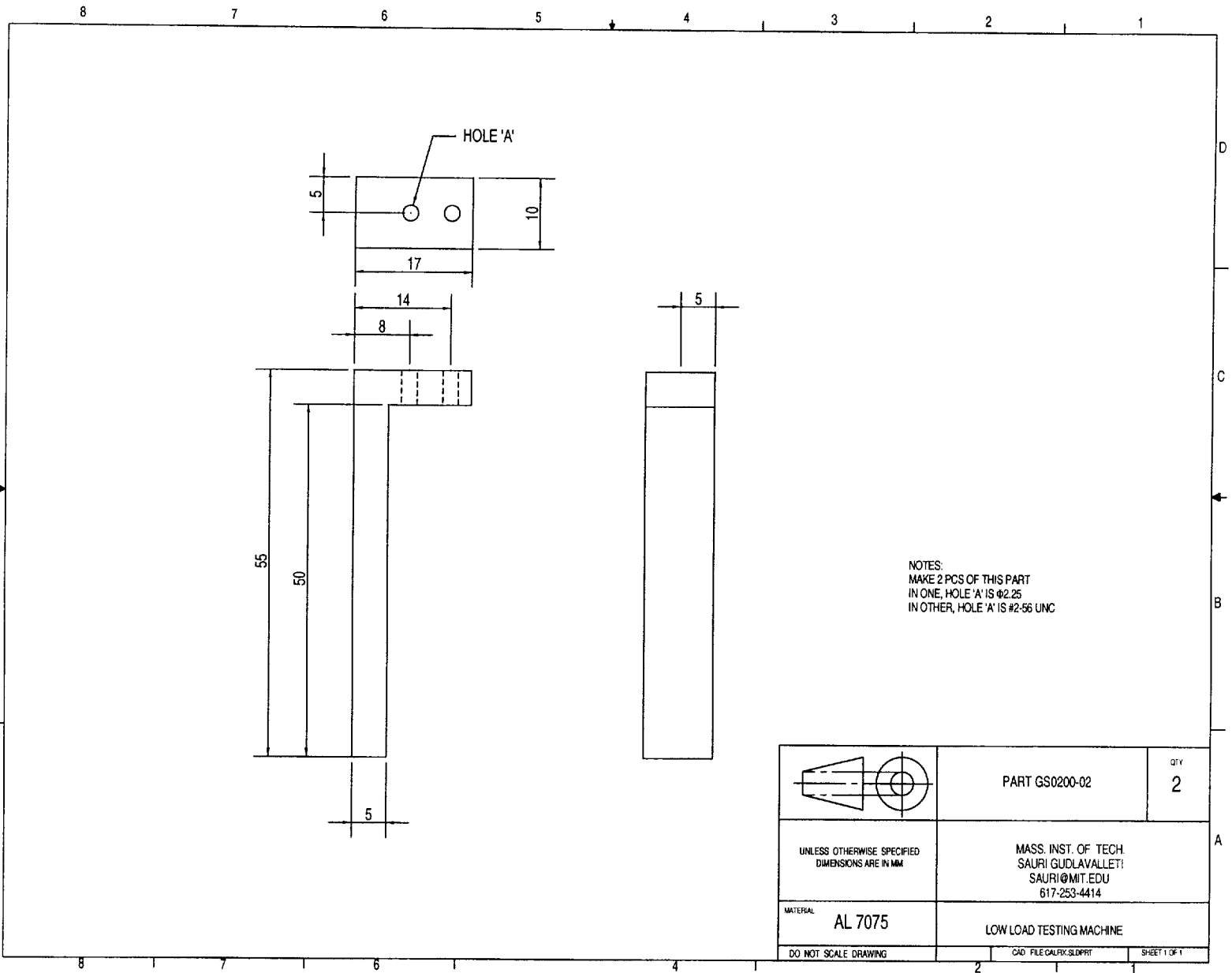


Figure C-4: Part GS 0200-02. Calibration fixtures. Assembly shown in Fig. 3-8.

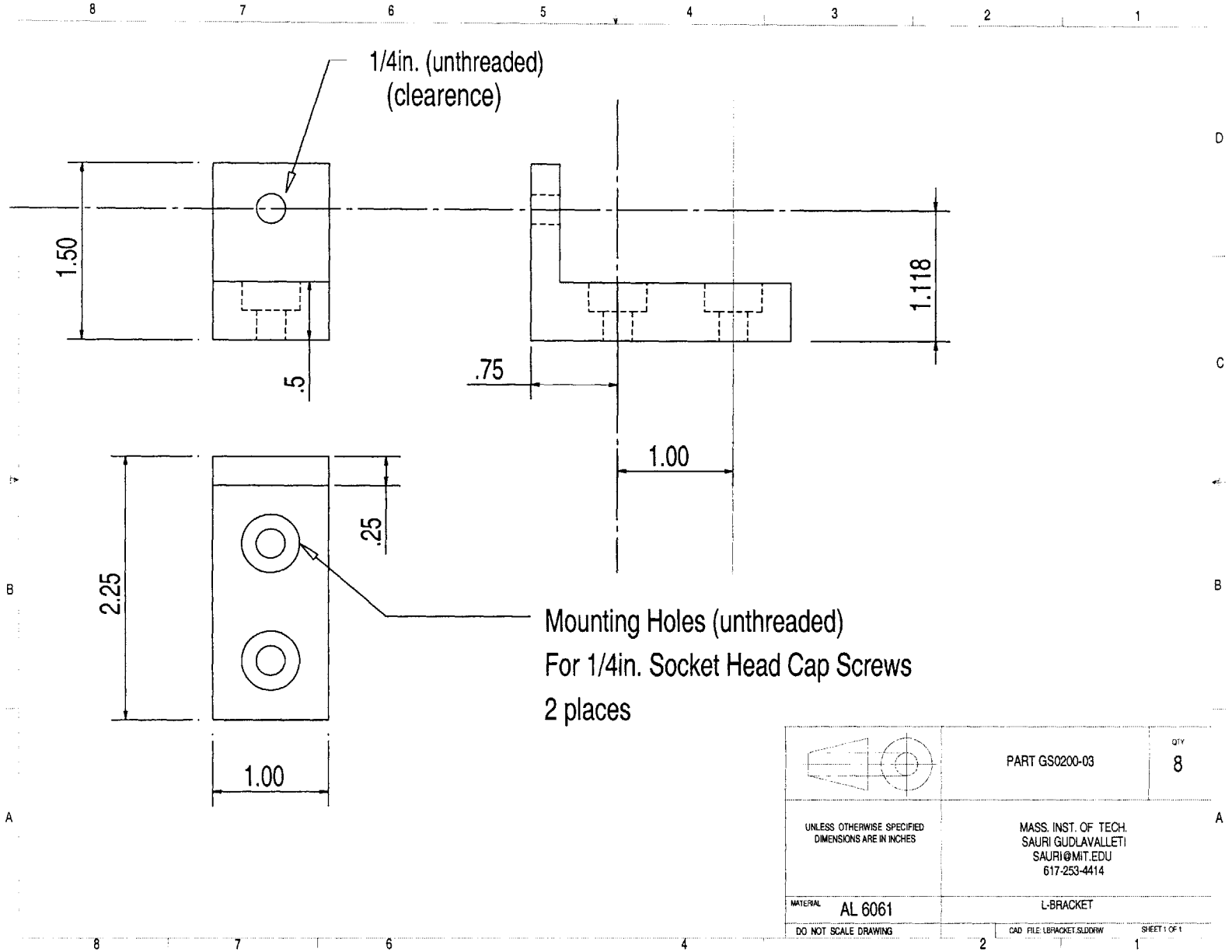
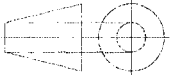


Figure C-5: Part GS 0200-03. L-Brackets for general mounting purposes.

	PART GS0200-03	QTY 8
UNLESS OTHERWISE SPECIFIED DIMENSIONS ARE IN INCHES	MASS. INST. OF TECH. SAURI GUDLAVALLETTI SAURI@MIT.EDU 617-253-4414	
MATERIAL AL 6061	L-BRACKET	
DO NOT SCALE DRAWING	CAD FILE: LBRACKET.SLDDRW	SHEET 1 OF 1

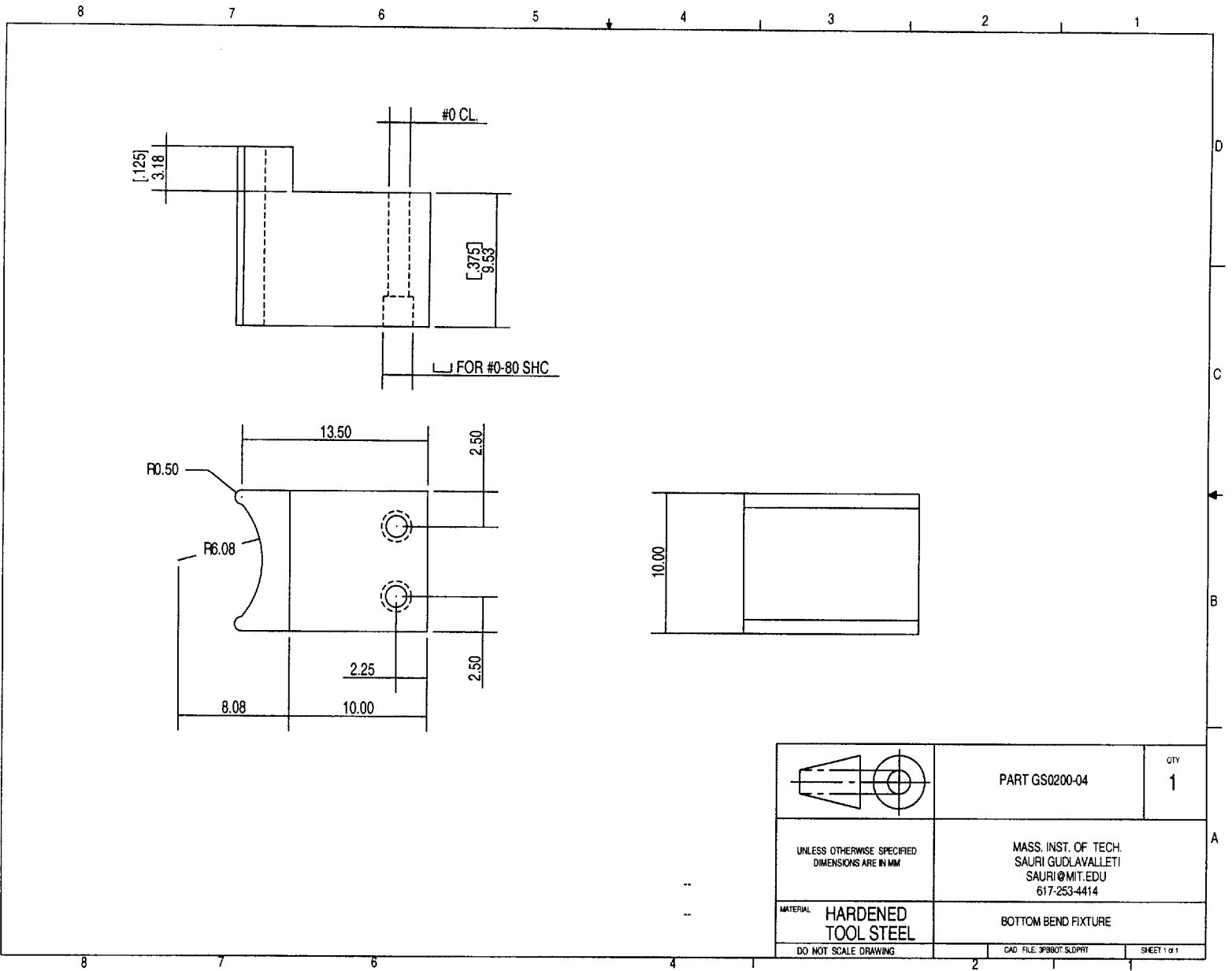


Figure C-6: Part GS 0200-04. Bend testing fixture (bottom).

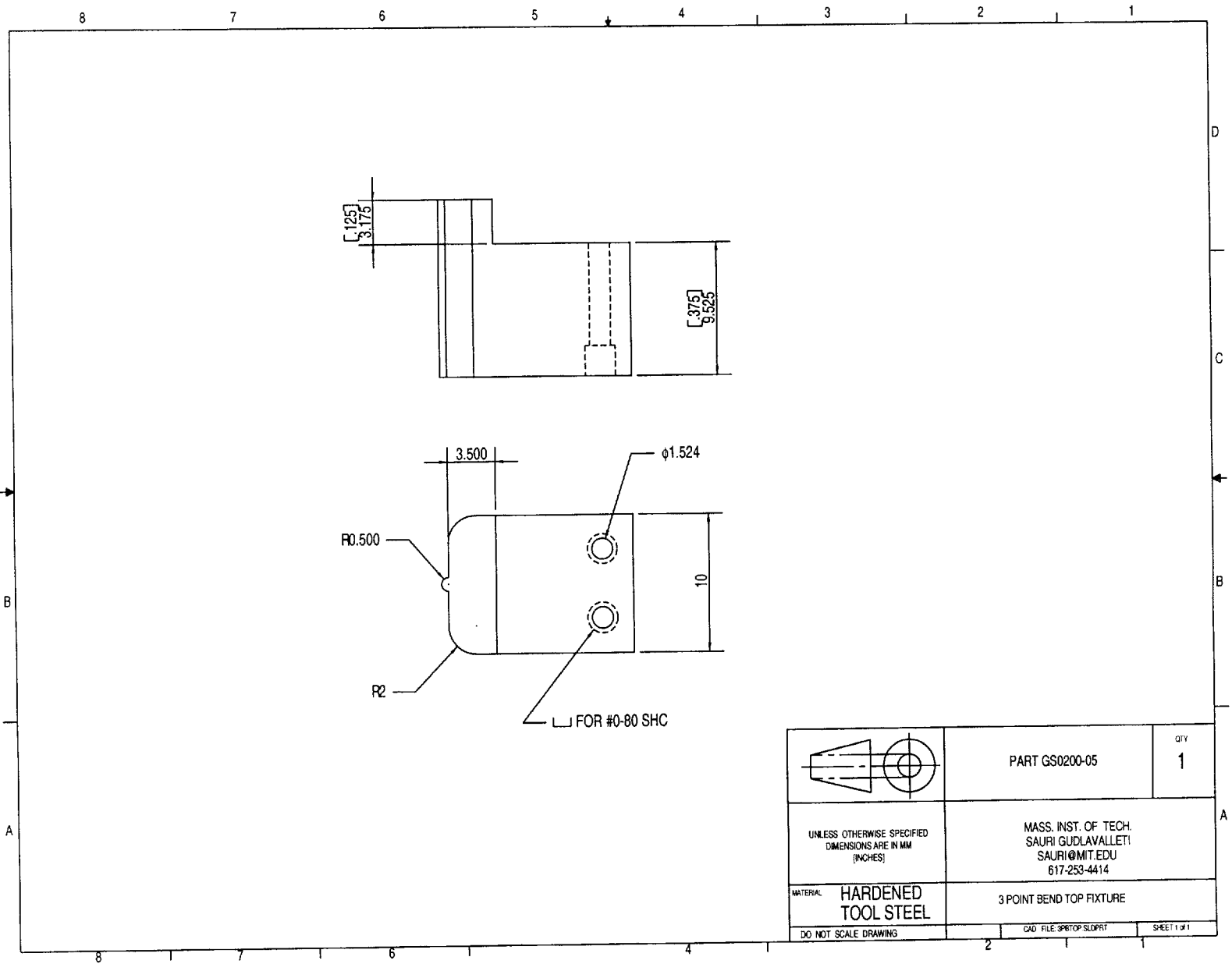


Figure C-7: Part GS 0200-05. 3-Point Bend testing fixture. Replaced by GS1201-01

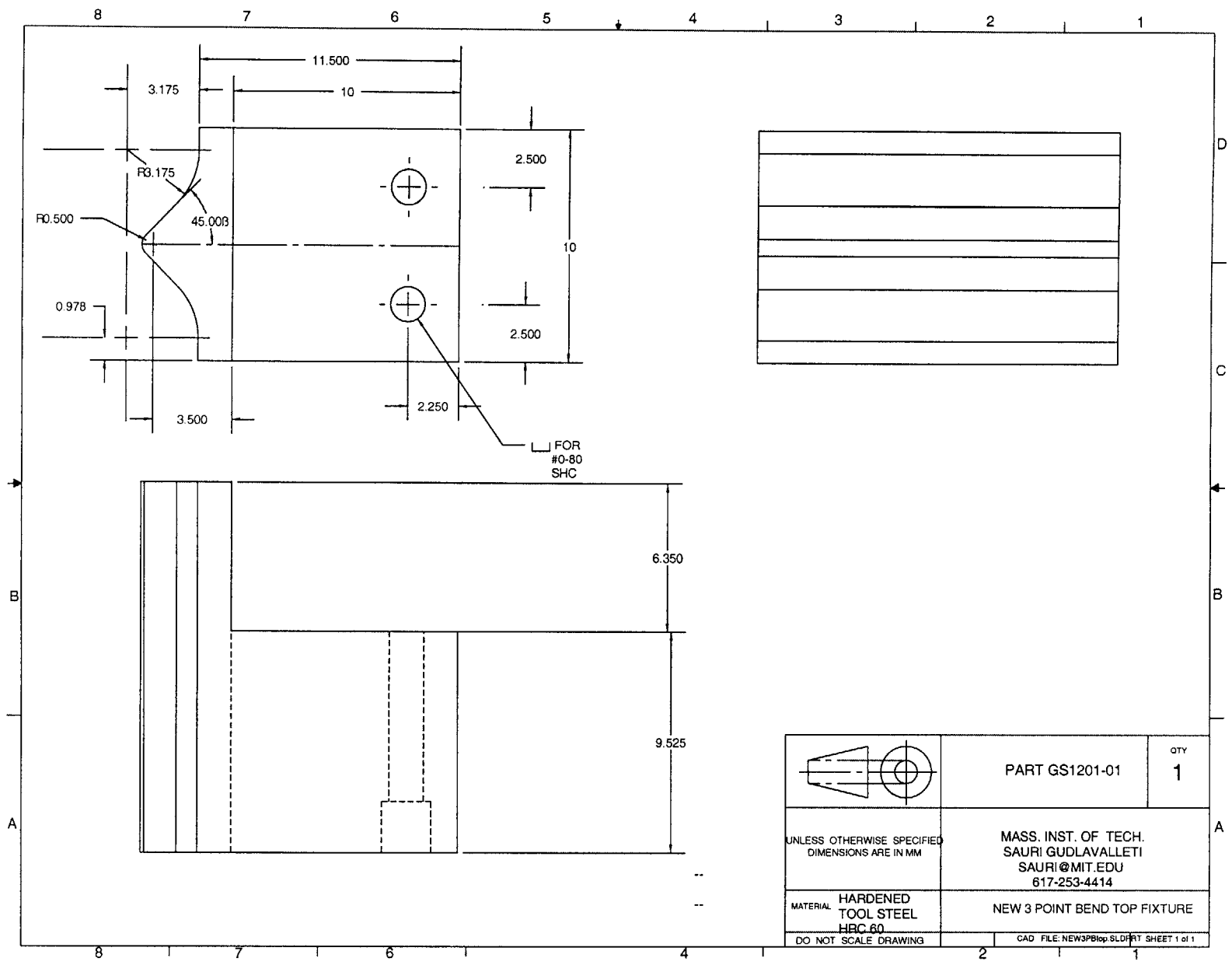
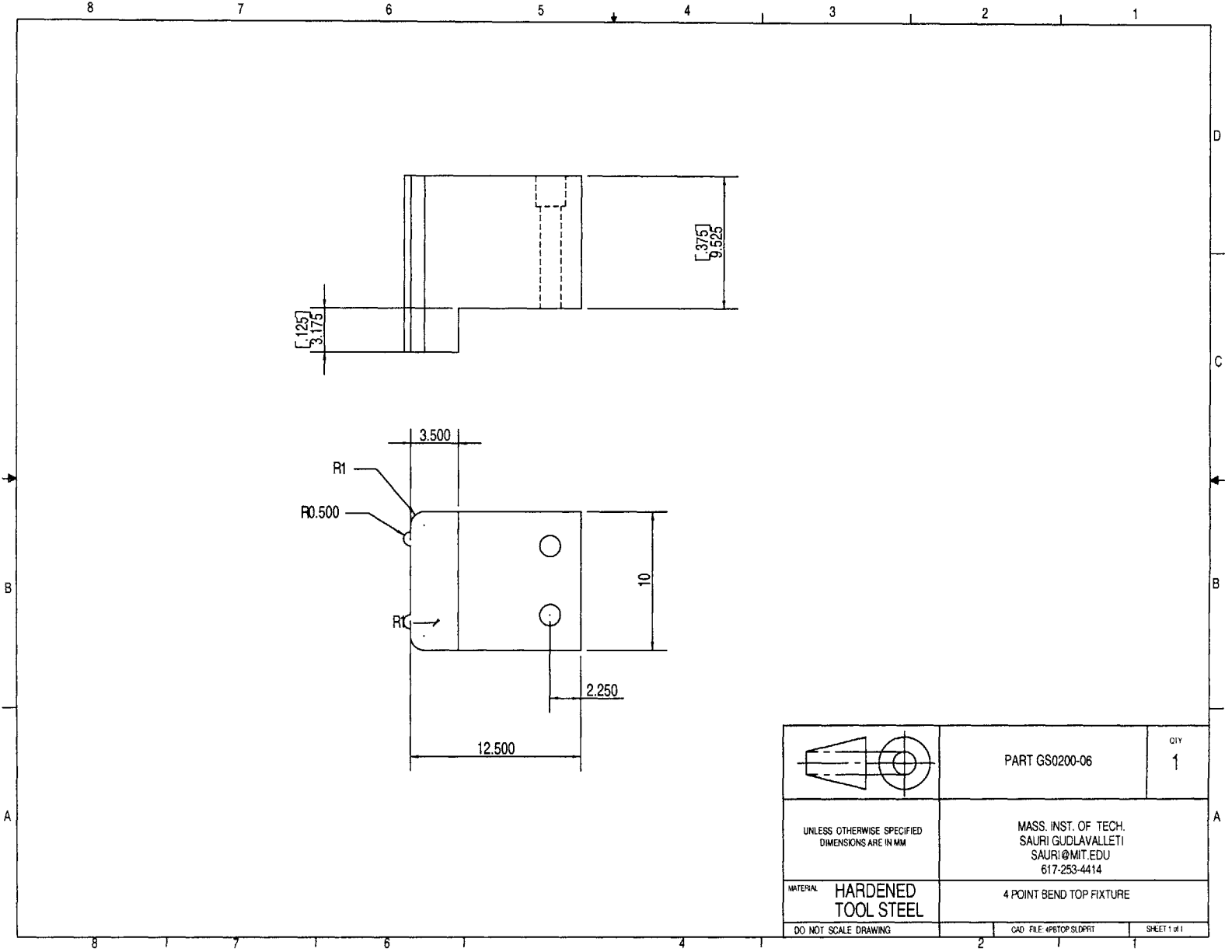


Figure C-8: Part GS 1201-01. Modified 3-Point Bend testing fixture.



	PART GS0200-06	QTY 1
UNLESS OTHERWISE SPECIFIED DIMENSIONS ARE IN MM	MASS. INST. OF TECH. SAURI GUDLAVALLETTI SAURI@MIT.EDU 617-253-4414	
MATERIAL HARDENED TOOL STEEL	4 POINT BEND TOP FIXTURE	
DO NOT SCALE DRAWING	CAD FILE: 4PBTOP.SLDPR1	SHEET 1 of 1

Figure C-9: Part GS 0200-06. 4-Point Bend testing fixture.

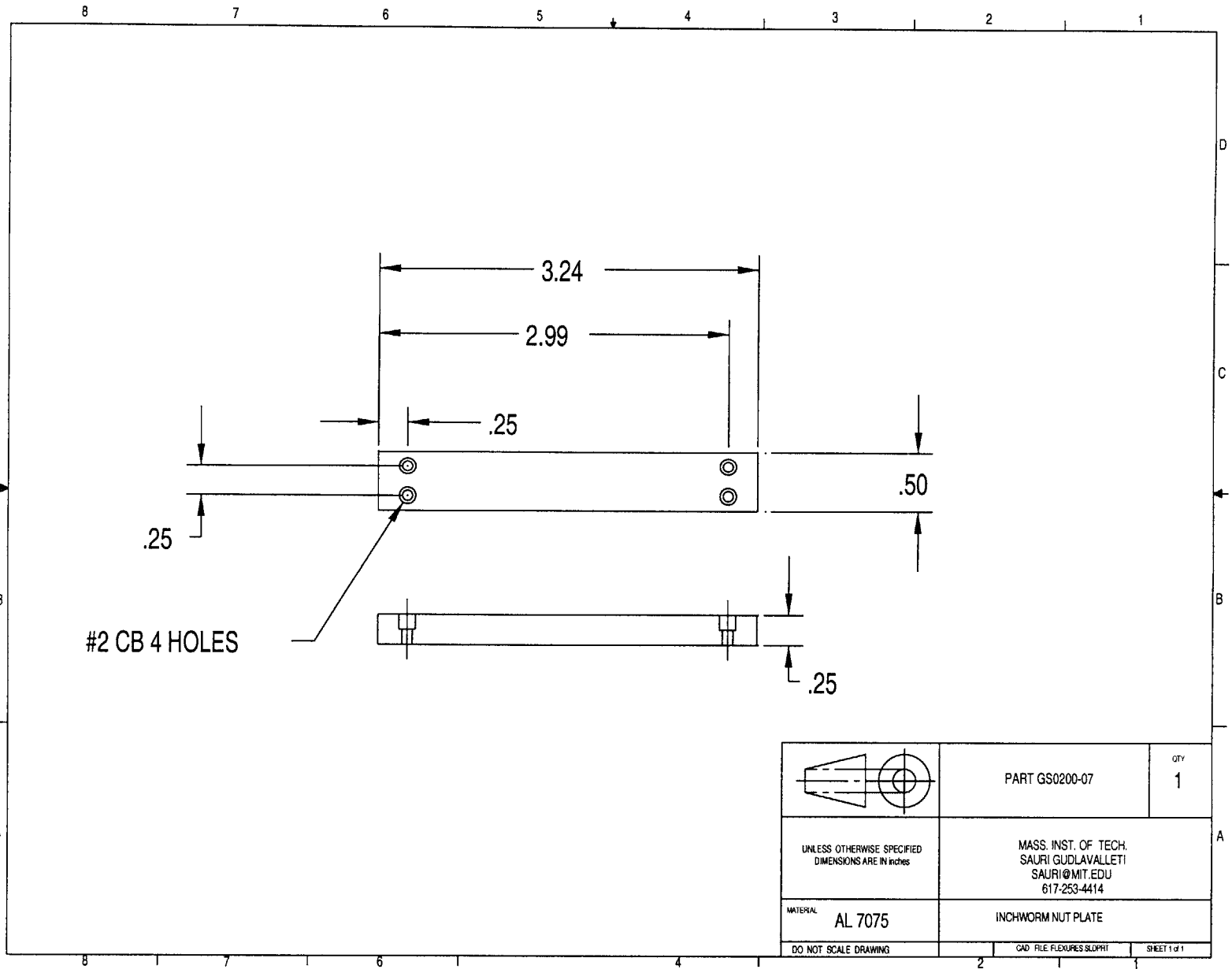


Figure C-10: Part GS 0200-07. Nutplate for mounting inchworm.

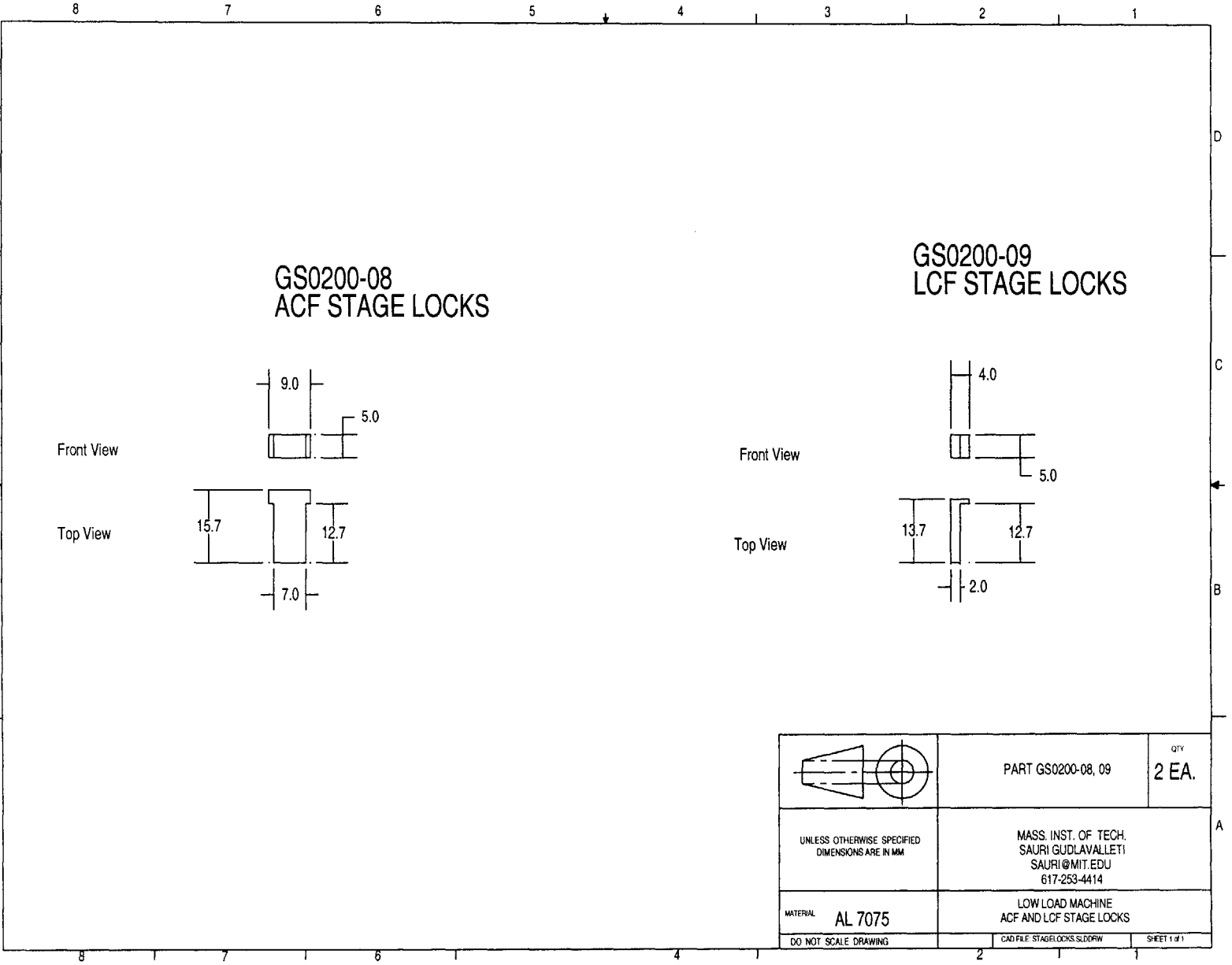


Figure C-11: Part GS 0200-08 and 09. Locks to prevent movement of flexures during set-up.

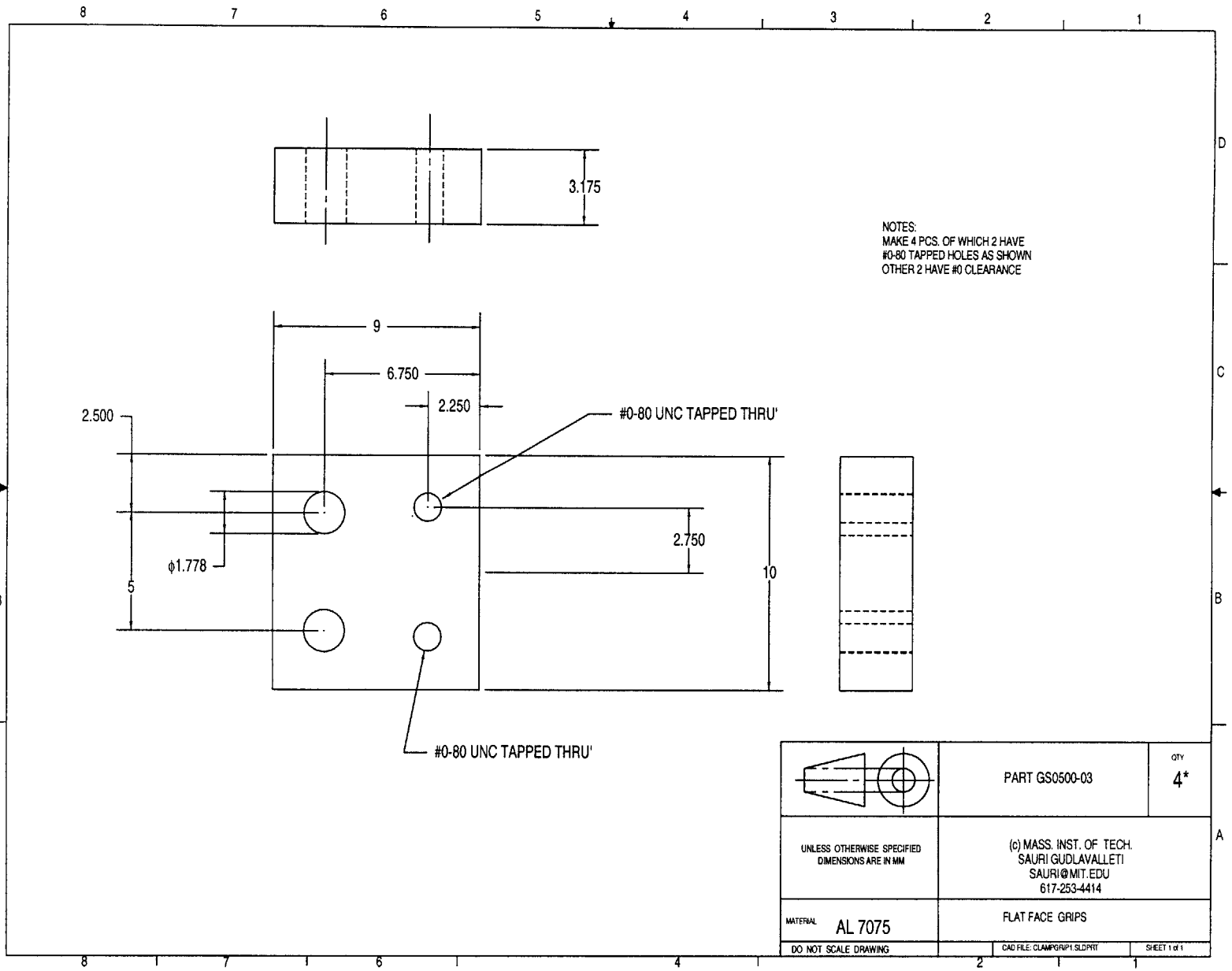


Figure C-12: Part GS 0500-03. Flat faced clamps for foil specimens.

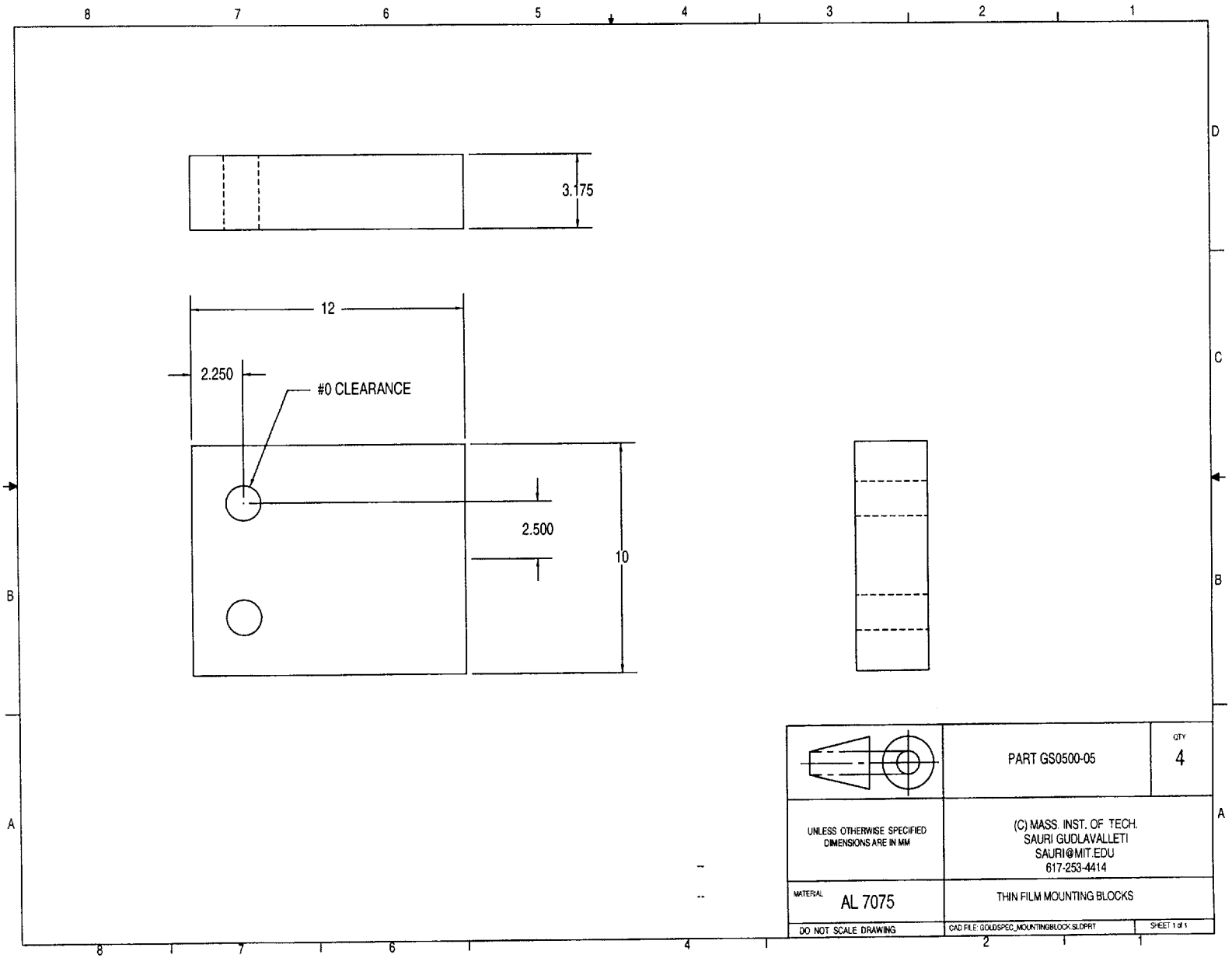



Figure C-13: Part GS 0500-05. Mounting blocks for thin film specimens

	PART GS0500-05	QTY 4
UNLESS OTHERWISE SPECIFIED DIMENSIONS ARE IN MM	(C) MASS. INST. OF TECH. SAURI GUOLAVALLETTI SAURI@MIT.EDU 617-253-4414	
MATERIAL AL 7075	THIN FILM MOUNTING BLOCKS	
DO NOT SCALE DRAWING	CAD FILE: GOLDSPEC_MOUNTINGBLOCK.SLDPRT	SHEET 1 of 1

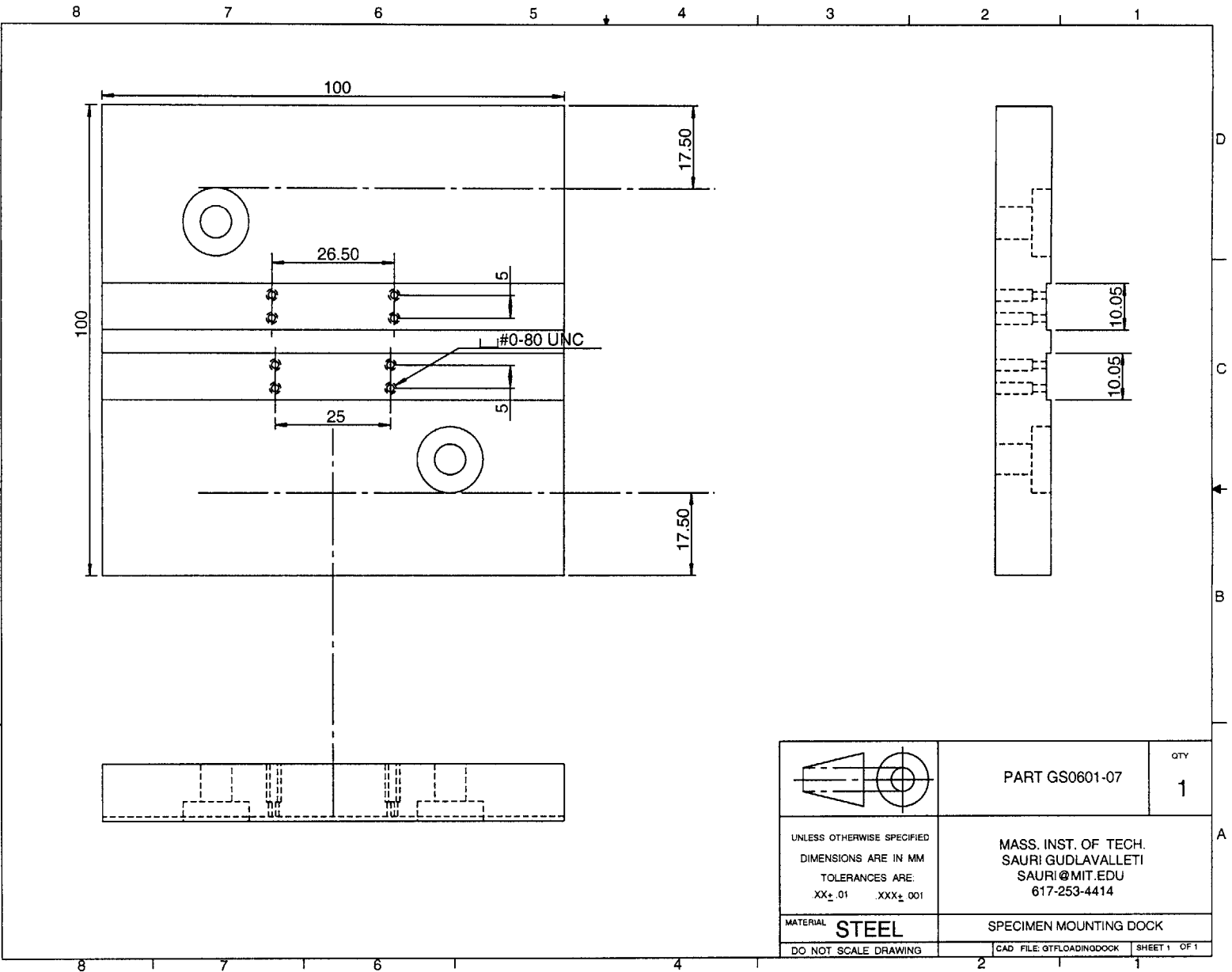


Figure C-14: Part GS 0500-07. Thin film mounting dock, provides an ex-situ specimen mounting station.

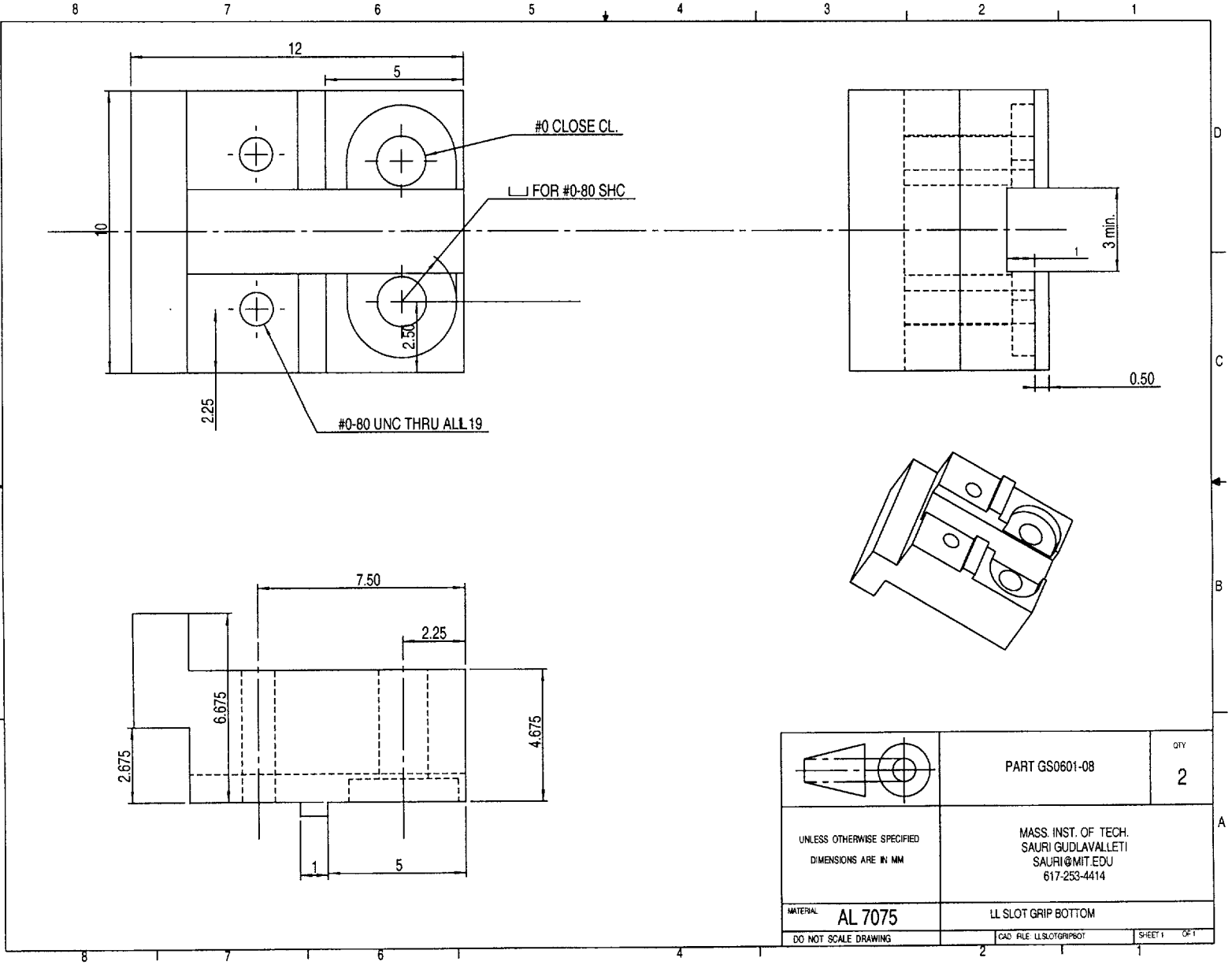


Figure C-15: Part GS 0601-08. Foil tension grip with slot for specimens with 3 mm wide grip section. Assembly shown in Fig. (3-5.)

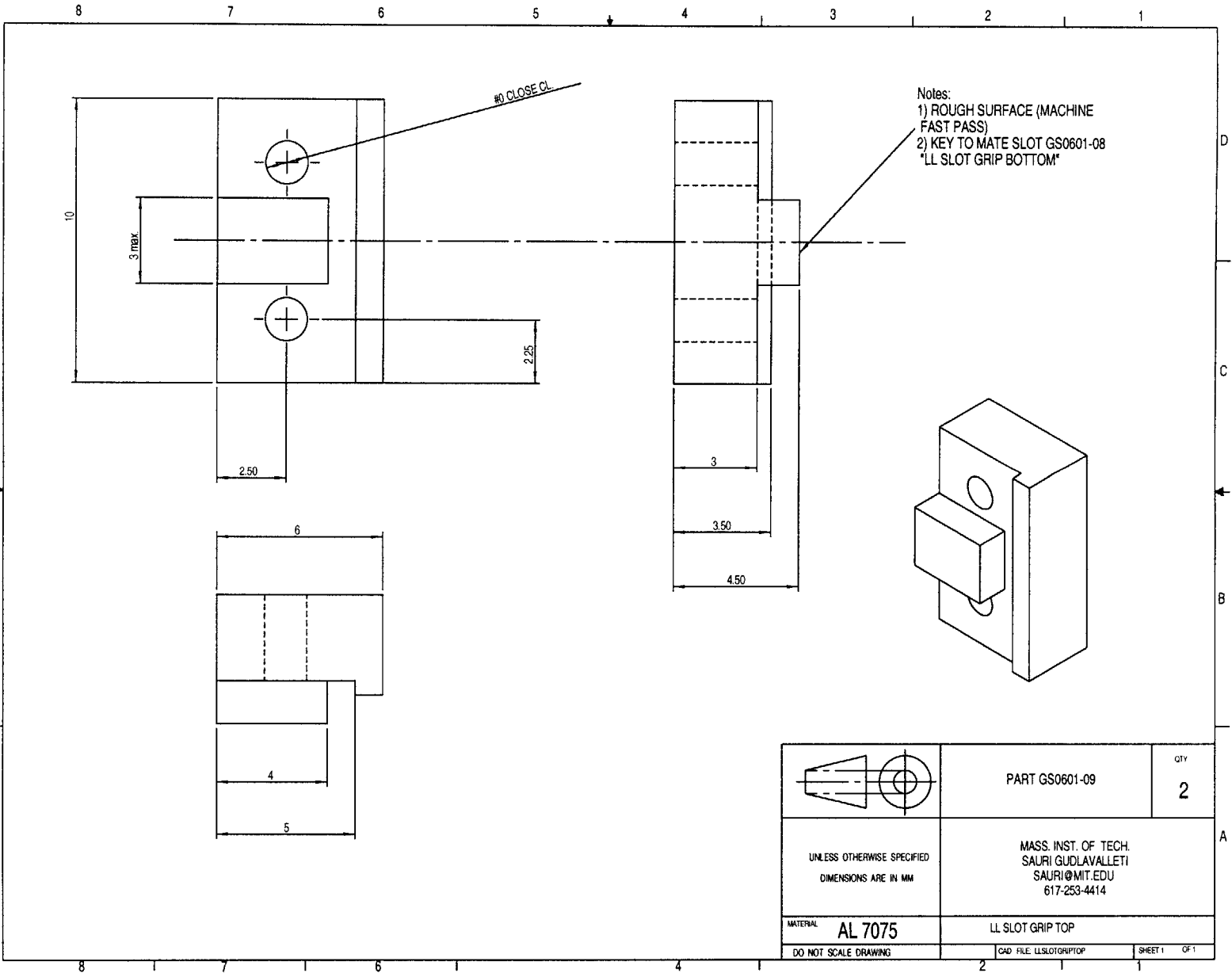
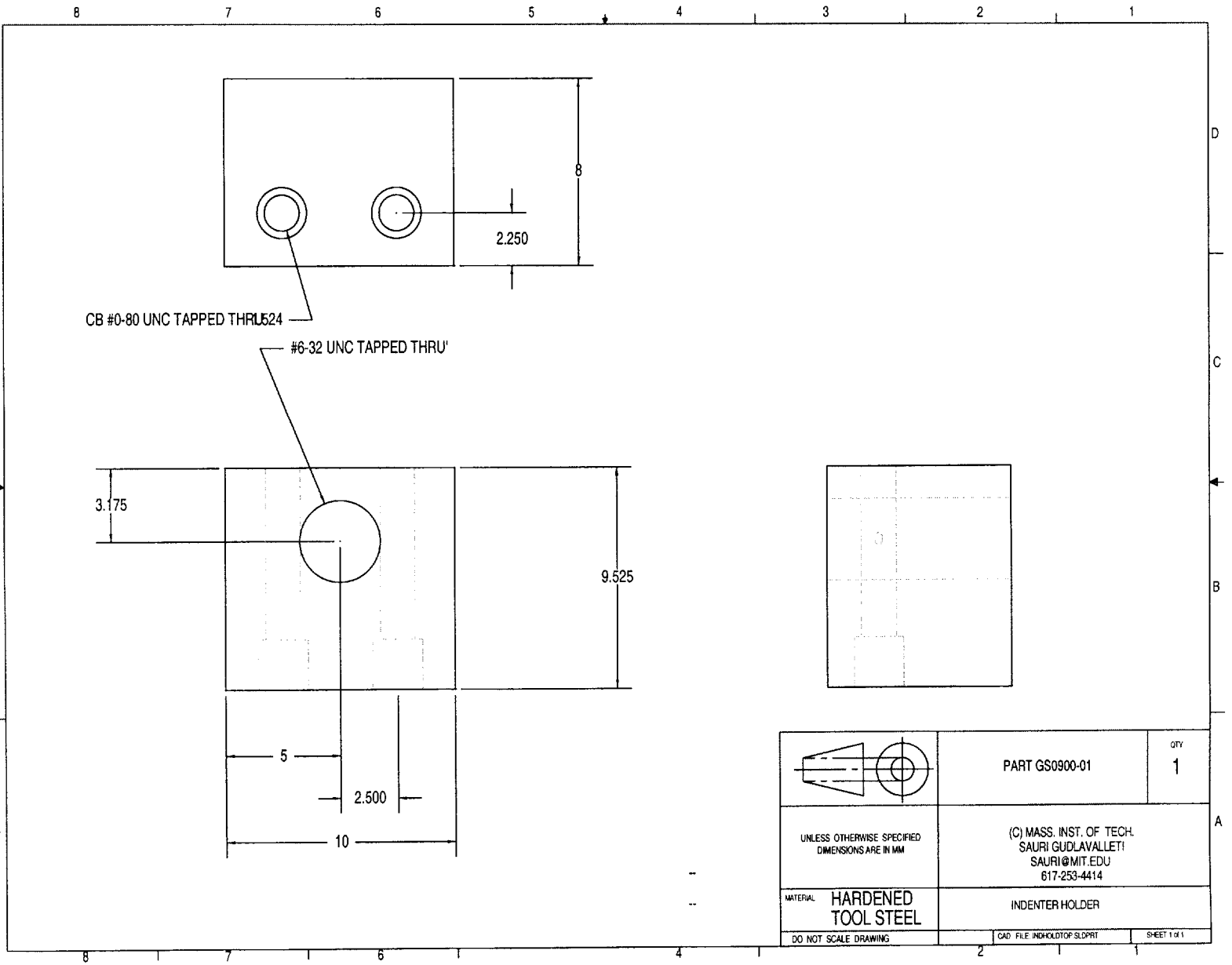


Figure C-16: Part GS 0601-08. Foil tension grip clamp. Assembly shown in Fig. (3-5.)



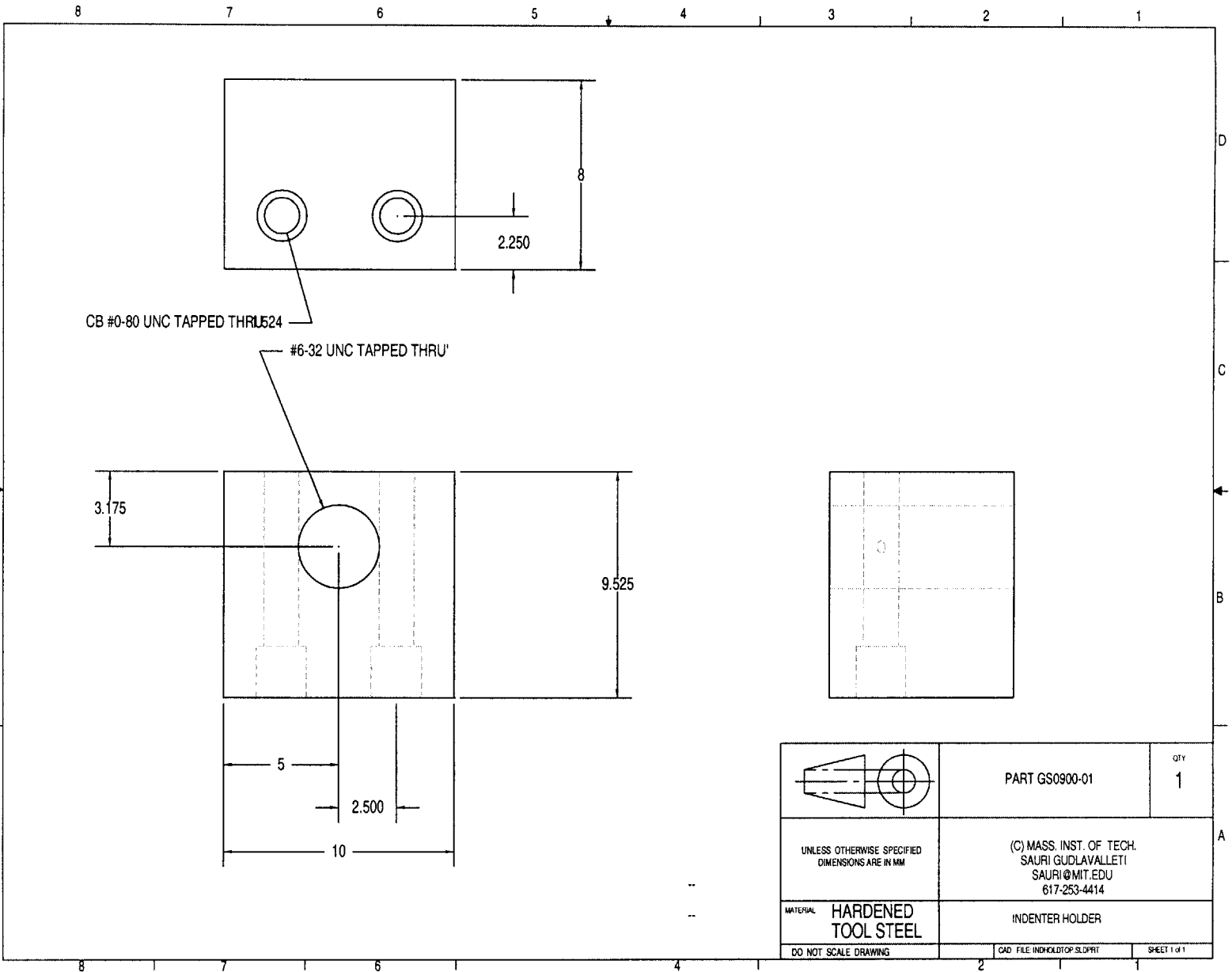


Figure C-18: Part GS 0900-02. Indentation specimen stage. Assembly shown in Fig. (3-7.)

Appendix D

High Load Testing Machine: Operation Manual

D.1 General Operating Procedure

1. Install load cell sensor as shown in the photograph (D-1). Displacement sensor may have to be re-installed/repositioned if performing first test in current configuration.
2. Install grips/fixtures. Fig. D-1 shows installation of foil tension grips. Figs. D-2 and 4-6 show installation of the multispan bend fixtures.
3. Open hlstatic.vi on LabVIEW; but do not start it.
4. In the VI, enter/set the following values:
 - Filename: enter desired data file name
 - Notes: notes about specimen (up to 32 characters)
 - "Write to File" button: NO
 - scan rate: 100
 - scan set: 10

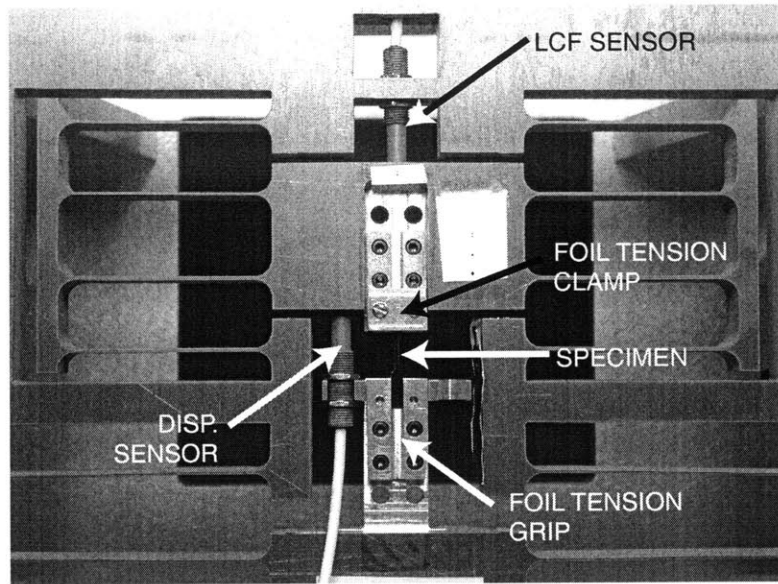


Figure D-1: Close-up of specimen stage region in high load testing machine showing displacement sensors and foil tension grips.

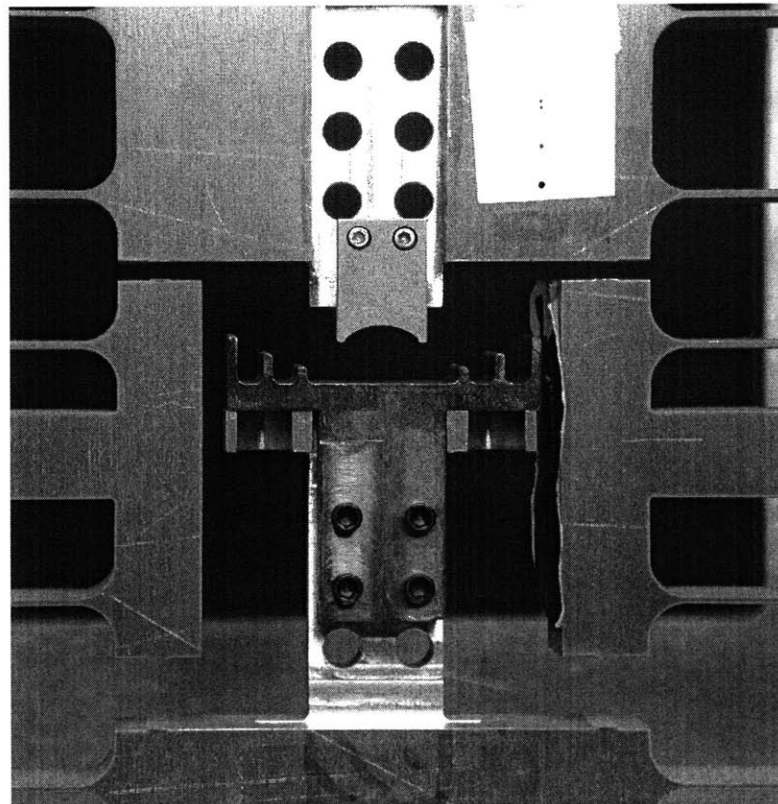


Figure D-2: Multi-span bend fixtures installed in high load testing machine. Assembly is shown in Fig. 4-6

- Load Channel: Channel on BNC2090 Board to which load channel is connected
- Disp Channel: Channel on BNC2090 Board to which displacement channel is connected
- Load Cell Sensor: Select sensor being used from drop down menu
- Displacement Sensor: Select sensor being used from drop down menu
- "PUSH to GO" button: out
- "GATHER DATA" button: OFF
- dV/dt: 0.000
- Vout(init): 0.001

Vout(init) is a very important parameter. It instructs the DAQ board to set the output signal voltage to the amplifier to a specified value. When the amplifier is being powered on for the first time, it is important that the signal input to it be zero; a non-zero value would cause a corresponding jump in stimulus to the voice coil, which may then move violently, damaging the machine and specimen.

When the VI starts to run, it sets the signal input to the amplifier to Vout(init). Hence, if the amplifier is powered off, the VI must be started with Vout(init)=0.001 V ($\approx 0V$) so that it does not "jump" when powered on. However, if the amplifier is already running, and a test was just concluded, the signal being sent to the amplifier may not be zero; the previous test may have stopped with a non-zero signal. Restarting the VI now may cause the voice coil to jump from the previous non-zero value to the zero Vout(init). In this case, it is important that when the VI is stopped, the Vout value (which is the present value of signal being sent to the amplifier) must be entered in the Vout(init) box. This way, when the VI is restarted, the position of the voice coil will not jump suddenly.

5. Start the VI.

6. Power on the amplifier, if not already on.

7. *Moving the voice coil:*

- (a) First set dV/dt to the desired value. This parameter is proportional to the rate of change of voice coil force. See section D.2 for details on calculation of dV/dt . The slowest possible value is 0.005 V/s. The fastest recommended is 0.1 V/s. For general jogging purposes, 0.02V/s is the recommended value.
- (b) Set direction: "PUSH" (ACF towards LCF) or "PULL" (ACF away from LCF).
- (c) Press the "PRESSED TO GO" button ONCE.
- (d) To stop, hit the "PRESSED TO GO" button again, which releases it.

8. Specimen installation and cross head displacement sensor positioning:

Tension Testing

- (a) Orient machine horizontal for convenience of inserting specimen. Place specimen in channel and put in clamps. Tighten the clamp on the ACF side, leave clamp on LCF side loose for adjustment.
- (b) Install the displacement sensor as shown in photograph. Adjust initial position of sensor (monitoring using the VI) to be as close to 0 μm as possible; the optimal range is 0 - 1250 μm .
- (c) Orient machine vertical for the test. The weight of the voice coil will cause the ACF to sag. The ACF has to be moved back into position.
- (d) Set dV/dt on VI to a low value, like 0.01
- (e) Set the direction of voice coil "PUSH" and press the "PUSH TO GO" button. The voice coil starts moving up. Stop the voice coil (by pressing the "PUSH TO GO" button again) when the displacement sensor has reached the value it was at in the horizontal position.

- (f) Note down the current V_{out} . This is the signal value which will place the voice coil back in "home" position.
- (g) If necessary, adjust LCF sensor position so that its maximum linear range may be used.
- (h) Tighten the specimen clamp on the LCF side. The set-up is ready for testing.

Bend Testing

- (a) Orient the machine vertical and install "local sensor mounts" on the back-side, as shown.
 - (b) Install the cross head displacement sensor in the local sensor mounts, keeping sufficient distance between sensor and target.
 - (c) Place specimen on the bend supports and move the voice coil up at a slow rate so the specimen is very close to the top bend fixture.
 - (d) During bend tests, both sensors move towards their targets. Hence, position LCF sensor and displacement sensor at the furthest end of their ranges and tighten them. The set-up is now ready for testing.
9. Set the desired loading rate dV/dt . For details on calculating dV/dt , see section D.2.
 10. Set direction of motion: "PULL" for a tension test, "PUSH" for a bend test.
 11. Turn ON the "GATHER DATA" button.
 12. Click the "WRITE TO FILE" button to "YES".
 13. Press "PRESSED TO GO" once. The ACF starts to move to load the specimen.
 14. The direction ("PUSH"/"PULL") and loading rate (dV/dt) may be changed at any time during the test.

15. To stop the test, first halt motion by hitting the "PRESSED TO GO" button to release it.
16. Click the "WRITE TO FILE" button off.
17. Jog the voice coil slowly towards so V_{out} becomes the same as the "home" value of V_{out} recorded in step 8f. This way, the specimen is under no load, and the ACF will not spring back when the clamps are released.
18. Loosen the clamps (in the case of a tension test) and/or remove the specimen.
19. Jog the voice coil again manually until V_{out} is close to 0.00. It is very important to ensure the output signal from the DAQ board is zero before powering off the voice coil; a non-zero signal will cause the voice coil to "jump" when powered off.
20. Power off the amplifier.
21. Change the filename entry in the VI, set $V_{out}(init)$ to 0.001 and briefly run the VI so that the output signal gets reset to zero.

D.2 Loading Rate Calculation

The voice coil is a force controlled actuator, *i.e.*, it converts its input signal, a current, into an output force (F_{VC}) with a transfer function K_{VC} of 21.33 N/A. In our case, the current is generated by an Aerotech 4020 Amplifier based on an input voltage signal. The transfer function (K_{amp}) of the amplifier is 2 A/V. The input signal for the amplifier is generated by the DAQ board according to the commands issued through the VI. The total force capacity of the actuator is around 86 N; 4 A is the maximum input current required by it. The amplifier, hence, requires a signal in the range 0 - 2 V. The DAQ has a range of ± 10 V. It is hence best to use a voltage divider to scale down the DAQ output in order to maximize resolution. The voltage divider has a transfer function K_{VD} of approximately 1:5. The net transfer function

of the system, relating an change in signal voltage to a change in voice coil force, is given (in rate form) by

$$\frac{dF_{VC}}{dt} = K_{VC} \times K_{amp} \times K_{VD} \times \frac{dV}{dt} \quad (D.1)$$

$$\approx 21.33 \times 2 \times 0.2 \frac{dV}{dt} \quad (D.2)$$

$$= 8.53 \frac{dV}{dt} \quad (D.3)$$

The approximate sign is used here because the transfer functions, especially that of the voltage divider, are approximate. This relation may be used to determine the dV/dt parameter to be used during a test for a desired rate of change of F_{VC} , or F_{TOT} in Fig. 2-5. When there is no specimen, *i.e.* when the voice coil is loading the ACF alone, the voltage signal rate dV/dt translates into a constant speed of the ACF (v_{ACF}), given by

$$v_{ACF} = \frac{1}{K_A} \times \frac{dF_{VC}}{dt} \quad (D.4)$$

$$\approx \frac{1}{4.59} \times 8.53 \frac{dV}{dt} \quad (D.5)$$

$$\approx 1.86 \frac{dV}{dt} \text{ mm/s} \quad (D.6)$$

This also tells us that a 1 V change in signal current may be expected to move the ACF by 1.86 mm in free travel.

D.3 Bill of Materials

Part #	Name	Material	Manufacturer	Cost(ea.)
GS1100-05	Finishing of Flexure Frame	Al 7075-T6	Ramco	\$875
GS0201-02	Frame Base	Al 6061	Ramco	\$210
GS0201-03	Frame Supports	Al 6061	Ramco	\$39
GS0201-04	Bearing Mount	Al 6061	Ramco	\$145
GS0201-04	Linear Slide Bearing		McMaster	\$210
GS0301-04	Voice Coil Mount	Al 6061	Ramco	\$60
GS0601-01	Foil Tension Grip (Bottom)	Al 7075	Ramco	\$60
GS0601-02	Foil Tension Grip (Top)	Al 7075	Ramco	\$50
GS0601-03	Fixture Nut Plate	Al 7075	Ramco	\$75
GS1100-03	Bowtie Tension Grip (Bottom)	Titanium	Ramco	\$75
GS1100-04	Bowtie Tension Grip (Top)	Titanium	Ramco	\$75
GS1100-01	Insulation Plate (Top)	Garolite G-7	Ramco	\$75
GS1100-02	Insulation Plate (Bottom)	Garolite G-7	Ramco	\$75
GS0601-06	Multi-Span Bend Fixture (Bottom)	Tool Steel	Ramco	\$225
GS0601-05	Bend Fixture (Top) ¹	Tool Steel	Ramco	\$180
GS0500-01	Local Sensor Mount	Al 6061	CMS	-
GS0500-02	Local Sensor Target	Al 6061	CMS	-
SMU9000	Inductive Transducer		Kaman	\$2240
5U Sensor	Inductive Sensor		Kaman	\$350
PS150	Power Supply		Kaman	\$175
LA25-42-000A	Voice Coil		BEI	\$450
PIC	Angle Bracket	Al 6061	PIC	\$8.00
33120A	Waveform Generator		Agilent	\$1203

Notes:

Ramco: Ramco Machine LLC, MA. <http://www.ramcomachine.com/>

CMS: MIT Central Machine Shop

McMaster: McMaster Supply Company, NJ. <http://www.mcmaster.com/>

Kaman: Kaman Instrumentation Inc., CO. <http://www.kamaninstrumentation.com/>

BEI: BEI Kimco Magnetics Division, CA. <http://www.beikimco.com/>

PIC: PIC Design Co. <http://www.pic-design.com/>

Agilent: Agilent Test & Measurement Instruments, CA. <http://www.tm.agilent.com>

D.4 Specifications

- Load Cell Flexure (LCF) length: 50 mm
- LCF fillet radius: 4 mm
- LCF web thickness: 1 mm
- Actuator Flexure (ACF) length: 85 mm
- ACF fillet radius: 4 mm
- ACF web thickness: 1 mm
- Out of plane system thickness: 12.7 mm (0.5 in)
- LCF stiffness (Calibrated): 21.85 N/mm
- ACF stiffness (Calibrated): 4.589 N/mm
- Material of flexures: Aluminum Alloy 7075-T6
- LCF travel range: 0-1.6mm
- ACF travel range: 6 mm
- Displacement sensors: Kaman Instrumentation Inc. Model SMU9000-5U 2 Channels

Range: 0-1.25 mm

Offset: 0.1 mm

Output signal: ± 5 V

Resolution with DAQ system: 20nm

- Data acquisition: National Instruments PCI 6035E 16 bit 16Channel System
- Actuation: BEI Kimco Voice Coil LA25-42-000A [Force Control]

Range: ± 12.7 mm

Actuator force constant: 21.33 N/Amp

Max continuous stall force: 86 N

Control (Quasistatic): Aerotech 4020 linear amplifier @ 2Amp/Volt

Control (Cyclic): Agilent 33120A Waveform/Arbitrary Function

Generator

System specifications:

- Load Range/Resolution: 0-35 N / 0.45 μ N
- Displacement Range/Resolution: 0-1.25 mm / 20 nm
- Extended Displacement Range : ± 12.7 mm
- Space for specimen and grips (Nominal): 70 x 15 x 10 mm³
- Available grips and fixtures: Foil tension grips, 3 and 4 point fixtures, multiple span bending fixture, thermal-electrical insulation grips (up to 220 °C).

Appendix E

High Load Testing Machine: Technical Drawings

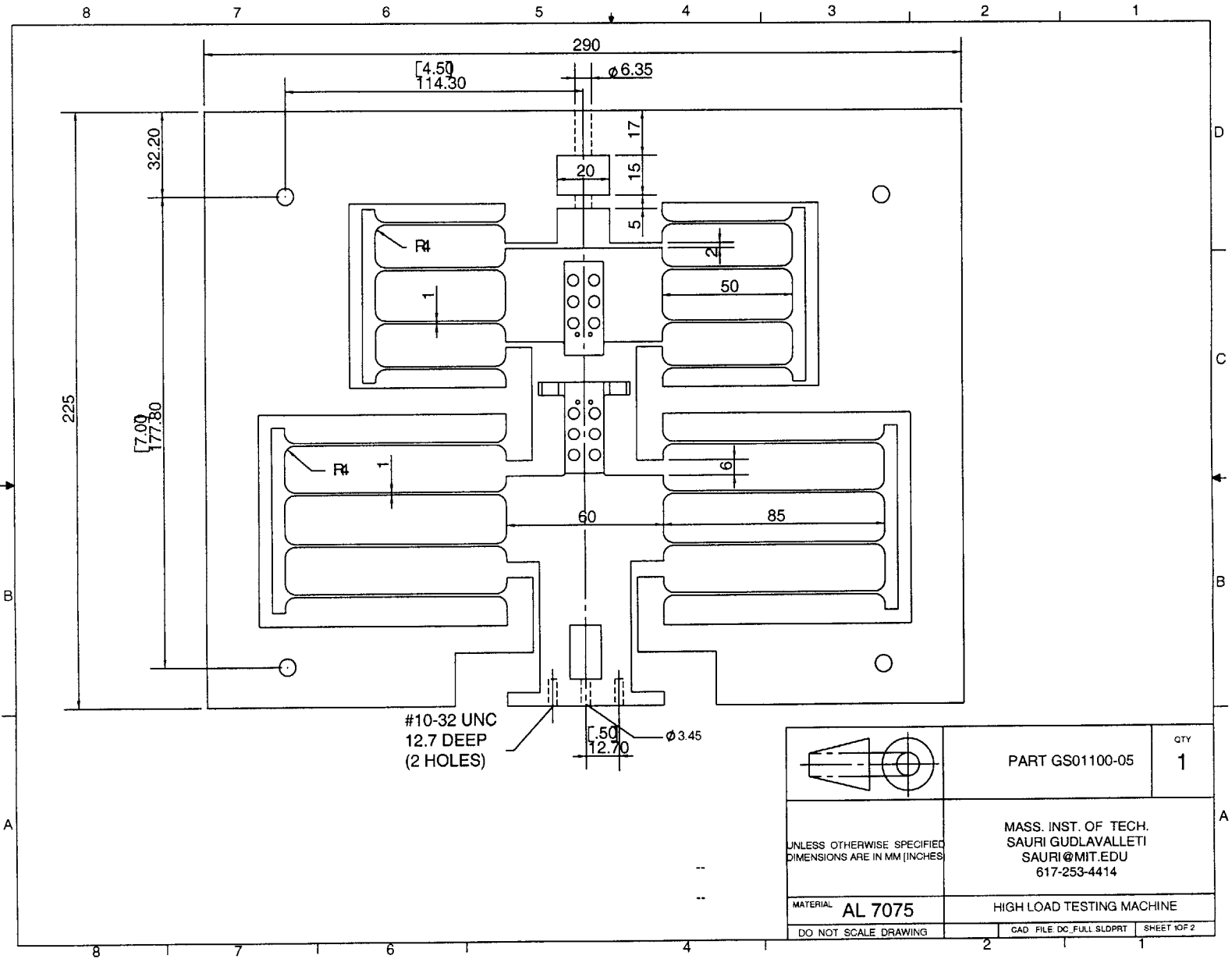
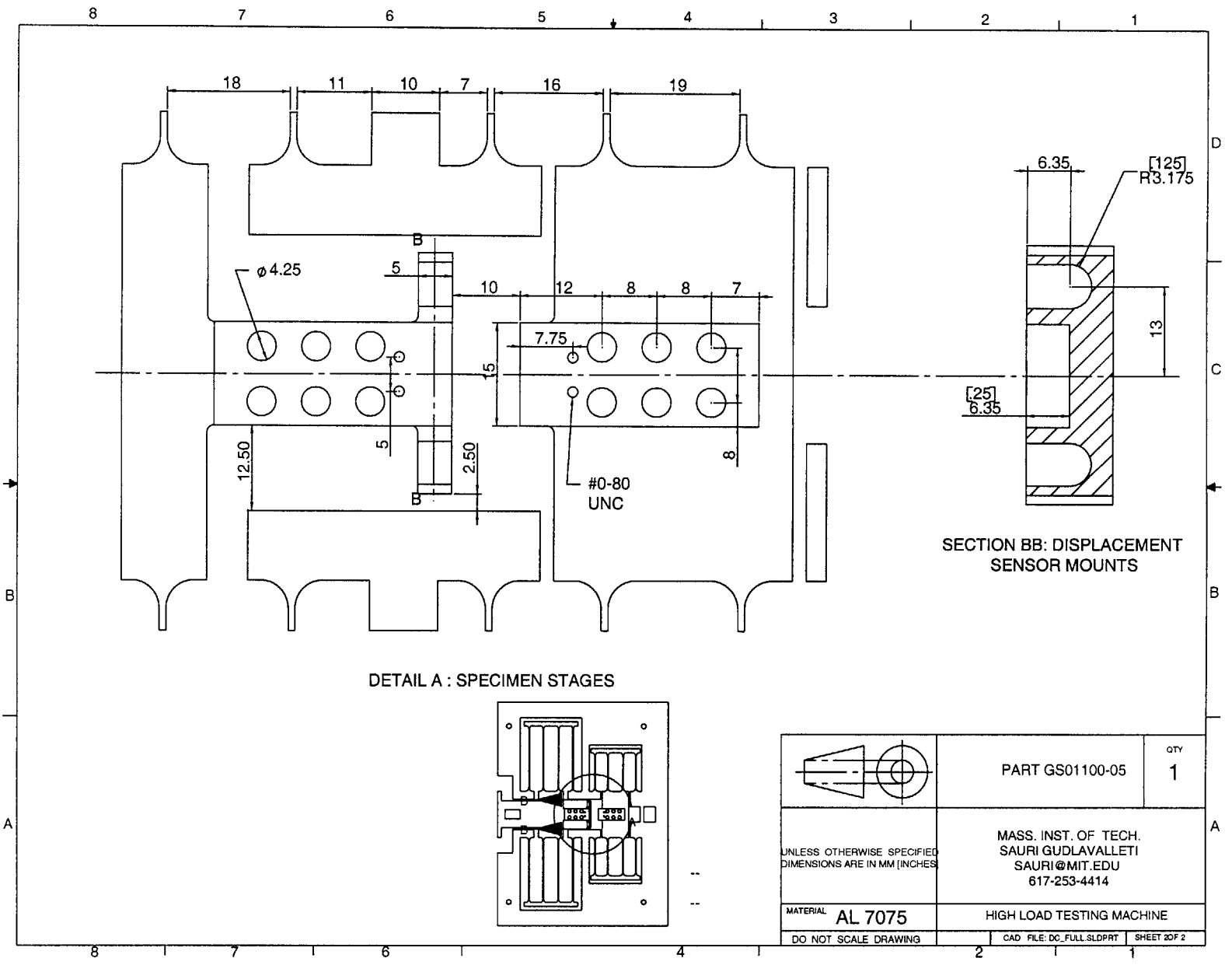


Figure E-1: Part GS 1100-05. High load testing machine flexure frame (Sheet 1 of 2)

Figure E-2: Part GS 1100-05. High load testing machine flexure frame (Sheet 2 of 2)



	PART GS01100-05	QTY 1
UNLESS OTHERWISE SPECIFIED DIMENSIONS ARE IN MM (INCHES)	MASS. INST. OF TECH. SAURI GUDLAVALLETI SAURI@MIT.EDU 617-253-4414	
MATERIAL AL 7075	HIGH LOAD TESTING MACHINE	
DO NOT SCALE DRAWING	CAD FILE: DC_FULL.SLDPRT	SHEET 2 OF 2

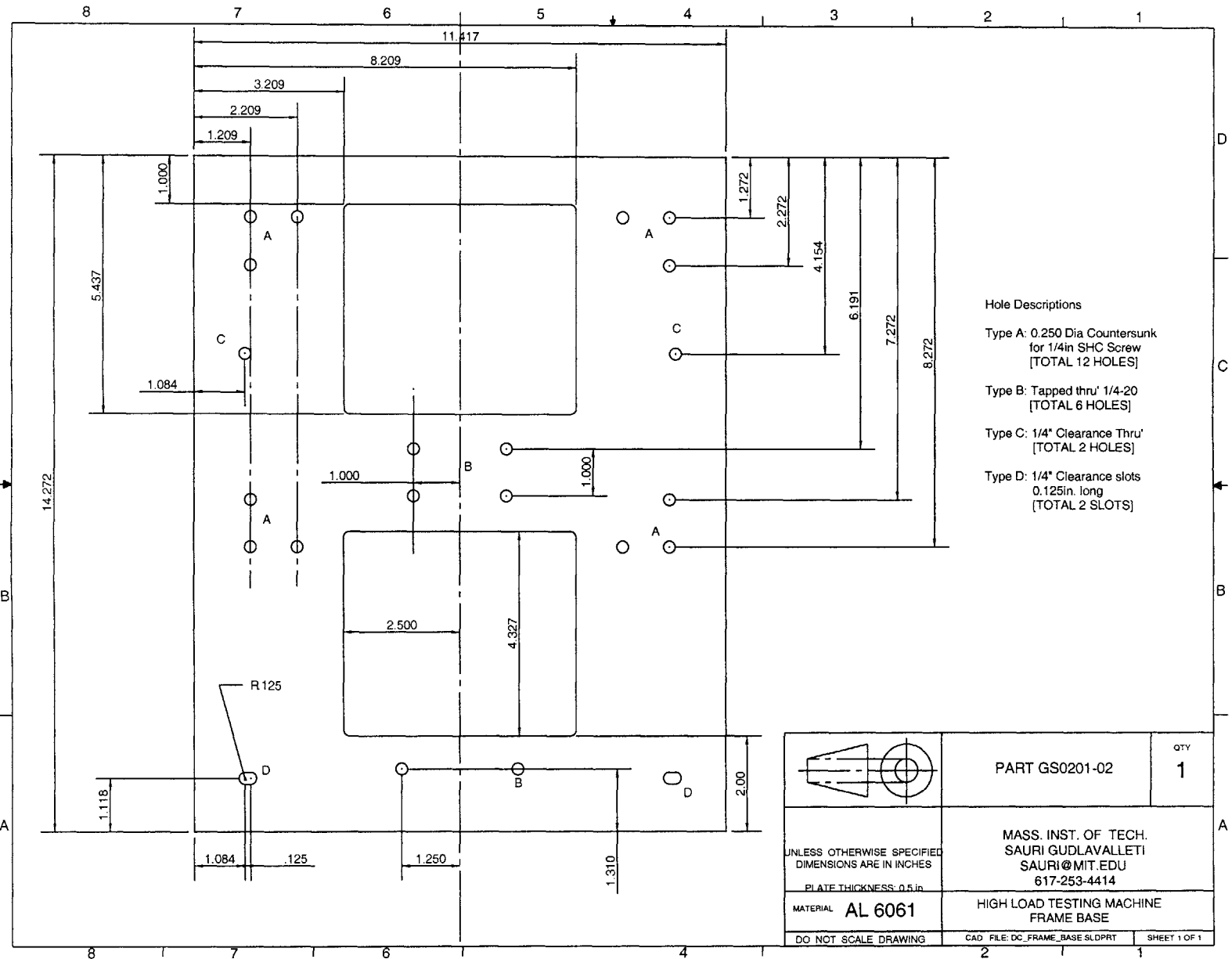
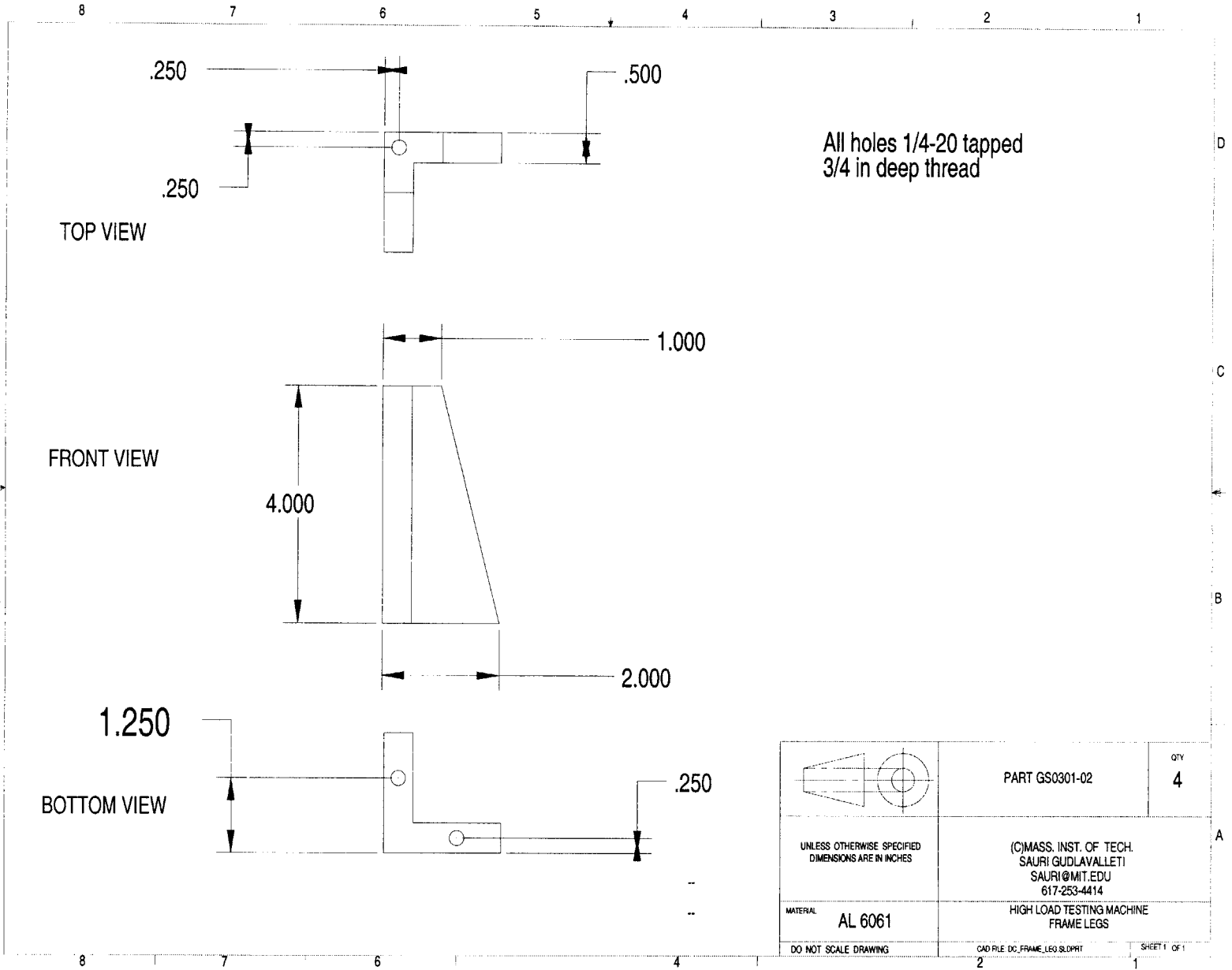


Figure E-3: Part GS 0201-02. High load testing machine frame base plate

Figure E-4: Part GS 0201-03. High load testing machine frame support stand-offs



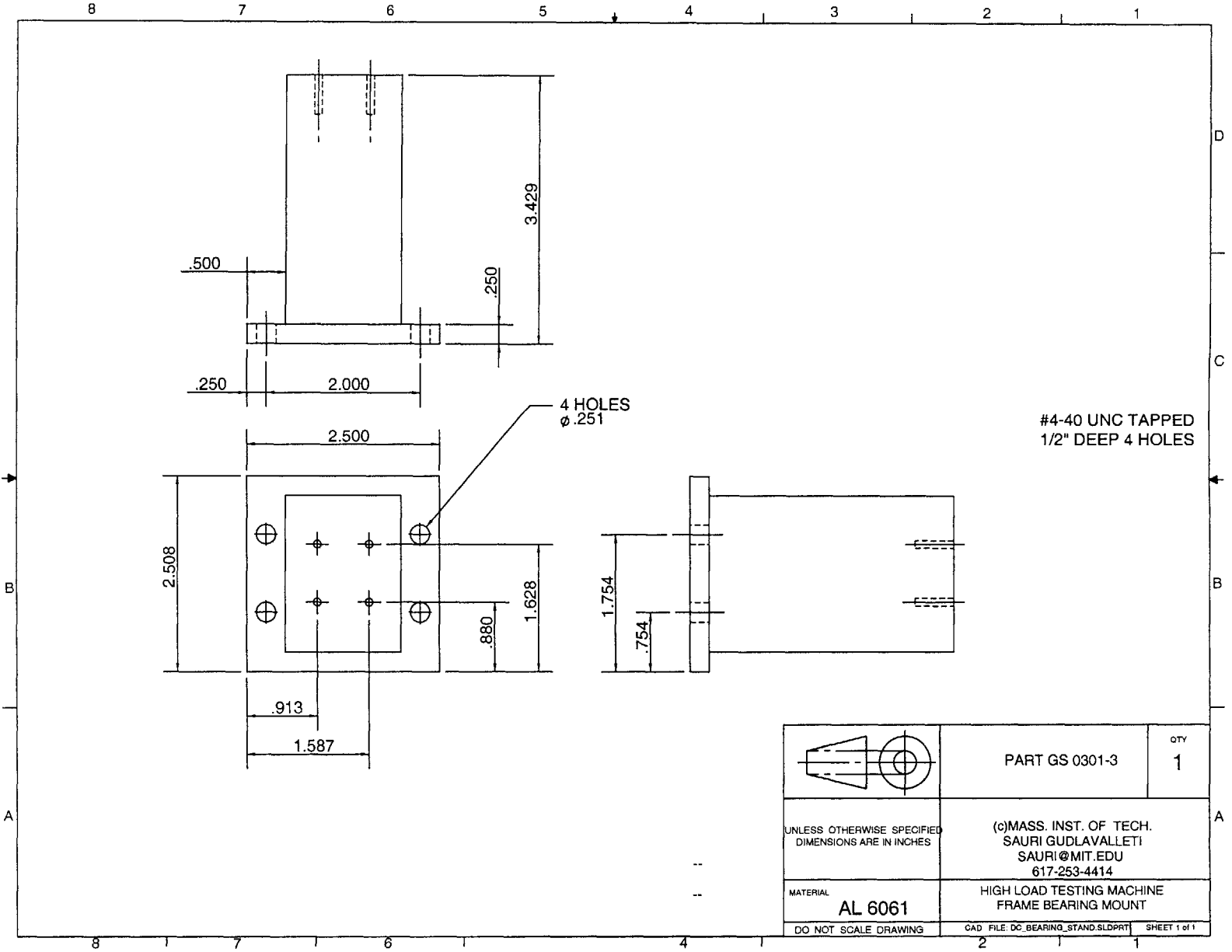


Figure E-5: Part GS 0201-04. High load testing machine bearing mount

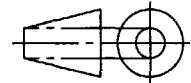
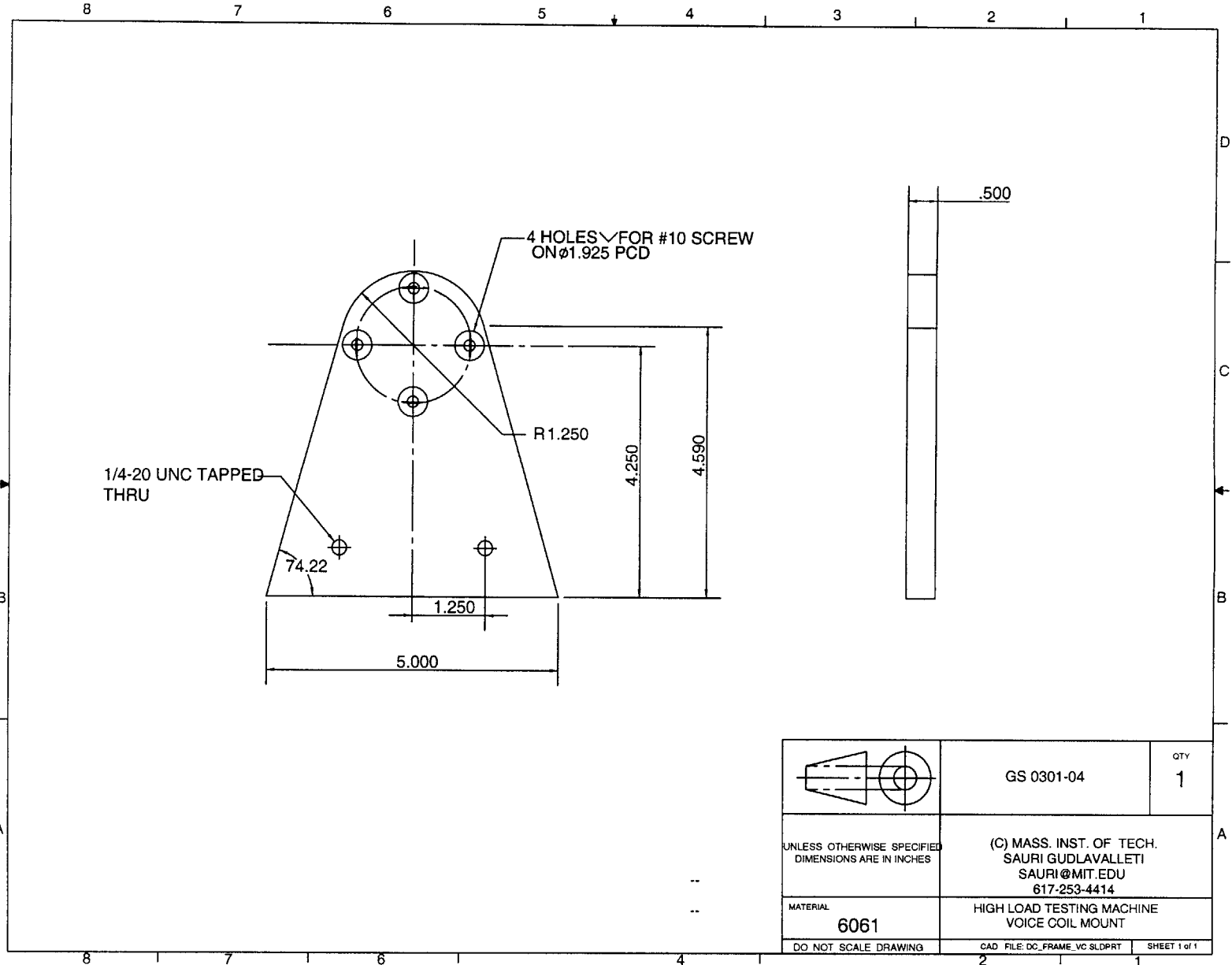
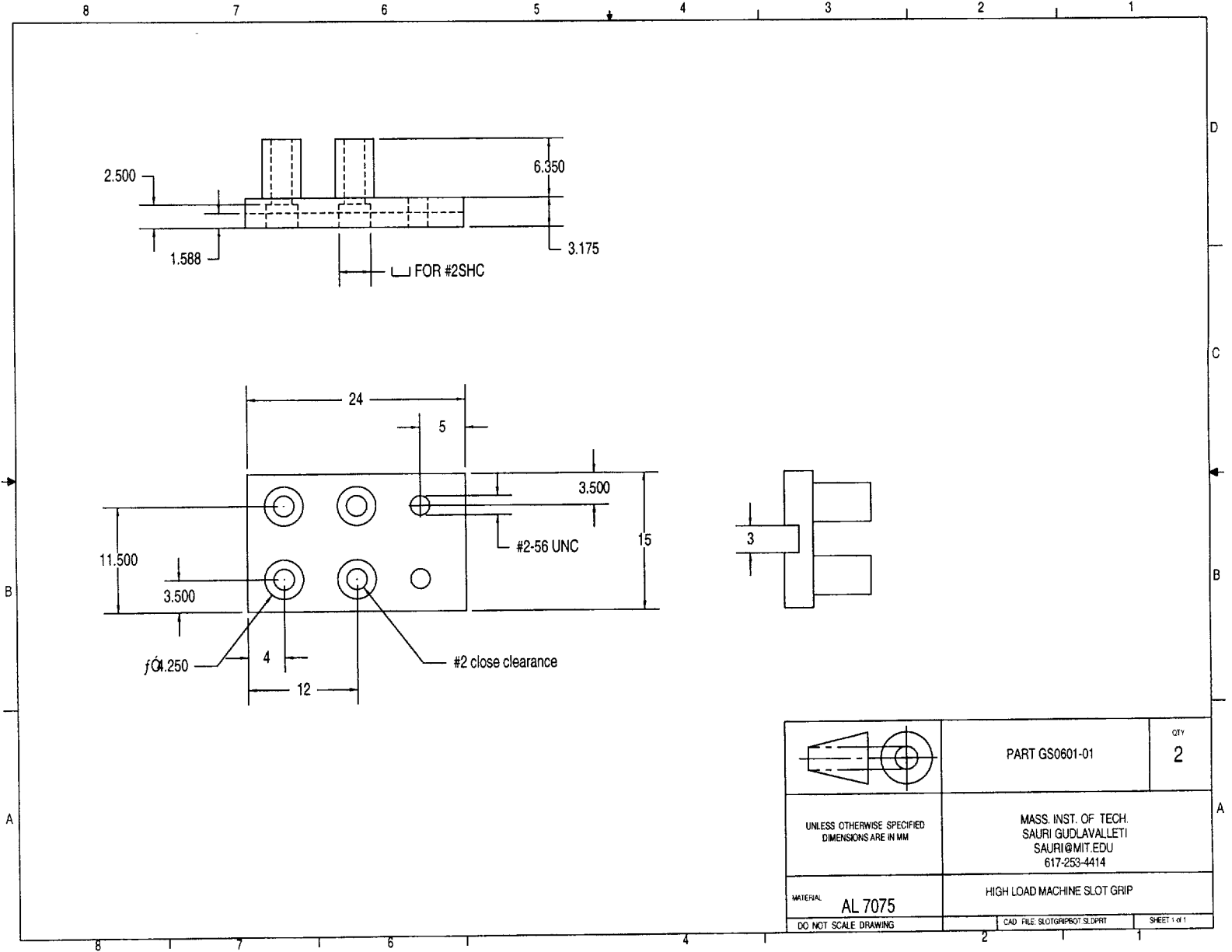
	<p>PART GS 0301-3</p>	<p>QTY 1</p>
<p>UNLESS OTHERWISE SPECIFIED DIMENSIONS ARE IN INCHES</p>		<p>(c)MASS. INST. OF TECH. SAURI GUDLAVALLETI SAURI@MIT.EDU 617-253-4414</p>
<p>MATERIAL AL 6061</p>	<p>HIGH LOAD TESTING MACHINE FRAME BEARING MOUNT</p>	
<p>DO NOT SCALE DRAWING</p>	<p>CAD FILE: DC_BEARING_STAND.SLDPRT</p>	<p>SHEET 1 of 1</p>

Figure E-6: Part GS 0301-04. High load testing machine voice coil mount





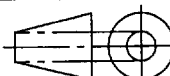
	PART GS0601-01	QTY 2
UNLESS OTHERWISE SPECIFIED DIMENSIONS ARE IN MM	MASS. INST. OF TECH. SAURI GUDLAVALLETI SAURI@MIT.EDU 617-253-4414	
MATERIAL AL 7075	HIGH LOAD MACHINE SLOT GRIP	
DO NOT SCALE DRAWING	CAD FILE SLOTGRIP01.SLDPR1	SHEET 1 of 1

Figure E-7: Part GS 0601-01. Foil tension grip (bottom grip). Ref. Fig. 4-3 for an assembly drawing

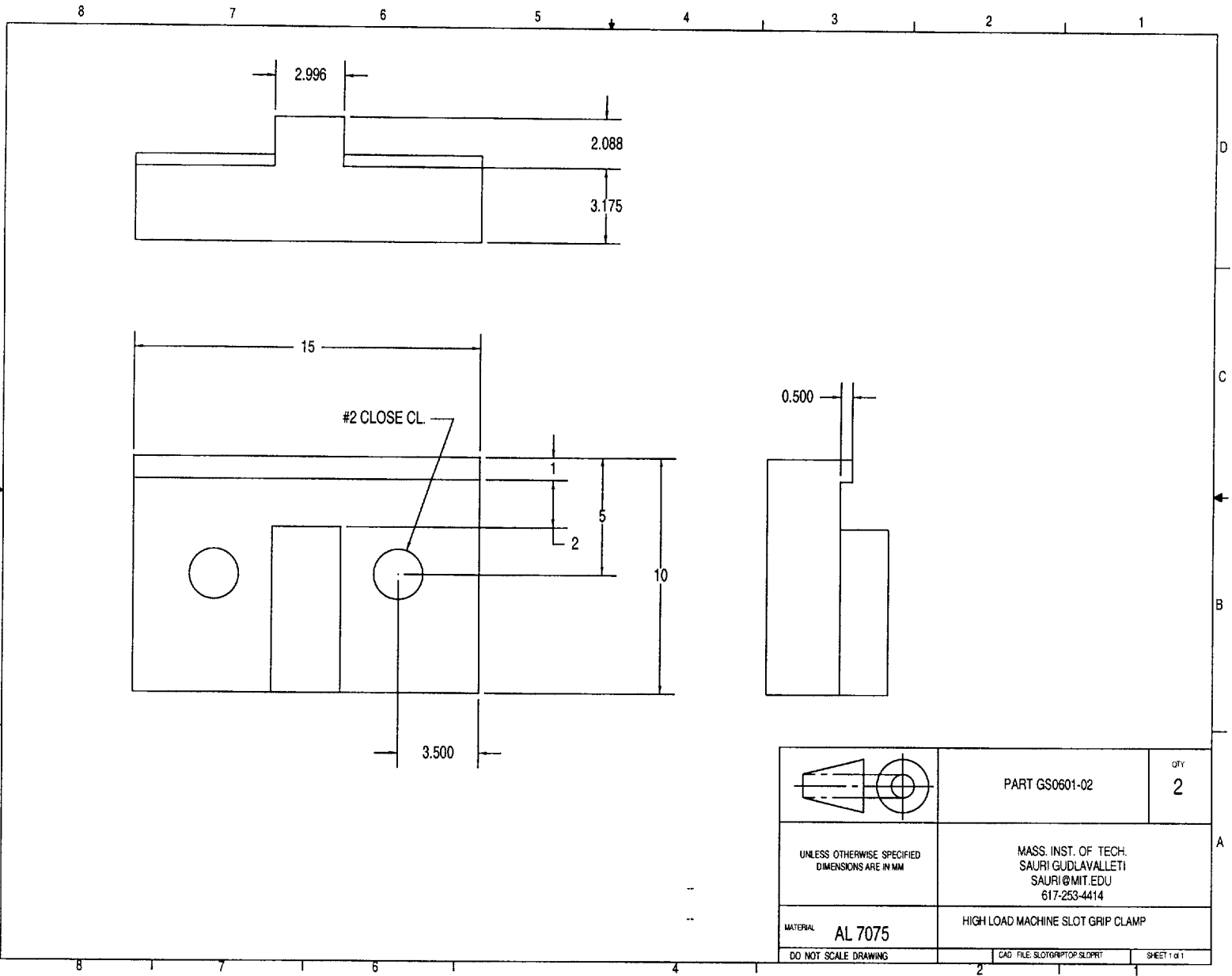
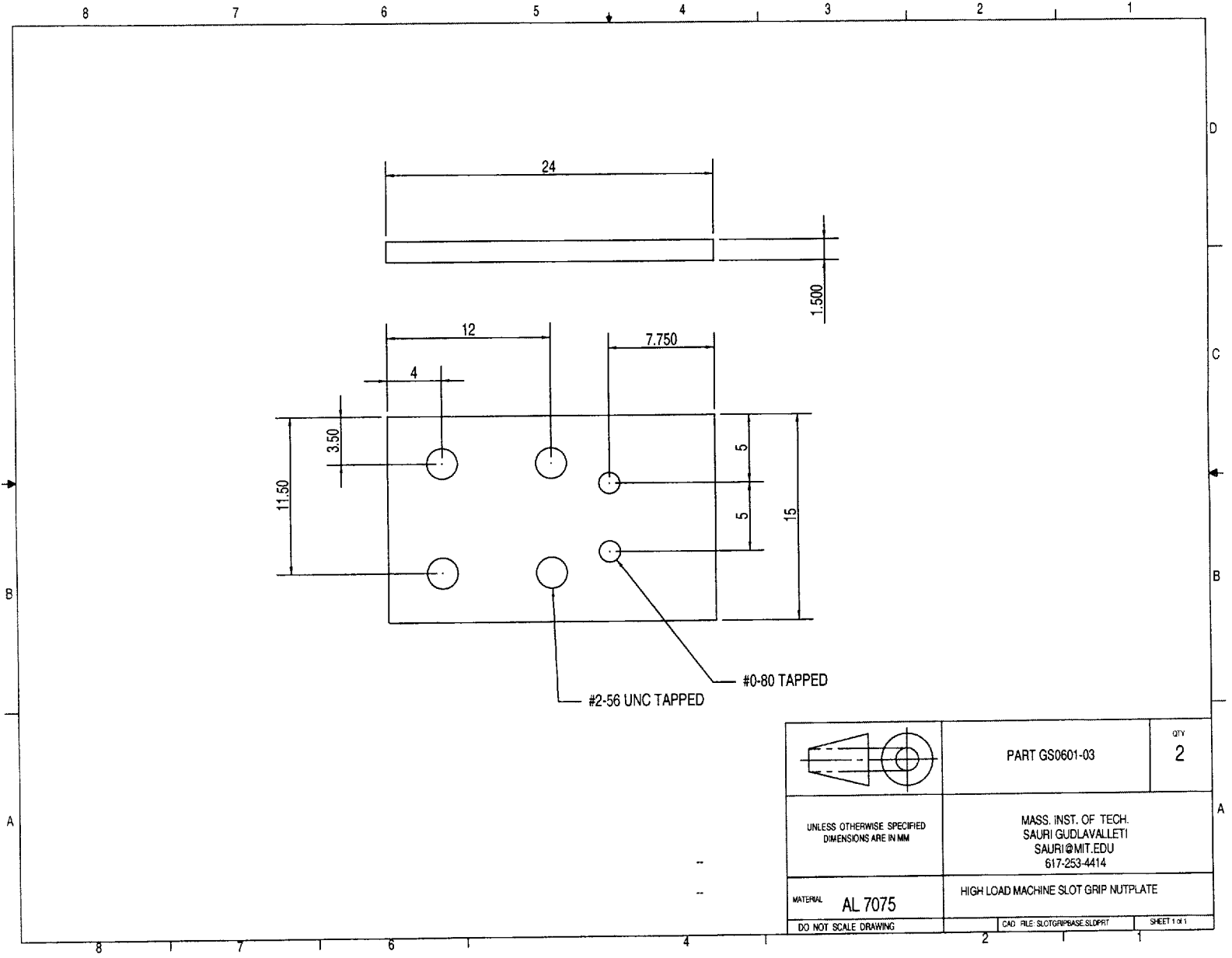


Figure E-8: Part GS 0601-02. Clamp for foil tension grip. Ref. Fig. 4-3 for an assembly drawing



#2-56 UNC TAPPED
#0-80 TAPPED

	<p>PART GS0601-03</p>	<p>QTY 2</p>
<p>UNLESS OTHERWISE SPECIFIED DIMENSIONS ARE IN MM</p>	<p>MASS. INST. OF TECH. SAURI.GUJLAVALLETI SAURI@MIT.EDU 617-253-4414</p>	
<p>MATERIAL AL 7075</p>	<p>HIGH LOAD MACHINE SLOT GRIP NUTPLATE</p>	
<p>DO NOT SCALE DRAWING</p>	<p>CAD FILE: SLOGRIPBASE.SLDPRT</p>	<p>SHEET 1 of 1</p>

Figure E-9: Part GS 0601-03. Nutplate for grips and fixtures

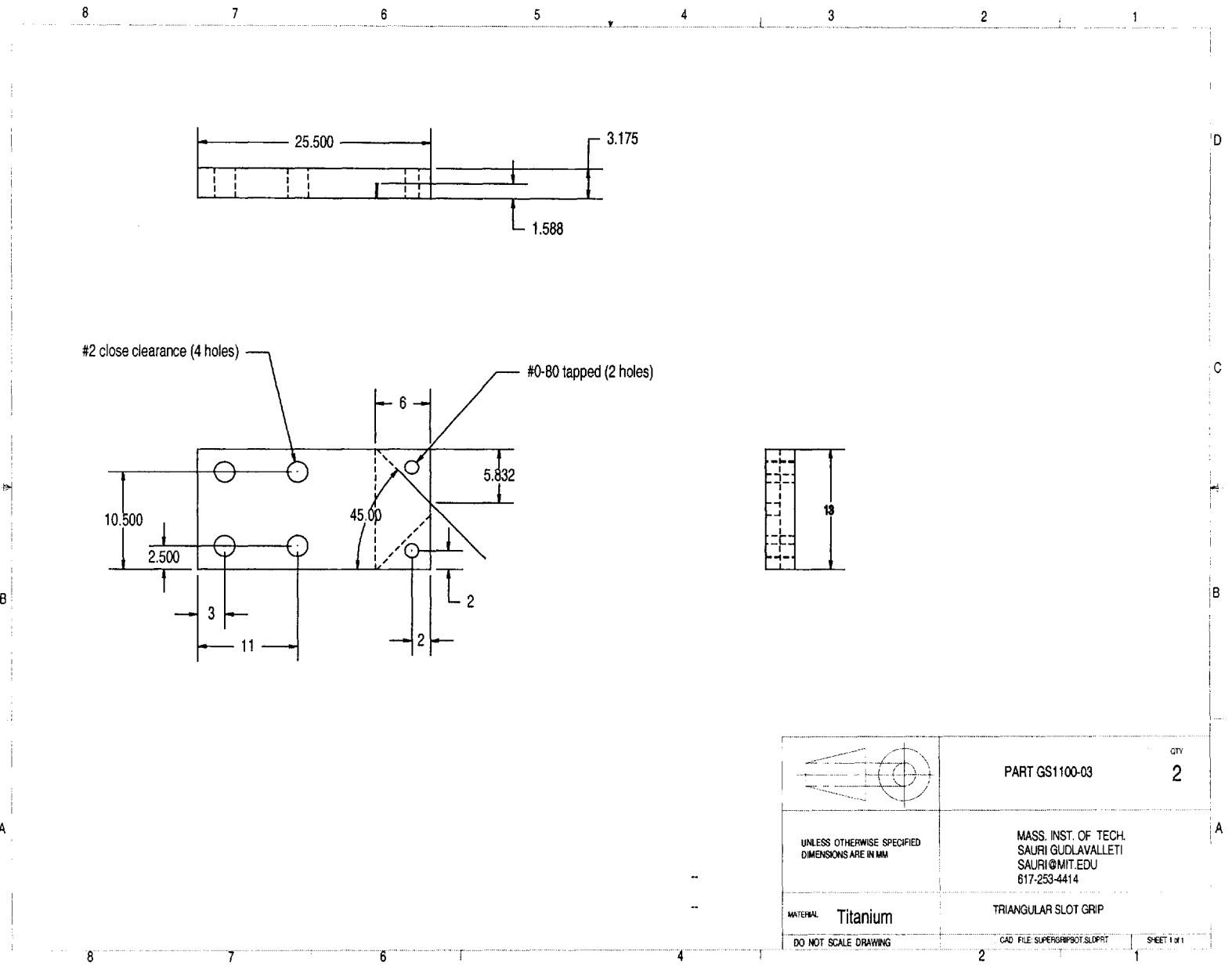


Figure E-10: Part GS 1100-03. Grip for bowtie shaped tension specimen. These grips need to be used in association with Part. GS1100-01 or GS0601-01. Ref. Fig. 4-4 for an assembly drawing.

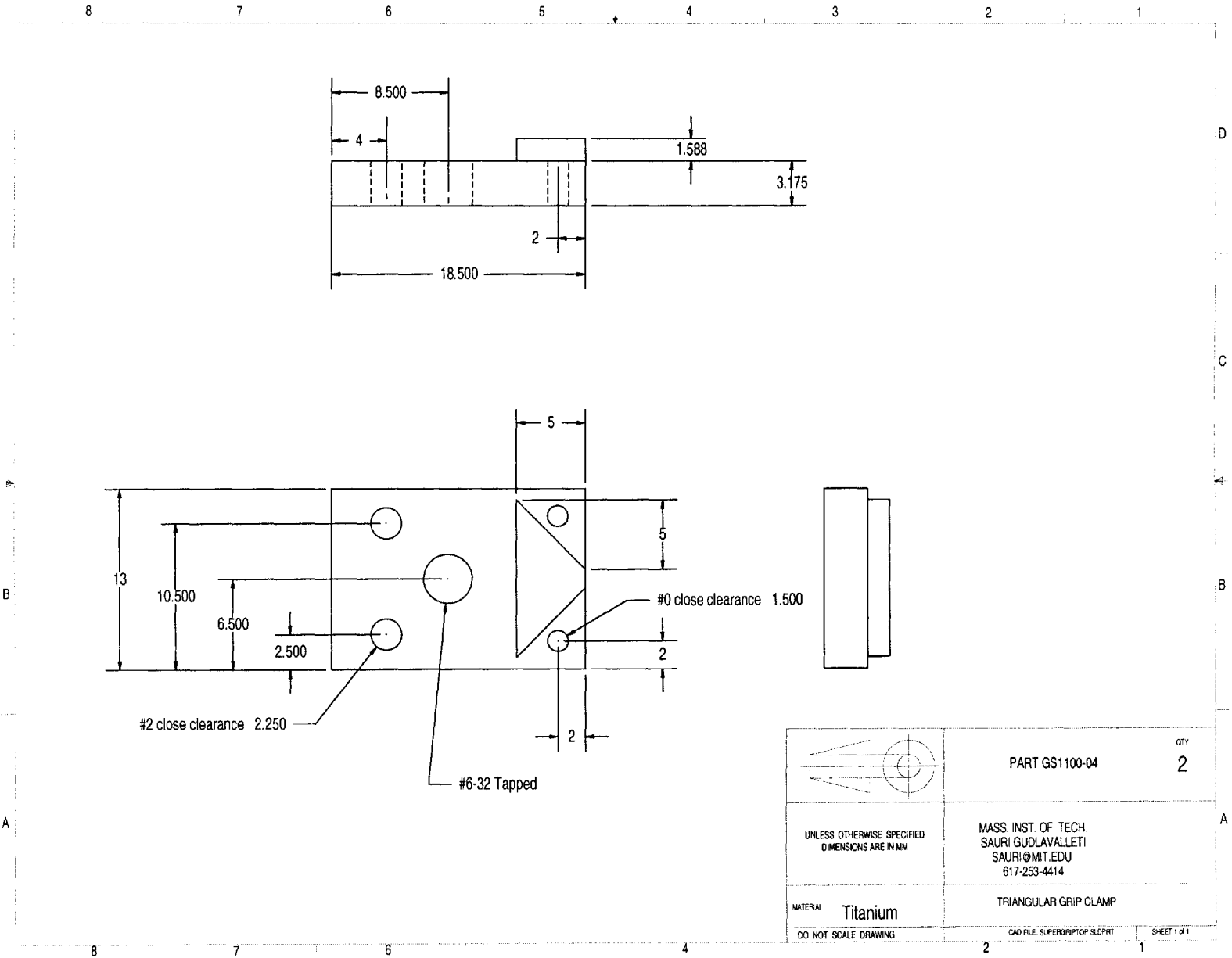


Figure E-11: Part GS 1100-04. Clamp for bowtie shaped tension specimen. These grips need to be used in association with Part. GS1100-01 or GS0601-01. Ref. Fig. 4-4 for an assembly drawing.

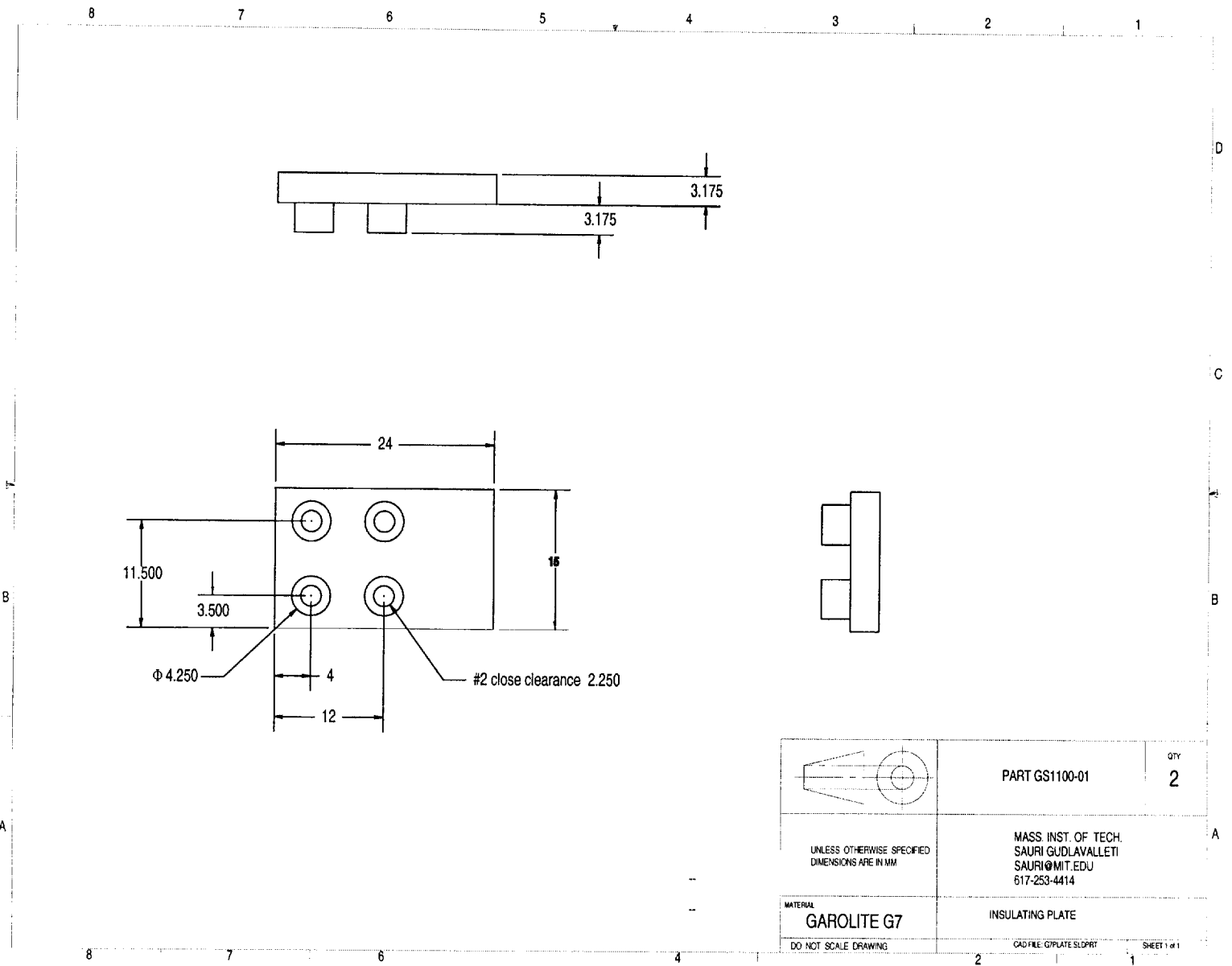


Figure E-12: Part GS 1100-01. Insulation plate for use with Part GS1100-03, 04 or other appropriately designed grips. Ref. Fig. 4-4 for an assembly drawing.

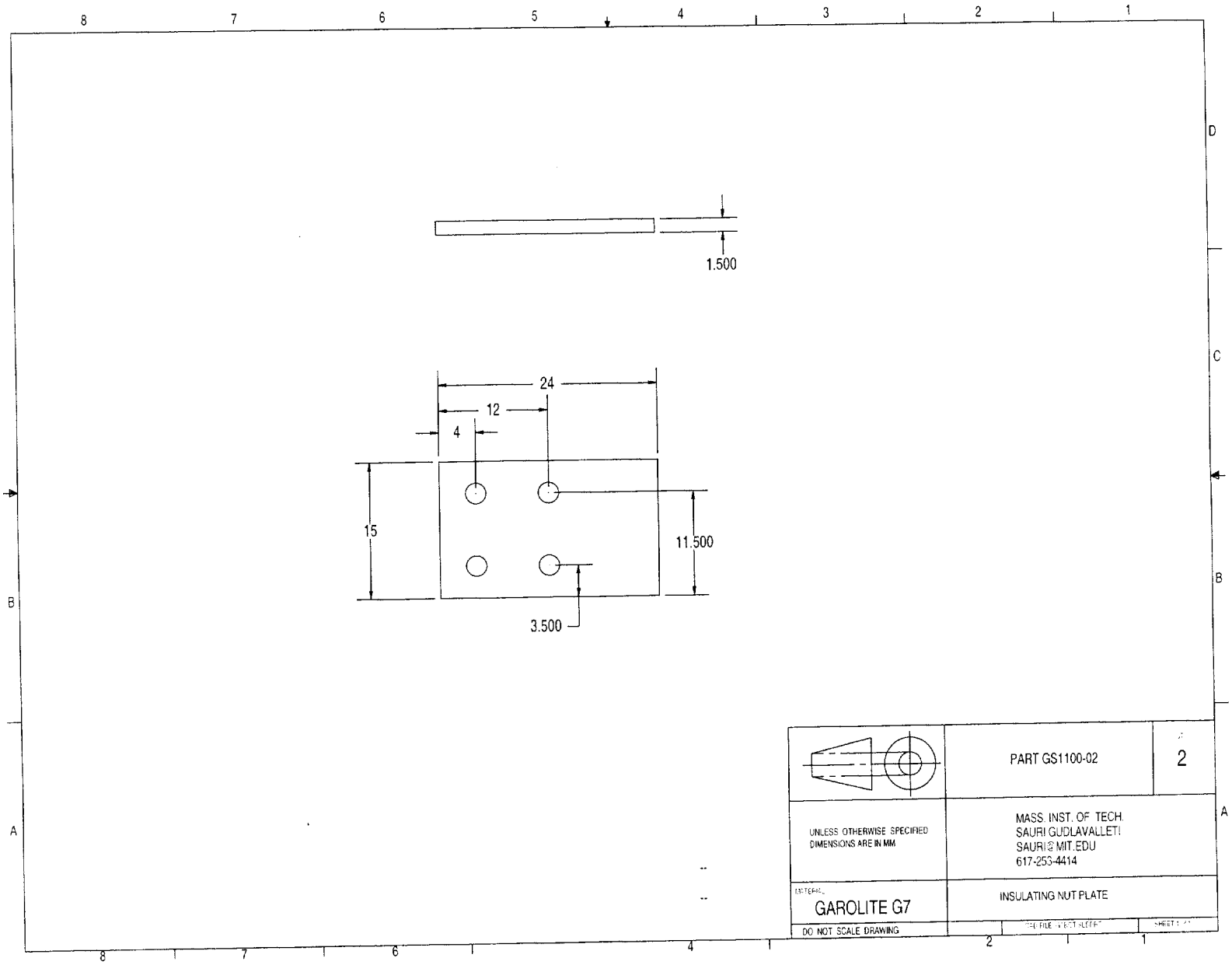


Figure E-13: Part GS 1100-02. Insulating nut-plate for use with Part GS1100-03, 04 or other appropriately designed grips. Ref. Fig. 4-4 for an assembly drawing.

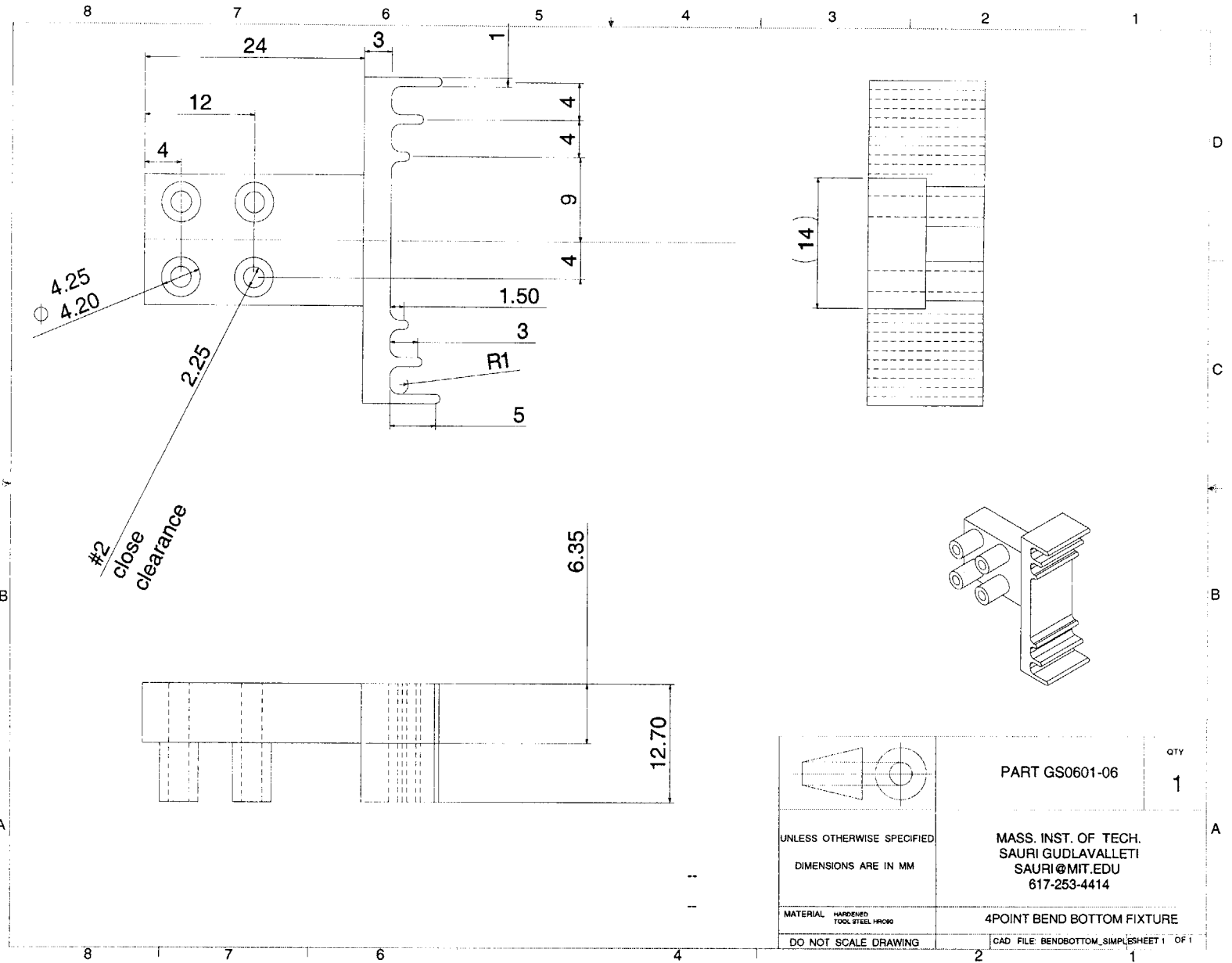


Figure E-14: Part GS 0601-06. Multiple span bending fixtures. Ref. Fig. 4-6 for an assembly drawing.

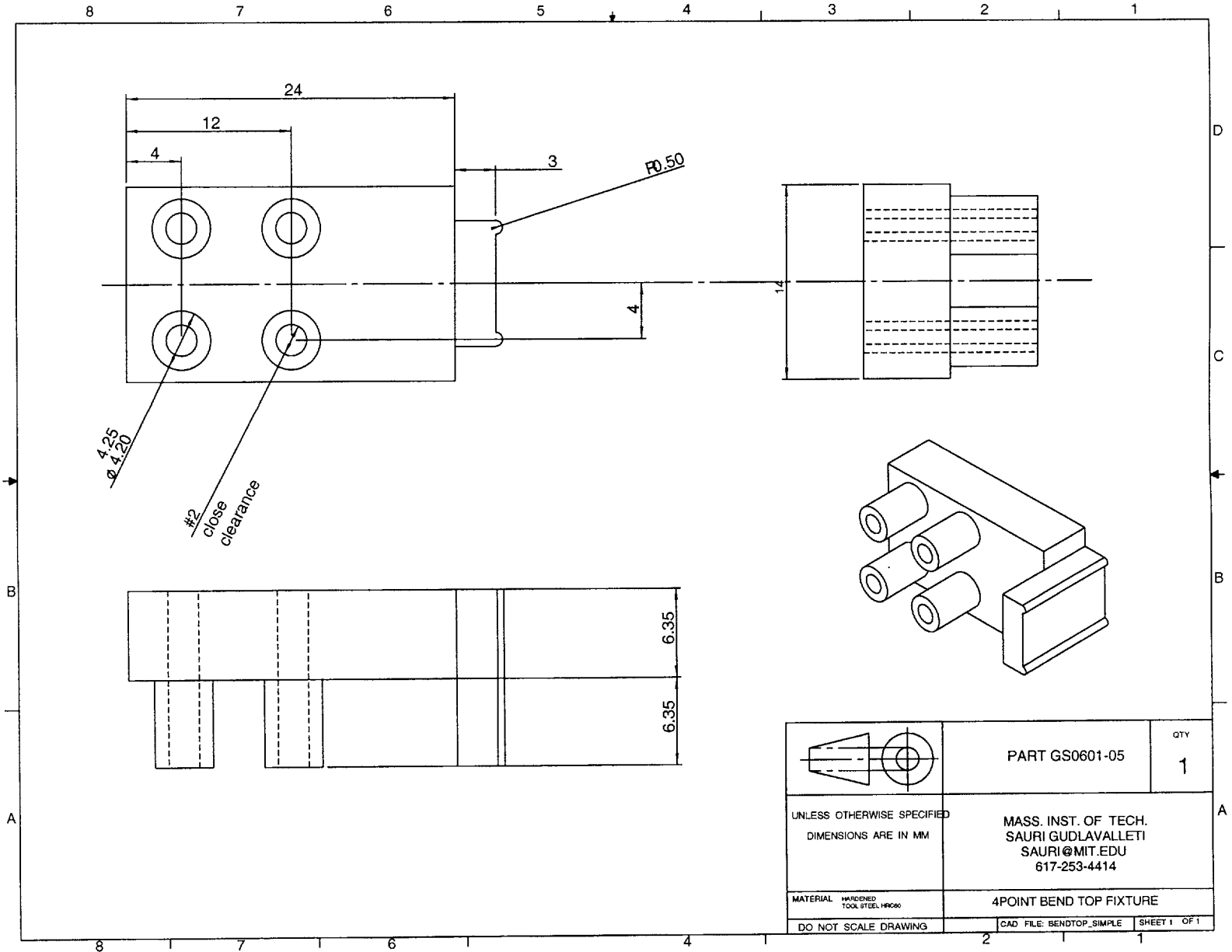


Figure E-15: Part GS 0601-05. 4 Point bend fixture with 8 mm span for use in the multiple span bending fixtures. Ref. Fig. 4-6 for an assembly drawing.

	<p>PART GS0601-05</p>	<p>QTY 1</p>
<p>UNLESS OTHERWISE SPECIFIED DIMENSIONS ARE IN MM</p>	<p>MASS. INST. OF TECH. SAURI GUDLAVALLETI SAURI@MIT.EDU 617-253-4414</p>	
<p>MATERIAL HARCENED TOOL STEEL HRC60</p>	<p>4POINT BEND TOP FIXTURE</p>	
<p>DO NOT SCALE DRAWING</p>	<p>CAD FILE: BENDTOP_SIMPLE</p>	<p>SHEET 1 OF 1</p>

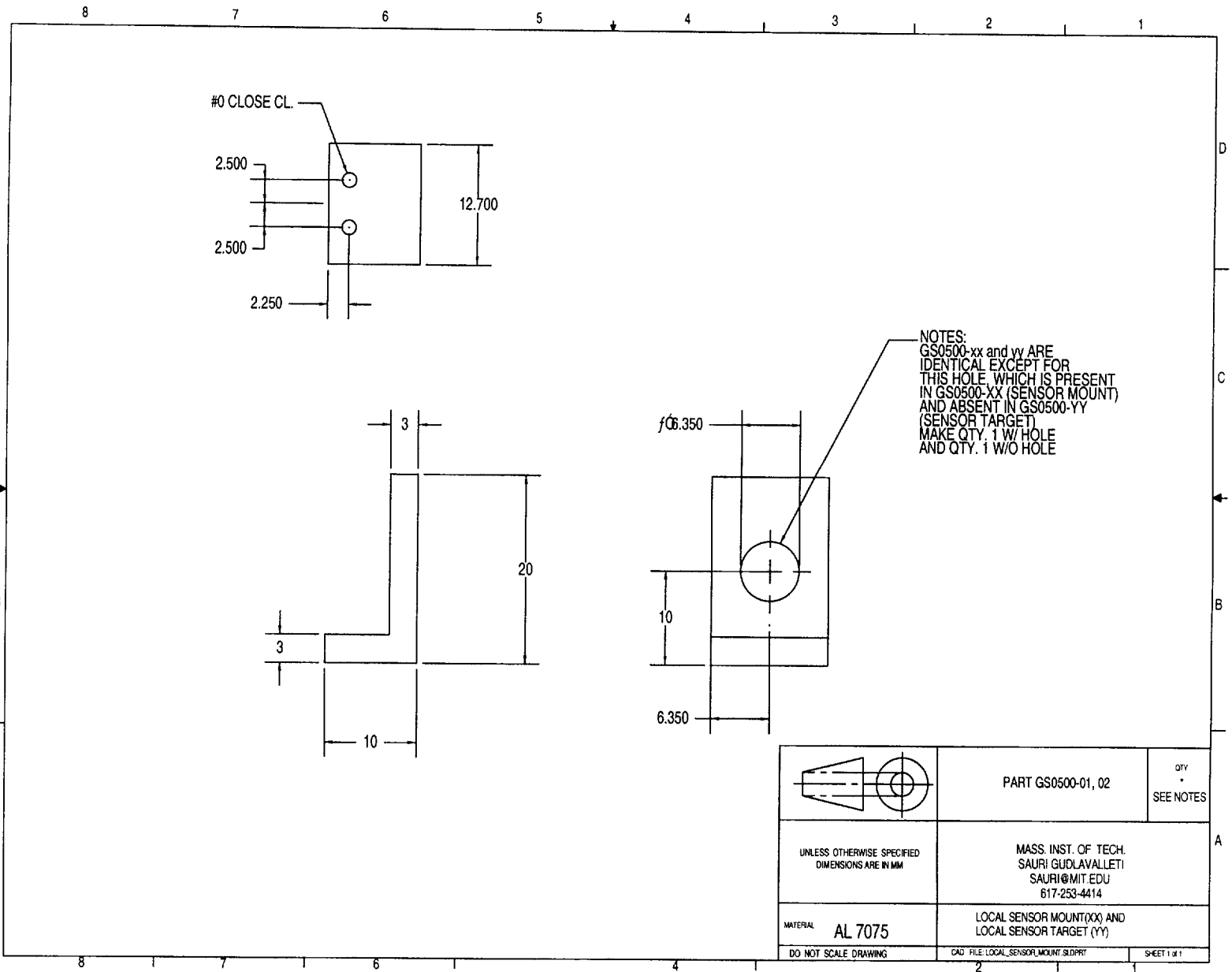


Figure E-16: Part GS 0500-01 and 02. Fixtures to mount displacement sensors locally on the specimen stages, for example, in the multispin bend fixtures, when the fixture blocks the designated sensor mount. Ref. Fig. 4-6 for an assembly drawing.

E.1 Fabrication of Free Standing Gold Thin Films

Free-standing gold thin film specimens were fabricated at MIT's Microsystems technologies laboratories (MTL). Fig. 5-4 is a dimensioned drawing of the tensile specimen. Each specimen has over-all dimensions of 16 mm x 8 mm. The specimens were arranged in an array as shown in Fig. E-17. Thirty seven specimens were prepared from each 4" wafer. Two masks were used. The drawings used for the masks are shown in Figs. E-18 and E-19. In both the figures, the hatched regions are darkfield. For the backside mask, the light lines indicate the pattern expected on the front side after anisotropic etching along the $\{111\}$ planes. The etching occurs at an angle 54.7° to the plane of the wafer. Dimensions shown in Fig. 5-4 apply to these light lines, the final front side product. The mask is hence designed assuming a $354 \mu\text{m}$ offset. The depth of the groove between two unit cells is $250 \mu\text{m}$, which requires a groove width of $354 \mu\text{m}$. This requires a $177 \mu\text{m}$ offset in the mask edge with respect to the unit cell boundaries, as shown in Fig. E-18. The front side mask, shown in Fig. E-19, is designed with no dimensional offset from those in Fig. 5-4.

The steps used in fabricating the specimens are:

1. Wafer cleaning: RCA clean double side polished wafers.
2. Nitride deposition: Deposit 2044 \AA thick layer of Si_3N_4 . Silicon nitride is used as an etch-stop since it is resistant to etching by KOH, which will be used to etch silicon to release the gold film at a later step.
3. Photoresist coating: Spin coat "back side" of wafer with $10 \mu\text{m}$ of standard resist, and then pre-bake for 30 minutes.
4. Exposure: Expose the coated side under the back side mask for 2.5 seconds under soft contact (Fig. E-20).
5. Developing: Develop exposed side in OCG 934 1:1 developer. Spin rinse, spin dry, inspect and postbake for 30 mins. The regions exposed under the mask are now stripped of photoresist.

6. Nitride removal: Dry etch nitride exposed by pattern in photoresist by backside mask..

The pattern on the backside with windows for releasing gold film and grooves for separating individual specimens is ready. It now remains to deposit and pattern gold thin film on the front side, followed by finally etching away all the silicon under the gold specimens to release them free-standing.

7. Photoresist coating: Repeat step 3 on the other side of the wafer (“front side”).
8. Exposure: Expose the front side under the front side mask for 1 second. The frontside pattern is to be aligned to the backside pattern. The alignment marks in the backside pattern can be viewed from the front side by shining infrared light through the wafer; the frontside mask can then be appropriately positioned.
9. Develop front side with image reversal developer AZ-5214 E. This causes the regions of the photoresist blocked by the mask to strip, leaving dogbone shaped regions exposed in the photoresist.
10. Deposition of metal layer: E-beam deposit 200 Å of titanium as an adhesion promoter followed by 8000 Å (nominal thickness) of gold.
11. Lift-off: Treat wafers with acetone in ultrasound. The acetone attacks the photoresist under the gold and lifts off the gold layer above along with it. The gold only remains in regions where the photoresist has been previously removed during step 9. This leaves dogbone shaped specimens of gold (Fig. E-21).
12. Thin film release: The penultimate step is to etch away the silicon under the gold dogbones and release them. This is done by anisotropic etching using KOH, which exposes the $\langle 111 \rangle$ planes in silicon while etching; the walls of the etched silicon are at an angle of 54.7° to the plane of the wafer. This must be taken into account while designing the masks. The wafers are held in a chuck that exposes only the backside of the wafers to ensure that none of the etchant

attacks the front side. The etch is performed in an solution of 1500 grams of KOH in 6000 ml of water continuously agitated at 80°C. These optimal etch conditions are determined by trial and error. The nitride layer on the front side of the wafer stops the etchant from attacking the front side once the silicon is etched through the thickness of the wafer. A post KOH clean is performed before the next step (Fig. E-22).

13. Nitride removal: The gold specimens now rest on the layer of nitride on the front side of the wafer. The nitride is etched using chemical etching for 760 seconds at an etch rate of 2.5 Å/s at room temperature (25 °C). The final specimen is shown in Fig. E-23

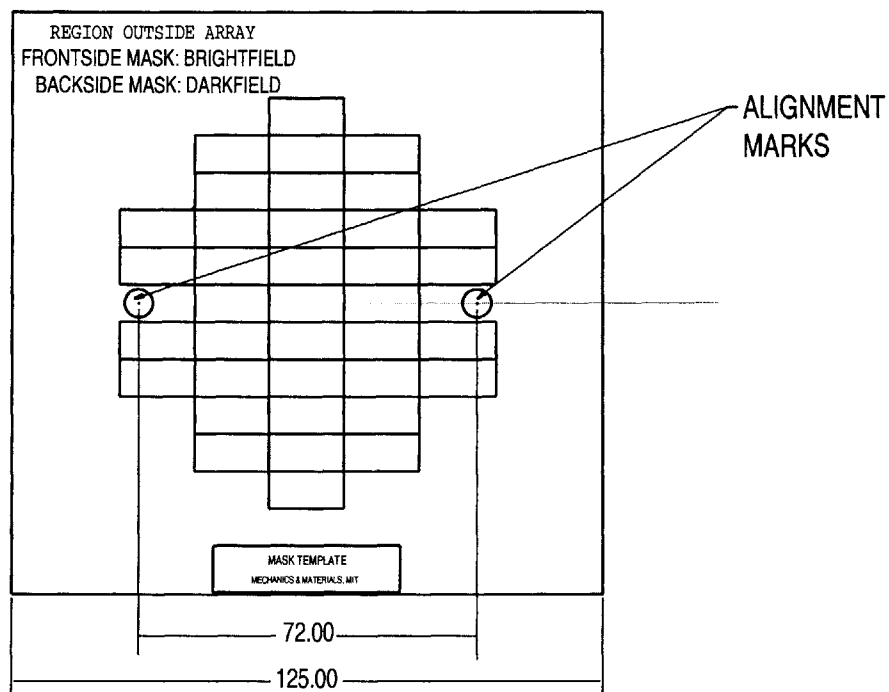


Figure E-17: Arrangement of tensile specimens on a 4" wafer

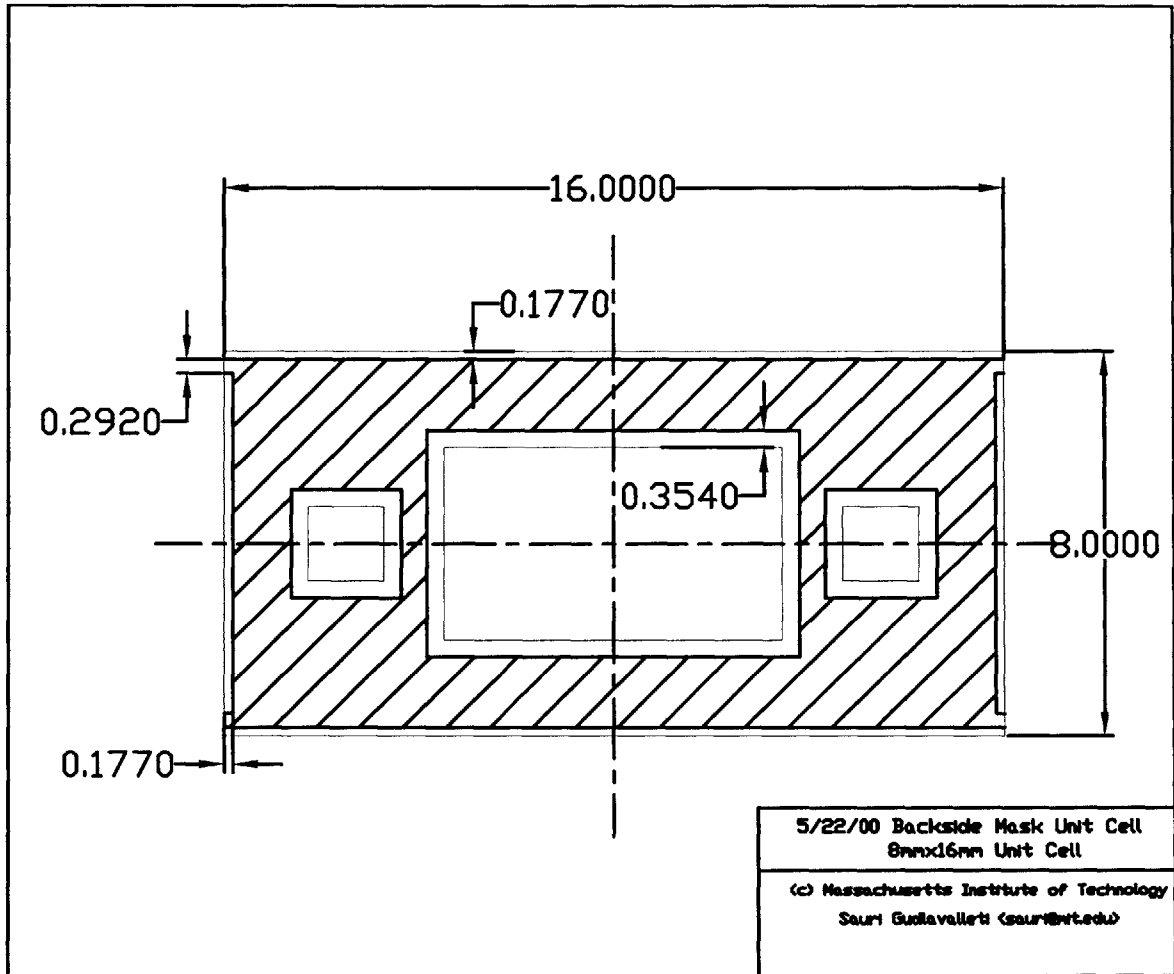


Figure E-18: Unit cell for backside mask. Dimensions are in mm.

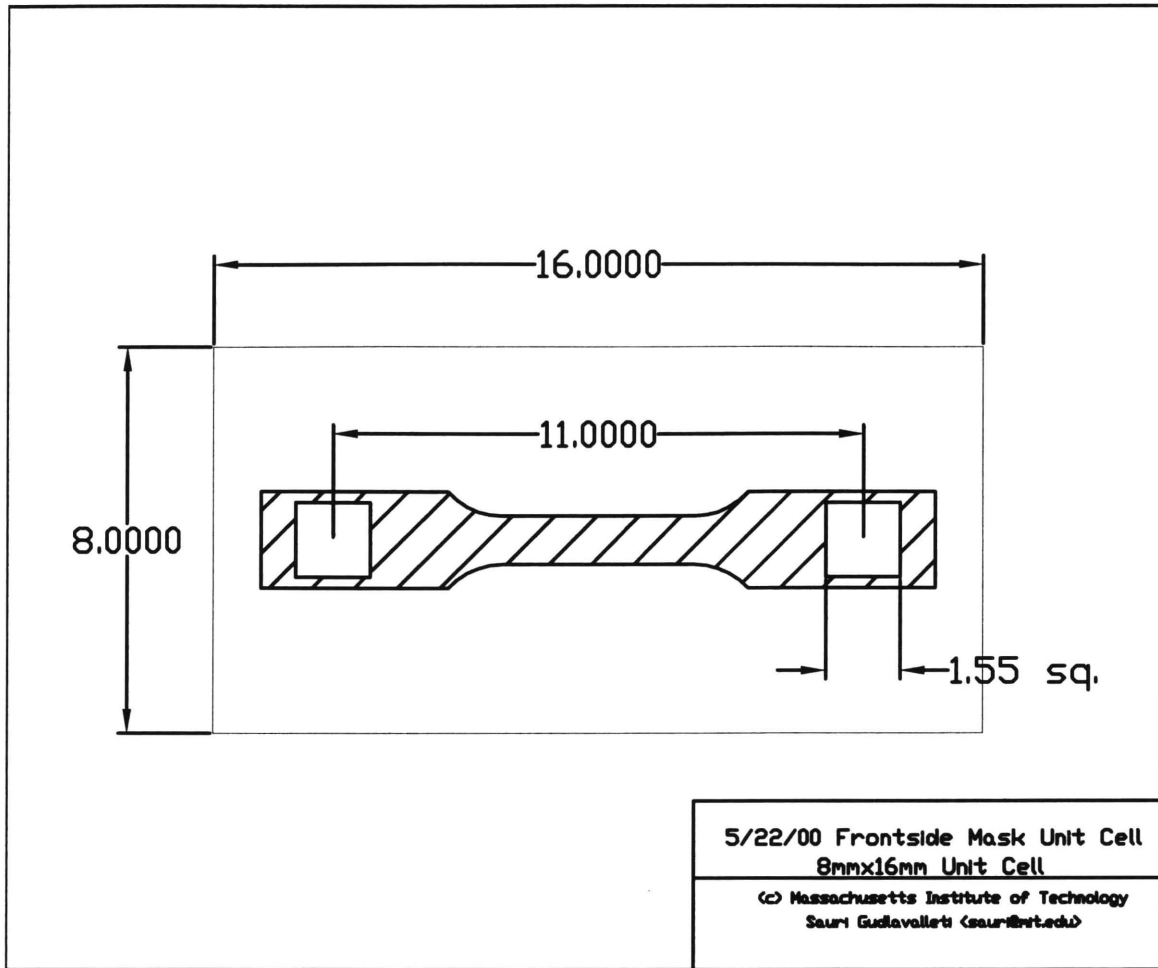


Figure E-19: Unit cell for backside mask. Dimensions are in mm.

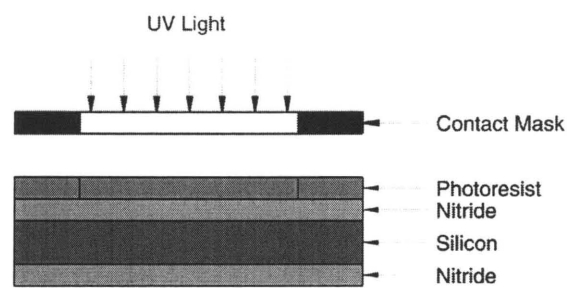


Figure E-20: Expose under backside mask.

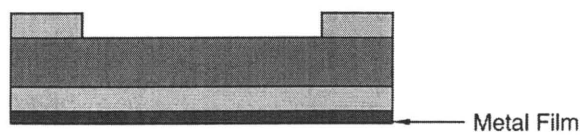


Figure E-21: The wafer now has a hard mask of nitride on the backside, and the patterned gold film on the front side.

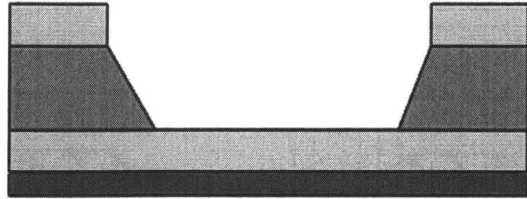


Figure E-22: Anisotropic etch of wafer using KOH.

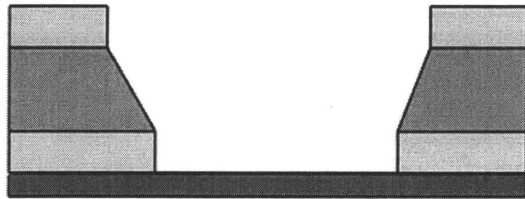


Figure E-23: Final step: Removal of nitride film.

Appendix F

MATLAB Script for Membrane Bend-Stretching Calculation

```
function [P,D]=numbend(filename,h)
L=2.75;
dmax=0.255
tets=load(filename);      % Load stress-strain data from file
dd=dmax/100;              % Set an increment in midpoint depth
i=1;                      % counter = 1
D(1)=0;                   % starting value of D and P are 0
P(1)=0;
tol=.0000001;            % Tolerance for convergence.
p=0;
for d=dd:dd:dmax          % start from 2nd point
i=i+1
lhs = sqrt(L^2+d^2)-L; % geometric measure of extension by pythagoras thm
dp = 0.001;             % Initial increment in load is 1 mN
p0=P(i-1)
p1=P(i-1)+dp           % new P is old P + 1 mN
rhs0=integrate(p0,d,h,L,tets);
rhs1=integrate(p1,d,h,L,tets);

iter1=1;
iter2=1;
```

```

maxiter1=20;
maxiter2=20;
% FIRST GET A p1 WHERE THE RHS > LHS
while(rhs1<lhs)
    iter1=iter1+1;
dp=2*dp;
    p1=p1+dp;
if(iter1>maxiter1)
    fprintf(1, 'MAXITER1 EXCEEDED');
    break;
end
end

% NOW INTERPOLATE FOR p
while((p1-p0)>tol)
    iter2=iter2+1;
if(iter2>maxiter2)
    fprintf(1, 'MAXITER2 EXCEEDED');
    break;
end
    p=(p0+p1)/2;
    rhs = integrate(p,d,h,L,tets);
if(rhs > lhs)
    p1=p;
else
    p0=p;
end
end

P(i)=p;
D(i)=d;
%figure(1)
%plot(D,P,'kp');
end
%%%%%%%%%%%%%%%%%%%%%%%%%%%%%%%%%%%%%%%%%%%%%%%%%%%%%%%%%%%%%%%%%%%%%%%%
function [W]=w(x)
L1=1.25;

```

30

40

50

```

w1=1;
w3=2;
R=1.5;
theta=acos(1-(w3-w1)(2*R));
L2=L1+R*sin(theta);
L3=2.75;
if (x < L1)
    W=w1;
elseif (x < L2)
    angle=asin((x-L1)/R);
    W=w1+2*R*(1-cos(angle));
else
    W=w3;
end
%%%%%%%%%%%%%%%%%%%%%%%%%%%%%%%%%%%%%%%%%%%%%%%%%%%%%%%%%%%%%%%%%%%%%%%%
function [integ]=integrate(P,d,h,L,tets)
dx=0.01;
integ=0;
e=0;
for x=0:dx:L
    sigma=P(h*atan(dL)*w(x));
    e=datf1(tets(:,1),tets(:,2),sigma);
    integ=integ + e*dx;
end
integ;
%%%%%%%%%%%%%%%%%%%%%%%%%%%%%%%%%%%%%%%%%%%%%%%%%%%%%%%%%%%%%%%%%%%%%%%%

```

60

70

80